NNT: 2024AIXM0277

DOCTORAL THESIS

Sustained at Aix-Marseille University

at October 2nd, 2024 by

Yosvany SILVA SOLÍS

A multiscale approach to modeling H interactions with the W/Cu interface: applications for the ITER divertor monoblocks

Discipline

Physics and Materials Science.

Specialty

Energy, Radiation and Plasma.

Doctoral school

Physics and Sciences of matter.
(ED 352)

Laboratory/ Research partners

Physics of the Interactions of Ions and Molecules (UMR 7345) /

Atomic Energy Commission of Cadarache (CEA-Cadarache) /

Centre National de la Recherche Scientifique (CNRS) /

EUROfusion /

Région Sud Provence-Alpes-Côte-d'Azur.

Jury composition

Flyura DJURABEKOVA Université de Helsinki	Reviewer
Kalle HEINOLA IAEA	Reviewer
Emeric BOURASSEAU IRESNE, CEA-Cadarache	Examiner
Marie-Pierre GAIGEOT UMR 8587, University of Evry Val d'Essonne	Examiner
Marie LANDEIRO DOS REIS UMR 7356, University of La Rochelle	Examiner
Jean-Paul CROCOMBETTE SRMP, CEA-Saclay	Jury President
Yves FERRO UMR 7345, Aix-Marseille University	PhD director
Etienne HODILLE IRFM, CEA-Cadarache	PhD co-director

Affidavit

I, undersigned, Yosvany Silva Solís, hereby declare that the work presented in this manuscript is my own work, carried out under the scientific direction of Dr. Yves Ferro and Dr. Etienne Hodille, in accordance with the principles of honesty, integrity and responsibility inherent to the research mission. The research work and the writing of this manuscript have been carried out in compliance with both the French National Charter for Research Integrity and the Aix-Marseille University charter on the fight against plagiarism.

This work has not been submitted previously either in this country or in another country in the same or in a similar version to any other examination body.

Marseille, on Friday 11th October, 2024.



This work is made available under the terms of the license
Creative Commons Attribution - Non Commercial - No Derivatives 4.0 International
(CC BY-NC-ND 4.0).

List of publications and participation in conferences

List of publications produced as part of the thesis project:

1. Y. Silva-Solís, et al. "A model of the W/Cu interface in the ITER cooling monoblocks from density functional theory". *Nuclear Materials and Energy* 37 (2023): 101516. doi: https://doi.org/10.1016/j.nme.2023.101516.

2. Y. Silva-Solís, et al. "Solution and solubility of H atoms at the W/Cu interface". *Journal of Physics and Condensed Matter* 36 (2024): 465001. doi: 10.1088/1361-648X/ad6f62.

Participation in events during the thesis period:

1. "Multi-scale modeling of H interactions on W surfaces and W/Cu interlayers."
   Y. Silva-Solís, J.D. Cremé, J. Denis, E. Hodille, and Y. Ferro
   Journées de la Matière Condensée
   Marseille, France. October 28-31, 2024.
   Accepted for an Oral Presentation
   https://jmc2024.sciencesconf.org

2. "Diffusion modelling of H isotopes through the W/Cu interface in the ITER cooling monoblocks."
   Y. Silva-Solís, J.D. Cremé, J. Denis, E. Hodille, and Y. Ferro
   The 11th International Conference on Multiscale Materials Modeling
   Prague, Czech Republic. September 22-27, 2024.
   Oral Presentation
   https://mmm11.ipm.cz

3. "Multi-scale modeling of H interactions on W surfaces and W/Cu interlayers."
   Y. Silva-Solís, J.D. Cremé, J. Denis, E. Hodille, and Y. Ferro
   Decennial IAEA Technical Meeting on Atomic, Molecular and Plasma–Material Interaction Data for Fusion Science and Technology
   Helsinki, Finland. July 15-19, 2024.
   Oral Presentation
   https://conferences.iaea.org/event/384

4. "Diffusion modeling of H atoms and defects formation at the W/Cu interface."
   Y. Silva-Solís, J.D. Cremé, J. Denis, E. Hodille, and Y. Ferro
   17th International Workshop on Hydrogen Isotopes in Fusion Reactor Materials (HWS 2024)
   Chamonix, France. May 19-22, 2024.
   Oral Presentation
   https://hws2024.sciencesconf.org

5. "Diffusion of H atoms and defects formation at the W/Cu interface in the ITER cooling monoblocks."
   Y. Silva-Solís, J.D. Cremé, J. Denis, E. Hodille, and Y. Ferro
   26th International Conference on Plasma Surface Interaction in Controlled Fusion Devices (PSI-26)
   Marseille, France. May 12-17, 2024.
   Poster
   https://www.psi26.com

6. "Diffusion and segregation of H atoms at the W/Cu interface in the ITER cooling monoblocks."
   Y. Silva-Solís, J. Denis, E. Hodille, and Y. Ferro
   Machine Learning Interatomic Potential School for Young and Early Career Researchers (ML-IP 2023 school)
   Espoo, Finland. November 6-10, 2023.
   Poster
   https://www.mlip-workshop.xyz

7. "Diffusion and segregation of H atoms at the W/Cu interface in the ITER cooling monoblocks."
   Y. Silva-Solís, J. Denis, E. Hodille, and Y. Ferro
   3rd Workshop on Artificial Intelligence in Plasma Science (WAIPS-3)
   Aix-en-Provence, France. June 29-30, 2023.
   Oral Presentation
   http://www.camt.eng.osaka-u.ac.jp/WAIPS3

8. "Diffusion and segregation of H atoms at the W/Cu interface in the ITER cooling monoblocks."
   Y. Silva-Solís, J. Denis, E. Hodille, and Y. Ferro
   XVII Condensed and Molecular Matter Physics Workshop
   Cuernavaca Morelos, Mexico. June 26-28, 2023.
   Oral Presentation

9. "Diffusion and segregation of H atoms at the W/Cu interface in the ITER cooling monoblocks."
   Y. Silva-Solís, J. Denis, E. Hodille, and Y. Ferro
   6th International Workshop on Models and Data for Plasma-Material Interaction in Fusion Devices (MoD-PMI 2023)
   Aachen, Germany. May 29-31, 2023.
   Oral Presentation
   https://www.events.fz-juelich.de/modpmi-2023

10. "Dissolution and segregation of H atoms at the W/Cu interface in the ITER cooling monoblocks."

Y. Silva-Solís, J. Denis, E. Hodille, and Y. Ferro
19th International Conference on Plasma-Facing Materials and Components for Fusion Applications (PFMC-19)
Bonn, Germany. May 22-26, 2023.
Poster
https://www.events.fz-juelich.de/pfmc-19

11. "Model for solution and segregation of hydrogen atoms at the tungsten/copper interface based on Density Functional Theory."
Y. Silva-Solís, J. Denis, E. Hodille, and Y. Ferro
Virtual Winter School on Computational Chemistry
Virtual event. February 6-10, 2023.
Single Figure Presentation
https://winterschool.cc

12. "Solution energy of hydrogen at the tungsten / copper interface from Density Functional Theory calculations."
Y. Silva-Solís, J. Denis, E. Hodille, and Y. Ferro
The 10th International Conference on Multiscale Materials Modeling
Baltimore, United States. October 2-7, 2022.
Poster
https://mmm10.jhu.edu

13. "Model for the solubility and diffusion of H at the W/Cu interface based on DFT."
Y. Silva-Solís, J. Denis, E. Hodille, and Y. Ferro
Flagship School: Machine Learning and Quantum Computing for Quantum Molecular Dynamics
Paris, France. September 5-9, 2022.
Poster
https://www.cecam.org/MLQCDyn

14. "Model for the solubility and diffusion of H at the W/Cu interface in the ITER cooling monoblocks."
Y. Silva-Solís, J. Denis, E. Hodille, and Y. Ferro
Canadian-Cuban-American-Mexican Graduate Student Conference
Virtual event. August 2-3, 2022.
Oral Presentation

15. "Model for the solubility and diffusion of hydrogen at the tungsten/copper interface based on Density Functional Theory."
Y. Silva-Solís, J. Denis, E. Hodille, and Y. Ferro
CCP5 Summer School: Molecular simulations methods
Durham, United Kingdom. July 17-28, 2022.
Poster
https://summer2022.ccp5.ac.uk

Résumé et mots clés

Le divertor de type ITER est constitué de monoblocs en tungstène (W) refroidis par de l'eau circulant dans des tubes en alliage de cuivre (CuCrZr), tandis que l'intercalaire entre le W et l'alliage CuCrZr est en cuivre pur (Cu). On s'attend à ce que les isotopes d'hydrogène (HIs) diffusent à travers les monoblocs et s'accumulent éventuellement à l'interface W/Cu, entraînant la formation et la stabilisation de défauts. Les phénomènes de ségrégation et de diffusion auront tous deux un impact sur les propriétés mécaniques des monoblocs et peuvent poser des problèmes de sécurité. Par conséquent, il est fondamental de déterminer la quantité de combustible ségrégué à l'interface et perdu à travers le divertor.

Si la solubilité et la diffusivité de l'hydrogène sont déjà connues dans le W pur et le Cu, elles doivent être établies à l'interface. Pour atteindre cet objectif, nous avons construit un modèle théorique de l'interface W/Cu adapté aux calculs de la théorie de la fonctionnelle de la densité (DFT). Deux orientations différentes de l'interface ont été considérées, les orientations $W(001)/Cu^{fcc}(001)R45°$ et $W(001)/Cu^{bcc}(001)$, qui minimisent le désaccord entre les réseaux Cu et W. Après la relaxation du système, les deux tendaient vers la même structure finale, $W^{bcc}(001)/Cu^{hcp}(11\bar{2}0)$, qui a été adoptée comme modèle pour l'interface en raison de son bon accord avec les observations expérimentales. L'énergie de solution et les propriétés vibratoires de H ont été déterminées à l'interface, révélant la plus faible valeur d'énergie de solution au niveau de l'interface.

Ces valeurs d'énergie de solution et les fréquences vibratoires de H à l'interface W/Cu ont été utilisées pour développer un ensemble canonique grand basé sur la théorie thermodynamique. Ce modèle a été utilisé pour déterminer la variation de la solubilité de H en fonction du potentiel chimique et de la température du réservoir H_2 dans des conditions d'équilibre thermique. Ce modèle a montré que la solubilité de H au niveau de l'interface W/Cu était plus élevée que dans les réseaux W et Cu, ce qui signifie qu'il y a une ségrégation des atomes de H à l'interface. Cependant, les valeurs de solubilité au niveau de l'interface W/Cu sont inférieures à celles dans un volume parfait de Cu^{bcc}, ce qui signifie plus généralement que la ségrégation des atomes de H pourrait ne pas nécessairement se produire au niveau de l'interface W/Cu mais dans le volume de Cu loin de l'interface.

Une fois les sites interstitiels les plus stables identifiés à l'interface, les barrières d'activation pour la diffusion de H le long de ces sites ont été déterminées. La reconstruction du réseau Cu à l'interface a modifié les barrières d'activation de H, montrant deux chemins différents où les valeurs passent de 0.8 eV à 0.24 eV. Ces valeurs ont été utilisées pour développer un modèle cinétique 0D. Dans ce modèle, la solubilité de H hors des conditions d'équilibre thermique a été déterminée ainsi que le temps nécessaire

pour atteindre l'état stationnaire. La solubilité de H obtenue pour le modèle cinétique, une fois l'état stationnaire atteint, a été comparée aux valeurs obtenues à partir du modèle thermodynamique, montrant un bon accord entre eux.

Pour généraliser notre modèle cinétique et déterminer la quantité de H piégée dans le volume de Cu loin de l'interface, nous avons déterminé jusqu'à quelle profondeur la distorsion de Cu^{hcp} se propage dans le volume de Cu^{fcc}. Pour ce faire, nous avons utilisé la Dynamique Moléculaire Classique (CMD) et étudié la frontière entre deux structures de Cu^{hcp}/Cu^{fcc}. Nous avons observé la formation de défauts (lacunes, lignes de dislocations) à la frontière Cu^{hcp}/Cu^{fcc} pour toutes les températures, accompagnés de différentes limites de grains. Une propagation plus profonde de la structure Cu^{fcc} dans Cu^{hcp} se produit avec l'augmentation de la température. De plus, plus mince est la couche de Cu^{hcp}, plus grande est la quantité de défauts. Cela pourrait conduire à une augmentation de la rétention des HIs à l'interface W/Cu avec l'augmentation de la température.

Mots clés : interfaces, DFT, thermodynamique statistique, dynamique moléculaire.

Abstract and keywords

The ITER-like divertor is built with tungsten (W) monoblocks cooled by water flowing in copper alloy (CuCrZr) tubes, while the interlayer between W and CuCrZr alloy is made of pure copper (Cu). Hydrogen isotopes (HIs) are expected to diffuse across the monoblocks and possibly accumulate at the W/Cu interface, leading to defects formation and stabilization. Both, segregation and diffusion, phenomenon will affect the mechanical properties of the monoblocks and can lead to safety issues. Therefore, it is fundamental to determine the amount of fuel segregated at the interface and lost through the divertor.

If the solubility and diffusivity of hydrogen are already known in pure W and Cu, they are to be established at the interface. To accomplish this objective, we built a theoretical model of the W/Cu interface that is well suited for Density Functional Theory (DFT) calculations. Two different interfaces were considered, the W(001)/Cu^{fcc}(001)R45° and W(001)/Cu^{bcc}(001) orientations which minimize the mismatch between the Cu and W networks. After the relaxation of the system both tended to the same final structure, $W^{bcc}(001)/Cu^{hcp}(11\bar{2}0)$, which was adopted as model for the interface due to its good agreement against experimental observations. The solution energy and the vibrational properties of H were determined at the interface, revealing the lowest value of solution energy at the plane of the interface.

Those values of solution energies and the vibrational frequencies of H at the W/Cu interface were employed to develop a grand canonical ensemble based on thermodynamic theory. Such a model was used to determine the variation of the H solubility as a function of the chemical potential and the temperature of the H_2 reservoir at thermal equilibrium conditions. This model evidenced that the H solubility at the plane of the W/Cu interface was higher than in the W and Cu networks, which means that at the interface there is a segregation of H atoms. However, the values of solubility at the plane of the W/Cu interface are lower than those in a perfect Cu^{bcc} bulk, which in a more general picture means that the segregation of H atoms could be not necessarily at the plane of the W/Cu interface but at the Cu bulk far away from the interface.

Once the most stable interstitial sites were identified at the interface, the activation barriers for diffusing H along them was determined. The reconstruction of the Cu network at the interface changed the activation barriers of H, showing two different paths where the values change from 0.8 eV to 0.24 eV. Those values were employed to develop a 0-dimensional kinetic model. In such model, the H solubility out of thermal equilibrium conditions was determined as well as the time necessary to reach the steady state. The H solubility obtained for the kinetic model, once the steady state was reached, were compared against the values obtained from the thermodynamic model reporting good agreement between them.

To generalize our kinetic model and determine the amount of H trapped in the Cu bulk far from the interface, we determine how deep the Cu^{hcp} distortion propagates into the Cu^{fcc} bulk. To do so, we employed Classical Molecular Dynamics (CMD) and studied the boundary between two structures of Cu^{hcp}/Cu^{fcc}. We observed formation of defects (vacancy, dislocations line) at the Cu^{hcp}/Cu^{fcc} boundary for all temperatures, which were also accompanied with different grain boundaries. A deeper propagation of the Cu^{fcc} structure into Cu^{hcp} occurs with increasing temperature. Moreover, the thinner the Cu^{hcp} layer, the higher the amount of defects. This could lead to an increase of HIs retention at the W/Cu interface with increasing temperature.

Keywords: interfaces, DFT, statistical thermodynamics, macroscopic rate-equation modeling, molecular dynamics.

Résumé substantiel

L'électricité régit notre mode de vie moderne et constitue l'essence même de la société contemporaine. Avec l'avènement des technologies et des télécommunications, la population mondiale a massivement migré des zones rurales vers les zones urbaines, ce qui a entraîné une augmentation de la demande et de la production d'électricité [1–3]. Toutefois, répondre à cette demande vitale est entravé par deux limitations majeures : les réserves limitées de combustibles fossiles et les conséquences néfastes du changement climatique causées par la pollution environnementale. Pour relever ce défi, l'humanité s'est tournée vers de nouvelles solutions énergétiques, dont la fusion nucléaire [4], bien que cette technologie soit encore loin d'être rentable et nécessite des études approfondies sur son fonctionnement [5].

Le projet ITER [6], en cours de construction à Cadarache, en France, a pour objectif de démontrer la faisabilité de la production d'énergie par fusion nucléaire. Soutenu par sept membres internationaux, ITER représente l'avenir des centrales électriques à fusion et est conçu pour atteindre plusieurs objectifs, notamment la génération de plasma de deutérium-tritium (D-T) et la production de 500 MW d'énergie de fusion. Bien que les réacteurs de fusion soient encore en cours de développement, de nombreuses recherches théoriques et expérimentales sont en cours pour garantir leur bon fonctionnement. Cette thèse se concentre sur la modélisation des interactions des atomes d'hydrogène (H) avec les matériaux dans la partie du divertor d'ITER, contribuant ainsi à la compréhension fondamentale de la fusion nucléaire et ouvrant la voie à des avancées technologiques majeures dans ce domaine.

Le divertor d'ITER revêt une importance cruciale pour le fonctionnement optimal du réacteur, étant constitué de 54 "ensembles de cassettes", chacun étant soutenu par une structure en acier inoxydable et contenant trois composants du plasma-facine (PFCs, abréviation anglaise pour Plasma-Facing Components) : les cibles verticales internes et externes, ainsi que le dôme (voir Figure 1.6-a). Ces cibles sont positionnées à l'intersection des lignes magnétiques, où se produit un bombardement de particules de haute intensité. L'énergie cinétique des particules de plasma à haute énergie qui entrent en collision avec ces cibles est convertie en chaleur, puis extraite par refroidissement actif à l'eau. Chaque ensemble de cassette du divertor comprend une séquence d'unités en contact avec le plasma, appelées module face au plasma (PFUs, abréviation anglaise pour Plasma-Facing Units). Ces PFUs se composent de chaînes de monoblocs de tungstène (W) fixées à un tuyau composé d'un alliage cuivre-chrome-zirconium (CuCrZr), avec une couche intermédiaire de cuivre (Cu) entre eux.

Les particules et ions provenant du plasma dans la cuve sous vide, avec de hautes valeurs d'énergie cinétique, frapperont les PFUs du divertor. Ce phénomène a le

potentiel d'impacter significativement les performances du plasma, surtout si les isotopes d'hydrogène parviennent à s'échapper à travers le divertor. De telles occurrences peuvent entraîner non seulement des pertes de combustible, mais aussi des problèmes de contamination du système, exacerbant ainsi la situation [7]. Par conséquent, la question suivante se pose : ces ions possèdent-ils suffisamment d'énergie cinétique pour pénétrer l'armure de les PFUs et atteindre l'eau de refroidissement à l'intérieur du tuyau CuCrZr ?

Pour répondre à cette question, plusieurs études expérimentales et théoriques ont été menées pour examiner la rétention et la diffusion des isotopes d'hydrogène à travers le divertor de type ITER [8–15]. Cependant, la motivation de ce travail est née de notre environnement de recherche local, notamment lorsque Hodille et al. [16] ont étudié la rétention du tritium dans le divertor de type ITER, à la fois sur des surfaces de W non endommagées et endommagées, en utilisant la théorie cinétique dans le code MHIMS (Migration des Isotopes d'Hydrogène dans les Métaux). Ils ont déterminé la rétention du tritium et la profondeur de migration en fonction du flux implanté et du nombre de cycles. Pour le W non endommagé, à une profondeur de 6 mm par rapport au point de frappe (l'emplacement de l'interface W/Cu dans les PFUs, illustré à la Figure 1.7), ils ont obtenu une rétention de T entre $0,02$ gm^{-2} et $0,1$ gm^{-2} environ lorsque le nombre de cycles passait de 10 à 384. En revanche, pour le W endommagé, la rétention de T variait approximativement de $0,05$ gm^{-2} à 5 gm^{-2} lorsque le nombre de cycles passait de 10 à 60 852.

Les résultats de Hodille et al. [16] ont été corroborés par Delaporte-Mathurin et al. [10] en utilisant le code FESTIM (Finite Element Simulation of Tritium In Materials). Les deux études ont montré que les isotopes d'hydrogène, par diffusion à l'intérieur des monoblocs de tungstène, peuvent effectivement atteindre l'interface W/Cu. Cependant, leurs résultats se limitaient uniquement à la région W car le comportement de l'hydrogène à l'interface W/Cu était inconnu à l'époque. Avant de pouvoir caractériser de manière exhaustive la diffusion et la ségrégation des isotopes d'hydrogène à travers l'ensemble des PFUs, il est impératif d'examiner d'abord leur comportement à l'interface W/Cu. Cette analyse est essentielle pour déterminer si les isotopes d'hydrogène peuvent infiltrer la région Cu et continuer leur migration vers le liquide de refroidissement. C'est de cette nécessité qu'est né le début de ce projet.

Nous avons présenté une approche multi-échelle reposant sur des calculs de structure électronique basés sur la théorie de la fonctionnelle de la densité (DFT, abréviation anglaise pour Density Functional Theory), la dynamique moléculaire classique (CMD, abréviation anglaise pour Classical Molecular Dynamics) et les théories cinétiques et thermodynamiques. La DFT fournit une description précise de la structure du matériau basée sur ses propriétés électroniques ; cependant, en raison de sa précision, elle est limitée à des systèmes comportant seulement quelques centaines d'atomes. En revanche, la dynamique moléculaire classique permet de simuler, avec une précision moindre que la DFT, des systèmes plus grands comprenant des centaines de milliers d'atomes. Cela permet d'étudier des défauts et des phénomènes qui dépassent le cadre de la DFT seule. Enfin, les théories cinétiques et thermodynamiques reçoivent en entrée les données atomiques fournies par la DFT et la dynamique moléculaire classique et délivrent en sortie des quantités physiques à l'échelle macroscopique. Une telle approche multi-échelle offre une compréhension globale de l'interaction des isotopes d'hydrogène avec l'interface W/Cu.

Deux modèles de l'interface W/Cu ont été construits pour les calculs DFT : W(001)/Cu^{bcc}(001) et W(001)/Cu^{fcc}(001)R45°. Chaque modèle comprend une supercellule de $2 \times 2 \times 8$ (constituée de 4 cellules de W et de Cu dans la direction Z) sans couche de vide, ce qui fait que les cellules de travail sont séparées de leurs images répliquées par une autre interface W/Cu. Après une relaxation complète des modèles, les deux ont convergé vers la même structure $W^{bcc}(001)/Cu^{hcp}(11\bar{2}0)$, où le réseau de Cu est passé de ses structures initiales Cu^{bcc} et Cu^{fcc} à Cu^{hcp}. Cette reconstruction du réseau de Cu a été induite pour correspondre à la reconstruction de la surface $W^{bcc}(001)$ et était cohérente avec les résultats expérimentaux précédents [17, 18]. Cette reconstruction a stabilisé l'interface en réduisant le décalage entre les surfaces $Cu^{hcp}(11\bar{2}0)$ et $W^{bcc}(001)$ à 2.28%. Ce modèle d'interface a ensuite été utilisé pour incorporer H et déterminer sa rétention et sa diffusion.

Quatre-vingt-seize structures différentes de $W^{bcc}(001)/Cu^{hcp}(11\bar{2}0)$ ont été créées avec diverses positions interstitielles pour l'atome d'hydrogène à proximité de l'interface. Après la relaxation du système W/Cu+H, seules cinquante-trois positions ont conservé leur stabilité, tandis que les atomes d'hydrogène dans les quarante-trois autres sites ont migré vers ces sites stables. L'énergie de solution et les propriétés vibratoires de l'hydrogène ont ensuite été évaluées dans chacun de ces sites stables, ainsi que dans les volumes de W et de Cu pour comparaison. L'énergie de solution au plan de l'interface W/Cu était la plus basse parmi les sites environnants, avec une valeur de 0.46 eV. Cependant, cette valeur est comparable à celles obtenues dans les volumes Cu^{fcc}_{per} et Cu^{fcc}_{dis}, où certains sites ont donné des valeurs de 0.41 eV et 0.43 eV, respectivement. À partir de ces résultats, nous ne pouvons pas conclure qu'il y a ségrégation de l'hydrogène à l'interface W/Cu, car des valeurs plus basses d'énergie de solution ont été trouvées plus loin de l'interface, là où le Cu est censé avoir sa structure Cu^{fcc}_{per} la plus stable. Par conséquent, la question de savoir si les atomes d'hydrogène se ségrégueront à l'interface W/Cu est restée sans réponse à ce stade de la recherche.

Pour aborder cette question ouverte, un modèle thermodynamique a été développé en utilisant les données DFT précédentes pour déterminer la solubilité de l'hydrogène en fonction de la température du gaz et du potentiel chimique. Nous avons supposé que l'interface W/Cu était en équilibre avec un réservoir de H_2 dans un ensemble grand-canonique. Comme précédemment, le même modèle a été appliqué aux structures de Cu et de W pour comparaison. Le réservoir de H_2 a été traité à la fois comme un gaz idéal et réel, en utilisant la paramétrisation de référence [19]. Cette approche a montré que la solubilité de l'hydrogène au plan de l'interface W/Cu était plus élevée que dans les réseaux de W et de Cu au sein de la supercellule W/Cu. Cela était dû à la plus faible énergie de solution au plan de l'interface par rapport à d'autres sites au sein de la supercellule $W^{bcc}(001)/Cu^{hcp}(11\bar{2}0)$. Cependant, la solubilité de l'hydrogène dans le volume Cu^{fcc}_{per} était plus élevée qu'au plan de l'interface, suggérant que les atomes d'hydrogène ne se ségrégueront pas à l'interface mais se ségrégueront plutôt dans la couche intermédiaire de Cu au sein des PFUs. Néanmoins, ce résultat appartient au système dans des conditions d'équilibre. Qu'en est-il de l'évolution des atomes d'hydrogène avant que l'équilibre soit atteint ? En d'autres termes, comment les atomes d'hydrogène se comportent-ils dynamiquement dans des conditions non équilibrées ? Cela nous a amenés à la théorie cinétique, où nous avons pu comprendre la variation de la concentration d'hydrogène, et par conséquent sa solubilité, en fonction du temps dans des conditions non équilibrées.

Pour étudier la diffusion des atomes d'hydrogène, la détermination des barrières d'énergie d'activation est essentielle. Nous sommes donc revenus à notre modèle DFT où, en utilisant la méthode Nudged Elastic Band (NEB), ces barrières d'activation ont été déterminées le long de trois chemins de diffusion différents. Des calculs NEB, nous avons découvert que les plans (001) et (002) de l'interface W/Cu possèdent des propriétés de diffusion distinctes en raison de leurs différentes barrières d'activation au sein du réseau de Cu. Aucune variation n'a été observée dans le réseau de W en raison de la reconstruction du $W^{bcc}(001)$, qui ne s'étend pas dans le volume, mais la reconstruction dans le réseau de Cu a entraîné une disposition de canaux étroits et larges le long de la direction Y. Les sites considérés dans le plan (001) étaient situés dans un canal étroit, tandis que ceux du plan (002) se trouvaient dans un chemin plus large. Par conséquent, les énergies d'activation dans le plan (001) étaient plus élevées que celles dans le plan (002), influençant directement la diffusion de l'hydrogène à travers l'interface W/Cu.

Une fois toutes les barrières d'activation déterminées, notre première étape a été de calculer le coefficient de diffusion des atomes d'hydrogène parallèlement au plan de l'interface W/Cu en utilisant l'équation d'Arrhenius. Nous avons observé une diffusivité plus faible à ce plan par rapport aux volumes de W et Cu purs. En nous concentrant sur la supercellule W/Cu et en intégrant les résultats du modèle thermodynamique avec ceux de l'équation d'Arrhenius, il devient évident que les atomes d'hydrogène s'accumuleront au plan de l'interface. Cette conclusion peut sembler contredire notre modèle thermodynamique, mais ce n'est pas le cas. Le modèle thermodynamique indique que le plan de l'interface W/Cu et le volume de Cu^{fcc}_{per} présentent une haute solubilité de l'hydrogène à l'équilibre. Cependant, ces régions sont séparées par la région reconstruite Cu^{hcp}, qui a une solubilité en hydrogène beaucoup plus faible. Les atomes d'hydrogène provenant du côté W atteindront d'abord l'interface W/Cu, où ils rencontreront une diffusivité plus faible et une solubilité plus élevée, ce qui les conduira à s'accumuler initialement là. Avec le temps, les atomes d'hydrogène commenceront à diffuser à travers la région reconstruite Cu^{hcp} et atteindront finalement le volume de Cu^{fcc}_{per}, où ils trouveront des sites plus stables. Par conséquent, lorsque l'équilibre sera atteint, la solubilité dans le volume de Cu^{fcc}_{per} sera plus élevée que dans le plan de l'interface W/Cu.

Après avoir caractérisé la diffusion parallèle au plan de l'interface, nous avons étudié la diffusion des atomes d'hydrogène à travers l'interface W/Cu, perpendiculairement au plan. Nous avons construit un modèle cinétique à 0 dimension qui considère les réactions de piégeage/dépiégeage des atomes d'hydrogène interstitiels au sein de l'interface W/Cu. Ce modèle visait à déterminer comment la concentration d'hydrogène évolue avec le temps, en fixant la concentration d'hydrogène dans le réseau de W à l'interface. Les résultats ont montré que les sites correspondant au chemin qui se trouvait principalement dans le plan (002), atteignaient une stabilisation transitoire au début du processus de diffusion. Pendant cette période, les atomes d'hydrogène ont commencé à diffuser du plan (002) vers le plan (001), conduisant à une concentration inhomogène d'hydrogène à l'interface W/Cu. Ce phénomène a également été observé à l'interface Be/BeO [20]. La fréquence caractéristique du système, définie comme l'inverse du temps nécessaire pour atteindre un état stable, a été déterminée. Cela nous a permis de modéliser la dynamique des atomes d'hydrogène à travers l'interface W/Cu en utilisant un système simplifié avec une seule barrière d'activation de 1.01 eV et une fréquence de vibration de 7.84×10^{12} Hz.

Comme mentionné précédemment, les régions avec une plus grande solubilité pour les atomes d'hydrogène - le plan de l'interface W/Cu et le volume Cu^{fcc}_{per} - sont séparées par

la structure reconstruite Cu^{hcp}. Ainsi, la question suivante se pose : quelle est l'épaisseur de ces couches de Cu reconstruites ? En d'autres termes, jusqu'à quelle profondeur la reconstruction induite par l'interface W/Cu se propage-t-elle dans le volume de Cu ? Pour répondre à cette question, des simulations de dynamique moléculaire classique ont été réalisées sur les frontières $Cu^{hcp}/Cu^{fcc}_{per}(\theta = 0°)/Cu^{hcp}$ et $Cu^{hcp}/Cu^{fcc}_{per}(\theta = 28°)/Cu^{hcp}$. Notre objectif était uniquement de caractériser ces deux frontières en examinant la création de défauts ponctuels et étendus. Il a été obtenu que la Cu^{hcp} ne se propage pas dans le volume Cu^{fcc}_{per}, mais l'inverse. La propagation de la frontière de grain entre la Cu^{hcp} et la Cu^{fcc}_{per} a été accompagnée d'une augmentation des défauts ponctuels tels que les lacunes et les atomes auto-interstitiels de Cu, et des défauts 1-D tels que les lignes de dislocation. À mesure que la température augmente, la propagation de ces défauts devient plus marquée dans la Cu^{hcp}, ce qui signifie qu'une augmentation des défauts se produira à proximité de l'interface W/Cu en raison de la recristallisation du Cu.

Naturellement, de tels défauts auront un impact significatif sur la solubilité et la diffusion des atomes d'hydrogène au sein et à travers l'interface, des aspects qui n'ont pas été pris en compte dans cette étude. Aborder ces complexités nécessitera des modèles plus sophistiqués qui tiennent compte des défauts, ce qui sera l'objectif des prochaines étapes de ce projet. Développer un potentiel interatomique W-Cu et W-Cu-H nous permettra de modéliser entièrement l'interface W/Cu en utilisant la dynamique moléculaire classique, en tenant compte des défauts. Bien que cette recherche ait commencé avec des systèmes idéalisés pour fournir une perspective initiale, nous reconnaissons qu'il ne s'agit que du début, et qu'il y a beaucoup plus à explorer et à comprendre.

Ce travail visait à améliorer notre compréhension de la rétention et de la diffusion des atomes d'hydrogène à l'interface W/Cu, un système d'intérêt pour les PFU du divertor de type ITER. Bien que cette étude ne soit probablement qu'une petite contribution à une vaste quantité de recherches, nous pensons qu'elle met en lumière un autre aspect important de la rétention de l'hydrogène dans les PFC, crucial pour le fonctionnement sûr des machines de fusion comme ITER. Nous espérons avoir capté l'attention du lecteur et démontré avec succès que l'interface W/Cu agit comme un puits pour les atomes d'hydrogène, conduisant à leur ségrégation et favorisant la formation de défauts, un phénomène ayant des implications significatives pour la durée de vie des PFC et la faisabilité technologique et économique des futures centrales à fusion.



Les lecteurs peuvent apprécier des objets 3D et des animations de simulations de dynamique moléculaire en scannant le code QR fourni ci-dessus ou en visitant le site web suivant https://yosvanyss.github.io/phd_thesis [21].

Acknowledgments

This journey is nearly reaching its end. However, as my epigraph highlights, the journey itself holds more significance than the destination. Naturally, this journey has been memorable thanks to the people who stood by me and supported me over these three years. To steer clear of any rumble, I have chosen to acknowledge each of you in chronological order, based on when I met you. However, I had to break this rule for my wife (who insisted on being first!) and my family.

Despite her insistence on being mentioned first, I couldn't complain because she truly deserves it - my wife, Yamila. If I am achieving this milestone in my life today, it is only because of her unconditional support. She willingly put her dreams and aspirations on hold so that I could chase mine. Such sacrifices are made only by someone who truly loves you, and the least I can do is break my rule of chronological acknowledgments and give her the place she indisputably deserves - the first. Certainly my name appears as the author of this work, but she is undoubtedly the most important co-author.

Secondly, I must extend my heartfelt gratitude to my entire family. If I am the person I am today, it is thanks to the nurturing and education I received from my mom and my grandmother (God rest her soul). I wish I could name each and every one of them, but my goodness, I have such a large family, and it would be unfair to leave anyone out. However, I must especially thank my cousins Adrián and Yadián, and my uncles Alexander and Yolanda, who spared nothing and supported me wholeheartedly during the beginning of my Ph.D. journey.

And now, let's embark on our journey through chronological order. When I was accepted for this thesis, I experienced a blend of happiness and fear. I was on the verge of completely changing my life and career. Alejandro GUTIÉRREZ QUINTANILLA was the person who initially dispelled this fear. He welcomed me into his home and his family: Linnavel and Alejandra. They helped me gradually immerse myself in French culture. Linnavel even taught me how to enjoy foie gras and marmalade with bread. Alejandra, on the other hand, was my first French teacher, guiding me to flawlessly pronounce "Au revoir." Thank you all for being a part of my life and making my transition from Communism to Capitalism smoother.

I will forever be indebted to Eric ROSTANG. He assisted me with all the paperwork here in France, helped me find a place to live, and set up a bank account. He even went out of his way to pick me up from the airport when I arrived from Cuba, my very first time in France. Thank you for being such a dependable person and helping every Ph.D. student during our accommodation process.

The next person I had the pleasure of meeting in person was "el Comandante," my supervisor Yves FERRO. I'll never forget the first time I saw Yves; he was engrossed in a bibliographic review for a paper by Julien, surrounded by a towering stack of papers on his desk, and I thought to myself, "this is going to be tough." But it turned out to be quite the opposite. I consider myself extremely fortunate to have had him as my supervisor. He is a *crack*[1] in DFT and thermodynamics and possesses a teaching spirit that enables him to explain things in a way that everyone can grasp. I am extremely proud that over the years more than a supervisor, he was more like a friend, which made working together really easy. Thank you for all your knowledge and unconditional support.

Once I met Yves, he brought me to my office where there was the best friend I did during my Ph.D., "Juliano" also known as Julien DENIS. This guy is solely responsible for my transition to capitalism. He introduced me to McDonald's, took me to live soccer matches, and immersed me in electronic music festivals. It's worth noting that he did an impeccable job of selling Marseille to me. He's the crack who knows every breaking news about fusion science and the pickiest person you could ever meet. His partner, Marion, also played a pivotal role during my Ph.D., meticulously reviewing my CVs and cover letters for PostDoc applications. So, if any of you have ever come across my CVs or cover letters, they were meticulously vetted by Marion beforehand. Thank you both for being such important pillars in my life here.

I knew that my thesis would be co-supervised by a certain Etienne HODILLE and I was expecting a person in his 50s as Yves, but I wasn't the case. The first time I met Etienne I was in shock when Julien introduced him to me. I couldn't understand how someone so young could be a thesis co-director with such an impressive h-index. Needless to say, I baptized him as the biggest crack, hence we call him "Crackodille". He is the most reliable person you could ever work with and probably one of the cleverest and most productive person I've ever met. Remarkably, he is also incredibly humble and strikes the best poses for the group photos. Thank you so much, Crackodille, for being an inspiration to me.

I have to especially thank two people who were fundamental in improving my French over these three years: Manon and Anabel. They were my first French teachers (after Alejandro's daughter) and were incredibly patient with me. I remember starting with a French level of A-1, not even A0, and they, especially Manon, stood by me, working on it for two years. I will always be grateful for all the support and the warm welcome you extended to me and my wife.

I'd also like to thank our team, PATP, for their valuable advice on my presentations, which helped me improve them significantly. Especially, I must express my gratitude to a particular crack: Paul GÉNÉSIO. He was an essential person in everything related to programming, he understands computers in a way I have never seen anyone else do before. I remember a time when we were stuck with a code that kept crashing due to RAM memory issues. We spent an entire morning trying to figure out why, but eventually, we gave up and went to see Paul. In just 10 minutes, he understood the architecture of our code and identified the crashing lines. Truly a crack. Thanks for everything, Paul; I learned a lot from you and enjoyed every lunch we shared together.

I would also like to extend my thanks to another member of our team, Yannick MARANDET, who, after being bombarded with my endless questions about fusion,

[1] Term used by myself to defined a brilliant and cleaver person.

handed me the book "An Indispensable Truth" just to save his sanity. This book greatly helped me understand the historical background of fusion science. Additionally, I must thank Daniel GUERROUDJ for our early morning discussions. He helped me occasionally disconnect and get some exercise by making me trek from my office to his. Of course, I can't wrap up this paragraph without giving thanks to Madhusudan RAGHUNATHAN, Madhu. His engaging discussions and support have been essential in helping me manage stress over these past months.

Of course, the administrative staff of my lab have to be acknowledged in this section, especially Hulya KIRMACI, who guided me through every mission and managed them within ETAMINE and NOTILUS. Without Hulya's guidance, I would never have been able to embark on any missions, and, more importantly, to receive reimbursement for them. She exemplifies that machines cannot replace human beings.

In my last year of Ph.D., Yves recruited another Cuban student, José David CREMÉ, to continue developing this project. We were already acquainted, having begun our careers together in Cuba at the same university and in the same classroom. Life is much easier when you have a compatriot in the same city! He and his wife, Amisadai, were crucial for releasing stress during this last year when everything comes at the same time. Thanks a lot, guys, because your presence made this journey more enjoyable and less daunting, and for sharing both the laughs and the challenges.

The last person I met in our team arrived right after José David: David GARRIDO GONZÁLEZ, the "Golfillo gallego." He entered my life just to complain about the font sizes of my plots in Python, but I have to admit, he was right. Every time I was stuck on how to program something, I went to see him, and he was always ready to use ChatGPT to find an answer. I'm joking; the guy is a crack at programming and everything related to AI. He was constantly giving me new tips that I didn't know about Python programming. I have to say, my programming skills improved a lot thanks to him.

Last, but certainly not least, I have to thank Márcio SOARES. I met this guy at an Autumn School in Finland, and we hit it off right away. He was the one who taught me how to export my atomic structures as 3D objects in VMD and also how to create my own websites using GitHub.io. If today you can enjoy all of this animations in https://yosvanyss.github.io/phd_thesis [21] and in my presentations is only thanks to him.

I would like to conclude this section by expressing my sincere gratitude to EUROfusion, PACA Région, and the Fédération de Recherche sur la Fusion par Confinement Magnétique (FR-FCM) for sponsoring our research project.

Thank you all for being part of this journey and making it such an unforgettable experience.

¡MUCHAS GRACIAS POR TODO!

Jim Carrey once said:
"Behind every great man
is a woman rolling her eye".
I don't consider myself a great man,
but this endeavor was only possible thanks
to the unconditional support of my wife.
To her, who was extremely patient
and was always there for me,
even on the tough days.

"Life before death, strength before weakness, ***journey before destination****."*

Brandon SANDERSON.[1]

[1]B. Sanderson. "The Way of Kings" (The Stormlight Archive, Volume 1). Tor Books (2010).

Preface

Electricity power governs our way of life, it constitutes the soul of the modern society. In this new age of the technologies and telecommunications the world's population started to emigrate from rural zone to urban ones. This process has been increasing last decades up to the point that, in 2014, 54% of the world's population live in urban areas, up from 30% in 1950 and it is predicted that for 2050, 66% of the world's population will live in urban zones [1]. This "urban transition" brings with it an increment of electricity demand and, of course, electricity production. But supplying this vital demand is not a straightforward task due to there are two essential limitations to consider. For one side, the fossil fuels reserves are limited, in 2021 the remaining proven reserves of fossil fuel in the world was 1752 billion barrels of oil, 21 trillion cubic meters of natural gas and 1075 billion tonnes of coal [2, 3]. For the other hand, the climate change has become more and more prominent due to the environmental pollution [22]. In 2021, they were registered 36.6 gigatonnes of CO_2 that were emitted into the environment from the energy sector (the largest ever annual rise in emissions) and 4.2 million people experimented a premature death as direct consequence of the air pollution [2, 3]. To deal with this energy demand in an ecological way, the human being has been forced to look for new ways to produce energy. One of these new solutions is fusion power [4], which seems to be a promising solution but, like new technology, it is still far away from being rentable and it has a lot to be studied regarding the correct operation of the nuclear fusion reactors [5].

Nowadays, it is not possible to produce energy (with industrial purposes) from fusion reactors due to it is necessary more energy to produce the fusion of the nuclei than the energy extracted from the reactor. To tackle this problem and locking forward more complex and bigger machines, in 1985 at the Geneva Superpower Summit an international project to develop fusion energy was proposed and, in this way, the ITER ("The way" from Latin and originally an acronym for "International Experimental Thermonuclear Reactor") fusion project began to take its first steps. ITER is being built at Cadarache, France, with the main goal to provide the feasibility of producing energy from the nuclear fusion and it is supported by seven members: China, European Union, India, Japan, Korea, Russia and United States. As its acronyms indicates this reactor will point the way for the fusion power plants of the future and, therefore, it has been designed to accomplish the following tasks: achieve a deuterium-tritium plasma, generate 500 MW of fusion power, contribute to the integrated operation of technologies, test tritium breeding and demonstrate the safety features of a fusion power plant [6].

As ITER tokamak[2] is still under construction, a lot of experimental and theoretical

[2]The word *tokamak* comes from the Russian acronym for "toroidal chamber with magnetic coils". It is an experimental machine developed by the soviets in the mid-1950s with the goal of using fusion energy.

research work is being carried out with the goal of achieving the correct functioning of the reactor. A lot of scientists from different fields are contributing their small grains of sand to make fusion possible, such as physics, electrical engineering, mechanical engineering, computational mechanics, robotics, diagnostics, plasma operations, software engineering, mechatronics engineering, civil engineering, material science, chemistry and so on [6]. This thesis is an example of one of those theoretical works developed in the material science field, which is focused on describing the interactions of hydrogen isotopes with the materials in the divertor part, specifically in the interface between tungsten and copper.

The following chapters will explain how our theoretical model was created to study the interaction of hydrogen isotopes with the atoms at the tungsten/copper interface in the cooling monoblocks of the ITER's divertor. Also, we will summarize important concepts from quantum mechanics which will help to the readers understand the physics behind the results that are shown and the methods employed. Of course, these concepts have been summarized to achieve a logical sequence in the explanation, otherwise, this work would be huge, boring and hard to read. If the reader is interesting going deeper in the ideas exposed here, I recommend any modern book on quantum mechanics. I hope you enjoy reading as much as I have enjoyed writing.

The author.



Readers can appreciate 3D objects and animations of Molecular Dynamic simulations by scanning the QR code provided above or visiting the following website https://yosvanyss.github.io/phd_thesis [21].

Contents

Affidavit i

List of publications and participation in conferences iii

Résumé et mots clés vii

Abstract and keywords ix

Résumé substantiel xi

Acknowledgments xvii

Preface xxv

Contents xxx

List of Acronyms 1

1 Introduction 3

1.1 Nuclear fusion 3

1.2 Magnetic confinement 5

1.2.1 The stellarator system 6

1.2.2 The tokamak system 6

1.3 The world's largest tokamak: ITER 9

1.3.1 The ITER divertor 11

1.4 Motivation 12

1.4.1 The W/Cu interface 13
1.5 Structure of the manuscript 16

2 Density Functional Theory 19
2.1 Schrödinger equation 19
2.1.1 Many-particle systems 20
2.2 The Born-Oppenheimer approximation 22
2.2.1 Solving the electronic problem 23
2.3 The variational principle 24
2.4 The Hartree-Fock approximation 25
2.5 Electron density 28
2.5.1 Reduced density matrices for fermions 28
2.5.2 Exchange-correlation hole 31
2.6 Density-Functional Theory 34
2.6.1 The Thomas-Fermi model 35
2.6.2 The Thomas-Fermi-Dirac model 35
2.6.3 The Hohenberg-Kohn theorems 36
2.6.4 The Kohn-Sham approach 39
2.6.5 Different kinds of exchange-correlation functionals 43

3 A model of the W/Cu interface 47
3.1 Presentation of the study 47
3.1.1 Mismatch parameter 47
3.1.2 Convergence studies 51
3.2 Publication 56

4 Solution and solubility of H at the W/Cu interface 63
4.1 Presentation of the study 63
4.1.1 Thermodynamic model for H solubility 64

4.1.2 Solution energy of H at the W/Cu interface 69
4.2 Publication 71

5 Diffusion of H at the W/Cu interface 87

5.1 Presentation of the study 87
5.1.1 Diffusion parallel to the plane of the interface 89
5.1.2 Diffusion perpendicular to the interface 92
5.2 Publication 96

6 Propagation of the reconstruction in the Cu network 123

6.1 Misfit parameter 123
6.1.1 Supercell of the boundaries 125
6.2 Molecular Dynamics simulation setup 128
6.2.1 Interatomic potential 128
6.2.2 Geometry of the boundaries 129
6.2.3 Sequence of calculations 130
6.2.4 Physical quantities 130
6.3 Volume relaxation simulations 132
6.3.1 $Cu^{hcp}/Cu^{fcc}_{per}(\theta = 0°)/Cu^{hcp}$ supercell 132
6.3.2 $Cu^{hcp}/Cu^{fcc}_{per}(\theta = 28°)/Cu^{hcp}$ supercell 133
6.4 NPT ensemble 136
6.4.1 $Cu^{hcp}/Cu^{fcc}_{per}(\theta = 0°)/Cu^{hcp}$ supercell 136
6.4.2 $Cu^{hcp}/Cu^{fcc}_{per}(\theta = 28°)/Cu^{hcp}$ supercell 137
6.4.3 Point and extended defects 138
6.5 NVE ensemble 139

General conclusions 141

A Quantum states and Dirac notation 145

B Mismatch representations **149**

C Molecular dynamics simulations **151**

C.1 Volume relaxation of the boundaries 151

C.2 NPT ensembles 153

C.3 NVE ensembles 157

Bibliography **159**

List of Acronyms

AES	Auger electron spectroscopy
bcc	Body-centered cubic
BOA	Born-Oppenheimer approximation
CMD	Classical Molecular Dynamics
CNA	Common Neighbor Analysis
D	Deuterium
DXA	Dislocation Extraction Algorithm
DFT	Density functional theory
EBSD	Electron backscattered diffraction
EDS	Energy dispersive spectroscopy
fcc	Face-centered cubic
FEM	Field emission microscopy
GGA	Generalized gradient approximation
hcp	Hexagonal close packed
HRTEM	High resolution transmission electron microscopy
hTST	harmonic Transition State Theory
TST	Transition State Theory
ico	Icosahedral
ITER	"The way" from Latin, and originally an acronym for "International Experimental Thermonuclear Reactor"
JET	Joint European Torus
KS	Kurdjumov-Sachs crystallographic orientation
LDA	Local Density Approximation
LEED	Low-energy electron diffraction
LEEM	Low-energy electron microscopy
μLEED	Micro low-energy electron diffraction
MHIMS	Migration of Hydrogen Isotopes in Metals
NW	Nishiyama-Wassermann crystallographic orientation
Oh	Octahedral interstitial site
PFCs	Plasma-facing components
PFUs	Plasma-facing units
PTM	Polyhedral Template Matching

RHEED	Reflection high energy electron diffraction
SOL	Scrapped-off layer
Td	Tetrahedral interstitial site
T	Tritium
TDS	Thermal desorption spectrometry
TEM	Transmission electron microscopy
SEM	Scanning electron microscopy
ZPE	Zero-point energy

Chapter 1

Introduction

This chapter aims to provide an introduction to nuclear fusion alongside key concepts from nuclear and plasma physics. Sections 1.1 and 1.2 offer brief discussions on fundamental ideas pertaining to nuclear reactions and the magnetic confinement of plasma in nuclear reactors. Following this, Section 1.3 delves into an examination of the ITER tokamak and its primary components. The chapter concludes by elucidating the motivation behind the project and summarizing previous studies that contribute to our understanding of the current state of the W/Cu interface system, which is the focus of our interest.

1.1 Nuclear fusion

Nuclear fusion is a nuclear reaction where two or more atomic nuclei are fused to create one or more different atomic nuclei, subatomic particles like neutrons or protons, and energy. It was discovered in the 20's when, in 1924, Eddington [23] suggested that the primary source of stellar energy was the fusion of hydrogen (H) nuclei into helium (He); fact that was proved by Atkinson and Houtermans [24], in 1929, who theoretically demonstrated that huge amounts of energy could be released by fusing light nuclei. Its first experimental observations were done by Oliphant and Rutherford [25–28], in the early 30's, who used a particle accelerator to fire deuterium ($^{2}_{1}$H or D) at different targets, discovering the helium-3 ($^{3}_{2}$He) and tritium($^{3}_{1}$H or T) isotopes, and giving rise to the first case of human-caused fusion.

There are some basic concepts of nuclear physics that needs to be presented for a better comprehension of what we will present hereafter. *Binding energy* is the term used by physicists to measure the energy which the nucleons[1] are hold themselves together with. Its value is on the order of magnitude of MeV and it changes among the different elements of the periodic table, as it is shown in Figure 1.1. There, it is appreciable that elements close to the middle of the periodic table have the greatest values of binding energy per nucleon, which means that their nucleons are more tightly bound each other. At the pick of the curve, with the highest value of binding energy per nucleon, is the iron-56 ($^{56}_{26}$Fe) isotope with 8.79 MeV approximately. In a nuclear reaction, energy is released when product nuclei have higher binding energy than reactant nuclei. If the reactants are

[1] Nucleons is a term used to refer to the components of atomic nucleus: either a proton or a neutron.

heavy elements (right tail of the curve) like uranium (U), to reach elements with higher binding energy , it is necessary to split it to get nuclei with lower mass number, which is the well-known *nuclear fission*. On the contrary, if the reactants are light elements (left tail of the curve) like hydrogen, to get higher values of binding energy, it is necessary to fuse them in order to obtain nuclei with higher mass number, which is precisely nuclear fusion.

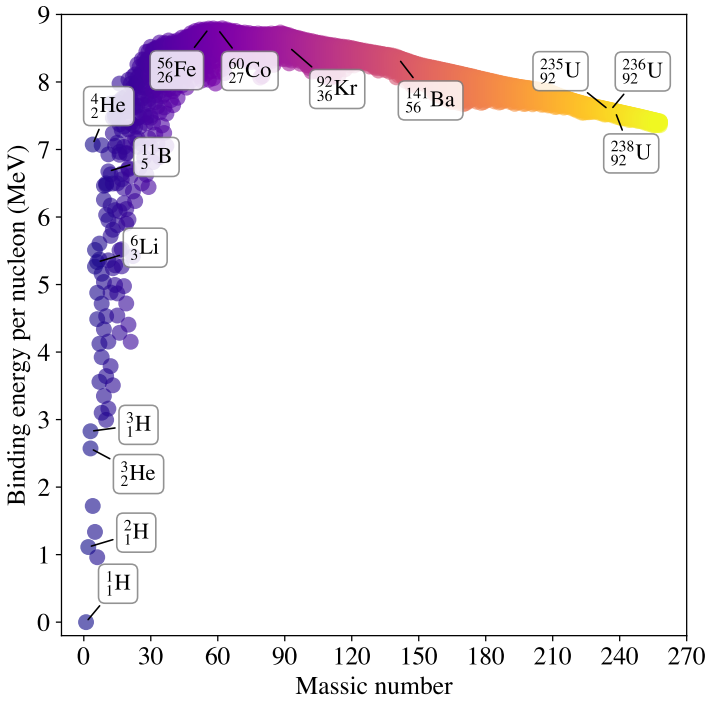

Figure 1.1. Binding energy per nucleon. Data extracted from reference [29].

The total energy produced or consumed by a nuclear reaction is inferred from the mass difference between products and reactants. It follows from Einstein's equation that energy and mass can be converted into each other:

$$\Delta E = \Delta m c^2, \tag{1.1}$$

where ΔE is the energy released in the reaction, $\Delta m = m_r - m_p$ represents the invariant mass between reactants (m_r) and products (m_p), and c is the velocity of light. Since c is a very large number, c^2 is even much larger, and a small values of Δm leads to a large energy amount. Since the ultimate goal of nuclear fusion is to provide electrical power supply, it is indispensable to carry out reactions where the Δm term be positive, resulting in a exothermic reaction ($\Delta E > 0$) and therefore energy is released at the expense of mass.

To fuse two atomic nuclei, it is necessary for the reactants to overcome their repulsion due to the Coulomb force. To reach that, the reactants must acquire enough kinetic energy which means, in other words, to heat the matter at very high temperatures (around 10^8 K). At these values of temperature, molecules dissociate and atoms ionize, resulting in an electrically charged gas mixture of positive ions and electrons called plasma, which is often called the fourth state of matter [30].

Numerous reactions exist for generating plasma through the fusion of different light elements. The probability of fusion reaction between these elements varies depending

on the reactants involved and is influenced by temperature at which the plasma is heated. The fusion reaction that needs the lowest temperature to get the highest probability of occurrence (highest likelihood of reactants collide each other), is by fusing deuterium and tritium (also known as D-T reaction) and producing helium (or α particle) with a kinetic energy of 3.5 MeV and one neutron with 14.1 MeV of kinetic energy [22, 30]. Which is, precisely, the nuclear fusion reaction that will take place in ITER device.

$$^{2}_{1}\mathrm{H} + ^{3}_{1}\mathrm{H} \rightarrow ^{4}_{2}\mathrm{He}\ (3.5\ \mathrm{MeV}) + ^{1}_{0}\mathrm{n}\ (14.1\ \mathrm{MeV}). \tag{1.2}$$

The total amount of energy (17.6 MeV) produced by the reaction in (1.2) is in the form of kinetic energy of the products. The α particle is used to keep the reaction going by transferring its kinetic energy to other particles in the plasma through collisions. In case of the neutron, it carries approximately 80% of the total energy released, and it has to be captured and its energy transformed into heat, replacing the heat we got from burning fossil fuels in a power plant.

It is evident that no solid material can withstand the high temperatures of the plasma, making it impossible to contain the plasma with walls. Therefore, it is necessary to employ forces such as gravity, electricity, or magnetism to confine it in a region far from the walls. The sun, for instance, holds its plasma in its core with a large gravitational field, thereby producing fusion energy. On Earth, it is impossible to use gravitational force because our gravity is much weaker than the sun's. While it might be possible to use very strong electric fields, this would not confine the plasma either, as the electric field would pull ions and push electrons in opposite directions, pulling the plasma apart rather than confining it. Thus, the only remaining option is to confine the plasma using magnetic fields[2].

1.2 Magnetic confinement

Heating a mixture of D and T up to 10^8 K is not enough to achieve a net energy production with the reaction (1.2). Particles must also be confined long enough to interact and fuse before losing their kinetic energy, which would otherwise prevent the reaction from occurring. This necessary condition to reach ignition in a fusion reactor and a self-sustaining plasma, is expressed by the following inequality, also known as *triple product* [30]:

$$nT\tau_E \geq \frac{12}{\langle \sigma v \rangle} \frac{T^2}{E_{ch}}. \tag{1.3}$$

The term n is the fuel density, which in case of reaction (1.2) is determined by adding the densities of D and T respectively: $n = n_D + n_T$. T is the temperature at which the plasma is heated during a certain energy confinement time τ_E. $\langle \sigma v \rangle$ is the reaction rate coefficient of D-T nuclear fusion reaction; and E_{ch} is the kinetic energy of the charged product nuclei, which in case of (1.2) is carried by the energy of the α particle ($E_{ch} = E_\alpha$). For the D-T reaction, the minimum of the triple product occurs in the temperature range $10 - 20$ keV which makes the ignition condition: $nT\tau_E \geq 3 \times 10^{21}$ m^{-3}keVs [30]. This ignition condition brings out the requirements on density, temperature and confinement time which could be reached, for example, by $n = 10^{20}$ m^{-3}, $T = 10$ keV and $\tau_E = 3$ s.

[2]There is another mechanism for the confinement called *inertial confinement* which initiates the nuclear fusion by compressing and heating small pellets filled, typically, with D and T. But in this work we will only present the magnetic confinement because it is the mechanism that ITER will use.

There are two main mechanism to confine the plasma on Earth: inertial confinement and magnetic confinement. In this work we will only focus in magnetic confinement which is the mechanism that ITER device will use. The *magnetic confinement*, as its name suggests, confines the plasma by using magnetic fields. Charged particles move along the direction of the magnetic field while gyrating in the plane transversal to them. The gyration orbit is called cyclotron orbit or Larmor orbit whose radius, also-called *Larmor radius*, is determined by the following expression:

$$r_L = \frac{mv_t}{qB}, \tag{1.4}$$

where m and q are the mass and charge of the particles; v_t is their average velocity in their transversal direction; and B is the magnetic field strength. In a fusion reactor, the r_L for a D nucleus is around 1 cm which is much smaller than the size of the plasma (around meters), which makes unnecessary to track the particle motions in such detail. This suggests that an homogeneous magnetic field can efficiently confine the plasma in the transversal direction, but what about in the parallel direction of the magnetic field lines? One of the solutions is to make field lines that they close on themselves forming closed trajectories, which is, precisely, the idea behind *stellarator* and *tokamak* devices.

1.2.1 The stellarator system

Stellarators and tokamaks are toroidal devices that differ from each other in the way of generating the poloidal magnetic field (the component that gives the magnetic field line their helical twists shape) [31]. The stellarator system was one of the first approaches proposed to confine the plasma in a thermonuclear device. It was initially proposed and developed by Lyman Spitzer at Princeton University in 1951. Its early development consisted in a figure-8-shape machine that was presented at the second Atoms for Peace conference in 1958 [31, 32].

Stellarator configurations are achieved by adding external magnetic fields to the toroidal solenoid, a coil wound in a helical shape to produce a torus-shaped magnetic field, aiming to create interlocking toroidal magnetic surfaces. A schematic of its magnetic coil structure is shown in Figure 1.2. The circular coils (toroidal field coils) generate the toroidal field whose lines are along the torus axis, whereas the poloidal field is added by the helical windings. These helical windings turn close on themselves returning to the starting meridian plane. They are even in number and are traversed by alternating currents that create a multipolar field which vanishes on the toroidal axis. There are variants of stellarator, such as Torsatron, where the number of helicoidal windings can be even or odd and the current flows in the same direction through them [31]. Nowadays, there are quite much complex designs of stellarators, for example, Wendelstein 7-X, where the circular and helical coils are combined into individual ones that produce the same magnetic field shown in Figure 1.2 [33].

1.2.2 The tokamak system

The tokamak constitutes the most widespread typology of fusion device based on magnetic field confinement. It was initially conceptualized by the Soviet physicists Tamm and

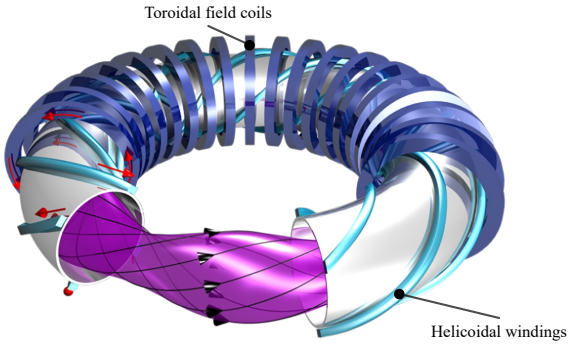

Figure 1.2. Sketch of the magnetic coil structure in a classical stellarator. The red arrows represent the current that circles in the toroidal and helicoidal coils generating the helical magnetic field represented by black arrows. Picture taken from reference [34] and modified by the author.

Sakharov in 1950 [35] and materialized, for the first time in history, by Yavlinsky, in 1958, who presented the T-1 design during the second Atoms for Peace conference in Geneva [36]. As mentioned in the Preface, tokamak is a Russian acronym for "toroidal chamber with magnetic coils", what suggests it is an axisymmetric machine with toroidal geometry and surrounded by magnetic coils, as is shown in Figure 1.3.

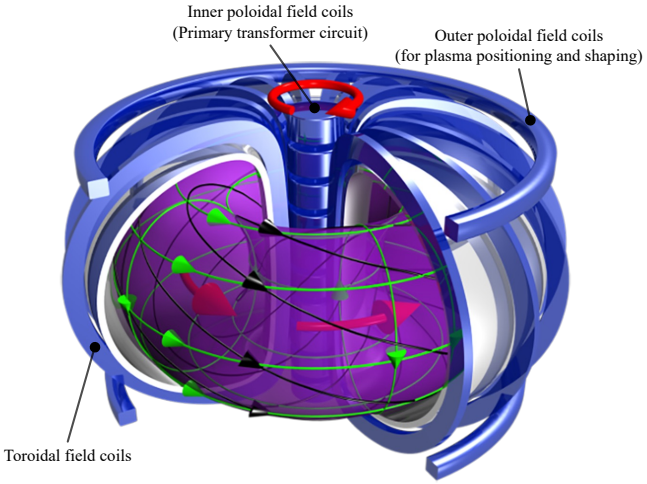

Figure 1.3. Sketch of a tokamak device. The big red arrows through the plasma (doughnut-shape in purple) represent the current induced by the inner poloidal field coils. The vertical and horizontal green arrows represent the poloidal and toroidal magnetic fields, respectively. The total resulting helical magnetic field is schematized by the black arrows. Picture taken from reference [34] and modified by the author.

The confinement of the plasma in the direction of the torus axis is achieved by the toroidal field (horizontal green arrows), thanks to the toroidal field coils. To avoid particle losses due to plasma drifts, a poloidal magnetic field (vertical green arrows) is generated by an electrical current (big red arrows) driven into the plasma (purple doughnut-shape) along the toroidal direction. This current is created by the electric field (red arrow on top) induced by the transformer action of a solenoid placed in the central column of the torus: the inner poloidal field coils. The resulting total magnetic field (black lines) from the combination of the poloidal and toroidal fields has helical field lines. These helical

magnetic field lines wrap around closed surfaces with constant poloidal magnetic flux, that are also called magnetic flux surfaces. These flux surfaces define different regions into the plasma which are important to summarize for a better explanation in the oncoming sections. Readers interested in more detailed explanation can find it in reference [30].

The *core region* is where magnetic field lines close within the vacuum chamber, confining plasma. Some field lines extend beyond the chamber, reaching the divertor and walls as open field lines. The *Scraped-Off Layer* (SOL) refers to the unconfined region where these open magnetic field lines allow particles and heat to reach the reactor's wall. Both regions are separated by the last closed flux surface or *separatrix* whose intersections with the wall are called *strike-points*. When the plasma geometry has only one strike-point, it is called *limited configuration*. In this setup particle fluxes and heat are concentrated around a plasma-facing component (PFC) called, *limiter*. This configuration, also known as *limited configuration*, allows sputtered atoms from the limiter to enter directly into the core region due to their direct contact, thus cooling down the plasma and degrading its performance by radiation and dilution.

As an alternative solution, and to mitigate plasma-wall interactions in the core region, the *diverted configuration* was developed, leading to the creation of a new PFC called *divertor*. In such configuration, the plasma flow is diverted towards the divertor targets, where the most intense plasma-wall interactions occur. The diverted configuration, unlike the limited configuration, has two strike-points and a region where the poloidal magnetic field is null: the *X-point*; being the zone below the X-point and between the strike-points the *Private Flux Region*. In Figure 1.4, we provide an illustration of the regions mentioned above to enhance comprehension.

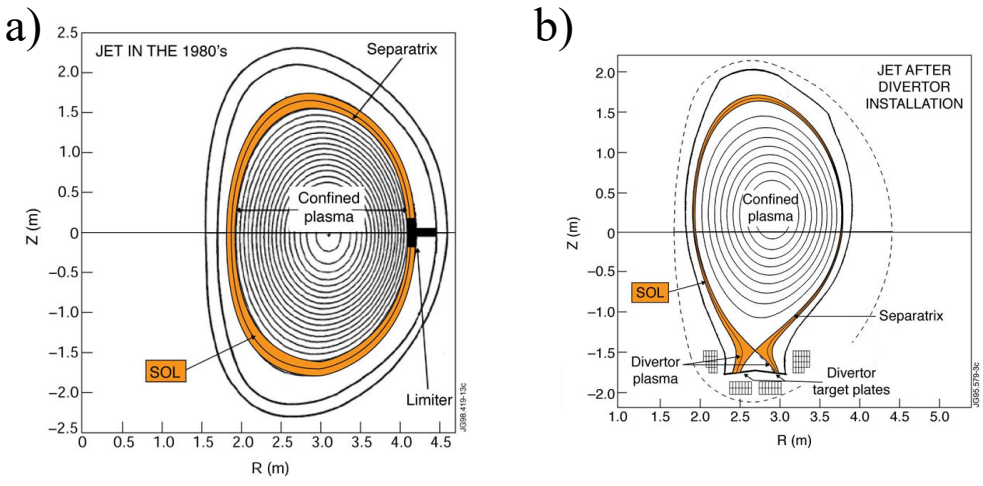

Figure 1.4. a) Limited and b) diverted configurations in the Joint European Torus (JET) tokamak. The dark lines in the plasma region delimite the magnetic flux surfaces in the poloidal cross section of the tokamak. Picture were taken from reference [37].

In case of the diverted configurations, the retention and diffusion of ions coming from the plasma in the divertor is an important subject to deal with because it can lead to fuel losses and degradation of the plasma performance [7]. Indeed, this thesis is dedicated to addressing these challenges.

1.3 The world's largest tokamak: ITER

The biggest tokamak ever designed is currently built in Cadarache, France. Its name is ITER, Latin for "The way" and originally an acronym for "International Experimental Thermonuclear Reactor". ITER project was set at the Geneva Superpower Summit in 1985. Design concepts were initiated in 1988, leading through various engineering phases until 2001 when the final design was approved by its founding members: the European Union, Japan, Russia, and the United States. Two years later, in 2003, China and South Korea joined the project, followed by India in 2005, being conformed the final consortium by seven members. The project was finally signed in 2006 by Ministers from the seven ITER Members and one year later the ITER Organization was officially established [6].

This colossal project, with an approximate cost of 20 billion euros and standing as one of the most significant technological challenges humanity has ever undertaken, has five main goals [6, 38]:

1. Achieve a D-T plasma (reaction (1.2)) sustained predominantly by internal fusion heating conditions.
2. Reach the breakeven, defined as the state where the heat generated by fusion reactions equals the input heating power used to initiate them, denoted by a power gain of $Q = 1$. Furthermore, ITER is expected to generate 500 MW of fusion power from 50 MW of injected heating power (achieving a power gain of $Q = 10$) during extended pulse operations lasting 400 to 600 seconds.
3. Contribute to demonstrating the integrated operation of technologies essential for a fusion power plant. ITER will serve as a connection between current smaller-scale experimental fusion devices and the future demonstration fusion power plants.
4. Conduct trials for tritium breeding from lithium-6 ($^6_3$Li) within the vacuum vessel. With the world's tritium supply insufficient for future fusion reactors, ITER will offer a unique opportunity to assess mockup in-vessel tritium breeding blankets within an authentic fusion environment.
5. Demonstrate the safety attributes of a fusion device. One of ITER's primary objectives is to showcase the ability to control the plasma and fusion reactions while ensuring minimal impact on the environment.

The central reaction chamber of ITER tokamak is composed by five main components and the supporting systems. The main components, including the magnets, vacuum vessel, blankets, cryostat, and divertor, are housed within the central reaction chamber as shown in Figure 1.5. Conversely, the supporting systems, encompassing powerful heating and current drive, diagnostic, cryogenic, cooling, fuelling, vacuum, and power supply systems, are situated around the central reaction chamber [6].

The ITER tokamak will weigh 23000 t and is designed to achieve a plasma temperature of 150×10^6 °C, which is ten times hotter than the core of the sun. This tokamak will feature a plasma major radius of 6.2 m, enclosed within a D-shaped vacuum vessel designed to contain a plasma volume of 840 m^3. To generate the necessary magnetic fields for initiating, confining, shaping, and controlling the plasma, 10000 t of magnets, storing

a combined magnetic energy of 51 GJ, are employed. These magnets are fabricated from niobium-tin (Nb_3Sn) or niobium-titanium (NbTi) alloys which attain superconductivity when cooled with supercritical He within the range of 4 K (−269 °C) [6].

The vacuum vessel, constructed from stainless steel, serves multiple crucial functions: it maintains a high-vacuum environment for the plasma, enhances radiation shielding and plasma stability, acts as the primary barrier for containing radioactivity, and offers structural support for in-vessel components like the blanket and the divertor. Additionally, the vessel's double steel walls facilitate the circulation of cooling water, which effectively dissipates the heat generated during operation. Its steel structure and the superconducting toroidal field magnets are shielded from heat and high-energy neutrons by 440 blanket modules, which entirely cover a surface area of 600 m^2 on the inner walls. These blankets serve to decelerate the neutrons, converting their kinetic energy into heat energy, which is then absorbed by the water coolant system [6].

The high vacuum in the main chamber is maintained by the cryostat, a stainless steel high-vacuum pressure chamber with a volume of 16000 m^3. Featuring a total of 223 penetrations (some as large as 4 m in size), the cryostat facilitates access for cooling systems, magnet feeders, auxiliary heating, diagnostics, as well as for maintenance and removal of blanket sections and parts of the divertor. The divertor is the component primarily tasked with extracting heat and ash generated by the fusion reaction, thereby minimizing plasma contamination and shielding the surrounding walls from thermal and neutronic loads [6].

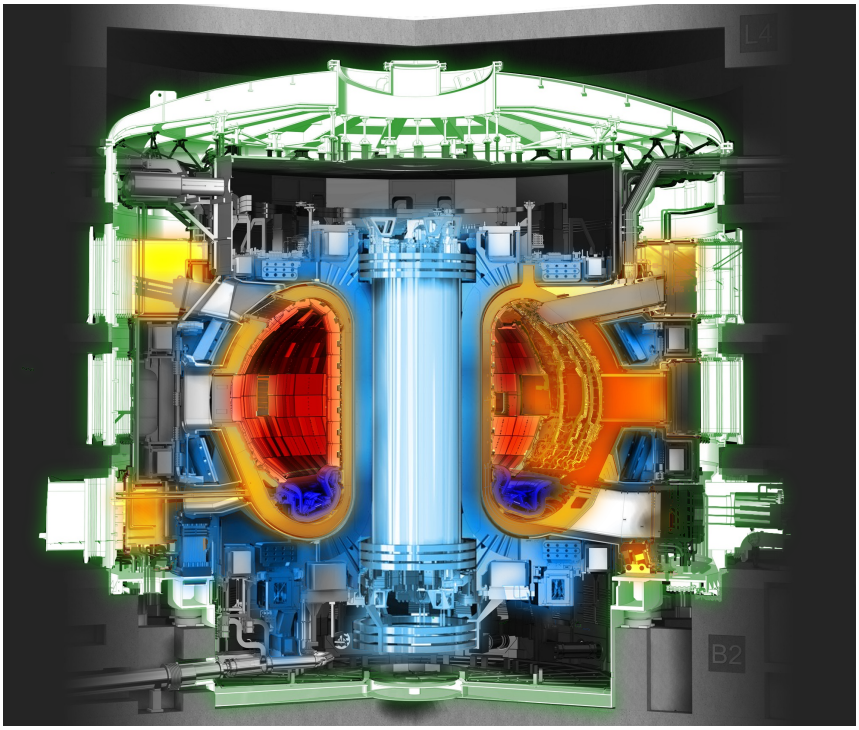

Figure 1.5. Sketch of the five main components of the ITER tokamak: **magnets**, **vacuum vessel**, **blankets**, **cryostat** and **divertor**. Picture taken from reference [6].

1.3.1 The ITER divertor

The efficient and controlled management of power exhaust is crucial for the successful and safe operation of future magnetic confinement nuclear fusion reactors such as ITER. Among the components crucial for these tasks, the divertor plays a significant role, whose vertical targets are expected to tolerate a heat flux of 10 MWm^{-2} in steady-state and 20 MWm^{-2} during slow transients [6, 39–41]. In the ITER tokamak it is located at the bottom of the vacuum vessel, as it is appreciable in Figure 1.5. As mentioned above, the main goal of this component is to extract heat and impurities produced by the fusion reaction, improving the plasma performance and protecting the surrounding walls from thermal and neutronic loads.

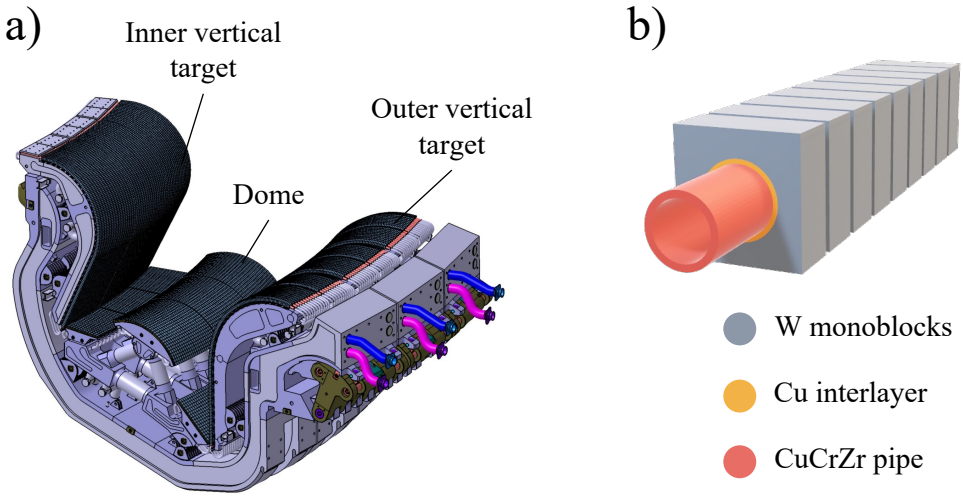

Figure 1.6. Sketch of the ITER-like divertor. a) Divertor cassette assemblies with their respective PFCs, and b) a single PFU. Picture (a) was taken from reference [6], whereas (b) was designed by the author in the free web app Tinkercad. Readers can visually perceive a 3D depiction of (b) in reference [21].

ITER's divertor comprises 54 "cassette assemblies", each supported by a stainless steel structure and housing three PFCs: the inner and outer vertical targets, and the dome. In Figure 1.6-a those PFCs are represented in a divertor cassette assembly. The inner and outer vertical targets are placed at the intersection of magnetic lines where high-intensity particle bombardment occurs. The kinetic energy of the plasma particles colliding with the vertical targets is converted into heat, which is then extracted through active water cooling. Each divertor cassette assembly comprises a sequence of plasma-facing units (PFUs). Such units consist of chains of W monoblocks affixed to a pipe composed of a copper-chromium-zirconium (CuCrZr) alloy, with a Cu interlayer placed between them. Figure 1.6-b illustrates a single PFU, providing a clear depiction of the arrangement of materials within it [41]. W, with the highest melting point among all metals, low sputtering yield, and low fuel retention, was chosen as the armor material after an international research and development endeavor. This decision was spurred by promising experimental results and successful prototype trials [39–43]. As said before, particles and ions coming from the plasma in the vacuum vessel with high values of kinetic energy will strike the PFUs of the ITER divertor. This phenomenon carries the potential to significantly impact plasma performance, especially if hydrogen isotopes (HIs) manage to escape through the divertor. Such occurrences can result not only in fuel losses but

also in system contamination issues, especially since $^{3}_{1}$H is a radioactive nuclei, thereby exacerbating the situation [7]. Therefore, the following question arises: do these ions possess sufficient kinetic energy to penetrate the armor of the PFU and reach the coolant water within the CuCrZr pipe?

1.4 Motivation

To address this question, several experimental and theoretical studies have been conducted to investigate the retention and diffusion of HIs through the ITER divertor [8–15]. The motivation for this work, however originated from our local research environment, specifically when Hodille et al. [16] studied the retention of T for the ITER-like divertor in undamaged and damaged[3] W using kinetic theory in MHIMS (Migration of Hydrogen Isotopes in Metals) code. They determined the T retention and migration depth as a function of the implanted flux and the number of cycles. Their conclusion was that, whether for undamaged or damaged tungsten at a depth of 6 mm from the strike point (the location of the W/Cu interface in the PFUs, as illustrated in Figure 1.7), tritium retention could reach up to 5 gm^{-2} when the number of cycles increased to 60852.

The findings from Hodille et al.[16] were corroborated by Delaporte-Mathurin [44], who modeled the retention of hydrogen within the monoblock geometry using the FESTIM code (Finite Elements Simulation of Tritium in Materials). This study investigates the solubility of hydrogen in the PFU, assuming continuity of the chemical potential across the material interfaces. The authors demonstrated, as previously found by Hodille et al. [16], that hydrogen atoms can reach the W/Cu interface and even penetrate to the coolant.

Given that the retention and diffusion of H in pure W and Cu are well characterized by both experimental and theoretical studies, our focus shifted to the interface between these two materials. The model developed by Delaporte-Mathurin [44], which assumes continuity of the chemical potential across the W/Cu interface, provides valuable insights but is limited by its purely thermodynamic nature. To gain a more comprehensive understanding, we aimed to develop a more complex and detailed model that studies the retention and diffusion of H atoms from a multiscale perspective. Thus, the following questions became our primary driving force: Is H trapped at the W/Cu interface? Does H diffuse at the interface? Is the model of chemical potential continuity valid?

Prior to comprehensively characterizing the diffusion and segregation of HIs throughout and at the full PFU, it is imperative to initially examine their behavior at the W/Cu interface. This analysis is essential for determining whether HIs can infiltrate the Cu region and subsequently continue their migration towards the coolant. It is from this necessity that the beginning of this project arose.

As previously said, the main goal of this thesis is to build a multiscale model for studying the segregation and diffusion of H atoms at the W/Cu interface in the ITER cooling monoblocks. Such a model encompasses various steps, starting from electronic

[3]The term undamaged (damaged) W refers to tungsten that has not been exposed (exposed) to fast neutrons (14.1 MeV) during the D/T phase in ITER. Exposure to fast neutrons can alter the material's structure, leading to its classification as undamaged or damaged, depending on the extent of such exposure.

structure calculations using density functional theory (DFT), progressing through classical molecular dynamics (CMD), and ultimately integrating kinetic and thermodynamic theories. DFT provides a precise description of the material structure at the scale of hundreds of atoms. Conversely, CMD facilitates the simulation of larger systems containing up to hundreds of thousands of atoms. Meanwhile, kinetic and thermodynamic theories utilize atomic data as input to deliver macroscopic physical quantities as output. The ultimate goal of the project, beyond this thesis, is to fully characterize the retention and diffusion of H in the PFU by using rate modeling tools such as MHIMS or FESTIM. This will predict numerically how much fuel will be lost through the divertor in the ITER tokamak.

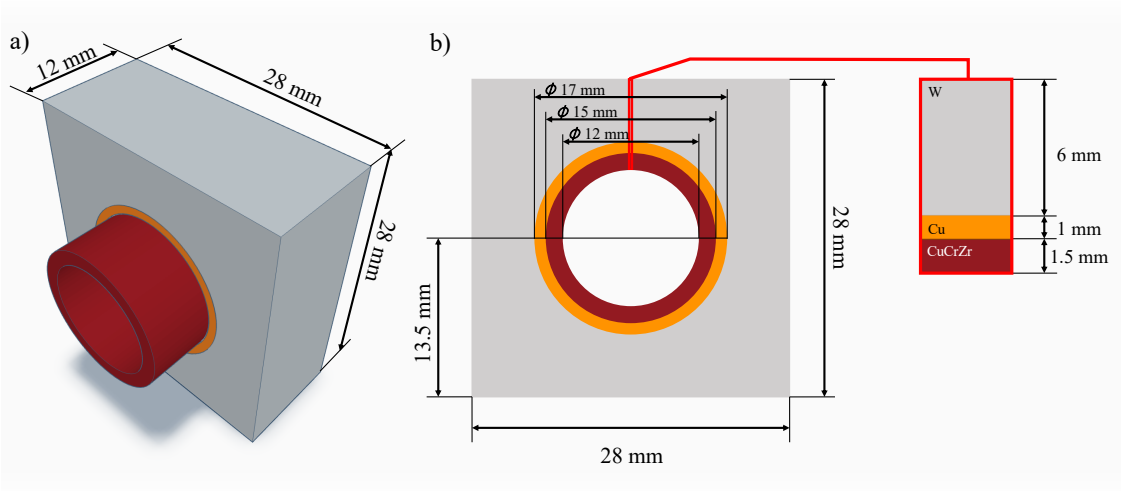

Figure 1.7. Sketch of one W monoblock in the ITER-like divertor. a) 3D representation and b) cross-section. Pictures were designed by the author in the free web app Tinkercad.

1.4.1 The W/Cu interface

The zero mutual solubility and significant differences in physical and chemical properties between W and Cu, such as the coefficient of thermal expansion ($\alpha_{Cu} \approx 4\alpha_W$) and the Young's modulus ($\varepsilon_{Cu} \approx 0.2\varepsilon_W$) [45], present considerable challenges in achieving effective bonding both materials [46, 47]. Several techniques have been developed to fabricate the W/Cu interface, such as direct and/or vacuum diffusion bonding [48, 49], vacuum brazing [50], friction stir welding [51], chemical vapor deposition [52], vacuum plasma spraying [53], explosive welding [46, 47], among others [54–57].

While many studies have primarily focused on macroscopic characterization of W/Cu [46–57], particularly in terms of tensile strength, some have also reported on the crystallographic structure at the W/Cu joint [46–48, 57]. As we are interested in model this interface by DFT, we will focus on those studies where its crystallographic structure was reported.

Zhang et al. [48], bonded W and Cu together through diffusion bonding without using an interlayer metal. The sample was exposed to a temperature of 980 °C (near the melting point of Cu) and a pressure of 106 MPa during 180 min. The microstructure of the W/Cu joint was characterized using Transmission Electron Microscopy (TEM) and High

Resolution Transmission Electron Microscopy (HRTEM). Their observations revealed a $Cu^{fcc}(111)$ structure adjoining the $W^{bcc}(110)$ plane, with a diffusion layer approximately 22 nm thick. Despite the slight deformation and widening of the Cu and W lattices within the diffusion layer, respectively, a continuous crystal interface was formed.

Oxide-dispersion-strengthened W (ODS-W) and Cu powders were combined by using spark plasma sintering technique in the study reported by Liu et al. [57]. In this case, they utilized ODS-W, a material composed of W with a volume ratio of 2% yttrium oxide (Y_2O_3). The incorporation of Y_2O_3 is intended to prevent the growth of grains and to refine them. The microstructure of the interface was characterized in a range of temperatures 850 °C−980 °C by Scanning Electron Microscopy (SEM), Energy Dispersive Spectroscopy (EDS) and TEM. In this study, similar to the findings reported by Zhang et al. [48], it was observed that the interface consisted of a $Cu^{fcc}(111)$ structure adjacent to the $W^{bcc}(110)$. However, in this instance, a thicker amorphous diffusion layer of 1.3 μm was observed, coinciding with compression of the Cu^{fcc} lattice and expansion of the W^{bcc} lattice.

Liu et al. [46, 47] employed the explosive welding technique to manufacture laminated composite materials consisting of W and Cu. In reference [46], the authors used a W plate with a thickness of 2 mm, which was preheated to 500 °C before being welded to a pure Cu plate. The microstructures of the crack-free W/Cu interface were examined using SEM, Electron Backscattered Diffraction (EBSD), and TEM. Their observations confirmed the formation of a wavy interface, with a $2-6$ nm thick amorphous transition layer formed along it. In reference [47] following the same methodology they studied the formation mechanism of the W/Cu wavy interface. In this work the preheating process was done at 860 °C instead of 500 °C, obtaining a discontinuous wavy structure that obeys the basic fractal principle. Furthermore, similar to the findings in reference [46], numerous sub-grain boundaries were observed on the Cu side of the interface. The authors attributed these observations to the plugging of dislocations resulting from significant plastic deformations. The results from the TEM observations revealed the $Cu^{fcc}(111)$ and $W^{bcc}(110)$ planes at the interface, similarly to the references [48, 57].

In contrast to the studies discussed previously, where the W/Cu interface was constructed at the macroscale, some experimentalists built it atom by atom by depositing Cu atoms onto bare W surfaces, including W(100) [17, 18, 58, 59], W(110) [58, 60–67], and W(111) [60, 61, 63, 64, 67]. These studies have reported controversial results regarding the crystalline orientation of the Cu layers and the evolution of the work function as the number of Cu layers increases.

Bauer et al. [58] studied the adsorption and condensation of Cu on W(100) and W(110) surfaces by combining different techniques, such as low-energy electron diffraction (LEED), Auger electron spectroscopy (AES) and thermal desorption spectrometry (TDS). They found that the growth of Cu depends on the atomic roughness of the surfaces, which can be understood as varying with the crystal orientation of the substrate. On both surfaces: W(100) and W(110), they observed the formation of two stable adsorbed layers of Cu whose structures were fully determined by the periodicity of the W surface whereas the third and higher layers were metastable and formed crystallites at high temperatures.

Cetronio et al. [59] analyzed Cu adsorption on W(100) using field emission microscopy (FEM), a technique different from that used by Bauer et al. [58], and obtained contrasting

results. The discrepancy lies in the fact that Cetronio et al. [59] observed that Cu spreads uniformly over the W surface, and the first and second layers, initially strained, relaxes towards Cu(100) as the layer thickness increases. This uniform spreading allowed the authors to conclude that Cu does not break up into crystallites, as Bauer previously reported in [58].

On the contrary to reference [59], Wormeester et al. [17, 68] using the reflection high energy electron diffraction (RHEED) technique observed that Cu could have a pseudomorphic growth on W(100) surface, as Bauer had already reported in [58]. They observed that the deposited Cu layers adopt the structure of the substrate, W(100) in their case, and grow up with a different crystallographic structure from that of its bulk. They reported two different pseudomorphic 2D layers for Cu: body-centered cubic (bcc) and hexagonal closed package (hcp). These results obtained by Wormeester [17, 68] were confirmed by Bollmann et al. [18] who studied the morphology of Cu deposits on W(100) during growth and desorption using low-energy electron microscopy (LEEM) and selective area low-energy electron diffraction (μLEED). Bollmann et al. [18] also observed Cu crystallites appreciated by Bauer et al. [58], and they concluded that those crystallites have a hcp structure with the $(11\bar{2}0)$ plane parallel to W(100).

The discrepancies in experimental data regarding the structure of the W/Cu interface and the variation in the work function with increasing Cu layers prompted theorists to undertake first-principles calculations to address these issues [69–73]. Liang et al. [69] were interested in solving the controversies regarding the work function shape as a function of the Cu layers. To tackle that, they built several W/Cu interface models based on density functional theory to study how the interface strength changes as a function of the number of overlayers (mainly Cu layers) on top of the substrate (mainly W bulk). They characterized five different structures by changing the crystallographic planes of the W and Cu bulks: (100)Cu/(100)W, (110)Cu/(110)W, (111)Cu/(111)W, (111)Cu/(110)W and (110)W/(111)Cu ,where the first and second parts represent the overlayers and substrate, respectively. These models were mainly built using a (1×1) surface unit cell with 6 substrate layers, (1-5) overlayers at the top of the substrate and a vacuum layer of 15 Å. Their results proved that the number of overlayers and the orientation of the interface affect the interface cohesion of the W/Cu.

In subsequent years, several theoretical studies were conducted on the (111)Cu/(110)W interface [70, 71, 74]. This interest stemmed from the fact that this orientation exhibits one of the smallest mismatches between their respective networks. Ma et al. [70] studied the effects of H on the cohesion properties of the W/Cu interface and to do that they built a model very similar to the one developed by Liang et al. [69]. Such a model was composed by a (2×2) surface working cell with the same cell parameter as the bulk W, 6 layers of W substrate, 4 layers of Cu added on top and 18 Å of vacuum. This method involved expanding the geometry (or surface cell parameters) of the (111)Cu to match the working cell and subsequently relaxing the atomic positions, without changing the volume and shape of the full model, to enable the system to reach its ground state. The same structure was used by Wang et al. [74] to study the effect of Zr alloying on the cohesion properties of the W/Cu interface. However, in their study, the surface cell was expanded to (3×3), necessitating a larger expansion of the Cu network.

Bodlos et al. [71] were interested in the Kurdjumov-Sachs (KS) and Nishiyama-Wassermann (NW) interfaces for the W/Cu system. Both the KS and

the NW lie in the (111) and (110) crystallographic planes of Cu and W, respectively. The KS orientation is defined by the directions parallel to each other, namely Cu[$1\bar{1}0$]//W[$\bar{1}11$], Cu[$11\bar{2}$]//W[$1\bar{1}2$] and Cu[111]//W[110]. In contrast, the NW orientation is characterized by Cu[$1\bar{1}0$]//W[$00\bar{1}$], Cu[$11\bar{2}$]//W[$\bar{1}10$], and Cu[111]//W[110]. The authors computed several supercells using both DFT and Molecular Dynamics, adopting a different methodology from previous studies [69, 70, 74]. They established the KS and NW model working cells according to the coherence of the W and Cu networks, defined by assessing the linear mismatch between them. Their surface working cells were sized at (1×1) and (4×5) for the KS and NW models, respectively. These dimensions were determined based on the arrangement derived from aligning the (111)Cu and (110)W surfaces on top of each other. After the relaxation of the interface, the authors reported values for the work of separation and the energy of the interface in agreement with those reported by Liang et al. [69].

Yang et al. [72], studying the influence of the W/Cu interface on the resistance against harmful He atoms built three structures: Cu(100)/W(100), Cu(110)/W(110) and Cu(111)/W(111). Their models were established by depositing the Cu layers on the (2×2) W surfaces with an initial distance of 2.01 Å and compressing the lattice parameter of Cu to match the W lattice. Similarly to the previous cases [69, 70, 74] a thick vacuum layer of 15 Å was added in the Z direction to avoid the interaction of the working cell with its image.

All of these models shared a common approach of modifying the Cu lattice to match the W network, followed by a geometry relaxation of the system, without changing the cell parameters of the working-cell [69–72, 74]. While some of these studies address controversies related to the shape of the work function [69, 71], others focused on investigating the interaction of the W/Cu interface with interstitial atoms [70, 72, 74]. However, the controversy stemming from experimental findings concerning the crystalline orientation of the Cu layers remained pending.

Therefore, our primary objective was to develop a model of the interface using a different methodology, specifically to address that controversy: the crystallographic structure of the W/Cu interface. Once the interface model was defined, H atoms were incorporated into the structure to characterize their segregation and diffusion properties. The data obtained from our DFT calculations were then used to develop thermodynamic and kinetic models. Such models allowed us to study how the solubility of H changes as a function of temperature under both thermal equilibrium and out of equilibrium conditions, respectively. Additionally, CMD simulations were conducted to examine the propagation of the reconstruction in the Cu structure at the interface.

1.5 Structure of the manuscript

The present work is structured as follows:

- Chapter 2 provides a brief overview of some basic concepts of solid-state physics and density functional theory (DFT). This chapter aims to help readers understand the underlying physics behind our results.

- Chapter 3 introduces our model of the W/Cu interface suitable for DFT calculations. This chapter discusses the characterization of the interface morphology and compares the model with experimental observations. The results of this chapter were published in *Nuclear Materials and Energy*.

- In Chapter 4, we investigate the solution energy and vibrational properties of H at the W/Cu interface. These findings serve as the basis for developing a grand canonical ensemble based on thermodynamic theory. This ensemble is used to determine the solubility of H as a function of temperature and chemical potential of the reservoir under thermal equilibrium conditions. The results of this chapter were part of a second paper published in *Journal of Physics and Condensed Matter*.

- In Chapter 5, we investigated the dynamic properties of hydrogen along the W/Cu interface. Specifically, we determined the activation barriers for diffusion across the interface. These values were then employed to develop a 0-dimensional kinetic model, which enabled us to determine the solubility of hydrogen in conditions out of thermal equilibrium. A third paper was prepared and submitted to *Nuclear Fusion*.

- In Chapter 6, we present the results of CMD simulations in the Cu bulk to investigate the propagation of the Cu^{hcp} structure formed at the W/Cu interface. CMD enables us to analyze this propagation on a larger scale and examine defect formation, which is not feasible with DFT.

- Finally, we present the conclusions, future perspectives and appendices.

Chapters 3–5 are presented in paper format, as they have already been submitted or published in journals. However, since not all results can be fully displayed in journals for clarity, an introduction is provided before each paper. These introductions to the studies include additional details and results that are not typically explained in full in the papers.

Chapter 2

Density Functional Theory

What is Density Functional Theory? This chapter will be devoted to answering this question and to review some of the fundamental aspects of electronic structure theory. DFT is rooted in quantum mechanics and therefore we will summarize some essential basic concepts which will help the reader follow a line of thought. The chapter is intended to guide the reader from the basic knowledge of quantum mechanics (Schrödinger equation) to the fundamentals of DFT. For mathematical clarifications of Dirac's notation [75], readers may refer to Appendix A, which provides a refresher on these concepts before diving into this chapter. While we can't cover all the details of this extensive theory, we aim to present the main foundations to illustrate how DFT was developed and why it is so powerful tool.

2.1 Schrödinger equation

Quantum Mechanics came out in the early 20th century when physicists realized that Newton's Laws do not correctly describe the behavior of quite small particles such as electrons, atomic nuclei and molecules [76]. The development of Quantum Mechanics was favored by the contribution of several studies among the most prominent are: Plank's study about the emitted light by heated solids [77] in 1900, the photoelectric effect developed by Einstein in 1905 [78] and the uncertainty principle discovered by Heisenberg in 1927 [79]. All of these studies pointed out that Classical Mechanics was not able to describe the state[1] of microscopic systems and for that reason a new formulation was necessary.

It was like that, as in 1926 Erwin Schrödinger proposed the concept of wave function and equation governing its change with time [80]. The time-dependent equation postulated by

[1]The word state in classical mechanics means a specification of the position and velocity of each particle, and the forces acting on them at some instant of time. The uncertainty principle of Heisenberg [79] dictates that the exact position and momentum (and in consequence velocity) of a microscopic particle cannot be determined simultaneously. Thus, in quantum mechanics the word state means a specification of wave function or state function of the system $\Psi(\vec{r}, t)$.

Schrödinger in 1926 for a system of only one particle is given by the following expression:

$$i\hbar\frac{\partial}{\partial t}\Psi(\vec{r},t) = -\frac{\hbar^2}{2m}\nabla^2\Psi(\vec{r},t) + V(\vec{r},t)\Psi(\vec{r},t). \tag{2.1}$$

Where $i = \sqrt{-1}$ is the imaginary unit, $\hbar = h/2\pi$ is the normalized Planck's constant, $\Psi(\vec{r},t)$ is the wave function of the system, $\vec{r}$ is the position vector of the particle in time t, m is the mass of the particle, ∇^2 is the Laplacian operator[2] and, $V(\vec{r})$ is the potential energy of the environment in which the particle exists.

The wave function contains all the information that can be known about the system and it is directly related with the probability of finding the particles of the system in a specific region of the space and in a particular state. The expression (2.1) contains the first derivate of the wave function with respect to time and allows us to calculate the future state at any time, if we start of a known state, i.e., if we know the wave function at time t_0.

In case of stationary solutions of the Schrödinger equation it is not necessary to use the expression (2.1), but one more straightforward: the time-independent Schrödinger equation, which in case of a system with only one particle under the action of stationary external forces is given by:

$$\left[-\frac{\hbar^2}{2m}\nabla^2 + V(\vec{r})\right]\psi(\vec{r}) = E\psi(\vec{r}), \tag{2.2}$$

$$\widehat{\mathrm{H}}\psi(\vec{r}) = E\psi(\vec{r}). \tag{2.3}$$

Such equation constitutes an eigenvalue problem[3] where the constant E represents the eigenvalues and $\psi(\vec{r})$ the eigenfunctions of the Hamiltonian operator. Thus, E is the observable corresponding to the total energy of the system, $\widehat{\mathrm{H}}$ its quantum-mechanical operator and $\psi(\vec{r})$ the stationary wave functions of the system. The main goal of most of quantum mechanical approaches is to find the solution of the time independent, non-relativistic Schrödinger equation and to do so, it is necessary to find those stationary wave functions $\psi(\vec{r})$ that satisfying equation (2.2).

2.1.1 Many-particle systems

In the previous section we presented the time-independent Schrödinger equation for a system with only one particle (such as one electron or one proton) with mass m and whose interactions with the environment are described by the potential $V(\vec{r})$. But, what if we are dealing with bigger systems such as atoms, molecules and solids where there are more than one interacting particles? In the following section, we will discuss how to solve the problem for many-body systems with N electrons and M atomic nuclei.

The full non-relativistic time-independent Schrödinger equation for a many-body system with N electrons and M atomic nuclei is given by:

$$\widehat{\mathrm{H}}\psi(\vec{r_1}s_1,\vec{r_2}s_2,...,\vec{r_N}s_N,\vec{R_1},\vec{R_2},...,\vec{R_M}) = E\psi(\vec{r_1}s_1,\vec{r_2}s_2,...,\vec{r_N}s_N,\vec{R_1},\vec{R_2},...,\vec{R_M}). \tag{2.4}$$

[2] An operator is a mathematical rule that transforms a given function into another function.

[3] The term eigenvalue problem is used when the transformation of a linear operator $\widehat{\mathrm{A}}$ on some function $f(x)$ is simply to multiply $f(x)$ by a certain constant k: $\widehat{\mathrm{A}}f(x) = kf(x)$. The function $f(x)$ is called eigenfunction of $\widehat{\mathrm{A}}$ with eigenvalue k.

Where $\widehat{\mathrm{H}}$ is the Hamiltonian operator of the system, $\psi(\vec{r_1}s_1, \vec{r_2}s_2, ..., \vec{r_N}s_N, \vec{R_1}, \vec{R_2}, ..., \vec{R_M})$ is the stationary wave function of the system which we will denote in a most compress way[4] as $\psi(\{\vec{r}s\}, \{\vec{R}\})$. $\vec{r_i}$ and $\vec{R_I}$ are the position vectors of the i electron and nucleus I respectively and s_i is the spin coordinates of the electron i which can only assume the values $\pm 1/2$, and E is the eigenvalue of energy. In case of the system with many particles $\psi(\{\vec{r}s\}, \{\vec{R}\})$ is a function that depends on $3(N+M)+N$ variables: $3N$ and $3M$ spatial coordinates of electrons and nuclei, respectively, due to $\vec{r_i}$ and $\vec{R_I}$ are vectors that belong to $\mathbb{R}^3$ space; and N spin coordinates.

In this case the Hamiltonian is given by:

$$\widehat{\mathrm{H}} = \widehat{\mathrm{T}}_{\mathrm{e}} + \widehat{\mathrm{T}}_{\mathrm{N}} + \widehat{\mathrm{V}}_{\mathrm{ee}} + \widehat{\mathrm{V}}_{\mathrm{Ne}} + \widehat{\mathrm{V}}_{\mathrm{NN}}, \tag{2.5}$$

where relativistic effects such as spin-orbits effects were neglected. $\widehat{\mathrm{T}}_{\mathrm{e}}$ and $\widehat{\mathrm{T}}_{\mathrm{N}}$ are the kinetic energy operators of the electrons and nuclei respectively. The remaining terms correspond to the potential energy associated with the electrostatic interaction between the electrons ($\widehat{\mathrm{V}}_{\mathrm{ee}}$), nuceli and electrons ($\widehat{\mathrm{V}}_{\mathrm{Ne}}$) and the nuclei ($\widehat{\mathrm{V}}_{\mathrm{NN}}$). These terms in the International Systems of Units are explicitly given by:

$$\widehat{\mathrm{T}}_{\mathrm{e}} = -\frac{\hbar^2}{2m_e}\sum_{i=1}^{N}\nabla_{r_i}^2, \tag{2.6}$$

$$\widehat{\mathrm{T}}_{\mathrm{N}} = -\frac{\hbar^2}{2}\sum_{I=1}^{M}\frac{1}{M_I}\nabla_{R_I}^2, \tag{2.7}$$

$$\widehat{\mathrm{V}}_{\mathrm{ee}} = \frac{1}{4\pi\varepsilon_0}\sum_{i=1}^{N}\sum_{j>i}^{N}\frac{e^2}{|\vec{r_i} - \vec{r_j}|}, \tag{2.8}$$

$$\widehat{\mathrm{V}}_{\mathrm{Ne}} = -\frac{1}{4\pi\varepsilon_0}\sum_{i=1}^{N}\sum_{I=1}^{M}\frac{Z_I e^2}{|\vec{r_i} - \vec{R_I}|}, \tag{2.9}$$

and

$$\widehat{\mathrm{V}}_{\mathrm{NN}} = \frac{1}{4\pi\varepsilon_0}\sum_{I=1}^{M}\sum_{J>I}^{M}\frac{Z_I Z_J e^2}{|\vec{R_I} - \vec{R_J}|}. \tag{2.10}$$

Where the subindexes i and j are used to denote the electrons while I and J the nuclei, m_e and e are the mass and charge of electron and ε_0 is the permittivity of free space. $\nabla_{r_i}^2$ and $\nabla_{R_I}^2$ are the Laplacian operators which act only on the coordinates of electrons ($\vec{r_i}$) and nuclei ($\vec{R_I}$) respectively. Z_I and M_I represent the charge (atomic number) and mass of nucleus I.

Several bibliographies used a more compact form for the operator terms of the Hamiltonian without any fundamental physics constants. That form is achieved by employing the so-called atomic units system, which is adapted to work at the atomic scale. In this units system, physical quantities are expressed as multiples of fundamental constants and/or a combination of such constants. The mass of electron m_e, the modulus of its charge $|e|$, the normalized Planck's constant $\hbar$ and the Coulomb constant $k = \frac{1}{4\pi\varepsilon_0}$ are set to unity:

[4]Where $\{\vec{r}s\}$ and $\{\vec{R}\}$ represent the ensemble of electronic ($\vec{r_i}s_i \;\forall\, i = 1, 2, ..., N$) and nuclear ($\vec{R_I} \;\forall\, I = 1, 2, ..., M$) coordinates.

$m_e = |e| = \hbar = k = 1$ [76, 81]. To get the operators in the atomic units systems we just need to change in the expressions (2.6) to (2.10) the constants m_e, $|e|$, $\hbar$ and k by unity.

Equation (2.4) only has analytical solution in case of hydrogen atom with only one electron. But if we are interested in any different system, even the hydrogen atom with two electrons (H^-) no an analytical solution is known, which means that every poly-atomic system must be solved numerically, based on approximations to which this chapter is dedicated.

2.2 The Born-Oppenheimer approximation

One year after Schrödinger published his time-dependent Schrödinger equation, in 1927, Born and Oppenheimer published a paper [82] with an approximation that could be used to solve numerically the full non-relativistic time-independent Schrödinger equation for a molecular system with N electrons and M atomic nuclei given by equation (2.4). The idea of Born-Oppenheimer approximation (BOA) or adiabatic approximation became, probably, the most important approximation in the modern quantum theory and the milestone for quantum chemistry. In this section we are going to briefly summarize it due to it is indispensable to understand how DFT works.

The BOA is based on the difference in mass between nuclei and electrons. Protons and neutrons are 1800 times heavier than electrons approximately, so the mass ratio between the nucleus I and one electron is $\frac{M_I}{m_e} > 1800A_I$, being the mass number[5] of the nucleus $A_I \geq 1$. This relationship tells us that every nucleus has a much larger mass than electrons and this value increases as the number of nucleons increases or, in other words, as the nucleus becomes heavier. This significant mass difference makes that nuclei move much slower than electrons, and it is precisely this difference between temporal scales what allows assuming that electrons move in a field of fixed nuclei [82]. Classically speaking, the changes in nuclear configurations are not significant during the time period of electronic motion. Therefore, it is assumable that electrons follow the nuclei motion almost instantaneously. The practical consequences is we can assume that the electrons are moving in the field of fixed nuclei and, of course, if the nuclei are fixed in space and do not move, their kinetic energy is zero ($\widehat{\mathrm{T}}_{\mathrm{N}} = \widehat{0}$) and the potential energy due to nucleus-nucleus repulsion is constant ($\widehat{\mathrm{V}}_{\mathrm{NN}} = \mathrm{cte}$). Thus, Hamiltonian given by equation (2.5) reduces to the so-called electronic Hamiltonian, since our system is only constituted of electrons now:

$$\widehat{\mathrm{H}} = \widehat{\mathrm{T}}_{\mathrm{e}} + \cancelto{\widehat{0}}{\widehat{\mathrm{T}}_{\mathrm{N}}} + \widehat{\mathrm{V}}_{\mathrm{ee}} + \widehat{\mathrm{V}}_{\mathrm{Ne}} + \cancelto{\mathrm{cte}}{\widehat{\mathrm{V}}_{\mathrm{NN}}},$$

then

$$\widehat{\mathrm{H}}_{\mathrm{e}} = \widehat{\mathrm{T}}_{\mathrm{e}} + \widehat{\mathrm{V}}_{\mathrm{ee}} + \widehat{\mathrm{V}}_{\mathrm{Ne}}. \tag{2.11a}$$

$$\widehat{\mathrm{H}}_{\mathrm{e}} = -\frac{\hbar^2}{2m_e}\sum_{i=1}^{N}\nabla_{r_i}^2 + \frac{1}{4\pi\varepsilon_0}\sum_{i=1}^{N}\sum_{j>i}^{N}\frac{e^2}{|\vec{r_i} - \vec{r_j}|} + -\frac{1}{4\pi\varepsilon_0}\sum_{i=1}^{N}\sum_{I=1}^{M}\frac{Z_I e^2}{|\vec{r_i} - \vec{R_I}|}. \tag{2.11b}$$

[5] The mass number defines the nucleons number of a determined atom, i.e. the number of protons and neutrons.

Some authors keep the $\widehat{\mathrm{V}}_{\mathrm{NN}}$ term in the expression (2.11), but like this term is merely a constant we can remove it from this expression and only take it into account in the total energy expression of the system. It is important to point out that the nuclear coordinates $\{\vec{R}\}$ do not act in the electronic Hamiltonian as variables but as parameters, for every specified set of nuclear coordinates $\{\vec{R}\}$, there is a well defined $\widehat{\mathrm{H}}_{\mathrm{e}}$ that acts on the electronic coordinates $\{\vec{r}\,s\}$. Usually in the bibliography the attractive potential exerted on the electrons because of the presence of the nuclei - the expectation value of $\widehat{\mathrm{V}}_{\mathrm{Ne}}$ - is called external potential ($\mathrm{V}_{\mathrm{ext}}$) since this term considers the influence of an external agent (nuclei) on our system (only electrons).

The solution of the Schrödinger equation with $\widehat{\mathrm{H}}_{\mathrm{e}}$ is the electronic wave function $\varphi_{\mathrm{e}_{\{\vec{R}\}}}(\vec{r}_1 s_1, \vec{r}_2 s_2, ..., \vec{r}_N s_N)$ and the electronic energy E_{e}. The $\varphi_{\mathrm{e}_{\{\vec{R}\}}}(\vec{r}_1 s_1, \vec{r}_2 s_2, ..., \vec{r}_N s_N)$ notation reminds us that, as we already said, the electronic wave function depends on the electronic coordinates and parametrically of the nuclear coordinates, but to simplify the nomenclature we will use $\varphi(\{\vec{r}, s\})$ or simply φ:

$$\widehat{\mathrm{H}}_{\mathrm{e}}\varphi(\{\vec{r}, s\}) = E_{\mathrm{e}}\varphi(\{\vec{r}, s\}). \tag{2.12}$$

Thus, the total energy of the system E_{tot} is the sum of the electronic energy E_{e} and the constant of the nuclear repulsion that we neglected in equation (2.11) - the expectation values of $\widehat{\mathrm{V}}_{\mathrm{NN}}$ - E_{nuc}:

$$E_{\mathrm{tot}} = E_{\mathrm{e}} + \frac{1}{4\pi\varepsilon_0}\sum_{I=1}^{M}\sum_{J>I}^{M}\frac{Z_I Z_J e^2}{|\overrightarrow{R_I} - \overrightarrow{R_J}|} = E_{\mathrm{e}} + E_{\mathrm{nuc}}. \tag{2.13}$$

2.2.1 Solving the electronic problem

The electronic wave function $\varphi(\{\vec{r}, s\})$ itself does not directly represent an observable quantity. Rather, a physical interpretation can only be attributed to its squared modulus:

$$\left|\varphi(\{\vec{r}, s\})\right|^2 d\vec{r_1}\, d\vec{r_2} \ldots d\vec{r_N}, \tag{2.14}$$

which represents the probability of finding the N electrons simultaneously with position coordinates between $\vec{r_i}$ and $\vec{r_i} + d\vec{r_i}$ and spin coordinates equal to s_i. Since electrons are indistinguishable, the probability density $\left|\varphi(\{\vec{r}, s\})\right|^2$ must remain exactly the same if the coordinate of any two electrons are swapped. However, and because electrons are fermions, the wave function φ must exhibit antisymmetry under such exchange.

For a given system, the equation (2.12) permits numerous acceptable independent solutions, represented by the eigenfunctions φ_i, each associated with corresponding energy eigenvalues E_i. The set $\{\varphi\}$ is constituted by the φ_i that are orthogonal and normalized:

$$\int \cdots \int \varphi_i^* \varphi_j \, d\vec{x_1}\, d\vec{x_2} \ldots d\vec{x_N} \doteq \langle \varphi_i | \varphi_j \rangle = \delta_{ij}, \tag{2.15}$$

where the $\int \cdots \int \varphi_i^* \varphi_j \, d\vec{x_1}\, d\vec{x_2} \ldots d\vec{x_N}$ means the integration over the $3N$ spatial coordinates and summation over the N spin coordinates. φ_i^* indicates the complex conjugated of φ_i, $\langle \varphi_i | \varphi_j \rangle$ is the the Dirac notation [75] for the dot product between φ_i and φ_j, and δ_{ij} is the well-know Kronecker delta which is is defined as 0 if $i \neq j$ and 1 if $i = j$.

To solve the equation (2.12) for an arbitrary system (molecules or atoms) is necessary first of all to set up the specific Hamiltonian operator that correctly describe it. In equation (2.11) is evident that the only information in $\widehat{\mathrm{H}}_\mathrm{e}$ that depends on the actual system is the number of electrons N and the external potential V_{ext}. All the remaining terms, such as the operators representing the kinetic energy ($\widehat{\mathrm{T}}_\mathrm{e}$) or the electron-electron repulsion ($\widehat{\mathrm{V}}_\mathrm{ee}$), are independent of the particular considered system. Once the $\widehat{\mathrm{H}}_\mathrm{e}$ is properly defined, considering the right values for N and V_{ext}, we have to find the eigenfunctions φ_i and corresponding eigenvalues E_i that satisfy the expression (2.12). Once the φ_i are determined, all properties of interest can be obtained by applying the appropriate operators to the wave function. Regrettably, despite its seemingly simple and innocuous appearance, this program holds little practical relevance. This is because, with only a few trivial exceptions, no known strategy exists to precisely solve the Schrödinger equation for many-body systems. Nevertheless, the situation is not completely hopeless.

2.3 The variational principle

There is a way to systematically approach the wave function of the ground state φ_0, which is the state that delivers the lowest energy E_0. This is the *variational principle*, which holds a very important place in quantum-mechanics applications. From quantum mechanics is known that the expectation values of a particular observable represented by the operator $\widehat{\mathrm{A}}$ are given by:

$$\langle\widehat{\mathrm{A}}\rangle = \frac{\int\cdots\int \varphi^*\widehat{\mathrm{A}}\varphi\, d\overrightarrow{x_1}\, d\overrightarrow{x_2}\ldots d\overrightarrow{x_N}}{\int\cdots\int \varphi^*\varphi\, d\overrightarrow{x_1}\, d\overrightarrow{x_2}\ldots d\overrightarrow{x_N}} \doteq \frac{\langle\varphi\big|\widehat{\mathrm{A}}\big|\varphi\rangle}{\langle\varphi\big|\varphi\rangle}. \tag{2.16}$$

Many measurements of the observable A average to $\langle\widehat{\mathrm{A}}\rangle$, whereas particular measurements give particular eigenvalues of $\widehat{\mathrm{A}}$. If φ is normalized according to equation (2.15), the expectation values of $\langle\widehat{\mathrm{A}}\rangle$ will be:

$$A[\varphi] = \langle\widehat{\mathrm{A}}\rangle = \int\cdots\int \varphi^*\widehat{\mathrm{A}}\varphi\, d\overrightarrow{x_1}\, d\overrightarrow{x_2}\ldots d\overrightarrow{x_N} = \big\langle\varphi\big|\widehat{\mathrm{A}}\big|\varphi\big\rangle. \tag{2.17}$$

Where the square brackets in $A[\varphi]$ denote that φ determines A and we will say that A is a *functional*[6] [83].

The variational principle states that the energy of a guessed φ computed via the equation (2.17) will be upper bound to the true energy of the ground state $E_0 = E[\varphi_0]$:

$$\big\langle\varphi\big|\widehat{\mathrm{H}}_\mathrm{e}\big|\varphi\big\rangle = E[\varphi] \geq E[\varphi_0] = \big\langle\varphi_0\big|\widehat{\mathrm{H}}_\mathrm{e}\big|\varphi_0\big\rangle, \tag{2.18}$$

where the equality holds if and only if φ is identical to φ_0. Then, minimizing the functional $E[\varphi]$ with respect to all allowed N-electron wave functions we will obtain the ground state φ_0 and energy E_0:

$$E_0 = E[\varphi_0] = \min_{\varphi} E[\varphi] = \min_{\varphi} \big\langle\varphi\big|\widehat{\mathrm{T}}_\mathrm{e} + \widehat{\mathrm{V}}_\mathrm{ee} + \widehat{\mathrm{V}}_\mathrm{Ne}\big|\varphi\big\rangle. \tag{2.19}$$

[6] A *functional* is a mathematical term referring to a function that operates on other functions, rather than on individual numbers or variables $F[f(x)]$ (where $f(x)$ is a function) delivering as output a number.

Although conducting a search over all φ functions is clearly impractical, we can still apply the variational principle to subsets of the entire set of possible functions. Typically, these subsets are chosen such that the minimization outlined in equation (2.19) can be performed using some algebraic approach. The result will provide the best possible approximation to the exact wave function achievable within this particular subset. It is essential to recognize that by confining the search to a subset, we cannot precisely identify the exact wave function itself (unless the exact wave function is encompassed within the subset, which is highly unlikely). A classic instance is the Hartree-Fock approximation, discussed below, where the subset comprises all antisymmetric products of one-electron functions, known as Slater determinants, formed from N spin-orbitals.

To summarize, once N and V_{ext} (uniquely determined by Z_I and $\overrightarrow{R_I}$) are known, the $\widehat{\mathrm{H}}_\mathrm{e}$ can be constructed by using the expression (2.11). Through the variational principle (2.19) we can then - at least in principle - obtain the ground state wave function φ_0, thereby facilitating the determination of the ground state energy E_0 and of all the properties of the system:

$$\{N, Z_I, \overrightarrow{R_I}\} \Rightarrow \widehat{\mathrm{H}}_\mathrm{e} \Rightarrow \varphi_0 \Rightarrow E_0 \text{ (and all other properties).} \tag{2.20}$$

Thus, N and V_{ext} completely and uniquely determine φ_0 and E_0, therefore, we can say that the ground state energy is a functional of the number of electrons N and the external potential V_{ext}:

$$E_0 = E[N, V_{ext}]. \tag{2.21}$$

It's important to note that this statement does not mention the kinetic energy or the electron-electron repulsion, as these aspects are universal in that they are determined solely by the number of electrons N.

2.4 The Hartree-Fock approximation

As previously discussed, solving equation (2.19) by exhaustively searching through all acceptable N electron wave functions is impractical. Instead, we must define a suitable subset that provides a physically reasonable approximation to the exact wave function while remaining manageable in practice. In the Hartree-Fock scheme [84], we employ the simplest yet physically sound approximation to the intricate many-electron wave function. It consists in approximating the wave function of N indistinguishable interacting electrons by the exact wave-function of N indistinguishable non-interacting electrons. In the later case, it can be written as an antisymmetrized product of N orthonormal spin orbitals $\chi_i(\overrightarrow{x_i})$, each a product of a spatial orbital $\phi_i(\overrightarrow{r_i})$ and a spin function $\sigma(s) = \alpha(s)$ or $\beta(s)$. Such a product is usually referred as a Slater determinant:

$$\varphi^{\mathrm{HF}} = \frac{1}{\sqrt{N!}} \begin{vmatrix} \chi_1(\overrightarrow{x_1}) & \chi_2(\overrightarrow{x_1}) & \cdots & \chi_N(\overrightarrow{x_1}) \\ \chi_1(\overrightarrow{x_2}) & \chi_2(\overrightarrow{x_2}) & \cdots & \chi_N(\overrightarrow{x_2}) \\ \vdots & \vdots & \ddots & \vdots \\ \chi_1(\overrightarrow{x_N}) & \chi_2(\overrightarrow{x_N}) & \cdots & \chi_N(\overrightarrow{x_N}) \end{vmatrix}. \tag{2.22}$$

The pre-factor of $1/\sqrt{N!}$ ensures the normalization of the Hartree-Fock wave function, φ^{HF}, taking into account the expression (2.15). The Slater determinant exhibits

antisymmetry, as determinants change sign when two rows or columns are exchanged, equivalent to exchanging two electrons. Once the form of the wave function is decided, the next step is to use the variational principle to find the Slater determinant that minimizes the $E[\varphi^{\mathrm{HF}}]$ functional.

The energy expectation value in this case is found to be given by the expression:

$$E_{\mathrm{HF}} = \left\langle \varphi^{\mathrm{HF}} \middle| \widehat{\mathrm{H}}_{\mathrm{e}} \middle| \varphi^{\mathrm{HF}} \right\rangle = \sum_{i=1}^{N} H_i + \frac{1}{2} \sum_{i=1}^{N} \sum_{j=1}^{N} (J_{ij} - K_{ij}) \tag{2.23}$$

where

$$H_i = \int \chi_i^*(\vec{x}) \left[-\frac{1}{2}\nabla^2 + V_{ext}(\vec{x}) \right] \chi_i(\vec{x})\, d\vec{x}, \tag{2.24a}$$

$$J_{ij} = \iint \chi_i(\vec{x_1}) \chi_i^*(\vec{x_1}) \frac{1}{r_{12}} \chi_j^*(\vec{x_2}) \chi_j(\vec{x_2})\, d\vec{x_1}\, d\vec{x_2}, \tag{2.24b}$$

$$K_{ij} = \iint \chi_i^*(\vec{x_1}) \chi_j(\vec{x_1}) \frac{1}{r_{12}} \chi_i(\vec{x_2}) \chi_j^*(\vec{x_2})\, d\vec{x_1}\, d\vec{x_2}. \tag{2.24c}$$

The integral H_i defines the contribution to the kinetic energy and the electron-nucleus attraction. On the other hand, J_{ij} and K_{ij} represent what are commonly referred to as the *Coulomb* and *exchange integrals*, respectively, with the stipulation that $J_{ij} \geq K_{ij} \geq 0$. The term r_{12} is a simplified way of representing relative distance $|\vec{r_1} - \vec{r_2}|$ between the electrons $i = 1$ and $j = 2$.

In the double summation of equation (2.23), the inclusion of the term $i = j$ is permissible. This implies that if $i = j$, expression (2.24b) delineates the Coulomb repulsion of an electron's charge distribution with itself, a scenario known as *self-interaction*, which lacks physical meaning. However, the exchange term (2.24c) rectifies this, as when $i = j$, the exchange integral precisely matches the Coulomb term but with an opposite sign, effectively overriding the self-interaction component.

It is evident that E_{HF} is a functional of the spin orbitals $\chi_i(\vec{x_i})$, $E_{\mathrm{HF}} = E[\{\chi_i\}]$. In accordance with the variational principle, the objective is to determine the set of spin orbitals $\chi_i(\vec{x_i})$ that minimizes the E_{HF}, while adhering to the orthonormalization conditions specified in expression (2.15):

$$\left\langle \chi_i^* \middle| \chi_j \right\rangle = \delta_{ij}. \tag{2.25}$$

This presents a classical optimization problem, which can be tackled using the method of Lagrange multipliers [85]. The outcome of this approach yields the Hartree-Fock differential equations,

$$\widehat{\mathrm{F}} \chi_i(\vec{x}) = \sum_{j=1}^{N} \varepsilon_{ij} \chi_j(\vec{x}), \tag{2.26}$$

where the Fock operator $\widehat{\mathrm{F}}$ is an effective one-electron operator defined as:

$$\widehat{\mathrm{F}} = -\frac{1}{2}\nabla^2 + V_{ext}(\vec{x}) + \widehat{\mathrm{g}}. \tag{2.27}$$

The initial pair of terms denotes the kinetic energy and potential energy arising from the electron-nucleus interaction. $\widehat{\mathrm{g}}(x_1)$ is the Coulomb-exchange operator whose expected value is the Hartree-Fock potential. This potential represents the mean repulsive effect experienced by the i-th electron in the presence of the remaining $N-1$ electrons. The expression for the $\widehat{\mathrm{g}}(x_1)$ operator is as follows:

$$\widehat{\mathrm{g}} = \widehat{\mathrm{j}} - \widehat{\mathrm{k}}, \tag{2.28}$$

where the Coulomb operator is defined as:

$$\widehat{\mathrm{j}}(\overrightarrow{x_1}) f(\overrightarrow{x_1}) \doteq \sum_{k=1}^{N} \int \chi_k^*(\overrightarrow{x_2}) \chi_k(\overrightarrow{x_2}) \frac{1}{r_{12}} f(\overrightarrow{x_1})\, d\overrightarrow{x_2}, \tag{2.29}$$

and the exchange one as:

$$\widehat{\mathrm{k}}(\overrightarrow{x_1}) f(\overrightarrow{x_1}) \doteq \sum_{k=1}^{N} \int \chi_k^*(\overrightarrow{x_2}) f(\overrightarrow{x_2}) \frac{1}{r_{12}} \chi_k(\overrightarrow{x_1})\, d\overrightarrow{x_2}, \tag{2.30}$$

being $f(\overrightarrow{x_1})$ an arbitrary function.

The Coulomb operator characterizes the potential felt by an electron positioned at $\overrightarrow{x_1}$ owing to the mean charge distribution of another electron within the spin orbital $\chi_k(\overrightarrow{x_2})$. As the outcome of applying $\widehat{\mathrm{j}}(\overrightarrow{x_1})$ to a spin orbital $f(\overrightarrow{x_1}) = \chi_l(\overrightarrow{x_1})$ solely relies on the value of χ_l at position $\overrightarrow{x_1}$, both this operator and its associated potential are called *local*. Conversely, the exchange operator $\widehat{\mathrm{k}}(\overrightarrow{x_1})$ and its corresponding exchange potential are called *non-local*. This comes from the definition of $\widehat{\mathrm{k}}(\overrightarrow{x_1})$, where considering $f(\overrightarrow{x_1}) = \chi_l(\overrightarrow{x_1})$ elucidates that such an operator induces an exchange of variables between the two spin orbitals. Consequently, the outcomes of operating with $\widehat{\mathrm{k}}(\overrightarrow{x_1})$ on $\chi_l(\overrightarrow{x_1})$ depends on the value of χ_l across all points in space, as χ_l is now related to $\overrightarrow{x_2}$, the variable over which integration is performed.

The matrix ε in the Hartree-Fock differential equations (2.26) consists of Lagrange multipliers associated with the constraints (2.25). Multiplying (2.26) by χ_i^* and integrating, it is obtained the formula for "orbital energies":

$$\varepsilon_i \doteq \varepsilon_{ii} = \left\langle \chi_i \middle| \widehat{\mathrm{F}} \middle| \chi_i \right\rangle = H_i + \sum_{j=1}^{N} (J_{ij} - K_{ij}). \tag{2.31}$$

Summing over i and comparing with (2.23), we obtain:

$$E_{\mathrm{HF}} = \sum_{i=1}^{N} \varepsilon_i - V_{ee}, \tag{2.32}$$

where V_{ee} stands the total electron-electron repulsion energy:

$$V_{ee} = \frac{1}{2} \sum_{i=1}^{N} \sum_{j=1}^{N} (J_{ij} - K_{ij}). \tag{2.33}$$

It is important to recognize that because the Fock operator is contingent upon the spin orbitals via the Hartree-Fock potential, which in turn relies on the solutions of the eigenvalue problem at hand, equation (2.26) represents a non-standard eigenvalue problem that cannot be straightforwardly solved in closed form. Instead, we encounter a *pseudo-eigenvalue* problem necessitating iterative methods for resolution. The technique used is commonly known as the *self-consistent field* (SCF) procedure, as the orbitals are determined from their own effective potential. In brief, such method begins with an initial guess of orbitals, which are used to solve the equation (2.26). The resulting orbitals are then iteratively refined in subsequent iterations until the difference between input and output orbitals falls below a predefined threshold.

2.5 Electron density

We can significantly reduce the dimensionality of the problem by employing the electronic density instead of the wave function to describe the state of the system. In an electronic system, the quantity representing the number of electrons per unit volume in a specific state is termed *electron density*. Denoted by $\rho(\vec{r})$, it is defined as the result of a multiple integral over the spin coordinates of all electrons and over all spatial variables except one, as follows:

$$\rho(\vec{r_1}) = N \int \cdots \int \left|\varphi(\vec{x_1}, \vec{x_2}, ..., \vec{x_N})\right|^2 ds_1 \, d\vec{x_2} \ldots d\vec{x_N}. \tag{2.34}$$

This term determines the probability of finding any of the N electrons within the volume element $d\vec{r_1}$ with spin s_1. Strictly speaking $\rho(\vec{r})$ is a probability density, but in practice is common to call it electron density. $\rho(\vec{r})$ is a non-negative function of three spatial variables, x, y and z, which vanishes at infinity for molecular systems, but not for periodic ones, and integrates to the total number of electrons:

$$\rho(\vec{r} \to \infty) = 0, \tag{2.35a}$$

$$\int \rho(\vec{r}) \, d\vec{r} = N. \tag{2.35b}$$

$$\tag{2.35c}$$

Unlike the wave function, this quantity is an observable and can be measured experimentally. Some maps of electron densities can be found in [86].

2.5.1 Reduced density matrices for fermions

Considering an even more general description of a quantum state, we could defined the *density matrix* as:

$$\gamma_N(\vec{x_1}', \vec{x_2}', \ldots, \vec{x_N}'; \vec{x_1}, \vec{x_2}, \ldots, \vec{x_N}) \doteq \varphi_N(\vec{x_1}', \vec{x_2}', \ldots, \vec{x_N}')\varphi_N^*(\vec{x_1}, \vec{x_2}, \ldots, \vec{x_N}), \tag{2.36}$$

where the variables of the first factor are primed. Expression (2.36) might be thought as an element of a matrix, where if we set $\vec{x_i} = \vec{x_i}'$ for all i, we get a diagonal element of this matrix, the original $\varphi_N(\vec{x_1}, \vec{x_2}, \ldots, \vec{x_N})\varphi_N^*(\vec{x_1}, \vec{x_2}, \ldots, \vec{x_N})$ term. Considering the

definition of operator presented in Appendix A, the term 2.36 can be viewed as the coordinate representation of the *density operator*,

$$\widehat{\gamma}_N = \big|\varphi_N\big\rangle\big\langle\varphi_N\big|. \tag{2.37}$$

Thus, for normalized φ_N, we have:

$$\mathrm{tr}(\widehat{\gamma}_N) = \int\cdots\int \varphi_N(\overrightarrow{x_1},\overrightarrow{x_2},\ldots,\overrightarrow{x_N})\varphi_N^*(\overrightarrow{x_1},\overrightarrow{x_2},\ldots,\overrightarrow{x_N})\,d\overrightarrow{x_1}\,d\overrightarrow{x_2}\ldots\,d\overrightarrow{x_N} = 1, \tag{2.38}$$

where the *trace* of the operator $\widehat{\mathrm{A}}$ is defined as the sum of diagonal elements of the matrix representing $\widehat{\mathrm{A}}$, or the integral if the representation is continuous as in (2.38). It is also verifiable that:

$$\langle\widehat{\mathrm{A}}\rangle = \mathrm{tr}(\widehat{\gamma}_N\widehat{\mathrm{A}}) = \mathrm{tr}(\widehat{\mathrm{A}}\widehat{\gamma}_N) \tag{2.39}$$

of which (2.16) is the coordinate representation.

The density operator $\widehat{\gamma}_N$ of (2.37) contains the same information of the N-electron wave function $\big|\varphi_N\big\rangle$. Such operator can be generalized to the *ensemble density operator*:

$$\widehat{\Gamma} = \sum_i p_i\big|\varphi_i\big\rangle\big\langle\varphi_i\big|, \tag{2.40}$$

where p_i is the probability of the system being found in the state $\big|\varphi_i\big\rangle$, and the sum is taken over the entire set of accessible pure states[7].

Having defined the density matrix and its operator, we can now introduce the concept of the *reduced density matrix*. The density matrix given in (2.36) is typically referred to as the Nth *order density matrix* for a pure state of an N-electron system. The *reduced density matrix of order p* is defined as [87]:

$$\begin{aligned}&\gamma_p(\overrightarrow{x_1}',\overrightarrow{x_2}',\ldots,\overrightarrow{x_p}';\overrightarrow{x_1},\overrightarrow{x_2},\ldots,\overrightarrow{x_p}) \doteq \binom{N}{p}\times\\ &\int\cdots\int \gamma_N(\overrightarrow{x_1}',\overrightarrow{x_2}',\ldots,\overrightarrow{x_p}',\overrightarrow{x_{p+1}},\overrightarrow{x_{p+2}},\ldots,\overrightarrow{x_N};\overrightarrow{x_1},\overrightarrow{x_2},\ldots,\overrightarrow{x_N})\,d\overrightarrow{x_{p+1}}\,d\overrightarrow{x_{p+2}}\ldots\,d\overrightarrow{x_N},\end{aligned} \tag{2.41}$$

where $\binom{N}{p}$ is a binomial coefficient. We are specially interested in first and second-order density matrix γ_1 and γ_2, respectively:

$$\gamma_1(\overrightarrow{x_1}';\overrightarrow{x_1}) = N\int\cdots\int \varphi(\overrightarrow{x_1}',\overrightarrow{x_2},\ldots,\overrightarrow{x_N})\varphi^*(\overrightarrow{x_1},\overrightarrow{x_2},\ldots,\overrightarrow{x_N})\,d\overrightarrow{x_2}\ldots\,d\overrightarrow{x_N}, \tag{2.42}$$

and

$$\begin{aligned}&\gamma_2(\overrightarrow{x_1}',\overrightarrow{x_2}';\overrightarrow{x_1},\overrightarrow{x_2})\\ &= \frac{N(N-1)}{2}\int\cdots\int \varphi(\overrightarrow{x_1}',\overrightarrow{x_2}',\overrightarrow{x_3},\ldots,\overrightarrow{x_N})\varphi^*(\overrightarrow{x_1},\overrightarrow{x_2},\overrightarrow{x_3},\ldots,\overrightarrow{x_N})\,d\overrightarrow{x_3}\ldots\,d\overrightarrow{x_N}.\end{aligned} \tag{2.43}$$

[7] A state is called *pure* if it can be described by a wave function and *mixed* if it is described by a linear superposition of wave functions.

The first-order density matrix γ_1 normalizes to the number of electrons, while the second-order density matrix γ_2 does it to the number of electron pairs:

$$\mathrm{tr}(\gamma_1(\vec{x_1}';\vec{x_1})) = \int \gamma_1(\vec{x_1}';\vec{x_1})\, d\vec{x_1} = N, \tag{2.44}$$

$$\mathrm{tr}(\gamma_2(\vec{x_1}',\vec{x_2}';\vec{x_1},\vec{x_2})) = \iint \gamma_2(\vec{x_1}',\vec{x_2}';\vec{x_1},\vec{x_2})\, d\vec{x_1}\, d\vec{x_2} = \frac{N(N-1)}{2}. \tag{2.45}$$

Thus the γ_1 can be obtained from γ_2 by the following relation:

$$\gamma_1(\vec{x_1}';\vec{x_1}) = \frac{2}{N-1}\int \gamma_2(\vec{x_1}',\vec{x_2};\vec{x_1},\vec{x_2})\, d\vec{x_2}, \tag{2.46}$$

where the full four-variable $\gamma_2(\vec{x_1}',\vec{x_2}';\vec{x_1},\vec{x_2})$ is no longer required, but instead, the three-variable term $\gamma_2(\vec{x_1}',\vec{x_2};\vec{x_1},\vec{x_2})$.

These reduced matrices are coordinate representations of operators $\widehat{\gamma}_1$ and $\widehat{\gamma}_2$. Like $\widehat{\gamma}_N$, these operators are positive and Hermitian. Such Hermitian operators can be decomposed into their eigenfunctions by the following expression:

$$\widehat{\gamma}_1 = \sum_i n_i \big|\psi_i\big\rangle\big\langle\psi_i\big|, \tag{2.47}$$

and

$$\widehat{\gamma}_2 = \sum_i g_i \big|\theta_i\big\rangle\big\langle\theta_i\big|. \tag{2.48}$$

The eigenfunctions $\psi_i(\vec{x})$ and $\theta_i(\vec{x_1};\vec{x_2})$ are referred to as the *natural spin orbitals* and *natural geminals*, respectively, while the eigenvalues n_i and g_i are known as *occupation numbers*. Thus, n_i corresponds to the probability of the one-electron state being occupied, while g_i corresponds to the probability of the two-electron state being occupied.

Now considering the expectation value of an one-electron operator for an antisymmetric N-body wave function φ defined as:

$$\widehat{\mathrm{O}}_1 = \sum_{i=1}^{N} O_1(\vec{x_i};\vec{x_i}'), \tag{2.49}$$

it is obtained:

$$\langle\widehat{\mathrm{O}}_1\rangle = \mathrm{tr}(\widehat{\mathrm{O}}_1\gamma_N) = \iint O_1(\vec{x_1},\vec{x_1}')\gamma_1(\vec{x_1}';\vec{x_1})\, d\vec{x_1}\, d\vec{x_1}'. \tag{2.50}$$

If the one-electron operator is local in the sense of (A.21), typically only the diagonal part is written,

$$\widehat{\mathrm{O}}_1 = \sum_{i=1}^{N} O_1(\vec{x_i}), \tag{2.51}$$

and its expectation-value changes to:

$$\langle\widehat{\mathrm{O}}_1\rangle = \int \big[O_1(\vec{x_1})\gamma_1(\vec{x_1}';\vec{x_1})\big]_{\vec{x_1}'=\vec{x_1}}\, d\vec{x_1}. \tag{2.52}$$

As all the two-electron operators that concern us are local, we directly denote their diagonal part, neglecting the two delta functions that come out from (A.21). Thus it is written as:

$$\widehat{\mathrm{O}}_2 = \sum_{i<j}^{N} O_2(\vec{x_i}; \vec{x_j}), \tag{2.53}$$

which leads to the following expectation value:

$$\langle \widehat{\mathrm{O}}_2 \rangle = \mathrm{tr}(\widehat{\mathrm{O}}_2 \gamma_N) = \iint \left[O_2(\vec{x_1}; \vec{x_2}) \gamma_2(\vec{x_1}', \vec{x_2}'; \vec{x_1}, \vec{x_2}) \right]_{\vec{x_1}'=\vec{x_1}; \vec{x_2}'=\vec{x_2}} d\vec{x_1}\, d\vec{x_2}. \tag{2.54}$$

As the electronic Hamiltonian $\widehat{\mathrm{H}}_\mathrm{e}$ of expression (2.11) can be thought as the sum of two diagonal "one-electron" operators ($\widehat{\mathrm{T}}_\mathrm{e}$ and $\widehat{\mathrm{V}}_\mathrm{Ne}$) and a symmetric "two-electron" operator ($\widehat{\mathrm{V}}_\mathrm{ee}$), its expectation value can be written as:

$$\begin{aligned} E = \langle \widehat{\mathrm{H}}_\mathrm{e} \rangle &= \mathrm{tr}(\widehat{\mathrm{H}}_\mathrm{e} \gamma_N) \\ &= \int \left[\left(-\frac{1}{2} \nabla_{r_1}^2 + V_{ext}(\vec{r_1}) \right) \gamma_1(\vec{x_1}'; \vec{x_1}) \right]_{\vec{x_1}'=\vec{x_1}} d\vec{x_1} \\ &\quad + \iint \frac{1}{r_{12}} \gamma_2(\vec{x_1}, \vec{x_2}; \vec{x_1}, \vec{x_2})\, d\vec{x_1}\, d\vec{x_2}. \end{aligned} \tag{2.55}$$

Where the atomic units system, previously discussed, was employed to simplify the equation. Thanks to expression (2.46), only the second-order density matrix is needed to determine the energy of the system. Thus, using the concept of a functional presented in Section 2.3, we can conclude that the total energy of the system is a functional of the second-order density matrix:

$$E = E[\gamma_1, \gamma_2] = E[\gamma_2]. \tag{2.56}$$

This mathematical development was undertaken to demonstrate how the dimensionality of the problem changes from $4N$ variables (three spatial and one spin variable for each of the N electrons) to only eight variables if spin is considered, or to six variables if spin is not considered, by simply shifting the representation of the system from its wave function to its density matrix.

2.5.2 Exchange-correlation hole

The operators that constitute $\widehat{\mathrm{H}}_\mathrm{e}$ do not involve spin coordinates, making it desirable to further reduce the γ_1 and γ_2 density matrices presented above by summing over the spin coordinates s_1 and s_2 [88]. This leads to the first-order and second-order *spinless density matrices*:

$$\begin{aligned} \rho_1(\vec{r_1}'; \vec{r_1}) &= \int \gamma_1(\vec{r_1}' s_1; \vec{r_1} s_1)\, ds_1 \\ &= N \int \cdots \int \varphi(\vec{r_1}' s_1, \vec{x_2}, \ldots, \vec{x_N}) \varphi^*(\vec{r_1} s_1, \vec{x_2}, \ldots, \vec{x_N})\, ds_1\, d\vec{x_2} \ldots d\vec{x_N}, \end{aligned} \tag{2.57}$$

and

$$\begin{aligned}\rho_2(\vec{r_1}', \vec{r_2}'; \vec{r_1}, \vec{r_2}) &= \iint \gamma_2(\vec{r_1}' s_1, \vec{r_2}' s_2; \vec{r_1} s_1, \vec{r_2} s_2)\, ds_1\, ds_2 \\ &= \frac{N(N-1)}{2} \int \cdots \int \varphi(\vec{r_1}' s_1, \vec{r_2}' s_2, \vec{x_3}, \ldots, \vec{x_N}) \\ &\quad \times \varphi^*(\vec{r_1} s_1, \vec{r_2} s_2, \vec{x_3}, \ldots, \vec{x_N})\, ds_1\, ds_2\, d\vec{x_3} \ldots\, d\vec{x_N}.\end{aligned} \tag{2.58}$$

Introducing a shorter notation for the diagonal element ($\vec{r_i}' = \vec{r_i}$) of ρ_1 and ρ_2 we obtained that:

$$\rho_1(\vec{r_1}) = \rho_1(\vec{r_1}; \vec{r_1}) = N \int \cdots \int |\varphi(\vec{r_1} s_1, \vec{x_2}, \ldots, \vec{x_N})|^2\, ds_1\, d\vec{x_2} \ldots\, d\vec{x_N}, \tag{2.59}$$

and

$$\begin{aligned}\rho_2(\vec{r_1}; \vec{r_2}) &= \rho_2(\vec{r_1}, \vec{r_2}; \vec{r_1}, \vec{r_2}) \\ &= \frac{N(N-1)}{2} \int \cdots \int |\varphi(\vec{r_1} s_1, \vec{r_2} s_2, \vec{x_3}, \ldots, \vec{x_N})|^2\, ds_1\, ds_2\, d\vec{x_3} \ldots\, d\vec{x_N}.\end{aligned} \tag{2.60}$$

The diagonal element of $\rho_1(\vec{r_1}'; \vec{r_1})$ in expression (2.59) is simply the electron density defined in (2.34). Taking into account that $\rho(\vec{r_1}) = \rho_1(\vec{r_1})$ and considering the relationship (2.46) it follows that:

$$\rho(\vec{r_1}) = \frac{2}{N-1} \int \rho_2(\vec{r_1}, \vec{r_2})\, d\vec{r_2}. \tag{2.61}$$

As discussed in Section 2.5, $\rho(\vec{r_1})$ provides insights into the likelihood of finding any of the N electrons within the volume element $d\vec{r_1}$ with spin s_1. Similarly, $\rho_2(\vec{r_1}; \vec{r_2})$ can be understood as the probability of finding not one but a pair of two electrons with spins s_1 and s_2 simultaneously within two volume elements $d\vec{r_1}$ and $d\vec{r_2}$.

In the previous section we stated that all the reduced density matrices change their signs on exchange of two primed of two unprimed particle indices to conserve the antisymmetric property of the φ. This property is also transferable to ρ_2, which changes its sign on the exchange of two electrons:

$$\rho_2(\vec{r_1}; \vec{r_2}) = -\rho_2(\vec{r_2}; \vec{r_1}). \tag{2.62}$$

If we look at the special case where $\vec{r_1} = \vec{r_2}$, which is the probability of having two electrons with the same spin are found within the same volume element, we find that:

$$\rho_2(\vec{r_1}; \vec{r_1}) = -\rho_2(\vec{r_1}; \vec{r_1}), \tag{2.63}$$

which holds true if and only if $\rho_2(\vec{r_1}; \vec{r_1}) = 0$. In other words, the probability of finding two electrons with the same spin at the same point in space is exactly zero (Pauli principle). Hence, electrons with the same spin do not move independently of each other; they are correlated. This effect is known as *exchange* or *Fermi correlation*. Additionally, there is an electrostatic repulsion among the electrons that prevents them from coming too close to each other. This can be considered another type of correlation, completely independent of spin, and is usually referred to as *Coulomb correlation*.

The expectation values for the one-electron (2.52) and two-electron operators (2.54), now referred as spin-free operators $\widehat{\mathcal{O}}_1$ and $\widehat{\mathcal{O}}_2$, respectively, are:

$$\langle \widehat{\mathcal{O}}_1 \rangle = \int \left[\mathcal{O}_1(\vec{r_1}) \rho_1(\vec{r_1}'; \vec{r_1}) \right]_{\vec{r_1}' = \vec{r_1}} d\vec{r_1}. \tag{2.64}$$

and

$$\langle \widehat{\mathcal{O}}_2 \rangle = \iint \left[\mathcal{O}_2(\vec{r_1}; \vec{r_2}) \rho_2(\vec{r_1}', \vec{r_2}'; \vec{r_1}, \vec{r_2}) \right]_{\vec{r_1}' = \vec{r_1}; \vec{r_2}' = \vec{r_2}} d\vec{r_1}\, d\vec{r_2}. \tag{2.65}$$

Therefore, the expression for the energy (2.55) becomes

$$\begin{aligned} E &= E[\rho_1(\vec{r_1}'; \vec{r_1}), \rho_2(\vec{r_1}; \vec{r_2})] = E[\rho_2(\vec{r_1}', \vec{r_2}; \vec{r_1}, \vec{r_2})] \\ &= \int \left[-\frac{1}{2} \nabla_r^2 \rho_1(\vec{r}'; \vec{r}) \right]_{\vec{r}' = \vec{r}} d\vec{r} + \int V_{ext}(\vec{r}) \rho(\vec{r})\, d\vec{r} \\ &\quad + \iint \frac{1}{r_{12}} \rho_2(\vec{r_1}; \vec{r_2})\, d\vec{r_1}\, d\vec{r_2}. \end{aligned} \tag{2.66}$$

The three terms in expression (2.66) correspond to the electronic kinetic energy, the nuclear-electron potential energy, and the electron-electron potential energy, respectively. It is important to highlight, that now the energy of the system is a problem that involves one function of three coordinates ($\rho(\vec{r})$), and two functions of six coordinates ($\rho_1(\vec{r}'; \vec{r})$ and $\rho_2(\vec{r_1}; \vec{r_2})$).

Let's focus in the third term of (2.66), the electron-electron repulsion energy. In a purely classical environment , this term would be just the self-repulsion energy of a distribution $\rho(\vec{r})$:

$$J[\rho] = \frac{1}{2} \iint \frac{1}{r_{12}} \rho(\vec{r_1}) \rho(\vec{r_2})\, d\vec{r_1}\, d\vec{r_2}, \tag{2.67}$$

where the 1/2 was considered to prevent the double counting. This suggests that the $\rho_2(\vec{r_1}; \vec{r_2})$ can be written as:

$$\rho_2(\vec{r_1}; \vec{r_2}) = \frac{1}{2} \rho(\vec{r_1}) \rho(\vec{r_2}) [1 + h(\vec{r_1}; \vec{r_2})], \tag{2.68}$$

where $h(\vec{r_1}; \vec{r_2})$ is the *pair correlation function*, which is a symmetric function that incorporates all nonclassical effects, such as Fermi correlation. If (2.68) is substituted in (2.61) the following equality is achieved:

$$\frac{N-1}{2} \rho(\vec{r_1}) = \frac{1}{2} \rho(\vec{r_1}) \left[N + \int \rho(\vec{r_2}) h(\vec{r_1}; \vec{r_2})\, d\vec{r_2} \right]. \tag{2.69}$$

The equality (2.69) is valid only if:

$$\int \rho(\vec{r_2}) h(\vec{r_1}; \vec{r_2})\, d\vec{r_2} = -1. \tag{2.70}$$

Another way to write it is by defining the *exchange-correlation hole* as:

$$\rho_{xc}(\vec{r_1}; \vec{r_2}) = \rho(\vec{r_2}) h(\vec{r_1}; \vec{r_2}). \tag{2.71}$$

Interestingly, from (2.70) it is appreciable that the sum over the exchange-correlation hole correspond to minus one electron:

$$\int \rho_{xc}(\vec{r_1};\vec{r_2})\, d\vec{r_2} = -1. \tag{2.72}$$

The concept of the exchange-correlation hole is widely used in DFT, which is why its definition was carefully addressed. This concept is very useful for understanding how exchange and Coulomb correlations affect the electron distribution in a many-body system. We can imagine an electron creating a hole around itself, reducing the probability of finding another electron nearby. Considering this new concept it is worthwhile to take a look at the expectation value of $\widehat{\mathrm{V}}_{\mathrm{ee}}$ in (2.66). Thus, using expressions (2.67), (2.68) and (2.71), the V_{ee} term becomes

$$\begin{aligned} V_{ee} &= \iint \frac{1}{r_{12}} \rho_2(\vec{r_1};\vec{r_2})\, d\vec{r_1}\, d\vec{r_2} \\ &= J[\rho] + \frac{1}{2} \iint \frac{1}{r_{12}} \rho(\vec{r_1}) \rho_{xc}(\vec{r_1},\vec{r_2})\, d\vec{r_1}\, d\vec{r_2}. \end{aligned} \tag{2.73}$$

The first term corresponds to the classical electrostatic interaction of a charge distribution with itself, while the second term represents the energy of interaction between the charge density and the charge distribution of the exchange-correlation hole. The first term includes the unphysical self-interaction, whereas the second term provides the correction for this self-interaction and accounts for quantum correlation effects, such as Fermi correlation.

The exchange-correlation hole can be split into the *Fermi hole*, $\rho_x(\vec{r_1};\vec{r_2})$ and the *Coulomb hole*, $\rho_c(\vec{r_1};\vec{r_2})$:

$$\rho_{xc}(\vec{r_1};\vec{r_2}) = \rho_x(\vec{r_1};\vec{r_2}) + \rho_c(\vec{r_1};\vec{r_2}). \tag{2.74}$$

The Fermi hole accounts for Fermi correlation and the Pauli principle, which applies only to electrons with the same spin ($s_1 = s_2$). The Coulomb hole arises from the electrostatic repulsion between two electrons, regardless of their spin. While separating ρ_{xc} into exchange and correlation contributions is convenient, it is important to highlight that only the total hole has true physical meaning. More details regarding the properties and the shapes of the Fermi and Coulomb holes can be found in references [81, 89].

2.6 Density-Functional Theory

In the preceding section, we established that describing the state of a system of N electrons using the wave function is immensely intricate, as it relies on $4N$ variables and cannot be experimentally verified. However, by substituting the wave function with the observable electron density $\rho(\vec{r})$, a substantial reduction in problem dimensionality is achieved. This led to the reformulation of the Schrödinger equation in terms of first-order and second-order reduced density matrices, resulting in an equation dependent on only eight variables, regardless of system size. DFT emerges as the theory facilitating this transition from the wave function and its associated Schrödinger equation to the electron density and its corresponding calculational scheme. Truly remarkable, isn't it?

2.6.1 The Thomas-Fermi model

The initial endeavors to utilize electron density instead of the wave function to gain insights into atomic and molecular systems date back to the 1920s, with the pioneering works of Thomas and Fermi [90–92]. This approach constitutes a quantum statistical model of electrons, focusing solely on kinetic energy while treating nuclear-electron contributions in a fully classical way. They arrived to the following expression for the kinetic energy based on the uniform electron gas:

$$T_{TF}[\rho(\vec{r})] = C_F \int \rho(\vec{r})^{5/3}\, d\vec{r}, \tag{2.75}$$

where the pre-factor C_F is equal to:

$$C_F = \frac{3}{10}(3\pi^2)^{2/3} = 2.871. \tag{2.76}$$

The rigorous energy expression (2.66) provides the kinetic energy in terms of the first-order density matrix. By excluding the exchange and correlation terms in (2.66) to consider only the classical electrostatic energies of electron-nucleus attraction and electron-electron repulsion, we obtain, using (2.67), an energy expression for an atom solely in terms of the electron density:

$$E_{TF}[\rho(\vec{r})] = C_F \int \rho(\vec{r})^{5/3}\, d\vec{r} + \int V_{ext}(\vec{r})\rho(\vec{r})\, d\vec{r} + \frac{1}{2}\iint \frac{\rho(\vec{r_1})\rho(\vec{r_2})}{r_{12}}\, d\vec{r_1}\, d\vec{r_2}. \tag{2.77}$$

This expression represents the first genuine density functional for energy. In other words, it provides a method to map a density $\rho(\vec{r})$ onto an energy E without requiring any additional information.

2.6.2 The Thomas-Fermi-Dirac model

This model adopts the $T[\rho(\vec{r})]$ proposed by Thomas-Fermi theory and, for approximating $V_{ee}[\rho(\vec{r})]$ in (2.66), adds the exchange-energy expression for a uniform electron gas [93] to $J[\rho]$. Dirac's exchange-energy expression [93] aims to incorporate the quantum mechanical exchange effects into the electron-electron repulsion, and is defined as:

$$K_D[\rho(\vec{r})] = -C_x \int \rho(\vec{r})^{4/3}\, d\vec{r}, \tag{2.78}$$

with an pre-exponential factor of

$$C_x = \frac{3}{4}\left(\frac{3}{\pi}\right)^{1/3} = 0.739. \tag{2.79}$$

Thus, the energy expression (2.66) for this model results in:

$$\begin{aligned} E_{TFD}[\rho(\vec{r})] = C_F \int \rho(\vec{r})^{5/3}\, d\vec{r} + \int V_{ext}(\vec{r})\rho(\vec{r})\, d\vec{r} \\ + \frac{1}{2}\iint \frac{\rho(\vec{r_1})\rho(\vec{r_2})}{r_{12}}\, d\vec{r_1}\, d\vec{r_2} - C_x \int \rho(\vec{r})^{4/3}\, d\vec{r}, \end{aligned} \tag{2.80}$$

which is the Thomas-Fermi-Dirac energy functional. Notably, the Thomas-Fermi energy functional (2.77) can be derived by setting $C_x = 0$. To enhance the accuracy of this approximation, an adjustable semi-empirical parameter $2/3 \leq \alpha \leq 1$ was introduced into the pre-factor C_x by Slater in 1951 [94], resulting in the development of the X_α method:

$$C_x = \frac{3}{2}\alpha\left(\frac{3}{\pi}\right)^{1/3}. \tag{2.81}$$

Over the years, countless modifications and improvements have been made to the Thomas-Fermi model, such as the Thomas-Fermi-Dirac approach and the X_α method mentioned above. However, the situation changed with the publication of a landmark paper by Hohenberg and Kohn in 1964 [95]. They established fundamental theorems demonstrating that for ground states, the Thomas-Fermi model can be considered an approximation to an exact theory: the *density functional theory.*

2.6.3 The Hohenberg-Kohn theorems

In Section 2.3, we showed that the ground-state energy E_0 of an electronic system is a functional of the number of electrons N and the external potential V_{ext} (see expression (2.21)). However, the *first Hohenberg-Kohn theorem* [95] asserts that the electron density $\rho(\vec{r})$ can be used as the fundamental variable instead of N and V_{ext}. It states: "*The external potential $V_{ext}(\vec{r})$ is determined, within a trivial additive constant, by the electron density $\rho(\vec{r})$.*" Since ρ determines the number of electrons, it follows that $\rho(\vec{r})$ also determines the ground-state wave function φ and all other electronic properties of the system.

The proof of this theorem is relatively straightforward and is based on reductio ad absurdum. It relies on the minimum-energy principle for the ground state. Suppose there are two external potentials, V_{ext} and V'_{ext}, which differ by more than a constant but yield the same ground-state electron density ρ_0. These two external potentials would correspond to two different Hamiltonians, which differ only in their external potential components: $\widehat{\mathrm{H}}_\mathrm{e} = \widehat{\mathrm{T}}_\mathrm{e} + \widehat{\mathrm{V}}_\mathrm{ee} + \widehat{\mathrm{V}}_{ext}$ and $\widehat{\mathrm{H}}'_\mathrm{e} = \widehat{\mathrm{T}}_\mathrm{e} + \widehat{\mathrm{V}}_\mathrm{ee} + \widehat{\mathrm{V}}'_{ext}$. Clearly, the two Hamiltonians $\widehat{\mathrm{H}}_\mathrm{e}$ and $\widehat{\mathrm{H}}'_\mathrm{e}$ correspond to two distinct ground-state wave functions, φ_0 and φ'_0, and respective ground-state energies, E_0 and E'_0, with $E_0 \neq E'_0$. However, we assumed that both wave functions give to the same electron density, this can be schematically express as follows:

$$V_{ext} \Rightarrow \widehat{\mathrm{H}}_\mathrm{e} \Rightarrow \varphi_0 \Rightarrow \quad \rho_0(\vec{r}) \quad \Leftarrow \varphi'_0 \Leftarrow \widehat{\mathrm{H}}'_\mathrm{e} \Leftarrow V'_{ext}. \tag{2.82}$$

Using φ'_0 as trial function for $\widehat{\mathrm{H}}_\mathrm{e}$, by the variational principle we must have:

$$E_0 < \langle\varphi'_0|\widehat{\mathrm{H}}_\mathrm{e}|\varphi'_0\rangle = \langle\varphi'_0|\widehat{\mathrm{H}}'_\mathrm{e}|\varphi'_0\rangle + \langle\varphi'_0|\widehat{\mathrm{H}}_\mathrm{e} - \widehat{\mathrm{H}}'_\mathrm{e}|\varphi'_0\rangle, \tag{2.83}$$

as the two Hamiltonians only differ in the external potential:

$$E_0 < E'_0 + \langle\varphi'_0|\widehat{\mathrm{T}}_\mathrm{e} + \widehat{\mathrm{V}}_\mathrm{ee} + \widehat{\mathrm{V}}_{ext} - \widehat{\mathrm{T}}_\mathrm{e} - \widehat{\mathrm{V}}_\mathrm{ee} - \widehat{\mathrm{V}}'_{ext}|\varphi'_0\rangle, \tag{2.84}$$

which leads to

$$E_0 < E'_0 + \int \rho_0(\vec{r})\left[V_{ext}(\vec{r}) - V'_{ext}(\vec{r})\right] d\vec{r}. \tag{2.85}$$

Similarly taking φ_0 as a trial function for the $\widehat{\mathrm{H}}'_{\mathrm{e}}$ problem:

$$E'_0 < \langle\varphi_0|\widehat{\mathrm{H}}'_{\mathrm{e}}|\varphi_0\rangle = \langle\varphi_0|\widehat{\mathrm{H}}_{\mathrm{e}}|\varphi_0\rangle + \langle\varphi_0|\widehat{\mathrm{H}}'_{\mathrm{e}} - \widehat{\mathrm{H}}_{\mathrm{e}}|\varphi_0\rangle, \tag{2.86}$$

which yields

$$E'_0 < E_0 - \int \rho_0(\vec{r})\big[V_{ext}(\vec{r}) - V'_{ext}(\vec{r})\big]\, d\vec{r}. \tag{2.87}$$

By summing equations (2.85) and (2.87), we obtain $E_0+E'_0 < E_0+E'_0$, which is evidently a contradiction. This concludes the proof that there cannot be two distinct V_{ext} values that produce the same ground state electron density. In other words, the ground state density ρ_0 uniquely determines the external potential V_{ext}. Thus, reformulating the terminology of expression (2.20), we get:

$$\rho_0 \Rightarrow \{N, Z_I, \overrightarrow{R_I}\} \Rightarrow \widehat{\mathrm{H}}_{\mathrm{e}} \Rightarrow \varphi_0 \Rightarrow E_0 \text{ (and all other properties)}. \tag{2.88}$$

Since the complete ground state energy is a functional of the ground state electron density so must be its individual components and we can write:

$$E_0[\rho_0] = T_e[\rho_0] + V_{ee}[\rho_0] + V_{Ne}[\rho_0]. \tag{2.89}$$

It is convenient to separate this expression into parts that depend on the specific system and parts that are universal, meaning their form is independent of N, $\overrightarrow{R_I}$ and Z_I. For the system dependent terms we have only the $V_{Ne}[\rho_0] = \int \rho_0(\vec{r})V_{ext}(\vec{r})\, d\vec{r}$ in the equation (2.89), while the rest are system independent. Grouping the system independent parts into a new quantity, we obtain:

$$E_0[\rho_0] = F_{HK}[\rho_0] + \int \rho_0(\vec{r})V_{ext}(\vec{r})\, d\vec{r}, \tag{2.90}$$

where

$$F_{HK}[\rho_0] = T_e[\rho_0] + V_{ee}[\rho_0] \tag{2.91}$$

is the *Hohenberg-Kohn functional*.

If the Hohenberg-Kohn functional is fed with some arbitrary density $\rho(\vec{r})$, it cranks out the expectation value $\langle\varphi|\widehat{\mathrm{T}}_{\mathrm{e}} + \widehat{\mathrm{V}}_{\mathrm{ee}}|\varphi\rangle$. This is the sum of the kinetic energy and the electron-electron repulsion operator with the ground state wave function φ,

$$F_{HK}[\rho] = T_e[\rho] + V_{ee}[\rho] = \langle\varphi|\widehat{\mathrm{T}}_{\mathrm{e}} + \widehat{\mathrm{V}}_{\mathrm{ee}}|\varphi\rangle. \tag{2.92}$$

This term represents the pinnacle of DFT. If known, it would allow us to solve the Schrödinger equation exactly, rather than approximately. Furthermore, as a universal functional independent of any specific system, it is applicable to both simple atoms like hydrogen and complex structures such as large molecules and solids, including DNA. $F_{HK}[\rho]$ includes the functional for the electron kinetic energy, $T_e[\rho]$, as well as the functional for the electron-electron interaction, $V_{ee}[\rho]$. Currently, the exact forms of these functionals are entirely undefined. However, from the later we can extract the classical Coulomb part $J[\rho]$ of (2.67), since that is already well known,

$$V_{ee}[\rho] = \frac{1}{2}\iint \frac{1}{r_{12}}\rho(\vec{r_1})\rho(\vec{r_2})\, d\vec{r_1}\, d\vec{r_2} + V_{ncl}[\rho] = J[\rho] + V_{ncl}[\rho]. \tag{2.93}$$

$V_{ncl}[\rho]$ represents the nonclassical term, encompassing all the effects of self-interaction correction, exchange, and Coulomb correlation that were previously described. Finding explicit expressions for the unknown functionals, $T_e[\rho]$ and $V_{ncl}[\rho]$, represents the major challenge in DFT.

The *second Hohenberg-Kohn theorem* [95] provides the energy variational principle. It reads: "*For a trial density* $\tilde{\rho}(\vec{r})$*, such that* $\tilde{\rho}(\vec{r}) \geq 0$ *and* $\int \tilde{\rho}(\vec{r})\, d\vec{r} = N$,

$$E_0[\rho_0] \leq E[\tilde{\rho}], \tag{2.94}$$

where $E[\tilde{\rho}] = T_e[\tilde{\rho}] + V_{ee}[\tilde{\rho}] + V_{Ne}[\tilde{\rho}]$." In other words, this theorem asserts that the functional $F_{HK}[\rho]$ yields the lowest energy if and only if the input is the true ground state density, ρ_0. This is essentially the variational principle for wave functions discussed in Section 2.3.

To prove this theorem is quite easy since it makes use of the variation principle. From the previous theorem we have that any trial density $\tilde{\rho}(\vec{r})$ determines its own $\tilde{V}_{ext}(\vec{r})$, Hamiltonian $\widehat{\tilde{\mathrm{H}}}_{\mathrm{e}}$, and wave function $\tilde{\varphi}$, which can be taken as a trial function for the problem of interest having external potential $V_{ext}(\vec{r})$. Thus,

$$\left\langle \tilde{\varphi} \middle| \widehat{\mathrm{H}}_{\mathrm{e}} \middle| \tilde{\varphi} \right\rangle = F_{HK}[\tilde{\rho}] + \int \tilde{\rho}(\vec{r}) V_{ext}(\vec{r})\, d\vec{r} = E[\tilde{\rho}] \geq E_0[\rho_0]. \tag{2.95}$$

Having established the one-to-one correspondence between the ground-state electron density $\rho_0(\vec{r})$ and the ground-state wave function ψ_0, the following question arises: how can we determine ψ_0 from a given $\rho_0(\vec{r})$? The inverse problem is straightforward, as ψ_0 defines $\rho_0(\vec{r})$ by definition (2.34). However, there are an infinite number of antisymmetric wave functions (not necessarily ground states) that yield the same density. The Levy constrained-search approach offers a solution to this problem [96, 97]. We will present some key concepts necessary for the continuity of our chapter, but readers can find more details regarding this approach in references [81, 98]. The universal density functional is defined as:

$$F[\rho] = \min_{\varphi \to \rho} \left\langle \varphi \middle| \widehat{\mathrm{T}}_{\mathrm{e}} + \widehat{\mathrm{V}}_{\mathrm{ee}} \middle| \varphi \right\rangle, \tag{2.96}$$

for any ρ that is N-representable. The functional $F[\rho]$ searches all φ that yield the input density $\rho(\vec{r})$ and then delivers the minimum of $\langle \widehat{\mathrm{T}}_{\mathrm{e}} + \widehat{\mathrm{V}}_{\mathrm{ee}} \rangle$. It follows that:

$$F_{HK}[\rho_0] = F[\rho_0]. \tag{2.97}$$

This results in

$$E_0 = \min_{\rho} \left(F[\rho] + \int \rho(\vec{r}) V_{ext}(\vec{r})\, d\vec{r} \right). \tag{2.98}$$

The functional $F[\rho]$ differs from $F_{HK}[\rho]$ in that it is defined for all densities originating from an antisymmetric wave function ψ. This approach demonstrates the existence of the universal density functional $F[\rho]$ and establishes the energy-functional principle (2.98). As a result, it provides a rigorous density-functional method for determining the ground-state energy of any electronic system.

2.6.4 The Kohn-Sham approach

In 1965, just a year after the groundbreaking work by Hohenberg and Kohn [95], Kohn and Sham [99] proposed a method to approximate the elusive universal functional $F[\rho]$. They introduced the idea of a non-interacting reference system crafted from a set of orbitals (i.e., one-electron functions) capable of accurately computing most of the kinetic energy. The residual portion, alongside the unknown non-classical contributions to electron-electron repulsion, is combined. This approach aims to compute as much exact information as possible, with only a fraction of the total energy determined by an approximate functional.

In the preceding section, we demonstrated that the ground state energy of an atomic or molecular system can be expressed by equation (2.98). There, the universal density functional $F[\rho]$ incorporates the distinct components of kinetic energy, classical Coulomb interaction, and the non-classical term arising from self-interaction correction, exchange, and electron correlation effects:

$$F[\rho(\vec{r})] = T_e[\rho(\vec{r})] + J[\rho(\vec{r})] + V_{ncl}[\rho(\vec{r})]. \tag{2.99}$$

Among these terms, only $J[\rho(\vec{r})]$ is known, while the specific expressions for the other two terms remain elusive. Thomas-Fermi and related models offer a straightforward approach, in which one devises explicit approximate formulations for $T_e[\rho]$ and $V_{ee}[\rho]$. While these approximations offer simplicity, advancing beyond the basic level of approximation presents significant challenges. In a trade-off between simplicity and accuracy, Kohn and Sham [95] devised a clever indirect approach to the kinetic-energy functional $T_e[\rho(\vec{r})]$. This method transformed DFT into a practical tool for precise calculations.

To understand Kohn-Sham method, it is necessary to go back to the Hartree-Fock scheme of Section 2.4. There, the wave function of the system φ^{HF} is a single Slater determinant constructed from N one-electron spin-orbitals $\chi_i(\vec{x_i})$. While the Slater determinant serves as the approximation to the true N-electron wave function in the Hartree-Fock method, it has the form of an exact wave-function for a fictitious system featuring N *non-interacting* electrons (that is "electrons" which behaves as uncharged fermions and therefore do not interact with each other via Coulomb repulsion), moving in the effective potential V_{HF}. For this kind of wave functions, the kinetic energy can be exactly written as:

$$T_e^{HF} = \sum_{i=1}^{N} \big\langle \chi_i(\vec{x_i}) \big| -\frac{1}{2}\nabla^2 \big| \chi_i(\vec{x_i}) \big\rangle. \tag{2.100}$$

The Hartree-Fock spin orbitals $\chi_i(\vec{x_i})$ that appear in this expression are chosen such that the expectation value E_{HF} attains its minimum (under the usual constraint that the χ_i remain orthonormal)

$$E_{HF} = \min_{\Phi_{\mathrm{SD}}} \big\langle \Phi_{\mathrm{SD}} \big| \widehat{\mathrm{T}}_{\mathrm{e}} + \widehat{\mathrm{V}}_{\mathrm{ee}} + \widehat{\mathrm{V}}_{\mathrm{Ne}} \big| \Phi_{\mathrm{SD}} \big\rangle. \tag{2.101}$$

Where Φ_{SD} represents the Slater determinant of expression (2.22). This is simply a recap of the Hartree-Fock method, with no new concepts introduced at this stage. The crucial link to DFT lies in leveraging the above kinetic energy expression, which applies to non-interacting fermions, to calculate the major fraction of the kinetic energy for our interacting system.

Kohn and Sham invoked a corresponding *non-interacting reference system*, with a Hamiltonian in which we have introduced an effective, local potential $V_s(\vec{r})$:

$$\widehat{\mathrm{H}}_s = \sum_{i=1}^{N} -\frac{1}{2}\nabla_i^2 + \sum_{i=1}^{N} V_s(\vec{r}), \tag{2.102}$$

where are not electron-electron repulsion terms, and *the ground-state electron density is exactly* ρ. For this system there is an exact ground-state wave function represented by a Slater determinant:

$$\Theta_s = \frac{1}{\sqrt{N!}} \begin{vmatrix} \varphi_1(\vec{x_1}) & \varphi_2(\vec{x_1}) & \cdots & \varphi_N(\vec{x_1}) \\ \varphi_1(\vec{x_2}) & \varphi_2(\vec{x_2}) & \cdots & \varphi_N(\vec{x_2}) \\ \vdots & \vdots & \ddots & \vdots \\ \varphi_1(\vec{x_N}) & \varphi_2(\vec{x_N}) & \cdots & \varphi_N(\vec{x_N}) \end{vmatrix}. \tag{2.103}$$

In this expression Θ_s and φ_i replace Φ_{SD} and χ_i, respectively, to make the expression more general than the Hartree-Fock model. In (2.103), φ_i are the N lowest eigenstates of the one-electron Hamiltonian $\widehat{\mathrm{h}}_s$ (or Fock operator in the Hartree-Fock approximation):

$$\widehat{\mathrm{h}}_s\varphi_i = \left[-\frac{1}{2}\nabla_i^2 + V_s(\vec{r}) \right]\varphi_i = \varepsilon_i\varphi_i. \tag{2.104}$$

In Kohn-Sham theory, $\widehat{\mathrm{h}}_s$ is the Kohn-Sham operator $\widehat{\mathrm{f}}_{\mathrm{KS}}$, defined as:

$$\widehat{\mathrm{f}}_{\mathrm{KS}} = -\frac{1}{2}\nabla_i^2 + V_s(\vec{r}). \tag{2.105}$$

To differentiate these orbitals from their Hartree-Fock counterparts, they are termed *Kohn-Sham orbitals*. The link between this artificial system and the actual system of interest is established by selecting the effective potential V_s so that the density resulting from the summation of the squared moduli of the orbitals $\{\varphi_i\}$ precisely matches the ground state density of the real system with interacting electrons,

$$\rho_s(\vec{r}) = \sum_{i=1}^{N}\sum_{s} |\varphi_i(\vec{r}, s)|^2 = \rho_0(\vec{r}). \tag{2.106}$$

We must remember that our initial goal was to find a betetr method than the Thomas-Fermi approximation for determining the kinetic energy. Kohn and Sham's insight was that if we cannot precisely determine the kinetic energy through an explicit functional, we should adopt a less ambitious approach and focus on calculating as much of the true kinetic energy exactly as possible. The remaining terms would then be treated approximately. Consequently, they proposed using expression (2.100) to obtain the exact kinetic energy of the non-interacting reference system, which has the same density as the real, interacting system,

$$T_s[\rho] = T_e^{HF} = \sum_{i=1}^{N} \left\langle \varphi_i(\vec{x_i}) \middle| -\frac{1}{2}\nabla^2 \middle| \varphi_i(\vec{x_i}) \right\rangle. \tag{2.107}$$

Of course, the non-interacting kinetic energy is not equal to the true kinetic energy of the interacting system, even if the systems share the same density ($T_s[\rho] \neq T_e[\rho]$). Kohn and Sham addressed this discrepancy by introducing the following separation of the functional $F[\rho]$:

$$F[\rho] = T_s[\rho] + J[\rho] + E_{xc}[\rho], \tag{2.108}$$

where $E_{xc}[\rho]$ is the so-called *exchange-correlation energy*, which is defined as:

$$E_{xc}[\rho] \doteq T_e[\rho] - T_s[\rho] + V_{ee}[\rho] - J[\rho]. \tag{2.109}$$

The residual part of the true kinetic energy ($T_e[\rho] - T_s[\rho]$), not accounted for by $T_s[\rho]$, is simply added to the non-classical electrostatic contributions. In other words, the exchange-correlation energy $E_{xc}[\rho]$ is the functional that encompasses all the unknown factors. It's important to note that despite its name, $E_{xc}[\rho]$ includes not only the non-classical effects of self-interaction correction, exchange, and correlation contributions to the potential energy of the system, but also a portion of the kinetic energy, also called *dynamic-correlation*.

The foundations of the Kohn-Sham method have been outlined, but a crucial question remains: how can we define $V_s(\vec{r})$ so that it yields a Slater determinant characterized by exactly the same density as our real system? To address this challenge, we express the energy of our interacting real system in terms of the separation outlined in equation (2.108):

$$\begin{aligned} E[\rho(\vec{r})] &= T_s[\rho(\vec{r})] + J[\rho(\vec{r})] + E_{xc}[\rho(\vec{r})] + V_{Ne}[\rho(\vec{r})] \\ &= T_s[\rho(\vec{r})] + \frac{1}{2}\iint \frac{\rho(\vec{r_1})\rho(\vec{r_2})}{r_{12}}\, d\vec{r_1}\, d\vec{r_2} + E_{xc}[\rho(\vec{r})] + \int V_{ext}\rho(\vec{r})\, d\vec{r} \end{aligned} \tag{2.110}$$

The sole term lacking an explicit form, representing the significant unknown, is $E_{xc}[\rho(\vec{r})]$. Applying the variational principle to ascertain the orbitals $\{\varphi_i\}$ that minimize the energy of equation (2.110) under the constraint of $\langle \varphi_i | \varphi_j \rangle = \delta_{ij}$, yields the following equations:

$$\left(-\frac{1}{2}\nabla^2 + \left[\int \frac{\rho(\vec{r_2})}{r_{12}}\, d\vec{r_2} + V_{xc}(\vec{r_1}) - \sum_{I=1}^{M} \frac{Z_I}{r_{iI}} \right] \right) \varphi_i = \varepsilon_i \varphi_i. \tag{2.111}$$

The expression within the brackets is equivalent to $V_s(\vec{r})$ from equation (2.104), and it is termed the Kohn-Sham *effective potential*:

$$V_s(\vec{r}) \doteq V_{eff}(\vec{r}) = \int \frac{\rho(\vec{r_2})}{r_{12}}\, d\vec{r_2} + V_{xc}(\vec{r_1}) - \sum_{I=1}^{M} \frac{Z_I}{r_{iI}}. \tag{2.112}$$

The V_{xc} term represents the potential due to the exchange-correlation energy E_{xc}. Since the E_{xc} is unknown, the explicit shape of its corresponding potential is unknown too. Hence, V_{xc} is the functional derivate of E_{xc} with respect to ρ:

$$V_{xc}(\vec{r}) \doteq \frac{\delta E_{xc}[\rho]}{\delta \rho(\vec{r})}. \tag{2.113}$$

If the precise forms of the functional $E_{xc}[\rho]$ and consequently $V_{xc}(\vec{r})$ were known, the Kohn-Sham method would yield the exact energy, which is the correct eigenvalue of the Hamiltonian $\widehat{\mathrm{H}}_\mathrm{e}$ of the Schrödinger equation. This is why the Kohn-Sham approach is

considered to be exact in principle. The need for approximation arises when we must determine the explicit form of the unknown functional $E_{xc}[\rho]$ and its corresponding $V_{xc}(\vec{r})$. Thus, a primary objective of modern Density Functional Theory (DFT) is to develop better approximations for these two quantities, which will be briefly discussed in the following section.

Before moving on to the approximations of the functional $E_{xc}[\rho]$, we summarize how the Kohn-Sham method works in practice. In Figure 2.1, we outline the algorithm commonly used to implement the such method. The convergence criteria are determined by comparing the difference between the total energy in the current iteration and the previous one against the desired threshold. As previously mentioned, the only approximation arises in the separation functional $F[\rho]$ (2.108) within the blue square, where an approximate exchange-correlation functional is assumed.

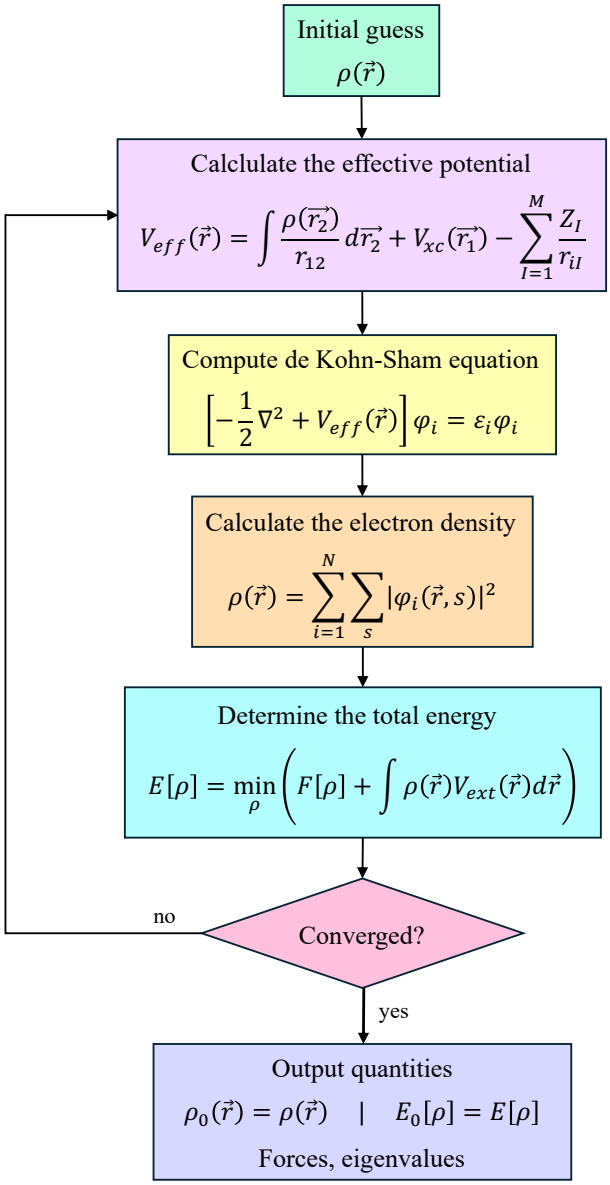

Figure 2.1. Practical algorithm for implementing the Kohn-Sham method.

2.6.5 Different kinds of exchange-correlation functionals

Currently, we've demonstrated that DFT is an exact theory, with the sole approximation found in the exchange-correlation functional $E_{xc}[\rho]$. However, we have yet to discuss the specific form of this term, which is the primary focus of this section.

Let's begin with the *Local Density Approximation (LDA)*. At the core of this model is the concept of a hypothetical uniform electron gas, wherein electrons move within a positive background charge distribution, resulting in an electrically neutral ensemble overall with constant electron density. This scenario resembles the model of an idealized metal, comprising a perfect crystal lattice of valence electrons and positive cores, with the cores diffused to form a uniform positive background charge. Despite this scenario is far away from any realistic situation, it places a prominent place in DFT since it is the only system for which the $E_{xc}[\rho]$ is exactly known. In this case the exchange-correlation functional is written as:

$$E_{xc}^{\mathrm{LDA}}[\rho] = \int \rho(\vec{r})\varepsilon_{xc}(\rho)\, d\vec{r}, \tag{2.114}$$

where $\varepsilon_{xc}(\rho)$ is the exchange-correlation energy per particle of a uniform electron gas of density $\rho(\vec{r})$. This quantity can be further split into exchange and correlation contributions,

$$\varepsilon_{xc}(\rho) = \varepsilon_x(\rho) + \varepsilon_c(\rho). \tag{2.115}$$

The exchange part is already known, it was given by Dirac exchange energy functional (see Section 2.6.2),

$$\varepsilon_x(\rho) = -C_x\rho(\vec{r})^{1/3}, \qquad C_x = \frac{3}{4}\left(\frac{3}{\pi}\right)^{1/3} = 0.739. \tag{2.116}$$

Currently, there is no explicit expression known for the correlation part, $\varepsilon_c(\rho)$. However, precise values are obtainable through the quantum Monte Carlo calculations carried out by Ceperley and Alder [100]. These values have been interpolated to yield an analytic form for $\varepsilon_c(\rho)$, with further details available in [98].

The LDA approximation is suitable for systems with slowly-varying densities but lacks formal justification for highly inhomogeneous systems like atoms and molecules. Consequently, successful extensions to the purely local approximation emerged in the early eighties. The initial advancement involved incorporating not only the information of the electron density $\rho(\vec{r})$ at the position $\vec{r}$ but also supplementing it with information about its gradient $\nabla\rho(\vec{r})$ to address the non-homogeneity of the true electron density. In other words, the local density approximation can be seen as the initial term in a Taylor-like expansion of the uniform density. By including the next term in this series, is expected to achieve a more accurate approximation of the exchange-correlation functional,

$$\begin{aligned} E_{xc}^{\mathrm{GEA}}[\rho_\alpha, \rho_\beta] = &\int \rho(\vec{r})\varepsilon_{xc}(\rho_\alpha, \rho_\beta)\, d\vec{r} \\ &+ \sum_{\sigma,\sigma'} \int C_{xc}^{\sigma,\sigma'}(\rho_\alpha, \rho_\beta) \frac{\nabla\rho_\sigma}{\rho_\sigma^{2/3}} \frac{\nabla\rho_{\sigma'}}{\rho_{\sigma'}^{2/3}}\, d\vec{r} + \ldots. \end{aligned} \tag{2.117}$$

Where σ and σ' are the spin functions of the α and β spin, respectively. ρ_α and ρ_β are the two spin densities, with $\rho_\alpha(\vec{r}) + \rho_\beta(\vec{r}) = \rho(\vec{r})$. This formulation is known as the *Gradient Expansion Approximation (GEA)*, which is applicable to systems with

non-uniform but slowly varying densities. However, the GEA doesn't perform well for real molecular problems and in some cases its accuracy is even worts than the simple LDA [81].

To improve the performance of the GEA, it was developed the *Generalized Gradient Approximation (GGA)*, presented by Perdew [101] and further simplified by Perdew and Yue [102]. In the GGA, the exchange-correlation functional is expressed as:

$$E_{xc}^{\mathrm{GGA}}[\rho_\alpha, \rho_\beta] = \int f(\rho_\alpha, \rho_\beta, \nabla\rho_\alpha, \nabla\rho_\beta)\, d\vec{r}. \tag{2.118}$$

Several proposals exist for the explicit dependence of the function $f(\rho_\alpha, \rho_\beta, \nabla\rho_\alpha, \nabla\rho_\beta)$ on the densities and their gradients. These include semiempirical functionals, which incorporate parameters that are calibrated against reference values instead of being derived purely from first principles. In practice, E_{xc}^{GGA} is usually split into its exchange and correlation contributions:

$$E_{xc}^{\mathrm{GGA}} = E_x^{\mathrm{GGA}} + E_c^{\mathrm{GGA}}. \tag{2.119}$$

Approximations for the two terms on expression (2.119) are individually searched.

Given that this functional will be employed in our forthcoming calculations, we aim to delve deeper into it, particularly focusing on the exchange functional of (2.119). It's noteworthy to mention that these functionals and their corresponding holes are constructed to satisfy specific conditions. In fact, some of them are not rooted in a physical model; rather, they are mathematically complex constructions. In essence, the actual expressions for E_x^{GGA} and E_c^{GGA} often do not directly aid in understanding the physics these functionals aim to capture. This underscores the pragmatic nature that is characteristic of approximate density functional theory in general.

The exchange part of E_{xc}^{GGA} is written as:

$$\begin{aligned} E_x^{\mathrm{GGA}}[\rho] &= -C_x \int \rho^{4/3} F(s)\, d\vec{r} \\ &= -\frac{3}{4}\left(\frac{3}{\pi}\right)^{1/3} \int \rho^{4/3} F(s)\, d\vec{r}. \end{aligned} \tag{2.120}$$

The argument of the function $F(s)$ is called *reduced density gradient*:

$$s = \frac{|\nabla\rho(\vec{r})|}{\rho(\vec{r})^{4/3}}, \tag{2.121}$$

which is to be understood as a local inhomogeneity parameter. This results in significant values not only in regions with large gradients but also in regions of low densities, such as the exponential tails far from the nuclei. Conversely, small values of s appear for small gradients, typically for bonding regions, but also for regions of large density. Certainly, the homogeneous electron gas exhibits $s = 0$ everywhere, attributed to $\nabla\rho(\vec{r}) = 0$. In (2.121) is divided by $\rho(\vec{r})^{4/3}$ and not by $\rho(\vec{r})$ itself to guarantee that s is dimensionless.

Regarding the function $F(s)$ of (2.120) two main classes of realizations have been put forward. The first one is based on a GGA exchange functional developed by Becke [103], which is abbreviated as B:

$$F^B(s) = \frac{\beta s^2}{1 + 6\beta s \sinh^{-1} s}. \tag{2.122}$$

β is an empirical parameter that was determined to 0.0042. Some functionals related to this approach include among the FT97 [104], the PW91 exchange functional [105, 106] and the CAM(A) and CAM(B) functionals developed by Handy and coworkers [107].

The second class of GGA exchange functionals use for $F(s)$ a rational function of the reduced density gradient. Some prominent representatives are the early functionals B86 developed by Becke [108], the P86 [109], the LG [110] and the PBE [111]. As an example we explicitly write down the $F(s)$ function for the PBE exchange functional, which is the one used in our calculations:

$$F^{PBE}(s) = 1 + \kappa - \frac{\kappa}{1 + \frac{\mu s^2}{\kappa}}, \tag{2.123}$$

where the parameters $\mu = 0.2195$ and $\kappa = 0.804$.

The gradient-corrected correlation functionals E_c^{GGA} in (2.119) possess even more intricate analytical expressions. As a result, we refrain from presenting their explicit formulations and limit our examination to a qualitative discussion of the most prevalent functionals. Among these are the correlation analogue of P86 [109], which incorporates an empirical parameter calibrated against the correlation energy of the neon (Ne) atom. In 1992, Perdew and Wang [112] improved their correlation functional, resulting in the parameter-free PW91. Another, even more widely adopted functional is the LYP developed by Lee, Yang, and Parr [113]. Unlike the preceding functionals, LYP does not rely on the uniform electron gas but instead derives from an expression for the correlation energy of the He atom. It is worth noting that all these correlation functionals are based on systems that solely incorporate short-range correlation effects.

In theory, any exchange functional could be paired with any correlation functional, but only a few combinations are commonly utilized. The exchange component is predominantly selected to be B86 functional, often combined with either P86 correlation functional or the LYP functional - abbreviated as BP86 and BLYP, respectively. Occasionally, the PW91 correlation functional is also employed, resulting in BPW91. In our case, we employed the PBE exchange-correlation functional [111], which has been extensively utilized for calculations of H atoms properties in W bulks [114–116] and for keeping consistency the same functional was used in the Cu-H system.

Another type of functional combines the gradient correction used in the exchange-correlation functional from GGA with the exchange functional of Hartree-Fock. These are known as *hybrid functionals*. Perdew, Burke, and Ernzerhof proposed a parameter-free hybrid functional of this kind, where the amount of exact exchange is theoretically derived to be 25% based on perturbation theory arguments [117, 118],

$$E_{xc}^{\mathrm{hybrid}} = E_{xc}^{\mathrm{GGA}} + 0.25(E_x^{\mathrm{HF}} - E_x^{\mathrm{GGA}}). \tag{2.124}$$

When the PBE exchange-correlation functional is selected as the GGA component, the PBE0 model is formed. This model demonstrates promising performance across all significant properties, competing effectively with the most reliable, empirically parameterized current functionals, as detailed in reference [119]. Novel forms of functionals aim to explore new formulations for exchange-correlation functionals. Extending the search for approximate exchange-correlation functionals beyond the GGA by incorporating second-order gradients and the (non-interacting) kinetic energy density has led to a new family of functionals known as *Meta-Generalized Gradient Approximation*

(meta-GGA) [120]. An example of this type of functional is the LAP correlation functional [121], which considers the Laplacian of the electron density ($\nabla^2\rho(\vec{r})$).

This way, we are arriving to the end of this chapter where an overview of the theoretical background of DFT was done. While it is impossible to cover all the intricate details of such a vast theory, readers interested in further information can refer to references [81, 99, 122]. For those looking to understand how DFT is applied to crystals, where the $V_{ext}(\vec{r})$ term is periodic, excellent references include [123–125]. And now, let's see part of this theory in practice!

Chapter 3

A model of the W/Cu interface

In this chapter the model of the W/Cu interface is presented. We discussed which criteria were taken into account to build it suitable for DFT calculations. The chapter is divided into two sections. The first section provides a detailed explanation of key terminologies, including Bramfitt's mismatch parameter. This parameter is crucial for understanding the rationale behind selecting our specific crystallographic orientations. Additionally, this section encompasses the results of the convergence study done to test the employed pseupotentials, allowing us to optimize the numerical parameters (such as number of k-points and cutoff energy) for the DFT simulations. The second section includes the paper where the results are published.

3.1 Presentation of the study

In this section, we will delve into the preliminary analyses conducted before defining any model. Typically, such details are condensed into a brief paragraph or sentence in research papers, potentially causing confusion for readers. To enhance clarity and facilitate a comprehensive understanding of the information presented in our paper, we have opted for a thorough explanation of key concepts that were considered in the definition of our model.

3.1.1 Mismatch parameter

Creating a W/Cu interface model suitable for DFT is a challenging task. On one hand, there is a huge number of different structures that can be considered changing the crystallographic orientation of both materials. On the other hand, it is necessary to create a unit cell with cell parameters closely aligned with those in the W and Cu networks. Simultaneously, optimizing the number of atoms becomes crucial, given that computational resources rise with the growing of considered atoms the number of atoms has to be optimized as much as possible because the computational resources increases with the number of considered atoms. Moreover, as W and Cu bulks possess different Bravais lattice and cell parameters, they have an intrinsic mismatch which also must

be minimized while creating their interface. In summary, to construct the interface, it is crucial to focus on crystallographic orientations that simultaneously minimize the number of atoms in the unit cell, reduce the mismatch between the W and Cu networks, and closely align with the cell parameters of the W and Cu cells. Let's focus, first of all, in minimizing the mismatch between both structures.

Bramfitt's lattice mismatch theory [126] is one of the method used in the literature to determine the contribution of the disregistry between two phases to the interfacial free energy. In his study he proposed a new formalism to determine the mismatch between the two planes at the interface of two phases, called substrate and nucleated solid[1]. On the contrary to the previous formalism established by Turnbull-Vonnegut [127] which was only valid for planes of similar atomic arrangement, Bramfitt's equation was generilized to any crystallographic combinations of two phases with planes of differing atomic arrangements. Bramfitt introduced three disregistry terms that define the crystallographic relationship at the interface of two phases, making possible to determine a planar mismatch, as opposed to the linear disregistry proposed by Turnbull-Vonnegut theory. Thus, the generalized form of his equation is:

$$\delta = \frac{\delta_1 + \delta_2 + \delta_3}{3} \times 100, \tag{3.1}$$

where δ_1, δ_2 and δ_3 are the linear disregistries along the three lowest-index directions within a 90° quadrant of the planes of the substrate and the nucleated. It can be also written, in a more specific way, as:

$$\delta^{(hkl)_s}_{(hkl)_n} = \frac{1}{3}\sum_{i=1}^{3} \frac{|(d_{[uvw]^i_s}\cos\theta_i) - d_{[uvw]^i_n}|}{d_{[uvw]^i_n}} \times 100, \tag{3.2}$$

where $(hkl)_s$ and $(hkl)_n$ represent a low-index plane of the substrate and in the nucleated solid, respectively; $[uvw]^i_s$ and $[uvw]^i_n$ are the low-index direction in the $(hkl)_s$ and $(hkl)_n$ planes, respectively; $d_{[uvw]^i_s}$ and $d_{[uvw]^i_n}$ stand the interatomic spacing along the $[uvw]^i_s$ and $[uvw]^i_n$ directions, respectively; and θ_i is the angle between the $[uvw]^i_s$ and $[uvw]^i_n$ directions. In Figure 3.1 is schematized the crystallographic relationship for δ in the case of Cu(110) and W(110) planes.

Bramfitt's theory was employed to determined which crystallographic orientation to choose for creating the W/Cu interface. As Bramfitt probed in his study [126], the lower the disregistry, the more effective the compound is in promoting nucleation and the lower its interfacial energy, which means that the interface will be more stable and more likely to form. Based on this criterion of stability, the mismatch parameter defined by the equation (3.2) was determined for several low-index directions in different crystallographic planes of W and Cu bulks. In Table 3.1 we summarize some of the most representative orientations with their respective values of δ. The representations of the vectors and lattice planes were done with the support of the softwares VESTA [128] and XCrySDen [129].

In Table 3.1 the first nine interfaces were constructed making a combinatory of different possible orientations on the (100), (110) and (111) planes of both materials. The No. 10 is symmetrically equivalent to the one employed in our model, and the No. 11 and No. 12

[1]The name of substrate and nucleated solid come from the fact that originally Bramfitt was study the heterogeneous nucleation process. But in a general way they can be called as substrate and adsorbate, being the adsorbate the species that is deposited on the substrate. In this work we will use both concepts, either nucleated solid or adsorbate.

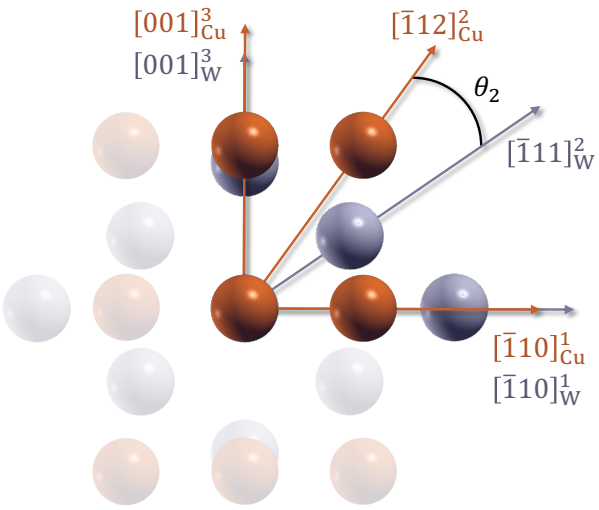

Figure 3.1. Crystallographic relationship for Cu(110) and W(110) planes. The brown and gray spheres represent the Cu and W atoms, respectively. Similarly, in brown and gray are represented their corresponding $[uvw]^i$ vectors. In the sketch is only shown θ_2 since θ_1 and θ_3 are zero in this case.

represent a different orientations of the W(110)/Cu(111), also known in the literature as Kurdjumov-Sachs (KS) and Nishiyama-Wassermann (NW) orientation relationships, respectively [130–133]. Indeed, the lowest mismatch parameter corresponds to the NW interface (No. 12) which, according to Bramfitt's theory, means that it should have the lowest energy and it should be the most stable one[2]. Despite this, we were interested in the W/Cu interface considering the W(100) surface as substrate based on our long-term goals. It is know that W(100) surfaces reconstructs below 370 K [134–136], which makes it of particular interest for its interaction with hydrogen, main goal of this thesis. Furthermore, given the structural complexity of this interface, it will serve as a valuable training set for developing a Machine Learning Potential to characterize W-Cu-H interactions. This advancement will enable the modeling of larger unit cells through Classical Molecular Dynamics, aligning with our long-term goal. Modeling larger unit cells through MD will allow us to study not only 0-dimensional defects but 1,2 and 3-dimensional ones, constituting a full system characterization.

In Table 3.1 there are four orientations on W(100) surface, of them, the lowest mismatch parameter corresponds to the W(100)/Cu(111) interface with a value of 11.38%. This interface could be a good model to consider, nevertheless, we chose the No. 10 to optimize the computational resources. Our DFT calculations were done in the open source package Quantum Espresso [137], where we employed ultrasoft pseudopotentials (USSPs) [138] generated with the PBE-GGA [139] exchange correlation functional. The employed USPPs consider 14 valence and semi-core electrons ($5s^25p^65d^46s^2$) for W atoms, and 11 valence electrons for Cu atoms ($4s^23d^9$). Such amount of electrons makes the DFT calculations more computationally expensive as the number of W and Cu atoms increases in the working-cell. Therefore, as it was already said, it is necessary to optimize the

[2]At least among the orientations shown in Table 3.1, the NW interface has the lowest misfit, but we cannot affirm that this is a general results due to the number of orientations is infinite and we only consider a small sample of it, which makes the possibility of finding another orientation with lower mismatch no null.

Table 3.1. Bramfitt's mismatch parameter for 12 different orientations of the W/Cu interface. W was considered as the substrate and Cu as the nucleated solid. The corresponding geometrical representation is done in Table B.1 of Appendix B.

No. 1	$(100)_W/(100)_{Cu}$			No. 2	$(110)_W/(100)_{Cu}$			No. 3	$(111)_W/(100)_{Cu}$		
$[uvw]_W$	[010]	[011]	[001]	$[uvw]_W$	$[\bar{1}10]$	$[\bar{1}11]$	[001]	$[uvw]_W$	$[\bar{1}10]$	$[\bar{2}11]$	$[\bar{1}01]$
$[uvw]_{Cu}$	[010]	[011]	[001]	$[uvw]_{Cu}$	[010]	[011]	[001]	$[uvw]_{Cu}$	[010]	[011]	[001]
θ_i	0°	0°	0°	θ_i	0°	9.74°	0°	θ_i	0°	15°	30°
d_W (Å)	3.187	4.507	3.187	d_W (Å)	4.507	2.760	3.187	d_W (Å)	4.507	7.807	4.507
d_{Cu} (Å)	3.620	2.560	3.620	d_{Cu} (Å)	3.620	2.560	3.620	d_{Cu} (Å)	3.620	2.560	3.620
δ_i	0.120	0.761	0.120	δ_i	0.245	0.063	0.120	δ_i	0.245	1.946	0.078
δ (%)		33.33		δ (%)		14.25		δ (%)		75.64	
No. 4	$(100)_W/(110)_{Cu}$			No. 5	$(110)_W/(110)_{Cu}$			No. 6	$(111)_W/(110)_{Cu}$		
$[uvw]_W$	[010]	[011]	[001]	$[uvw]_W$	$[\bar{1}10]$	$[\bar{1}11]$	[001]	$[uvw]_W$	$[\bar{1}10]$	$[\bar{2}11]$	$[\bar{1}01]$
$[uvw]_{Cu}$	$[\bar{1}10]$	$[\bar{1}12]$	[001]	$[uvw]_{Cu}$	$[\bar{1}10]$	$[\bar{1}12]$	[001]	$[uvw]_{Cu}$	$[\bar{1}10]$	$[\bar{1}12]$	[001]
θ_i	0°	9.74°	0°	θ_i	0°	19.47°	0°	θ_i	0°	24.74°	30°
d_W (Å)	3.187	4.507	3.187	d_W (Å)	4.507	2.760	3.187	d_W (Å)	4.507	7.807	4.507
d_{Cu} (Å)	2.560	4.434	3.620	d_{Cu} (Å)	2.560	4.434	3.620	d_{Cu} (Å)	2.560	4.434	3.620
δ_i	0.245	0.002	0.120	δ_i	0.761	0.413	0.120	δ_i	0.761	0.599	0.078
δ (%)		12.22		δ (%)		43.12		δ (%)		47.94	
No. 7	$(100)_W/(111)_{Cu}$			No. 8	$(110)_W/(111)_{Cu}$			No. 9	$(111)_W/(111)_{Cu}$		
$[uvw]_W$	[010]	[011]	[001]	$[uvw]_W$	$[\bar{1}10]$	$[\bar{1}11]$	[001]	$[uvw]_W$	$[\bar{1}10]$	$[\bar{2}11]$	$[\bar{1}01]$
$[uvw]_{Cu}$	$[\bar{1}10]$	$[\bar{2}11]$	$[\bar{1}01]$	$[uvw]_{Cu}$	$[\bar{1}10]$	$[\bar{2}11]$	$[\bar{1}01]$	$[uvw]_{Cu}$	$[\bar{1}10]$	$[\bar{2}11]$	$[\bar{1}01]$
θ_i	0°	15°	30°	θ_i	0°	5.26°	30°	θ_i	0°	0°	0°
d_W (Å)	3.187	4.507	3.187	d_W (Å)	4.507	2.760	3.187	d_W (Å)	4.507	7.807	4.507
d_{Cu} (Å)	2.560	4.434	2.560	d_{Cu} (Å)	2.560	4.434	2.560	d_{Cu} (Å)	2.560	4.434	2.560
δ_i	0.245	0.018	0.078	δ_i	0.761	0.380	0.078	δ_i	0.761	0.761	0.761
δ (%)		11.38		δ (%)		40.64		δ (%)		76.08	
No. 10	$(100)_W/(100)_{Cu}$			No. 11	$(110)_W/(111)_{Cu}$			No. 12	$(110)_W/(111)_{Cu}$		
$[uvw]_W$	[010]	[011]	[001]	$[uvw]_W$	$[\bar{1}11]$	$[1\bar{1}2]$	[001]	$[uvw]_W$	$[00\bar{1}]$	$[\bar{1}1\bar{1}]$	$[\bar{1}10]$
$[uvw]_{Cu}$	$[01\bar{1}]$	[011]	[010]	$[uvw]_{Cu}$	$[1\bar{1}0]$	$[11\bar{2}]$	$[\bar{1}01]$	$[uvw]_{Cu}$	$[1\bar{1}0]$	$[\bar{1}01]$	$[11\bar{2}]$
θ_i	0°	0°	0°	θ_i	0°	5.26°	0°	θ_i	0°	5.26°	0°
d_W (Å)	3.187	3.187	4.507	d_W (Å)	2.760	2.760	7.807	d_W (Å)	3.187	2.760	4.507
d_{Cu} (Å)	3.620	2.560	2.560	d_{Cu} (Å)	2.560	4.434	4.434	d_{Cu} (Å)	2.560	2.560	4.434
δ_i	0.245	0.245	0.245	δ_i	0.078	0.380	0.761	δ_i	0.245	0.074	0.017
δ (%)		24.51		δ (%)		40.64		δ (%)		11.18	

number of W and Cu atoms in the model. As we are particularly interested in the W/Cu interface considering the W(100) surface, to allow the W(100) surface to reconstruct the smallest super-cell must have a dimensionality of (2×2) in X and Y directions, which somehow penalizes the number of W atoms to consider in the interface model. So, the only way to decrease the computational cost of the DFT calculations is decreasing of Cu atoms at the interface, which is achieved choosing the Cu surface with lower atoms per unit cell. The unit cell of the Cu(100) surface has 2 Cu atoms, unlike the unit cells of the Cu(110) and Cu(111) surfaces where there are 4 Cu atoms. This result reduced our interest in the interfaces No. 1 and No. 10, and we finally decanted by the No. 10 because it has the lowest mismatch between them.

As we already explained in section 1.4.1, some experimental studies proved that Cu can

grow in an epitaxial way on W(100) surface leading to the formation of pseudomorphic layers, which means that the first layers of Cu adopt the same crystallographic structure of the substrate, in this case, the same Bravais lattice as W: body centered cubic (bcc). Considering this possibility we also created a second interface model by coupling W and Cu^{bcc} structures. Summarizing, two W/Cu interface models were created: $W(001)/Cu^{fcc}(001)R45°$ (equivalent to the No. 10 in Table 3.1) and $W(001)/Cu^{bcc}(001)$ (equivalent to the epitaxially grown of Cu on W(100) surface).

3.1.2 Convergence studies

Numerical parameters

In the Methodology section of papers where DFT calculations were performed, details about the cutoff energy (E_c) and the k-point mesh are always provided, as these numerical parameters significantly affect the accuracy of the calculations. In this section, we aim to explain our approach to determining these parameters for our system.

A numerical parameter set of $E_c = 40$ Ry (544 eV) and a mesh of $(20 \times 20 \times 20)$ k-points for a $(1 \times 1 \times 1)$ unit cell proves to be suitable for W bulks, at least for the pseudopotential here considered. Going higher would incur a higher computational cost without yielding appreciable changes in the results [116, 134, 135, 140]. However, these parameters need to be determined for Cu bulks. We investigated how cutoff energy and k-points influenced the energy of the Cu bulk and the solution energy of H in Cu. To examine the variation in bulk energy, we calculated the difference between the energy of the Cu bulk and a reference value. This reference value corresponds to the energy of the Cu bulk obtained with the parameters $E_c = 70$ Ry and $k = 35$, where k represents a mesh of $(k \times k \times k)$ points in reciprocal space:

$$\Delta E_{bulk} = E_{bulk} - E_{ref}. \tag{3.3}$$

We determined the ΔE_{bulk} for the Cu^{fcc} and Cu^{bcc} bulks due to both of them are considered to create the W/Cu interface model. In Figure 3.2 we present those results. It was obtained that with values higher than $E_c = 55$ Ry and $k = 24$ the values of ΔE_{bulk} are lower than 4 meV. However, it is important to note that these values only represent the variation in the energy of the Cu bulk. Since our focus is on the interaction of H atoms with the Cu bulk, we also analyze the convergence of its solution energy.

The solution energy of H atoms is defined as follows:

$$\Delta_s E_{\mathrm{H}} = E_{sys,\mathrm{H}} - \left(E_{sys} + \frac{1}{2} E_{\mathrm{H}_2} \right), \tag{3.4}$$

where $E_{sys,\mathrm{H}}$ is the energy of the system with one interstitial H atom, E_{sys} is the energy of the system without H (bulk energy), and E_{H_2} is the energy of H_2 molecule. In this case, we kept constant the the numerical parameters in the bulk (fixing E_{sys}) and the H_2 molecule (fixing E_{H_2}) and we changed them in the bulk with H (changing $E_{sys,\mathrm{H}}$). Before proceeding to show the results, it is necessary to defined the interstitial sites where H will be placed in the bulk. Two interstitial sites for H atoms were considered in this job, not only within the Cu bulk but also within the W and at the W/Cu interface: octahedral (Oh) and

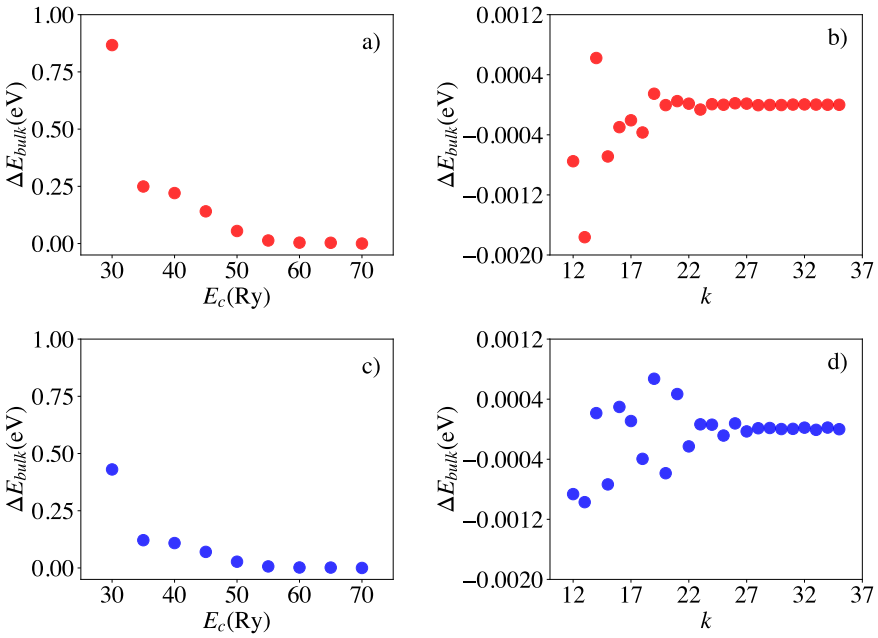

FIGURE 3.2. ΔE_{bulk} as function of the E_c and k in the Cu^{fcc} (a-b) and Cu^{bcc} (c-d) bulks. Values greater than $E_c = 55$ Ry and $k = 24$ for both bulks guarantee a value of ΔE_{bulk} lower than 4 meV.

tetrahedral (Td). H atoms assume an octahedral (tetrahedral) position when placed in the middle of the octahedron (tetrahedron) formed by the atoms of the cell. In the atomic representations of the upcoming chapters, Oh sites are represented as blue dots, and Td sites are illustrated as red points. This color scheme is employed for better visualization of the results and to maintain consistency in the legend.

Figure 3.3 displays the variation of the solution energy ($\Delta_s E_{\mathrm{H}}$) at Oh sites, whereas Figure 3.4 presents the results for Td positions. In both cases, the lavender region delimits the zone where a dispersion of ± 1 meV is obtained respect the reference value, which in these cases is the $\Delta_s E_{\mathrm{H}}$ for $E_c = 70$ Ry and $k = 35$. While the light-cyan region contains the values with a dispersion lower than ± 2 meV. We chose the values of $E_c = 45$ Ry and $k = 20$, which correspond to a grid of $(20 \times 20 \times 20)$ k-points for a $(1 \times 1 \times 1)$ unit cell as numerical parameters for our simulations in Cu bulk as they guarantee a dispersion lower than 2 meV respect the reference value.

For the W/Cu interface, we opted for the same values as those selected for the Cu bulk, as these parameters also meet the criteria necessary for the W bulk.

Size of the W/Cu interface unit cell

With the numerical parameters of the simulation defined, we proceed to build the W/Cu interface model. In section 3.1.1 we already said that we will work with two interfaces: $W(001)/Cu^{fcc}(001)R45°$ and $W(001)/Cu^{bcc}(001)$. Nevertheless, as previously mentioned, optimizing the number of considered atoms is crucial to minimize computational resource requirements. That is why, in this section we will focus on the convergence study conducted to determine the optimal size of the interface unit cell. Specifics on the

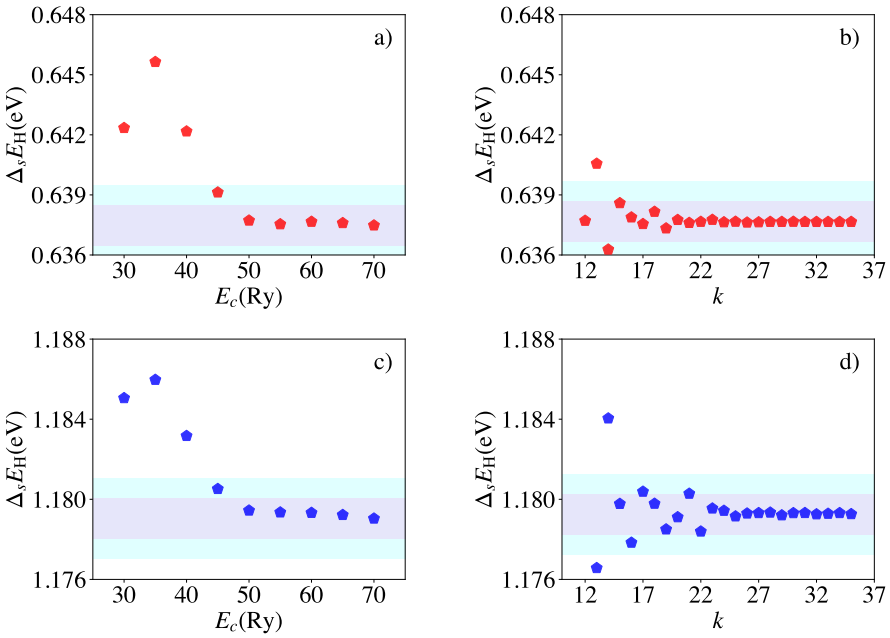

FIGURE 3.3. $\Delta_s E_H$ in Oh positions as function of the E_c and k in the Cu^{fcc} (a-b) and Cu^{bcc} (c-d) bulks. The lavender region contains the values with a dispersion of ± 1 meV, while the light-cyan contains those with a dispersion of ± 2 meV. Values greater than $E_c = 45$ Ry and $k = 20$ for both bulks guarantee a value of $\Delta_s E_H$ with a dispersion lower than 2 meV.

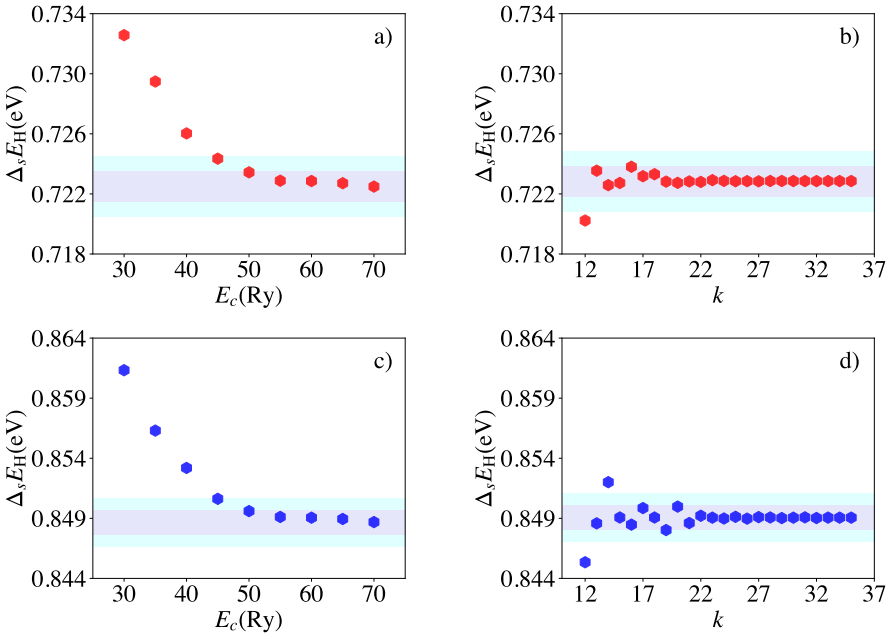

FIGURE 3.4. $\Delta_s E_H$ in Td positions as function of the E_c and k in the Cu^{fcc} (a-b) and Cu^{bcc} (c-d) bulks. The lavender region contains the values with a dispersion of ± 1 meV, while the light-cyan contains those with a dispersion of ± 2 meV. Values greater than $E_c = 45$ Ry and $k = 20$ for both bulks guarantee a value of $\Delta_s E_H$ with a dispersion lower than 2 meV.

construction of the interface are detailed in the Methodology section of the paper in the subsequent segment.

Two parameters used for this optimization were the energy of the interface (E_{int}) and the work of separation (W_{sep}), defined as follows:

$$E_{int} = \frac{E_{\mathrm{W/Cu}} - E_{\mathrm{W}_{bulk}} - E_{\mathrm{Cu}_{bulk}}}{2\mathrm{A}}, \tag{3.5}$$

$$W_{sep} = \frac{E_{\mathrm{W}} + E_{\mathrm{Cu}} - E_{\mathrm{W/Cu}}}{2\mathrm{A}}. \tag{3.6}$$

In equation (3.5), $E_{\mathrm{W/Cu}}$ is the energy of the W/Cu working-cell, $E_{\mathrm{W}_{bulk}}$ and $E_{\mathrm{Cu}_{bulk}}$ are the energy of W and Cu bulks, respectively, while A is the surface area of the W/Cu interface. In expression (3.6), E_{W} and E_{Cu} stand for the energies of the remaining W or Cu bulks after removing the Cu or W part from the interface.

As the reconstruction of the W(100) surface requires a (2×2) unit cell in the X and Y direction to be modeled [134, 135], the optimization of the number of cells is limited only to the Z direction. The number of cells in the Z direction is given by: $n_Z = \mathrm{N_{Cu}} + \mathrm{N_W}$, where $\mathrm{N_{Cu}}$ and $\mathrm{N_W}$ denote the number of cells in the Cu and W networks at the W/Cu interface respectively. In both models, we fixed $\mathrm{N_{Cu}} = \mathrm{N_W} = \mathrm{N}$, and therefore, $n_Z = 2\mathrm{N}$. The optimal number of cells in the Z direction, n_Z, was chosen such that E_{int} and W_{sep} fall below 1 meV/Å^2 with respect to the larger considered super-cell $(2 \times 2 \times 14)$.

In Figure 3.5, we plotted the variation of those variables as function of the number of cells in the Z direction, N, for the $\mathrm{W^{bcc}}(001)/\mathrm{Cu^{hcp}}(11\bar{2}0)$ unit cell, which is the one resulting from the relaxation of both $\mathrm{W}(001)/\mathrm{Cu^{bcc}}(001)$ and $\mathrm{W}(001)/\mathrm{Cu^{fcc}}(001)\mathrm{R45°}$ models (see paper for more details). For $N \geq 4$, the dispersion of $E_{\mathrm{W/Cu}}$ and W_{sep} meets the desired values (lower than 1 meV/Å^2). Consequently, the size of the W/Cu interface in the Z direction will be $n_Z = 8$, indicating 4 cells for both the Cu and W networks.

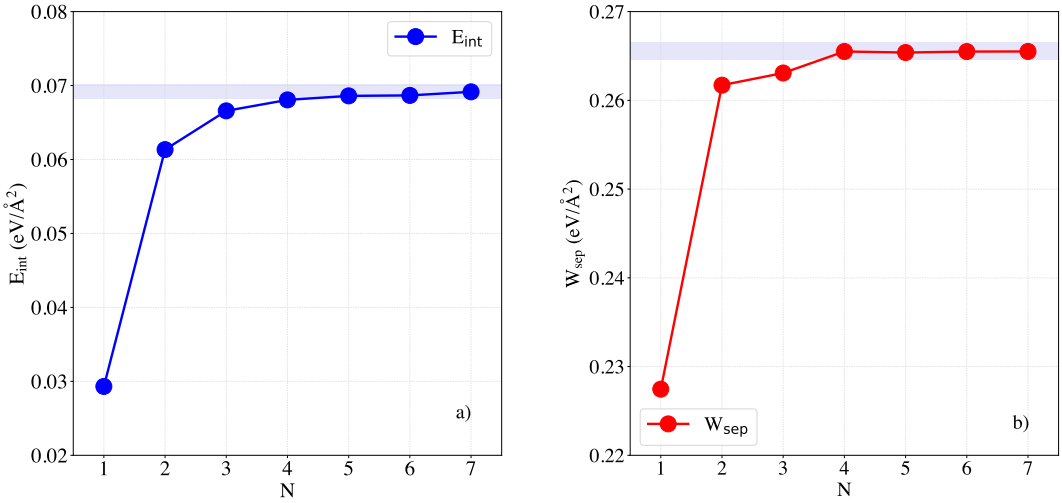

Figure 3.5. E_{int} (a) and W_{sep} (b) of the $\mathrm{W^{bcc}}(001)/\mathrm{Cu^{hcp}}(11\bar{2}0)$ unit cell respect to the number of cells in the Z direction, N. The lavender region represent the zone with a deviation of ± 1 meV/Å^2 respect to the super-cell $(2 \times 2 \times 14)$, where $\mathrm{N} = 7$.

With our interface model and its specified numerical parameters in place, we can now start the study of its morphology and the interaction between W and Cu atoms. The

objective of this paper is to characterize both interface models W(001)/Cu^{fcc}(001)R45° and W(001)/Cu^{bcc}(001) as part of a preliminary study before introducing H atoms into the structure. The subsequent investigation illustrates the process through which the W^{bcc}(001)/Cu^{hcp}(11$\bar{2}$0) structure is derived from the reconstruction of the W(001)/Cu^{fcc}(001)R45° and W(001)/Cu^{bcc}(001) cells. This resulting structure is then compared to experimental observations [17, 18], revealing a good agreement. Such a reconstruction process affects the charge density of the structure and subsequently the interstitial sites where H atoms can be placed.

3.2 Publication

A model of the W/Cu interface in the ITER cooling monoblocks from density functional theory.

Y. Silva-Solís, J. Denis, E.A. Hodille and Y. Ferro.

Published in Nuclear Materials and Energy.

Available online since September 27th, 2023.

https://doi.org/10.1016/j.nme.2023.101516

Nuclear Materials and Energy 37 (2023) 101516

Contents lists available at ScienceDirect

Nuclear Materials and Energy

journal homepage: www.elsevier.com/locate/nme

A model of the W/Cu interface in the ITER cooling monoblocks from density functional theory

Y. Silva-Solís [a], J. Denis [a], E.A. Hodille [b], Y. Ferro [a,*]

[a] Aix-Marseille University, CNRS, PIIM, F-13013 Marseille, France
[b] CEA, IRFM, F-13108 Saint-Paul-lez-Durance, France

ARTICLE INFO

Keywords:
Interface
DFT
Reconstruction
Charge density

ABSTRACT

ITER divertor is built with tungsten monoblocks that contain a tungsten–copper interface. There, hydrogen isotopes could possibly accumulate leading to safety and mechanical issues. As a consequence, the tungsten–copper interface has to be modeled and characterized, which is here performed at the atomic-scale by means of density functional theory calculations. In order to build the model, we selected the tungsten and copper orientations that minimizes the mismatch between both networks; this results in the W(001)/Cu^{bcc}(001) and W(001)/Cu^{fcc}(001)R45° interfaces. After relaxation, both systems converge to the same W^{bcc}(001)/Cu^{hcp}(11$\bar{2}$0) structure, which is consistent with previous experimental observations. Such reconstruction of the copper network has the effect of changing the charge density in the copper part of the interface, with possible effects on hydrogen interaction.

1. Introduction

In fusion devices such as ITER and DEMO, transport and retention of hydrogen isotopes (HIs) in plasma-facing components (PFCs) can lead to the formation of defects, fuel loss and degradation of the tokamak performance [1,2]. The PFCs of the divertor in ITER and WEST are built using tungsten (W) monoblocks [3]. The pipes inside the PFCs are made of a copper–chromium–zirconium (CuCrZr), whereas a copper (Cu) inter-layer is used to minimize the mechanical stress between W and CuCrZr [4]. This work specifically focuses on the W/Cu interface where HIs could possibly accumulate and stabilize and/or induce new types of defects. It is led at the atomic scale and is based on density functional theory (DFT) calculations. A model of the W/Cu interface is built with the main goal to determine the structural changes induced by the interface on the W and Cu structures. As an infinite number of W/Cu interfaces can be built considering different crystallographic plane orientations, we restricted this investigation by considering the two orientations for which experimental observations exist [5,6] and which have the lowest mismatch parameters between W and Cu networks [7,8]. This resulted in the W(001)/Cu^{bcc}(001) and W(001)/Cu^{fcc}(001)R45° models. This work constitutes a first step before evaluating the solution, segregation and diffusion properties of HIs at the W/Cu interface.

2. Methodology

2.1. Details of the electronic structure calculations

Our electronic structure calculations were done with the Quantum Espresso open-source package [9]. We employed ultrasoft pseudopotentials (USPP) with 14 valence and semi-core electrons for W atoms ($5s^2 5p^6 5d^4 6s^2$) and 11 valence electrons for Cu atoms ($4s^2 3d^9$), both of them were generated with the PBE-GGA [10] exchange–correlation functional. We used a cutoff energy value of 45 Ry and 360 Ry for the plane-waves and electronic density expansions, respectively. The working-cell contains 64 atoms (32 Cu and 32 W atoms); it was built with a $2 \times 2 \times 8$ repetition of the Cu and W unit-cells, which is detailed later on in this paper. Since a pseudo-2D model is built in the (X, Y) plane, the Brillouin zone was sampled with $10 \times 10 \times 1$ mesh of k-points. The calculated cell parameters for the Cu^{fcc} and Cu^{bcc} bulks structures are 3.620 Å and 2.871 Å, respectively. The cell parameter for W^{bcc} bulks structures was determined to 3.187 Å in a previous paper [11].

2.2. Building a W/Cu interface model

The difference between the cell parameters of W and Cu makes it difficult to build a model of the interface. From one hand the Cu part

* Corresponding author.
E-mail address: yves.ferro@univ-amu.fr (Y. Ferro).

https://doi.org/10.1016/j.nme.2023.101516
Received 2 July 2023; Received in revised form 15 September 2023; Accepted 19 September 2023
Available online 27 September 2023
2352-1791/© 2023 The Author(s). Published by Elsevier Ltd. This is an open access article under the CC BY-NC-ND license (http://creativecommons.org/licenses/by-nc-nd/4.0/).

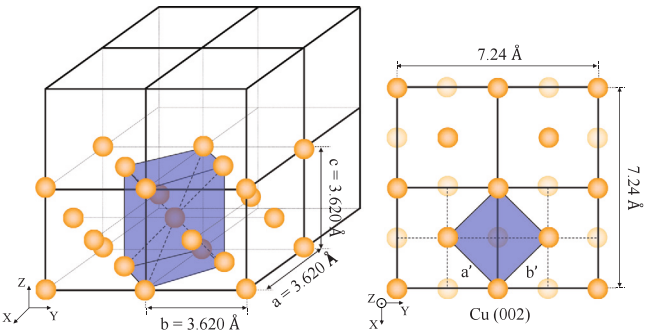

Fig. 1. Construction of Cu^{bct} bulk from the Cu^{fcc} structure. The blue volume represents the Cu^{bct} unit cell employed at the $W(001)/Cu^{fcc}(001)R45°$. In the right panel, we show the crystallographic plane (002) where the light orange balls correspond to the position of the Cu atoms in the crystallographic plane (004). (For interpretation of the references to color in this figure legend, the reader is referred to the web version of this article.)

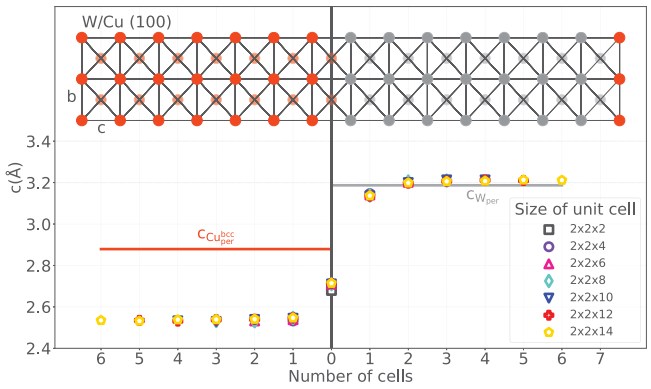

Fig. 2. Inter-layer distance c in the Z direction of the W/Cu super-cell. The black line displays the interface. We numbered the layers starting from the interface. Above the graph, we schematically represent the (100) crystallographic plane of the $(2 \times 2 \times 14)$ W/Cu: the orange and gray points are the positions of Cu and W atoms, respectively. The light-orange and light-gray points represent the positions of Cu and W atoms in the layer next to the (100) plane. The horizontal orange and gray lines the c parameter of Cu^{bcc} and W^{bcc} respectively: $c_{Cu^{bcc}} = 2.871$ Å and $c_{W^{bcc}} = 3.187$ Å. (For interpretation of the references to color in this figure legend, the reader is referred to the web version of this article.)

can be thought as being grown in epitaxy with the $W^{bcc}(001)$ surface leading to the formation of pseudomorphic Cu layers of bcc structure [6,8,12]. It can also be thought as having the same fcc structure as Cu in its most stable symmetry. Previous authors built similar W/Cu interface models considering a substrate metal, most often W, with the other metal deposited on top of it [13–15]. Each metallic part consists in several atomic 2D layers. In these previous works, the in-plane cell-parameters were fixed by the substrate, while the full W/Cu bilayer was separated from its repeated image by a vacuum of 10–20 Å. Such a model has one interface, two metallic surfaces, and is akin to dipole moment induced by the two different metals.

In the present work, the full geometry and volume of the working-cell are relaxed: starting from a mean-value of the Cu and W cell-parameters, we led a full geometry optimization of the atomic positions and of the cell-parameters to find the geometry of lowest energy. In addition, we consider no vacuum, making the working-cell separated from its repeated image by another W/Cu interface. As a consequence the pseudo-2D working-cell contains two W/Cu interfaces, no metallic surface and no vacuum.

We investigated two systems: $W(001)/Cu^{bcc}(001)$ for Cu grown in epitaxy over the W(001) surface, and $W(001)/Cu^{fcc}(001)R45°$ that keeps the same symmetry as Cu in its bulk geometry. In the latter case, the fcc structure was rotated by 45° (Fig. 1) such as the (002) surface of Cu continues the W^{bcc} network (or in other words, the [100] direction of W^{bcc} and the $[1\bar{1}0]$ direction of Cu^{fcc} are collinear). The thickness of both $W(001)/Cu^{bcc}(001)$ and $W(001)/Cu^{fcc}(001)R45°$ super-cells is given by n_z, which represents the total number of cells in the Z direction: $n_z = N_{Cu} + N_W$, with N_{Cu} and N_W being the number of cells in the Cu and W networks, respectively. We fixed $N_{Cu} = N_W = N$ and, therefore, $n_z = 2N$. In addition; it is known that the W(001) surface reconstructs. Such a surface reconstruction requires a 2×2 unit-cell in the (X, Y) plane to be modeled [16,17]. Because this surface reconstruction certainly plays a role in the structure of the W/Cu interface, we used a $(2 \times 2 \times n_z)$ model.

To find the optimal size of the system, the value of N was changed from 1 to 7. In the case of $W(001)/Cu^{bcc}(001)$, the initial cell parameters used to build the super-cell were: $a_{W/Cu^{bcc}} = b_{W/Cu^{bcc}} = 3.029$ Å, $c_{W/Cu^{bcc}} = 2.871$ Å in the Cu network and $c_{W/Cu^{bcc}} = 3.187$ Å in the W network. Where a, b and c represent the unit-cell parameters in X, Y and Z directions respectively. Thus, the $W(001)/Cu^{bcc}(001)$ resulted in a super-cell of size (6.06 Å × 6.06 Å × 6.06N Å). To create the $W(001)/Cu^{fcc}(001)R45°$ we made a body cubic tetragonal (bct) Cu structure from Cu^{fcc} rotated by 45° as is shown in Fig. 1. Employing the new $a' = b' = 2.560$ Å cell parameters for Cu network, we obtained a $W(001)/Cu^{fcc}(001)R45°$ of size (5.75 Å × 5.75 Å × 6.81N Å) before geometry optimizations.

For each model of the interface $W(001)/Cu^{bcc}(001)$ and $W(001)/Cu^{fcc}(001)R45°$, we determined the energy of the interface (E_{int}) and the work of separation (W_{sep}) using Eqs. (1) and (2) respectively:

$$E_{int} = \frac{E_{W/Cu} - E_{W_{bulk}} - E_{Cu_{bulk}}}{2A}, \quad (1)$$

$$W_{sep} = \frac{E_W + E_{Cu} - E_{W/Cu}}{2A}, \quad (2)$$

In Eq. (1), $E_{W/Cu}$ is the energy of the W/Cu working-cell, $E_{W_{bulk}}$ and $E_{Cu_{bulk}}$ are the energy of W and Cu bulks, respectively, while A is the surface area of the W/Cu interface. In Eq. (2), E_W and E_{Cu} are the energies of the remaining W or Cu bulk once the Cu or W part is removed from the interface. The optimal number of cells in the Z direction $n_z = 2N$ was chosen such that E_{int} and W_{sep} falls below 1 meV/Å^2 with respect to the larger super-cell ($2 \times 2 \times 14$) here considered.

3. Results and discussion

3.1. Model of the interface

Full relaxations were conducted for both interface models depending on the number of layers N in the Z direction. In a plane parallel to the interface, it resulted in identical changes of the a and b cell parameters along the X and Y directions. Perpendicular to the interface, geometry relaxations led to an inter-layer distance c that varies along the Z direction. These variations are shown in Fig. 2 for various N. In each cell whose number is displayed in the abscissa of Fig. 2, the c parameter converges starting from N = 3 resulting in a ($2 \times 2 \times 6$) interface model. In the end, the most noticeable result is that both $W(001)/Cu^{bcc}(001)$ and $W(001)/Cu^{fcc}(001)R45°$ models converged to the same final minimum energy structure, which geometry and symmetry are analyzed hereafter.

The values of E_{int} and W_{sep} are 0.069 eV/Å^2 (1.11 J/m^2) and 0.266 eV/Å^2 (4.26 J/m^2), respectively, for the largest ($2 \times 2 \times 14$) interface model here considered. Starting from N = 4, E_{int} and W_{sep} are well converged to 0.068 eV/Å^2 (1.09 J/m^2) and 0.266 eV/Å^2 (4.26 J/m^2), respectively. As a consequence, we selected the number of layers N = 4 consistent with the ($2 \times 2 \times 8$) interface model that leads to a well-converged working-cell. For this working-cell, a and b parameters

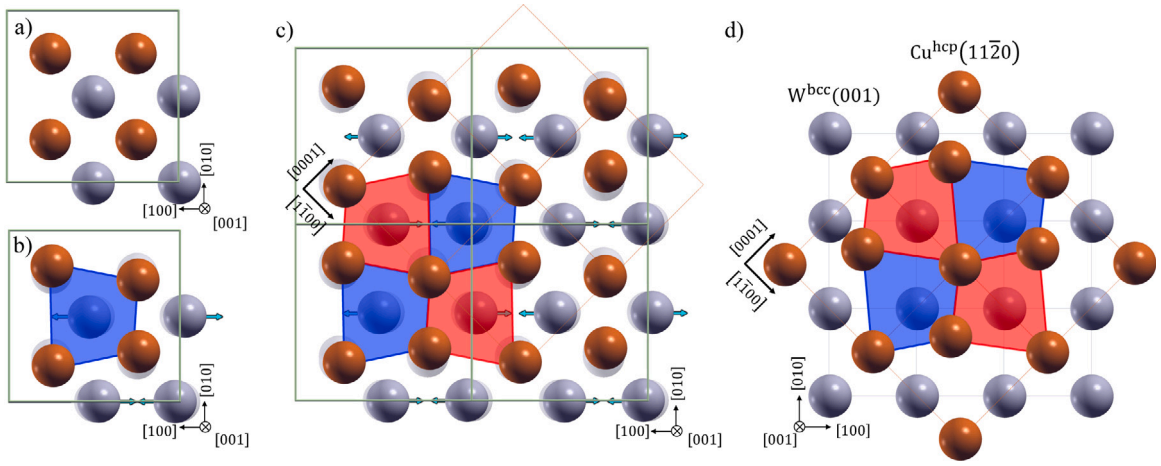

Fig. 3. Reconstruction of the Cu network. (a) Before geometry relaxation, (b) after geometry relaxation, (c) same as (b) but at a larger scale, and (d) the $Cu^{hcp}(11\bar{2}0)$ on W(100) experimentally observed by Wormeester et al. [6] and Bollmann et al. [8]. The blue and red surfaces represent the regions with similar deformations. (For interpretation of the references to color in this figure legend, the reader is referred to the web version of this article.)

converge to 3.162 Å, close to their value in perfect W at 3.187 Å. It means that at the interface, W imposes the geometry of the whole structure in the X and Y planes, leading to an expansion of the Cu network. The reverse was observed in the Z direction: the inter-layer distance of Cu compresses to c = 2.531 Å while W expands to c = 3.210 Å.

Bodlos et al. [18] determined $E_{int} = 0.71$ J/m^2, but on a different interface orientation W(110)/Cu(111). Liang et al. [13] calculated $W_{sep} = 4.57$ J/m^2 and $E_{int} = 0.76$ J/m^2 on the same interface investigated here Cu(100)/W(100). These values are close to the ones we calculated: $W_{sep} = 4.26$ J/m^2 and $E_{int} = 1.09$ J/m^2. The difference is probably due to the fact that Liang et al. [13] did not performed any volume relaxation but kept the cell parameter fixed to the one imposed by the tungsten substrate. In addition they used a (1×1) unit-cell in the (X, Y) plane, which does not allow tungsten and copper to reconstruct.

3.2. Reconstructed structure of the interface

We now have defined a well-converged $(2 \times 2 \times 8)$ interface model and focus on its reconstructed structure and geometry. Fig. 3a and b represent the Cu and W layers at the interface before and after geometry optimization respectively. W is the stiffer material and it keeps the same bcc structure as in the pure metal. However, at the interface, W atoms in the first layer in contact with the Cu network moves a bit (blue arrows in Fig. 3b and c) from their equilibrium position to adopt a zig-zag structure which does not propagate deeper into the W layers. The displacement of the Cu atoms of the interface is more pronounced, and the distortion propagates into the full Cu structure. Fig. 3c displays a larger view of how the atoms are displaced at the interface. It is to be compared with Fig. 3d that represents a $Cu^{hcp}(11\bar{2}0)$ structure deposited on top of $W^{bcc}(001)$ surface, with the [0001] direction of Cu^{hcp} collinear to the [110] direction of W^{bcc}. $Cu^{hcp}(11\bar{2}0)$ is a little bit distorted such as to match with the W^{bcc} network. Such a structure was experimentally observed by Wormeester et al. [6] and Bollmann et al. [8] for Cu deposited on top of W(001).

The hcp reconstruction propagates into the full Cu structure from one W/Cu interface to the other one in the $(2 \times 2 \times 8)$ working-cell. In order to check this propagation is not an artifact of having two W/Cu interfaces into the model, we fixed the atoms at the second interface (shown for N = 7 in Fig. 2) to their bcc (001) structure, and let the W/Cu interface in the middle of the working-cell (black line in Fig. 2) free to move. The hcp reconstruction propagates similarly up to the fixed layer of the frozen W/Cu interface. This indicates the W(001) surface induces a hcp reconstruction into Cu. This minimizes the mismatch between the W and Cu networks and ends-up in a $W^{bcc}(001)/Cu^{hcp}(11\bar{2}0)$ interface.

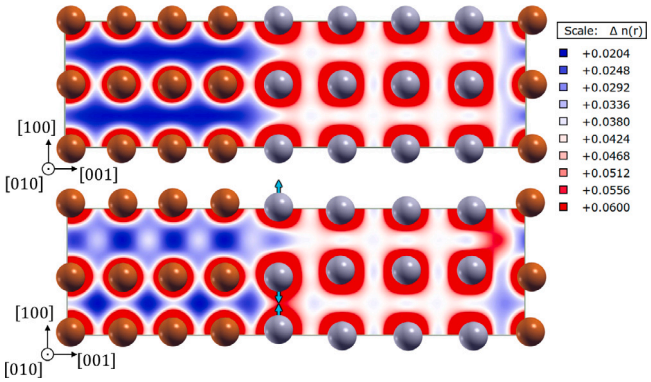

Fig. 4. Charge density along the $(2 \times 2 \times 8)$ W/Cu working cell. The top and bottom representations correspond to the (010) crystallographic plane before and after relaxation, respectively.

3.3. Effect on the charge density

The hcp reconstruction is shown in Fig. 4 in the (010) plane: the top part of Fig. 4 shows the undistorted structure while the lower part shows the minimum energy $W^{bcc}(001)/Cu^{hcp}(11\bar{2}0)$ interface. The reconstruction clearly induces two different channels along the [001] direction in between the Cu atoms: one channel is narrower while the other one is wider as compared to the undistorted structure. It is expected that these two channels will interact differently with hydrogen isotopes when they will diffuse through the interface.

A good indicator of where hydrogen atoms resides in a materials is given by the electronic density. Indeed, it already proved to be an efficient tool to predict the location of minimum energy interaction with hydrogen [19–22]. To this end, Fig. 4 displayed the electronic density in the (010) plane of the interface model. The regions of low charge density are located in the Cu network at the plane of the interface with a value of 0.0204 a.u. In the W network, the regions of low charge density have a value of 0.0380 a.u. approximately. The electron density of a homogeneous electron gas that minimizes its interaction with a hydrogen atom is $n_0 = 0.0026$ a.u. ≈ 0.018 eÅ^{-3} [23]. As the electronic densities above mentioned are higher than n_0, it is expected that hydrogen resides in locations of minimum electronic densities. It follows that the solutions energy will be lower (and the solubility of hydrogen higher) in the Cu part rather than in the tungsten part of the interface. The locations of low charge density in the Cu network

correspond to octahedral sites, which according to the bibliography is the most stable position for the H atoms in the Cu bulk [24–26]. In the case of the W network, the regions of lowest charge density correspond to tetrahedral sites, which are the positions where the solution energy of H is the lowest in W bulks [14,27,28]. Nevertheless, at the plane of the interface, the charge density takes its minimum value, which indicates a possible accumulation of hydrogen there.

4. Conclusions

In this work, an atomic-scale model of the W/Cu interface was built. The size of the working-cell was defined to $(2 \times 2 \times 8)$, which makes converge W_{sep}, E_{int} and the inter-layer distance c. We built two different crystallographic orientations $W(001)/Cu^{bcc}(001)$ and $W(001)/Cu^{fcc}(001)R45°$ that minimizes the mismatch between both Cu and W networks. After geometry relaxation, the Cu networks of both systems reconstruct, leading to the same $W^{bcc}(001)/Cu^{hcp}(11\bar{2}0)$ final structure. This reconstruction affect the charge density which led us to conclude that the interface is a possible place of high solubility for HIs.

CRediT authorship contribution statement

Y. Silva-Solís: Methodology, Software, Validation, Writing – original draft, Writing – review & editing , Visualization. **J. Denis:** Formal analysis, Writing – review & editing, Supervision. **E.A. Hodille:** Data curation, Writing – review & editing, Supervision. **Y. Ferro:** Conceptualization, Writing – review & editing, Supervision, Project administration.

Declaration of competing interest

The authors declare that they have no known competing financial interests or personal relationships that could have appeared to influence the work reported in this paper.

Data availability

Data will be made available on request.

Acknowledgments

This work is supported by Région PACA, France. It has been carried out within the framework of the EUROfusion Consortium, funded by the European Union via the Euratom Research and Training Programme (Grant Agreement No 101052200 — EUROfusion). Views and opinions expressed are however those of the author(s) only and do not necessarily reflect those of the European Union or the European Commission. Neither the European Union nor the European Commission can be held responsible for them. The authors were granted access to the high-performance computing resources of IDRIS under Allocation No. A0120806612 made by Grand Equipement National de Calcul Intensif and to the Marconi Supercomputer at CINECA Super Computing Application and Innovation Department, Bologna, Italy.

References

[1] D. Perrault, Safety issues to be taken into account in designing future nuclear fusion facilities, Fusion Eng. Des. 109 (111) (2016) 1733–1738, URL: https://doi.org/10.1016/j.fusengdes.2015.10.012.

[2] E.A. Hodille, E. Bernard, S. Markelj, J. Mougenot, C.S. Becquart, R. Bisson, C. Grisolia, Estimation of the tritium retention in ITER tungsten divertor target using macroscopic rate equations simulations, Phys. Scr. 170 (2017) 14033–14040, http://dx.doi.org/10.1088/1402-4896/aa8787.

[3] M. Missirlian, J. Bucalossi, Y. Corre, F. Ferlay, M. Firdaouss, P. Garin, A. Grosman, D. Guilhem, J. Gunn, P. Languille, The WEST project: current status of the ITER-like tungsten divertor, Fusion Eng. Des. 89 (7–8) (2014) 1048–1053.

[4] T. Hirai, S. Panayotis, V. Barabash, C. Amzallag, F. Escourbiac, A. Durocher, M. Merola, J. Linke, T. Loewenhoff, G. Pintsuk, M. Wirtz, I. Uytdenhouwen, Use of tungsten material for the ITER divertor, Nucl. Mater. Energy 9 (2016) 612–622, URL: https://doi.org/10.1016/j.nme.2016.07.003.

[5] E. Bauer, H. Poppa, G. Todd, F. Bonczek, Adsorption and condensation of Cu on W single-crystal surfaces, J. Appl. Phys. 45 (12) (2003) 5164–5175, URL: https://doi.org/10.1063/1.1663211.

[6] H. Wormeester, M.E. Kiene, E. Hüger, E. Bauer, Growth of hcp Cu on W (100), Surf. Sci. 377 (1997) 988–991.

[7] B.L. Bramfitt, The effect of carbide and nitride additions on the heterogeneous nucleation behavior of liquid iron, Metall. Trans. 1 (1970) 1987–1995, URL: https://doi.org/10.1007/BF02642799.

[8] T.R.J. Bollmann, R. van Gastel, H. Wormeester, H.J.W. Zandvliet, B. Poelsema, Growth and decay of hcp-like Cu hut-shaped structures on W(100), Phys. Rev. B 85 (2012) 125417, http://dx.doi.org/10.1103/PhysRevB.85.125417.

[9] P. Giannozzi, O. Andreussi, T. Brumme, O. Bunau, M.B. Nardelli, M. Calandra, R. Car, C. Cavazzoni, D. Ceresoli, M. Cococcioni, N. Colonna, I. Carnimeo, A.D. Corso, S. de Gironcoli, P. Delugas, R.A. DiStasio, A. Ferretti, A. Floris, G. Fratesi, G. Fugallo, R. Gebauer, U. Gerstmann, F. Giustino, T. Gorni, J. Jia, M. Kawamura, H.-Y. Ko, A. Kokalj, E. Küçükbenli, M. Lazzeri, M. Marsili, N. Marzari, F. Mauri, N.L. Nguyen, H.-V. Nguyen, A.O. de-la Roza, L. Paulatto, S. Poncé, D. Rocca, R. Sabatini, B. Santra, M. Schlipf, A.P. Seitsonen, A. Smogunov, I. Timrov, T. Thonhauser, P. Umari, N. Vast, X. Wu, S. Baroni, Advanced capabilities for materials modelling with Quantum ESPRESSO, J. Phys.: Condens. Matter 29 (46) (2017) 465901, http://dx.doi.org/10.1088/1361-648X/aa8f79.

[10] J.P. Perdew, K. Burke, M. Ernzerhof, Generalized gradient approximation made simple, Phys. Rev. Lett. 77 (18) (1996) 3865–3868, URL: https://doi.org/10.1103/PhysRevLett.77.3865.

[11] N. Fernandez, Y. Ferro, D. Kato, Hydrogen diffusion and vacancies formation in tungsten: density functional theory calculations and statistical models, Acta Mater. 94 (2015) 307–318.

[12] H. Wormeester, E. Hüger, E. Bauer, hcp and bcc Cu and Pd films, Phys. Rev. Lett. 77 (8) (1996) 1540.

[13] C.P. Liang, J.L. Fan, H.R. Gong, X. Liao, X. Zhu, S. Peng, Interface structure and work function of W-Cu interfaces, Appl. Phys. Lett. 103 (21) (2013) 211604, URL: https://doi.org/10.1063/1.4833249.

[14] G.C. Ma, J.L. Fan, H.R. Gong, Fundamental effects of hydrogen on cohesion properties of Cu/W interfaces, Solid State Commun. 250 (2017) 79–83, URL: https://doi.org/10.1016/j.ssc.2016.11.018.

[15] Q. Yang, C. Lu, Y. Han, X. Chen, J. Yang, J. Huang, S. Chen, Z. Ye, Influence of Cu/W interfacial structure on the resistance against harmful helium atoms: A mechanism analysis, J. Alloy. Compd. 903 (2022) 163817, URL: https://doi.org/10.1016/j.jallcom.2022.163817.

[16] Z.A. Piazza, M. Ajmalghan, Y. Ferro, R.D. Kolasinski, Saturation of tungsten surfaces with hydrogen: A density functional theory study complemented by low energy ion scattering and direct recoil spectroscopy data, Acta Mater. 145 (2018) 388–398, URL: https://doi.org/10.1016/j.actamat.2017.12.029.

[17] Z.A. Piazza, R.D. Kolasinski, M. Ajmalghan, E.A. Hodille, Y. Ferro, Predictive atomistic model for hydrogen adsorption on metal surfaces: Comparison with low-energy ion beam analysis on tungsten, J. Phys. Chem. C 125 (29) (2021) 16086–16096, URL: https://doi.org/10.1021/acs.jpcc.1c01068.

[18] R. Bodlos, V. Fotopoulos, J. Spitaler, A.L. Shluger, L. Romaner, Energies and structures of Cu/Nb and Cu/W interfaces from density functional theory and semi-empirical calculations, Materialia 21 (2022) 101362.

[19] Y.L. Liu, Y. Zhang, H.-B. Zhou, G.-H. Lu, F. Liu, G.-N. Luo, Vacancy trapping mechanism for hydrogen bubble formation in metal, Phys. Rev. B 79 (17) (2009) 172103.

[20] L. Yang, B.D. Wirth, Surface stability and H adsorption and diffusion near surfaces of W borides: a first-principles study, Nucl. Fusion 63 (6) (2023) 066002, http://dx.doi.org/10.1088/1741-4326/acc6de.

[21] L. Yang, B.D. Wirth, First-principles study of hydrogen behavior near W/WC interfaces, J. Appl. Phys. 127 (11) (2020) 115107, URL: https://doi.org/10.1063/1.5141761.

[22] L. Yang, B.D. Wirth, First-principles study of hydrogen diffusion and self-clustering below tungsten surfaces, J. Appl. Phys. 125 (16) (2019) 165105, URL: https://doi.org/10.1063/1.5092595.

[23] M.J. Puska, R.M. Nieminen, M. Manninen, Atoms embedded in an electron gas: immersion energies, Phys. Rev. B 24 (6) (1981) 3037, URL: https://doi.org/10.1103/PhysRevB.24.3037.

[24] W. Eichenauer, W. Löser, H. Witte, Löslichkeit und diffusionsgeschwindigkeit von wasserstoff und deuterium in einkristallen aus nickel und kupfer, J. Mater. Res. 56 (5) (1965) 287–293, URL: https://doi.org/10.1515/ijmr-1965-560504.

[25] H. Wenzl, Properties and applications of metal hydrides in energy conversion systems, Int. Met. Rev. 27 (1) (1982) 140–168, URL: https://doi.org/10.1179/imr.1982.27.1.140.

[26] H.B. Zhou, Y. Zhang, X. Ou, Dissolution and diffusion behaviors of hydrogen in copper: A first-principles investigation, Comput. Mater. Sci. 79 (2013) 923–928, URL: https://doi.org/10.1016/j.commatsci.2013.08.002.

[27] R. Frauenfelder, Solution and diffusion of hydrogen in tungsten, J. Vac. Sci. Technol. 6 (3) (1969) 388–397, URL: https://doi.org/10.1116/1.1492699.

[28] H.B. Zhou, Y.L. Liu, S. Jin, Y. Zhang, G.N. Luo, G. Lu, Investigating behaviours of hydrogen in a tungsten grain boundary by first principles: from dissolution and diffusion to a trapping mechanism, Nucl. Fusion 50 (2) (2010) 025016, http://dx.doi.org/10.1088/0029-5515/50/2/025016.

Chapter 4

Solution and solubility of H at the W/Cu interface

In the previous chapter, we developed a model of the W/Cu interface specifically designed for DFT calculations. This model enabled us to determine the solution energy and the vibrational properties of hydrogen within the interface, which constitute the primary results presented in this chapter. These findings were then utilized to construct a grand canonical ensemble, based on statistical thermodynamics, allowing us to predict macroscopically how the solubility of hydrogen changes as a function of temperature and chemical potential of the reservoir. The first section of the chapter is dedicated to present the study and explain in details the developed thermodynamic model. The chapter ends presenting the submitted paper where the results are exposed.

4.1 Presentation of the study

In the preceding chapter, it was probed how the Cu network undergoes a reconstruction at the W/Cu interface, changing its structure from fcc to hcp. This reconstruction results in a reduction of the mismatch between the $W^{bcc}(001)$ and $Cu^{hcp}(11\bar{2}0)$ surfaces from an initial value of 24.51% (as noted in No. 10 of Table 3.1) to 2.28%. In the $W^{bcc}(001)/Cu^{hcp}(11\bar{2}0)$ structure, the linear disregistry values were found to be $\delta_1 = 6.07\%$ and $\delta_3 = 0.78\%$, which are consistent with those reported by experimentalists [18], which were 6.9% and 1.2%, respectively. This minimal misfit value suggests that the $W^{bcc}(001)/Cu^{hcp}(11\bar{2}0)$ interface exhibits a notably high probability of formation owing to its remarkable stability [126]. Based on that, such a model was used to study the segregation and diffusion of H atoms. For clarity and ease of reading, we will henceforth refer to the $W^{bcc}(001)/Cu^{hcp}(11\bar{2}0)$ structure as the W/Cu interface. In instances where a different orientation is being discussed, we will explicitly specify it.

As said above, this chapter focuses only on the solubility of H at the W/Cu interface. The reconstruction of the Cu network requires the placement of additional H atoms to gain a comprehensive understanding of the alterations in their solution energies. Two interstitial sites were considered: octahedral (Oh) and tetrahedral (Td). These sites are consistently represented by blue and red colors, respectively, for clarity and consistency

in visualization.

Additionally, we calculated the solution energy of H within the bulk structures of both W and Cu. These values serve as reference points, enabling us to discern and appreciate the impact of the interface on the solution behavior of H. In case of the W bulk we computed two different structures: W^{bcc}_{per} and W^{bcc}_{dis}. The W^{bcc}_{per} bulk has the same cell parameters to the ones in a perfect W bulk, it means, without the reconstruction of the (011) surface. On the contrary, W^{bcc}_{dis} structure was built using the cell parameters of the W network at the W/Cu interface, where the reconstruction of the (001) surface was considered. Three different Cu bulks were considered: Cu^{fcc}_{per}, Cu^{bcc}_{per} and Cu^{fcc}_{dis}. The Cu^{fcc}_{per} and Cu^{bcc}_{per} bulks were modeled with the cell parameters of a perfect Cu bulk, the Cu^{bcc}_{per} was considered due to its potential formation, as reported by experimental observations [17, 18, 58, 68]. Conversely, the Cu^{fcc}_{dis} was built to reflect the reconstruction observed in the Cu network at the W/Cu interface.

By calculating the solution energy of H in all of these bulk structures, we can obtain a comprehensive understanding of how it varies away from the interface: far from the interface, where W and Cu are expected to exhibit their perfect bulk configurations (W^{bcc}_{per}, Cu^{fcc}_{per} and Cu^{bcc}_{per}), in the vicinity of the interface, where the reconstruction of both W and Cu becomes more pronounced, the structures W^{bcc}_{dis} and Cu^{fcc}_{dis} become relevant, and at the W/Cu interface. Such values of energies constitute the input of a developed thermodynamic model that delivers the solubility of H as function of the chemical potential and temperature of the reservoir in thermal equilibrium conditions. In the following section it is explained in details how such a model is built and how the solubility is determined.

4.1.1 Thermodynamic model for H solubility

The solubility of a gas phase denotes the degree to which a gas can blend into a liquid or solid phase, resulting in a uniform mixture under specific conditions of temperature T and pressure P. Typically quantified as the quantity of gas dissolved per unit volume of the solvent, it's commonly referred to as the atomic fraction [141]. In our investigation, we aim to ascertain the solubility of H atoms within metallic bulk materials, which could be either the W/Cu interface or the W and Cu bulks. This analysis is conducted under conditions where the H_2 reservoir is in thermal equilibrium with the metallic solvent.

Let's consider a perfect bulk sample without vacancies in thermal equilibrium with a H_2 atmosphere at pressure P and temperature T. In a grand canonical ensemble $(\mu VT)_{cte}$ the reservoir is represented by the hydrogen atmosphere containing N_H hydrogen atoms, equivalent to $N_H/2$ hydrogen molecules. The number of hydrogen atoms absorbed within the bulk sample and retained as interstitials is denoted by n_{int}, thus the initial and equilibrium states of the system are defined as:

	H_2 (reservoir)	H_{int} (bulk sample)
Initial state	$\frac{1}{2}N_H$	0
Equilibrium	$\frac{1}{2}(N_H - n_{int})$	n_{int}

Given that N_{H} is significantly greater than n_{int}, it is reasonable to make the assumption that the pressure of the reservoir remains constant, and consequently, the chemical potential imposed on the system. Under these conditions, the number of possible configurations or microstates for the same macrostate conforms to a standard scenario in combinatorics, and it can be mathematically described by the well-established binomial coefficient:

$$\Omega = \frac{(\gamma N)!}{(\gamma N - n_{int})!\ n_{int}!}, \tag{4.1}$$

where γ represents the number of interstitial sites per atom in the bulk and N denotes the number of atoms in the bulk sample. Thus, the configurational entropy is expressed as:

$$S_{conf} = k_B \ln \left[\frac{(\gamma N)!}{(\gamma N - n_{int})!\ n_{int}!} \right], \tag{4.2}$$

being k_B the Boltzmann's constant. The configurational entropy encompasses all possible arrangements that can be formed by distributing n_{int} hydrogen atoms within the lattice of the bulk sample. The pertinent physical quantity for investigating this equilibrium is the Gibbs free energy of the system. This is essentially the summation of the Gibbs free energy per particle of each constituent of the system, along with a configuration term:

$$G = \frac{1}{2}(N_{\mathrm{H}} - n_{int})g_{\mathrm{H}_2} + n_{int}g_{int} - TS_{conf}, \tag{4.3}$$

where g_{H_2} and g_{int} are the Gibbs free energies of H_2 molecule in the gas phase and H as interstitial, respectively. Considering that the thermal equilibrium condition is characterized by $\left(\frac{\partial G}{\partial n_{int}}\right)_{T,P} = 0$, the expression (4.3) gives:

$$\left(\frac{\partial G}{\partial n_{int}}\right)_{T,P} = \frac{\partial}{\partial n_{int}} \left[\frac{1}{2}(N_{\mathrm{H}} - n_{int})g_{\mathrm{H}_2} + n_{int}g_{int} - TS_{conf} \right]_{T,P} = 0, \tag{4.4}$$

solving the partial derivatives for the two first term:

$$-\frac{1}{2}g_{\mathrm{H}_2} + g_{int} - \frac{\partial}{\partial n_{int}} \left[TS_{conf} \right]_{T,P} = 0. \tag{4.5}$$

The initial term represents the chemical potential of hydrogen in the reservoir: $\mu \doteq \frac{1}{2}g_{\mathrm{H}_2}$. By substituting the expression of S_{conf} from equation (4.2) into (4.5) and solving the partial derivative separately to enhance clarity of the procedure, we obtain:

$$\frac{\partial}{\partial n_{int}} \left[TS_{conf} \right]_{T,P} = k_B T \frac{\partial}{\partial n_{int}} \left\{ \ln \left[\frac{(\gamma N)!}{(\gamma N - n_{int})!\ n_{int}!} \right] \right\}_{T,P}. \tag{4.6}$$

Which also can be written as:

$$\frac{\partial}{\partial n_{int}} \left[TS_{conf} \right]_{T,P} = k_B T \frac{\partial}{\partial n_{int}} \left\{ \ln \left[(\gamma N)! \right] - \ln \left[(\gamma N - n_{int})! \right] - \ln \left(n_{int}! \right) \right\}_{T,P}. \tag{4.7}$$

Making use of the simplest version of the Stirling formula [142]:

$$\ln x! = x \ln x, \tag{4.8}$$

the expression (4.7) becomes in:

$$\frac{\partial}{\partial n_{int}}\Big[TS_{conf}\Big]_{T,P} = k_B T \frac{\partial}{\partial n_{int}}\Big\{\gamma N \ln(\gamma N) - (\gamma N - n_{int})\ln(\gamma N - n_{int}) - n_{int}\ln n_{int}\Big\}_{T,P}. \tag{4.9}$$

This results in obtaining:

$$\frac{\partial}{\partial n_{int}}\Big[TS_{conf}\Big]_{T,P} = k_B T \ln\left(\frac{\gamma N}{n_{int}} - 1\right). \tag{4.10}$$

Thus, the expression (4.5) is as follows:

$$-\mu + g_{int} - k_B T \ln\left(\frac{\gamma N}{n_{int}} - 1\right) = 0. \tag{4.11}$$

Following some algebraic operations, we derive the expression for the atomic fraction or solubility of hydrogen in the bulk sample at equilibrium with a reservoir of chemical potential μ:

$$x_{int} = \frac{n_{int}}{N} = \frac{\gamma}{1 + \exp\left(\frac{g_{int}-\mu}{k_B T}\right)}. \tag{4.12}$$

Equation (4.12) defines the solubility of a gas phase in a bulk sample without vacancies under thermal equilibrium conditions, expressed as a function of temperature T and chemical potential μ within a grand canonical ensemble. This expression will be utilized in our paper (see Section 4.2) to ascertain the solubility of H at the W/Cu interface and within the W and Cu bulks independently.

To determine the atomic fraction of H in a bulk sample, it is essential to identify the most stable interstitial sites where the absorbed atoms will be located. The value of γ is dependent on both the type of interstitial site and the Bravais lattice of the bulk sample. Table 4.1 provides a summary of γ values for bcc and fcc bulks, taking into account two interstitial sites: octahedral (Oh) and tetrahedral (Td).

Table 4.1. Values of γ (interstitial sites/atoms) for bcc and fcc bulks.

Structure type	Atoms/unit cell	Td/unit cell	Oh/unit cell
bcc	2	12	6
fcc	4	8	4
		Td/atoms	Oh/atoms
bcc		6	3
fcc		2	1

In equation (4.12) the Gibbs free energies of H as interstitial g_{int} can be determined as follows:

$$g_{int} = \Delta_s E_{\mathrm{H}} + f_{vib}, \tag{4.13}$$

being $\Delta_s E_{\mathrm{H}}$ the solution energy of H atoms in the bulk without considering the zero-point energy (ZPE) correction and f_{vib} the vibrational Helmholtz free energy. The $\Delta_s E_{\mathrm{H}}$ values are obtaining from the DFT calculations (see Section 4.2) whereas the f_{vib} is defined as:

$$f_{vib} \doteq h_{vib} - T s_{vib}. \tag{4.14}$$

In (4.14), h_{vib} and s_{vib} are the vibrational enthalpy and entropy, respectively, which are calculated as follow:

$$h_{vib} = \sum_{j=1}^{n_{vib}} h\nu_j \left[\frac{1}{2} + \frac{1}{\exp\left(\frac{h\nu_j}{k_B T}\right) - 1} \right], \tag{4.15}$$

$$s_{vib} = k_B \sum_{j=1}^{n_{vib}} \left\{ \frac{h\nu_j}{k_B T} \frac{1}{\exp(\frac{h\nu_j}{k_B T}) - 1} - \ln\left[1 - \exp\left(\frac{h\nu_j}{k_B T} \right) \right] \right\}. \tag{4.16}$$

n_{vib} represents the total of vibrational modes of H atoms as interstitial in the bulk sample, h is the Planck's constant and ν_j is the vibrational frequency of the j-th mode. The values of ν_j are established through phonon calculations conducted in DFT simulations.

For determining the last variable in expression (4.12), the chemical potential $\mu \doteq \frac{1}{2} g_{\mathrm{H}_2}$ of the gas phase, it is necessary to calculate the Gibbs free energy for the gas phase g_{H_2} at pressure P and temperature T, which relies on whether the H_2 reservoir is considered as an ideal or real gas:

$$g_{\mathrm{H}_2} = g^{\circ}_{\mathrm{H}_2} + k_B T \ln \frac{P}{P^{\circ}}, \qquad \text{(ideal gas)} \tag{4.17a}$$

$$g_{\mathrm{H}_2} = g^{\circ}_{\mathrm{H}_2} + k_B T \ln \frac{\mathcal{F}}{\mathcal{F}^{\circ}}. \qquad \text{(real gas)} \tag{4.17b}$$

In equations (4.17), $g^{\circ}_{\mathrm{H}_2}$ represents the Gibbs free energy of H_2 in the gas phase at the standard pressure $P^{\circ} = 10^5$ Pa, while $\mathcal{F}$ and $\mathcal{F}^{\circ}$ denote the fugacity terms at pressures P and P°, respectively. In our case, the H_2 reservoir was analyzed considering both ideal and real gas behaviors. Consequently, both expressions (4.17) were used to ascertain the chemical potential μ. To model the H_2 reservoir as a real gas, we employ the parametrization provided by Tkacz and Litwiniuk [19], where the reported fugacity at pressure P(MPa) and temperature T(K) is described by:

$$\mathcal{F}(P,T) = \frac{1.5aP^{2/3} + 3bP^{1/3} + (d + eT)\ln P - 3cP^{-1/3}}{RT}. \tag{4.18}$$

In this parametrization, R represents the ideal gas constant, while a, b, c, d, and e are parameters. These parameters are defined as follows: $a = 176.330$, $b = -633.675$, $c = -304.574$, $d = 731.393$, and $e = 8.59805$. It is worth noting that in this parametrization, the pressure and temperature must be provided in MPa and K units, respectively.

In expressions (4.17), the Gibbs free energy of H_2 in the gas phase at the standard pressure P°, $g^{\circ}_{\mathrm{H}_2}$, is defined as:

$$g^{\circ}_{\mathrm{H}_2} \doteq E_{\mathrm{H}_2} + f_{vib} + f_{rot} + f^{\circ}_{trans} + k_B T. \tag{4.19}$$

f_{vib}, f_{rot}, and f°_{trans} signify the vibrational, rotational, and translational Helmholtz free energy of the H_2 molecule, respectively. The determination of f_{vib} follows the same equations as those presented above (4.14)-(4.16), with the distinction that, in this case, the vibrational frequencies ν_j are those specific to the H_2 molecule rather than those of the H interstitial atom in the bulk.

Making use of the definition of Helmholtz free energy we can determine the rest of terms in (4.19):

$$f_{rot} \doteq h_{rot} - Ts_{rot}, \tag{4.20}$$

$$f^{\circ}_{trans} \doteq h_{trans} - Ts^{\circ}_{trans}. \tag{4.21}$$

Analogously to (4.14), h_{rot} and h_{trans} represent the rotational and translational energy respectively, whereas s_{rot} and s°_{trans} are the rotational and translational entropies. As H_2 is a homonuclear diatomic molecule all of these terms are given by:

$$h_{rot} = k_B T, \tag{4.22}$$

$$h_{trans} = \frac{3}{2} k_B T, \tag{4.23}$$

$$s_{rot} = k_B \left[1 + \ln \left(\frac{8\pi^2 I k_B T}{\sigma h^2} \right) \right], \tag{4.24}$$

$$s^{\circ}_{trans} = k_B \left\{ \frac{5}{2} + \ln \left[\frac{k_B T}{P^{\circ}} \left(\frac{2\pi m k_B T}{h^2} \right)^{3/2} \right] \right\}. \tag{4.25}$$

In expression (4.24) I is the inertia momentum of the H_2 molecule and σ is a parameter that depends on the symmetry of the molecule, which is 2 in the case of a homonuclear diatomic molecule. The inertia momentum is given by $I = \frac{m}{2} d^2_{H_2}$, being m the mass of one H atom and d_{H_2} the interatomic distance in the H_2 molecule.

Given this, our thermodynamic model is now completely defined. However, it's important to note that its validity is restricted by the temperature range. Since phonons are computed using the quasiharmonic approximation, the temperature range is confined to below 1000 K. Beyond this range, it becomes necessary to account for anharmonic effects [143].

When $x_{int} < 10^{-2}$ $at.fr.$, Sievert's law can be derived from expression (4.12). This condition implies that the number of atoms in the bulk is significantly greater than the number of interstitial H atoms: $N \gg n_{int}$. Considering that the number of interstitial sites is greater than the number of atoms in the bulk: $\gamma N > N$, it follows that $\gamma N \gg n_{int}$ by transitivity. This physical approximation can be mathematically expressed as: $\gamma N - n_{int} \approx \gamma N$, changing the expression (4.10) to:

$$\frac{\partial}{\partial n_{int}} \Big[TS_{conf} \Big]_{T,P} = k_B T \ln \left(\frac{\gamma N}{n_{int}} \right). \tag{4.26}$$

As result, the solubility is expressed now as:

$$x_{int} = \frac{n_{int}}{N} = \frac{\gamma}{\exp\left(\frac{g_{int} - \mu}{k_B T}\right)}. \tag{4.27}$$

Substituting the expression for the chemical potential μ and for the Gibbs free energy of H_2 in the gas phase g_{H_2} by their respective equations, it is obtaining that:

$$x_{int} = \gamma \exp\left(- \frac{g_{int} - \frac{1}{2}g^{\circ}_{H_2} + \frac{1}{2}k_B T \ln\left(\frac{P}{P^{\circ}}\right)}{k_B T} \right). \tag{4.28}$$

Where after performing some algebraic operations, the well-known Sievert's law is derived:

$$x_{int} = \gamma \sqrt{\frac{P}{P^{\circ}}} \exp\left(- \frac{g_{int} - \frac{1}{2}g^{\circ}_{H_2}}{k_B T} \right). \tag{4.29}$$

4.1.2 Solution energy of H at the W/Cu interface

In the Methodology section of the paper, we provide an overview of the numerical parameters utilized to conduct our Density Functional Theory (DFT) calculations and determine the solution energy of hydrogen at the W/Cu interface. Table 4.2 presents the results for the solution energy and the adjusted value, considering the ZPE, for the 96 interstitial sites where H atoms were positioned. Figure 2 in the paper depicts this data and compares it to the corresponding values in bulk W and Cu. However, for enhanced precision, we opted to include this table in the Appendix of the paper.

Table 4.2. Values of the $\Delta_s E_H$, ΔZPE and $\Delta_s E_H^{ZPE}$ determined in the Td and Oh interstitial positions in the $W^{bcc}(001)/Cu^{hcp}(11\bar{2}0)$ super-cell. The initial and final columns represent the initial positions where the H atoms were placed and the final positions where they end after the geometry relaxation respectively (see Figures 1-a and 1-b in the paper). The $\Delta_s E_H$ and $\Delta_s E_H^{ZPE}$ in bold represent the 53 final most stable positions. In orange, dark gray and teal colors, we highlighted all the positions that correspond to the Cu_{IN}, W_{IN} and IN groups, respectively. The non-highlighted values correspond to repeated positions.

Initial	Final	$\Delta_s E_H$	ΔZPE	$\Delta_s E_H^{ZPE}$	Initial	Final	$\Delta_s E_H$	ΔZPE	$\Delta_s E_H^{ZPE}$
Td-9	**Td-9**	**0.54**	0.365	**0.91**	**Oh-1**	**Td-9**	0.54	0.365	0.91
Td-10	**Oh-40**	0.34	0.369	0.71	**Oh-2**	**Oh-2**	**0.34**	0.369	**0.71**
Td-11	**Oh-2**	0.34	0.369	0.71	**Oh-3**	**Td-17**	1.12	0.365	1.49
Td-12	**Td-12**	**0.51**	0.365	**0.88**	**Oh-4**	**Oh-4**	**0.11**	0.350	**0.46**
Td-13	**Td-13**	**0.51**	0.365	**0.88**	**Oh-5**	**Td-25**	0.51	0.415	0.93
Td-14	**Oh-40**	0.34	0.369	0.71	**Oh-6**	**Td-27**	0.37	0.415	0.79
Td-15	**Oh-2**	0.34	0.369	0.71	**Oh-7**	**Td-33**	0.88	0.415	1.30
Td-16	**Oh-44**	0.11	0.350	0.46	**Oh-8**	**Td-8**	**0.90**	0.415	**1.32**
Td-17	**Td-17**	**0.62**	0.365	**0.99**	**Oh-38**	**Oh-38**	**0.37**	0.369	**0.74**
Td-18	**Oh-44**	0.11	0.350	0.46	**Oh-39**	**Oh-39**	**0.37**	0.369	**0.74**
Td-19	**Oh-4**	0.11	0.350	0.46	**Oh-40**	**Oh-40**	**0.34**	0.369	**0.71**
Td-20	**Oh-44**	0.11	0.350	0.46	**Oh-41**	**Td-13**	0.50	0.365	0.87
Td-21	**Oh-4**	0.11	0.350	0.46	**Oh-42**	**Oh-42**	**0.46**	0.369	**0.83**

Td-22	Oh-44	0.11	0.350	0.46
Td-23	Oh-4	0.11	0.350	0.46
Td-24	Td-24	0.47	0.350	0.82
Td-25	Td-25	0.51	0.350	0.86
Td-26	Td-26	0.37	0.415	0.79
Td-27	Td-27	0.37	0.415	0.79
Td-28	Td-28	0.69	0.415	1.11
Td-29	Td-29	0.69	0.415	1.11
Td-30	Td-30	0.89	0.415	1.31
Td-31	Td-31	0.90	0.415	1.32
Td-32	Td-32	0.88	0.415	1.30
Td-33	Td-33	0.88	0.415	1.30
Td-34	Td-34	0.89	0.415	1.31
Td-35	Td-35	0.91	0.415	1.33
Td-36	Td-36	0.90	0.415	1.32
Td-37	Td-37	0.91	0.415	1.33
Td-76	Oh-54	0.37	0.369	0.74
Td-77	Td-77	0.51	0.365	0.88
Td-78	Oh-60	0.46	0.369	0.83
Td-79	Td-79	0.51	0.365	0.88
Td-80	Oh-60	0.46	0.369	0.83
Td-81	Td-81	0.38	0.350	0.73
Td-82	Oh-63	0.37	0.350	0.72
Td-83	Td-83	0.38	0.350	0.73
Td-84	Td-84	0.37	0.415	0.79
Td-85	Td-85	0.69	0.415	1.11
Td-86	Td-86	0.89	0.415	1.31
Td-87	Td-87	0.69	0.415	1.11
Td-88	Oh-60	0.46	0.369	0.83
Td-89	Td-89	0.50	0.350	0.85
Td-90	Oh-61	0.42	0.369	0.79
Td-91	Oh-65	0.11	0.350	0.46
Td-92	Oh-65	0.11	0.350	0.46
Td-93	Td-93	0.47	0.350	0.82
Td-94	Td-94	0.36	0.415	0.78
Td-95	Oh-4	0.12	0.350	0.47
Td-96	Td-96	0.89	0.415	1.31

Oh-43	Oh-43	0.46	0.369	0.83
Oh-44	Oh-44	0.11	0.350	0.46
Oh-45	Oh-45	0.38	0.350	0.73
Oh-46	Td-26	0.37	0.415	0.79
Oh-47	Td-27	0.37	0.415	0.79
Oh-48	Td-26	0.37	0.415	0.79
Oh-49	Td-29	0.69	0.415	1.11
Oh-50	Td-30	0.89	0.415	1.31
Oh-51	Td-31	0.90	0.415	1.32
Oh-52	Td-52	0.90	0.415	1.32
Oh-53	Td-37	0.90	0.415	1.32
Oh-54	Oh-54	0.37	0.369	0.74
Oh-55	Oh-55	0.36	0.369	0.73
Oh-56	Td-56	0.47	0.365	0.84
Oh-57	Oh-54	0.37	0.369	0.74
Oh-58	Td-58	0.47	0.365	0.84
Oh-59	Oh-59	0.33	0.369	0.70
Oh-60	Oh-60	0.46	0.369	0.83
Oh-61	Oh-61	0.42	0.369	0.79
Oh-62	Oh-62	0.12	0.350	0.47
Oh-63	Oh-63	0.37	0.350	0.72
Oh-64	Oh-62	0.12	0.350	0.47
Oh-65	Oh-65	0.11	0.350	0.46
Oh-66	Oh-4	0.11	0.350	0.46
Oh-67	Td-84	0.37	0.415	0.79
Oh-68	Td-94	0.36	0.415	0.78
Oh-69	Td-87	0.69	0.415	1.11
Oh-70	Td-84	0.37	0.415	0.79
Oh-71	Td-85	0.69	0.415	1.11
Oh-72	Td-94	0.36	0.415	0.78
Oh-73	Td-73	0.69	0.415	1.11
Oh-74	Td-86	0.88	0.415	1.30
Oh-75	Td-75	0.88	0.415	1.30

4.2 Publication

Solution and solubility of H at the W/Cu interface.

Y. Silva-Solís, J. Denis, E.A. Hodille and Y. Ferro.

Published in Journal of Physics and Condensed Matter.

Available online since August 28th, 2024.

10.1088/1361-648X/ad6f62

IOP Publishing Journal of Physics: Condensed Matter
J. Phys.: Condens. Matter **36** (2024) 465001 (15pp) https://doi.org/10.1088/1361-648X/ad6f62

Solution and solubility of H atoms at the W/Cu interface

Y Silva-Solís[1], J Denis[1], E A Hodille[2] and Y Ferro[1,*]

[1] Aix-Marseille University, CNRS, PIIM, F-13013 Marseille, France
[2] CEA, IRFM, F-13108 Saint-Paul-lez-Durance, France

E-mail: yves.ferro@univ-amu.fr

Received 18 June 2024, revised 28 July 2024
Accepted for publication 14 August 2024
Published 28 August 2024



Abstract

Metallic interfaces are locations where hydrogen (H) is expected to segregate and lead to the formation and stabilization of defects. This work focuses on the tungsten/copper (W/Cu) interface built according to the $W^{bcc}(001)/Cu^{hcp}(11\bar{2}0)$ orientation. H behavior is subsequently determined at the interface and in its vicinity with electronic structure calculations based on the density functional theory (DFT). The electronic and vibrational properties determined in this way followed a thermodynamic treatment to deliver the solubility of H as a function of the temperature and chemical potential. The 96 interstitial positions we investigated reveal that H predominantly occupies the octahedral (Oh) sites in the copper network. Reversely, H exclusively occupies the tetrahedral (Td) sites in the tungsten network. The solubility of H is higher in the interface plane where both octahedral and tetrahedral sites are occupied. Despite this work is a first step toward kinetic modeling of hydrogen transport across the W/Cu interface, we conclude that the $W^{bcc}(001)/Cu^{hcp}(11\bar{2}0)$ would behave like a sink where hydrogen isotopes could accumulate.

Supplementary material for this article is available online

Keywords: metallic interfaces, DFT, solution energy, solubility

1. Introduction

Solute in materials might segregate at various defects, among them surfaces and interfaces. In this work, we specifically focus on the W/Cu interface in the presence of H as a solute. The W/Cu interface is found in multilayered systems of interest for their enhanced hardness and tunable properties [1, 2]. It is also found in nuclear fusion devices called tokamaks, at the junction between the plasma facing components (PFCs) made of W and the cooling system constituted by pipes made of a copper—chromium—zirconium (CuCrZr) alloy [3, 4]. In between the W PFC and the CuCrZr alloy is a 1 mm thick Cu layer that helps reduce the mechanical stress [3]. The full PFC *plus* cooling system is called a monoblock. In ITER, monoblocks constitute the divertor; it is located in the tokamak where the plasma-wall interactions are the strongest [5]. It follows that the transport and retention of hydrogen isotopes (HIs) there is significant, and with tritium, it might lead to system contamination and fuel losses [6]. This motivated the present work that paves the way toward a full understanding of H interaction with W, Cu and the W/Cu interface.

Some studies have already been carried out on diffusion, permeation and solubility of HIs in W [7–11] and in Cu bulks [12–16]. However, to our knowledge, these properties are still to be determined at the W/Cu interface. Kinetic investigations of HIs transport across the monoblocks exist and were performed with the macroscopic rate equation codes FESTIM [8, 17, 18] despite no model of the interface was available at that time and as a consequence not included in their modeling. To build such a model, the energy of hydrogen at the W/Cu interface has to be determined, which we herein

* Author to whom any correspondence should be addressed.

© 2024 IOP Publishing Ltd. All rights, including for text and data mining, AI training, and similar technologies, are reserved.

propose to do by means of density functional theory (DFT) calculations followed by thermodynamics modeling to include the temperature dependency.

As a consequence, the first step is to define a model of the W/Cu interface that is suitable for DFT calculations, and that can be compared to experimental observations for validation.

Many experimental studies were conducted to determine the structure and morphology of the W/Cu interface [1, 19–30]. In these studies, the growth of Cu ad-layers is analysed on different W surface orientations: W(100) [19, 20, 26, 30], W(110) [1, 19, 21–24, 27–29] and W(111) [1, 21, 23, 28, 29]. Bauer *et al* [19] monitored the adsorption and condensation of Cu on W(100) and W(110) surfaces by combining different techniques, such as low-energy electron diffraction (LEED), Auger electron spectroscopy (AES) and thermal desorption spectrometry (TDS). On both surfaces they observed the formation of two stable adsorbed layers of Cu whose structures were fully determined by the periodicity of the W surface. Using field emission microscopy (FEM), Cetronio *et al* [20] did the same observation for the first two layers, which adopt a pseudomorphic growth on W(100) surface as shown later on by Wormeester *et al* [25, 26] using reflection high-energy electron diffraction (RHEED). Bollmann *et al* [30] shown that further Cu adsorption leads to the formation of crystallites with hcp structure having the $(11\bar{2}0)$ plane parallel to W(100) surface.

Modeling a metallic interface by DFT [31] is challenging: on one hand, both Cu and W metal have different Bravais lattices and cell parameters, which induces an intrinsic mismatch. On the other hand, models based on DFT have to be small enough to reduce the computational cost of the simulations. In the end, as the model is periodically reproduced in space and contains a limited number of atoms, the number of interface orientations that can be investigated is limited too. However, some theoretical works have been done on the W/Cu interface [32–37]. Liang *et al* [32] investigated five different W/Cu interface orientations. They are the (100)Cu/(100)W, (110)Cu/(110)W, (111)Cu/(111)W, (111)Cu/(110)W and (110)W/(111)Cu orientations built in a (1×1) surface unit-cell which does not allow for surface reconstruction as observed for example on the (100)W surface [10]. They showed that the (111)Cu/(111)W, (111)Cu/(110)W and (100)Cu/(100)W interfaces are among the most stable with the highest work of separation and the lowest formation energy. Wang *et al* [34] showed that the (100)Cu/(100)W induces the lowest mismatch followed by the (111)Cu/(111)W orientation. All these previous models share a common approach; it consists in freezing the unit-cell parameters to the one of perfect W and adjusting the Cu network such that it matches the W one. A geometry optimization is further done while keeping the cell parameters frozen [32–36]. In addition, a thick vacuum layer of around 15 Å is inserted in the Z direction to avoid the interaction of the working cell with its image. Following the same approach, Ma *et al* [33] investigated the interaction of at H the (111)Cu/(110)W interface. The authors' finding is a smooth transition of hydrogen's solution energy from the W side of the interface to the Cu side.

The model we built [37] follows a different scheme. We suppressed the vacuum layer and built instead a system of two symmetric interfaces to get rid of any dipole moment. In addition, the full geometry and cell parameters were relaxed such as to find the optimal geometry of the interface. We started with two orientations $W(001)/Cu^{fcc}(001)R45°$ and $W(001)/Cu^{bcc}(001)$ and ended up with a $W^{bcc}(001)/Cu^{hcp}(11\bar{2}0)$ interface consistent with experimental observations [19, 25, 26, 30].

To this model, we herein add hydrogen and consider its interaction in the W and Cu networks either in their perfect or distorted geometry as it exists at the interface. The solubility is further calculated across the fully reconstructed $W^{bcc}(001)/Cu^{hcp}(11\bar{2}0)$ interface. We determined the vibrational properties of H atoms in each position to deliver the solubility of H (x_{int}) as a function of temperature at thermal equilibrium. The details regarding the numerical parameters of the DFT calculations and the thermodynamic model approach are given in section 2. The solution energy and temperature-dependent solubility are presented in section 3, and a discussion of our results against experimental data and other works available in the literature is organized in section 4 before the conclusions are given in section 5.

2. Methodology

As our investigation focuses on the solubility of H at the W/Cu interface, it is essential to compare these values against reference values such as in W and Cu bulks. Hence, we considered the following structures: Cu^{fcc}_{per}, Cu^{bcc}_{per}, W^{bcc}_{per}, Cu_{dis}, W_{dis}, and $W^{bcc}(001)/Cu^{hcp}(11\bar{2}0)$ where the sub-index *per* and *dist* stand for perfect and distorted networks, respectively. Cu^{bcc}_{per} bulk was also considered due to its possible formation from a pseudomorphic growth of Cu on top of W(001) surface [19, 25, 26, 30]. Cu_{dis} and W_{dis} are structures formed in the vicinity of the interface such as to connect both copper and tungsten networks that have different geometries. The cell parameters employed to build both distorted bulk structures are taken from [37].

2.1. Numerical parameters for DFT

The electronic structure calculations were performed using the quantum espresso open source code [38]. All the supercells were computed employing periodic boundary conditions [39]. While the ultrasoft pseudopotentials [40] employed consider 14 semi-core and valance electrons for W atoms ($5s^25p^65d^46s^2$) and 11 for Cu ($4s^23d^9$). They were generated with the nonlinear core correction [41] and the PBE-GGA exchange-correlation functional [42]. To broaden the density of states and to smooth the discontinuities at the Fermi level, the cold-smearing technique from Marzari *et al* [43] was used with a value of 0.27 eV. As both Cu and W are non-magnetic metals, no spin-polarization was considered. The convergence thresholds for the forces and selfconsistency were set to 2.6×10^{-3} eV·Å^{-1} and to 1.4×10^{-6} eV, respectively.

We employed a $(2\times2\times2)$ super-cell for Cu^{fcc}_{per}, Cu^{bcc}_{per}, Cu_{dis}, W^{bcc}_{per}, W_{dis} bulks and a $(2\times2\times8)$ for the $W^{bcc}(001)/Cu^{hcp}(11\bar{2}0)$ interface within the optimized geometry from [37]. The Cu^{bcc}_{per}, Cu_{dis}, W^{bcc}_{per}, and W_{dis} bulks structures are made up of 16 atoms, Cu^{fcc}_{per} of 32 atoms, and the $W^{bcc}(001)/Cu^{hcp}(11\bar{2}0)$ of 64 atoms (32 W and 32 Cu). The calculated cell parameters for Cu^{fcc}_{per} and Cu^{bcc}_{per} bulks structures are 3.620 Å and 2.871 Å, respectively. For W^{bcc}_{per} it was determined to 3.187 Å by Fernandez *et al* [44]. The Cu_{dis} and W_{dis} models were built with the cell parameters of Cu and W when relaxed at the interface [37]; this is $a=b=3.162$ Å, $c=2.531$ Å for Cu_{dis} and $a=b=3.162$ Å, $c=3.209$ Å for W_{dis}. The k-point samplings of the Brillouin Zone are $(10\times10\times10)$ for Cu^{fcc}_{per}, $(12\times12\times12)$ for Cu^{bcc}_{per}, Cu_{dis}, W^{bcc}_{per} and W_{dis}, and $(10\times10\times1)$ for the interface model as in [37].

2.2. Solubility of hydrogen

To find the most stable interstitial positions for H atoms, we determined the solution energy at octahedral (Oh) and tetrahedral (Td) interstitial sites. The solution energy was calculated according to :

$$\Delta_s E_H = E_{sys,H} - \left(E_{sys} + \frac{1}{2}E_{H_2}\right), \tag{1}$$

where $E_{sys,H}$ is the energy of the system with one interstitial H atom, E_{sys} is the energy of the system without H, and E_{H_2} is the energy of H_2 molecule. This expression provides the increase in solution energy when a single H atom is added to the bulk of the material. H_2 was not considered as an interstitial in the bulk due to the repulsion between two H atoms in close proximity within the material, making the existence of an interstitial H_2 molecule much less likely than individual H atoms.

We also corrected the solution energy of the zero-point energy (ZPE). To this end, we carried out phonon calculations at the Γ point with all the atoms in the super-cell frozen to their equilibrium position considering the vibration of the super-cells atoms and H decoupled due to their mass difference. In the end, $\mathrm{ZPE}=\frac{1}{2}\sum_i h\nu_i$ where ν_i is the frequency of the i vibrational normal mode. Finally, the ZPE corrected solution energy is:

$$\Delta_s E_H^{ZPE} = \Delta_s E_H + (\mathrm{ZPE}_{H,sys} - \mathrm{ZPE}_{H,H_2}), \tag{2}$$

where $\Delta_s E_H$ is the solution energy of H without ZPE, $\mathrm{ZPE}_{H,sys}$ and ZPE_{H,H_2} are the ZPE of H in the system and the H_2 molecule, respectively.

2.3. Thermodynamic model

The solubility of hydrogen was subsequently calculated as a function of the temperature. It was determined in Cu, W, and at the W/Cu interface considering an equilibrium with a H_2 atmosphere. H_2 is considered either as an ideal or a real gas using the parametrization from Tkacz and Litwiniuk [45]. As we found no experimental data of H solubility at the W/Cu interface, we validated our model against experimental data on W^{bcc}_{per} [46] and in Cu^{fcc}_{per} [13–16, 47]. Phonons were computed in the quasiharmonic approximation neglecting the anharmonic terms [48], reason why our thermodynamic model is valid only in the range of temperatures lower than 1000 K.

Considering N atoms in the bulk and n_{int} hydrogen atoms trapped at interstitial sites, the hydrogen solubility $x_{int}=\frac{n_{int}}{N}$ is given by :

$$x_{int} = \frac{\gamma}{1+\exp\left(\frac{g_{int}-\mu}{k_B T}\right)}. \tag{3}$$

Where γ is the number of interstitial sites per atom in the bulk: $\gamma=6$ in W^{bcc}_{per} at Td positions (most stable interstitial site in W, table 2); for Cu^{fcc}_{per}, $\gamma=1$ at Oh positions (most stable interstitial site in Cu, table 2). In the case of the interface, the value of γ is determined depending on the symmetry of the site, which will be discussed later on. In the end, k_B is the Boltzmann constant, T the temperature of the gas, and g_{int} the Gibbs free energy per interstitial hydrogen, which is calculated as in previous works from us [49]. Finally, μ is the chemical potential of hydrogen and is given by:

$$\mu = \frac{1}{2}g_{H_2}. \tag{4}$$

The Gibbs free energy of H_2 takes the form below:

$$g_{H_2}(P,T) = g^{\circ}_{H_2}(T) + k_B T \ln\frac{f}{P^{\circ}}, \tag{5}$$

where $g^{\circ}_{H_2}(T)$ is the Gibbs free energy of H_2 as determined in previous works from us [10, 49] at standard pressure $P^{\circ}=10^5$ Pa and temperature T, and f is the fugacity. In the case of an ideal gas, the fugacity f is equal to the pressure P of the hydrogen gas, while for a real gas we followed the equation of state proposed by Tkacz and Litwiniuk [45] which allows easy calculation of fugacity and chemical potentials up to a pressure of 100 GPa.

3. Results

3.1. Solution energy of H in Cu and W bulks

In this section, we provide the solution energies $\Delta_s E_H$ and $\Delta_s E_H^{ZPE}$ of hydrogen computed in various environments : Cu^{fcc}_{per}, Cu^{bcc}_{per}, Cu_{dis}, W^{bcc}_{per} and W_{dis} calculated using equations (1) and (2), with or without ZPE correction ΔZPE. Beforehand, we calculated the binding energy of H_2 and its ZPE correction. We obtained $E_{H_2}=4.526$ eV and $\Delta\mathrm{ZPE}=0.135$ eV, corresponding to a vibrational frequency of 4342 cm^{-1}, in good agreement with the experimental value of 4395 cm^{-1} [50].

We further determined $\Delta_s E_H$, $\mathrm{ZPE}_{H,sys}$ and $\Delta_s E_H^{ZPE}$ for H located in Oh or Td interstitial sites of the W and Cu networks. These locations are shown in table 1: Oh sites are represented as blue points, and Td sites as red points. For a better comprehension of the positions, see tables A1 and A2 of

Table 1. Positions in which $\Delta_s E_{\mathrm{H}}$, ΔZPE and $\Delta_s E_{\mathrm{H}}^{\mathrm{ZPE}}$ were determined in Cu and W bulks. The orange and grey balls represent the Cu and W atoms, respectively, whereas the blue and red points correspond with Oh and Td positions, respectively. The projections in different crystallographic planes are shown in table A1 of appendix A.

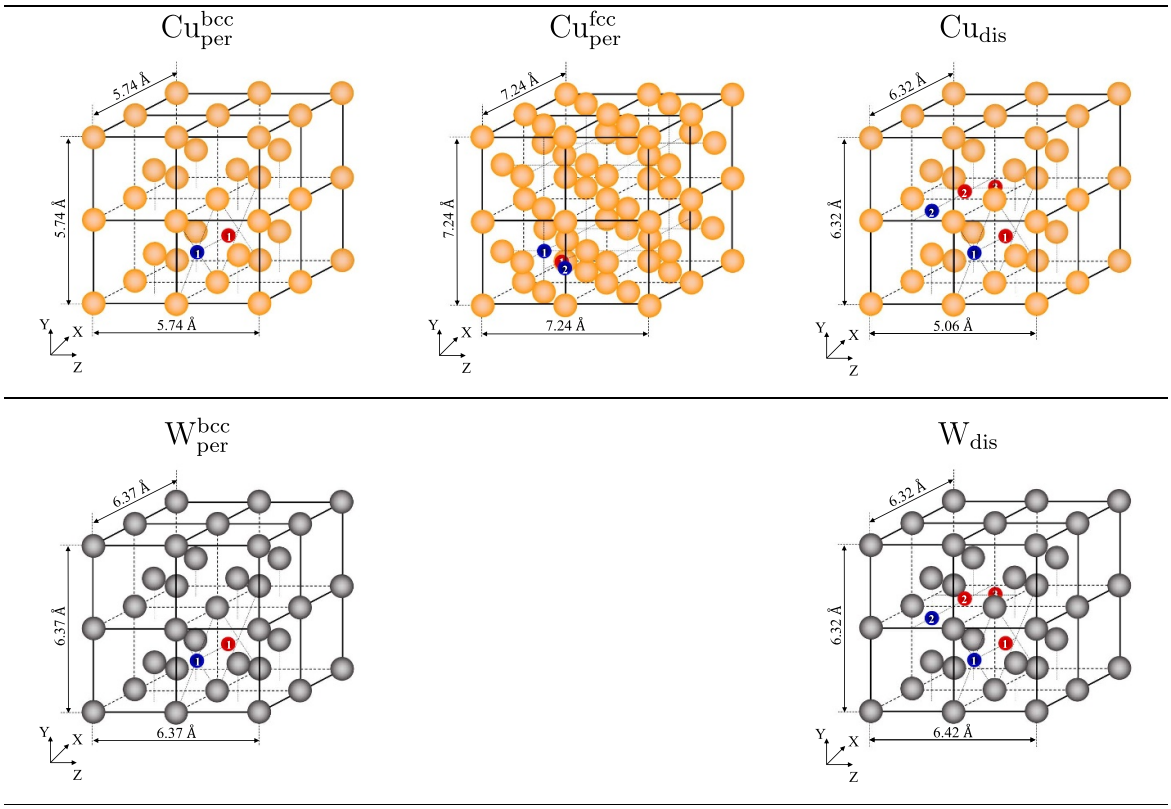

the appendix A, where different projections of the crystallographic planes are represented. Due to the symmetry of the network, the selected Oh and Td positions describe every other interstitial site.

$\Delta_s E_{\mathrm{H}}$ and $\Delta_s E_{\mathrm{H}}^{\mathrm{ZPE}}$ are provided in table 2 for Cu and W bulks. Without ZPE, $\Delta_s E_{\mathrm{H}}$ at Oh sites is lower than at Td sites, by 0.05 eV and 0.17 eV in Cu_{per}^{bcc} and Cu_{per}^{fcc}, respectively. These differences increase with adding the ZPE, making Oh the most stable interstitial site for hydrogen in copper. Distortions in the Cu_{dis} matrix introduce significant variations in solution energy. The most stable position corresponds to Oh-2, with a value of 0.42 eV without ZPE consideration and 0.41 eV with it. Conversely, Oh-1 exhibits the highest solution energy value in Cu_{dis} with 0.71 eV and 0.76 eV when ZPE is accounted for. Comparing only among the Td sites, Td-1 and Td-2 demonstrate the highest solution energy values, at 0.58 eV and 0.66 eV respectively. When the ZPE correction is considered, both surpass Td-3 solution energy, which stands at 0.43 eV. The solution energy of H in Cu_{dis} undergoes a significant deviation compared to the values observed in Cu_{per}^{bcc} and Cu_{per}^{fcc}. This difference primarily stems from the distortion present in the bulk, this is analyzed and discussed in section 4.

In perfect tungsten, H is known to prefer the Td interstitial site where the solution energy is computed to 1.06 eV[3]. As tungsten is stiffer than copper, its distortion is smaller at the interface and the effect of the distortion on the solution energy is smaller too. After distortion, the lowest solution energy corresponds to Td-3, at 0.93 eV without ZPE and 1.06 eV with ZPE considered. However, the remaining Td positions exhibit similar solution energy values, with a variation of less than 5.37% when neglecting ZPE and 4.71% with ZPE. The smaller variation in $\Delta_s E_{\mathrm{H}}$ as compared to copper is attributed to the smaller distortion of the W network at the W/Cu interface [37].

3.2. Solution energy of H at the interface

To determine $\Delta_s E_{\mathrm{H}}$, ΔZPE, and $\Delta_s E_{\mathrm{H}}^{\mathrm{ZPE}}$ at the interface, we initially positioned hydrogen in 96 sites near the plane

[3] Fernandez *et al* [44] reported an energy of 1.04 eV using the same pseudopotential, exchange-correlation functional, and electrons as in our work. However, we employed cutoff energies of 50 Ry for the wave function and 400 Ry for the electronic density, whereas [44] used 40 Ry and 320 Ry, respectively.

Table 2. Values of the $\Delta_s E_H$, ΔZPE and $\Delta_s E_H^{ZPE}$ determined at Oh (blue points) and Td (red points) sites in Cu and W bulks. The schematic representation appears in table 1.

		$\Delta_s E_H$ (eV)			ΔZPE (eV)			$\Delta_s E_H^{ZPE}$ (eV)		
Sites		Cu_{per}^{bcc}	Cu_{per}^{fcc}	Cu_{dis}	Cu_{per}^{bcc}	Cu_{per}^{fcc}	Cu_{dis}	Cu_{per}^{bcc}	Cu_{per}^{fcc}	Cu_{dis}
Oh	**1**	0.55	0.41	0.71	−0.007	0.004	0.050	0.54	0.41	0.76
	2			0.42			−0.007			0.41
Td	**1**	0.60	0.58	0.58	0.038	0.087	0.075	0.64	0.67	0.66
	2			0.58			0.075			0.66
	3			0.43			0.002			0.43
		W_{per}^{bcc}		W_{dis}	W_{per}^{bcc}		W_{dis}	W_{per}^{bcc}		W_{dis}
Oh	**1**	1.37		1.33	0.126		0.129	1.50		1.47
	2			1.47			0.132			1.60
Td	**1**	0.93		0.97	0.126		0.129	1.06		1.10
	2			0.98			0.133			1.11
	3			0.93			0.129			1.06

of the interface, as shown in figure 1(a). Similar to previous cases, the blue and red points denote the Oh and Td sites, while the orange and gray balls represent Cu and W atoms, respectively. After geometry optimization, the 96 initial positions converged to 53 stable interstitial sites as illustrated in figure 1(b). Table C1 of appendix C provides the full energy values of $\Delta_s E_H$ before and after geometry optimization along with ΔZPE and $\Delta_s E_H^{ZPE}$ for all stable positions. This full energies is plotted in figure 2, which compares the solution energies of hydrogen in all environments, starting from W_{per}^{bcc}, through the $W^{bcc}(001)/Cu^{hcp}(11\bar{2}0)$, and up to Cu_{per}^{bcc}.

For a clear understanding of how hydrogen interacts with the $W^{bcc}(001)/Cu^{hcp}(11\bar{2}0)$, we further divided the model into three regions: Cu_{IN}, W_{IN}, and IN. In the Cu_{IN} and W_{IN} regions, interstitial hydrogen atoms are surrounded only by copper and tungsten atoms, respectively. In the IN region, the atomic tetrahedral and octahedral environment that surrounds H is composed of a mixture of tungsten and copper atoms, making of the IN region the plane of the interface.

In figure 2, the solution energies $\Delta_s E_H^{ZPE}$ at Td interstitial sites in the W_{IN} region are clearly higher than in W_{dis} and W_{per}^{bcc}. $\Delta_s E_H^{ZPE}$ decreases approaching the IN region. Then, in the IN region, 12 stable positions were identified: 6 corresponding to Oh sites and 6 to Td sites. The lowest in energy are of Oh symmetry (Oh-44, Oh-4, and Oh-65) with $\Delta_s E_H^{ZPE}$ around 0.46 eV. This is one of the lowest $\Delta_s E_H^{ZPE}$ values among all the environments considered in this study. In the Cu_{IN} region, Oh sites provide the most stable location for interstitial hydrogen atoms with a value of 0.41 eV. Interestingly, the minimum solution energy value at the plane W/Cu interface in Oh sites is comparable to the minimum energy observed in the Cu_{per}^{fcc} and Cu_{per}^{bcc} bulks. This means that the interface could behave as a sink for H atoms by itself, with its main trap in the IN region.

In the following, and in order to bring new elements of understanding, we investigate the effect of temperature on the solubility of hydrogen in these various environments.

3.3. Solubility of H with temperature

We built the Gibbs free energy state functions g_{int} for interstitial hydrogen based on the solution energies and vibrational properties of hydrogen in the various environments across the interface: Cu_{per}^{bcc}, Cu_{per}^{fcc}, Cu_{dis}, $W^{bcc}(001)/Cu^{hcp}(11\bar{2}0)$, W_{per}^{bcc} and W_{dis}. We also built the Gibbs free energy of molecular hydrogen g_{H_2} in the ideal and real gas phases. With this, we determined the solution energies of hydrogen according to equation (3). We found no experimental data on hydrogen solubility at the Cu/W interface. Consequently, we first validated our model against experimental data for tungsten W_{per}^{bcc} and copper Cu_{per}^{fcc}.

In figure 3, the solubility of hydrogen in W_{per}^{bcc} and Cu_{per}^{fcc} are plotted and compared to experimental data. For tungsten, the solubility is compared with the high temperature fit to Frauenfelder's data [46] by Heinola and Ahlgren [51]. For copper, it is done versus several sets of experimental data [13–16, 47]. For tungsten, the comparison is known to be satisfactory. For copper, we calculated a solution energy of 0.41 eV for H in the Oh site of Cu_{per}^{fcc}. This is a dispersion of less than 7.3% as compared to the fitted value from the experimental data shown in table 3; this also constitutes a satisfactory agreement, enabling us to move to the solubility of hydrogen at $W^{bcc}(001)/Cu^{hcp}(11\bar{2}0)$. To do so, we have to determine γ in equation (3). In W_{IN} we employed $\gamma = 6$, as in W_{per}^{bcc} the Td site is the most stable. Conversely, in Cu_{IN} the Oh site is the most stable and we defined $\gamma = 1$. In the IN region, $\gamma = 1/2$ because there are 0.5 equivalent Oh-4 sites per metallic atom (since other Oh sites, such as Oh-63, have higher $\Delta_s E_H$).

The solubility of hydrogen is plotted in the W_{IN}, IN and Cu_{IN} regions in figure 4(a) under a hydrogen pressure of $P = 10^5$ Pa. Under this pressure, there is no difference between the ideal and real gas models and the solubility plots are superimposed. However, a hydrogen flux on a metal imposes a high chemical potential of hydrogen [49], leading to a high interstitial hydrogen concentration in the metal. If a vacuum or void exists, it is filled by hydrogen up to reach an equilibrium

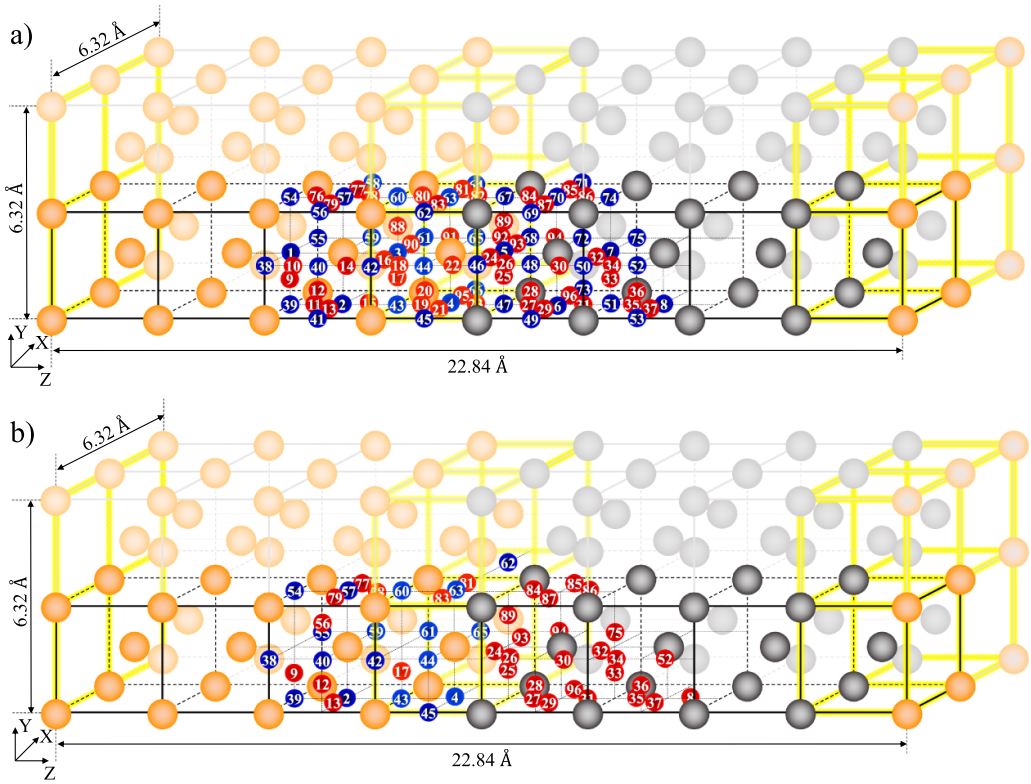

Figure 1. (a) 96 initial interstitial positions where H atoms were placed to determine $\Delta_s E_{\mathrm{H}}$ and $\Delta_s E_{\mathrm{H}}^{\mathrm{ZPE}}$ at the $\mathrm{W}^{\mathrm{bcc}}(001)/\mathrm{Cu}^{\mathrm{hcp}}(11\bar{2}0)$ super-cell. (b) 53 final interstitial positions where H atoms reside at the $\mathrm{W}^{\mathrm{bcc}}(001)/\mathrm{Cu}^{\mathrm{hcp}}(11\bar{2}0)$ structure after geometry relaxation. The gray and orange balls represent the W and Cu atoms respectively and the blue and red points correspond with Oh and Td interstitial sites respectively.

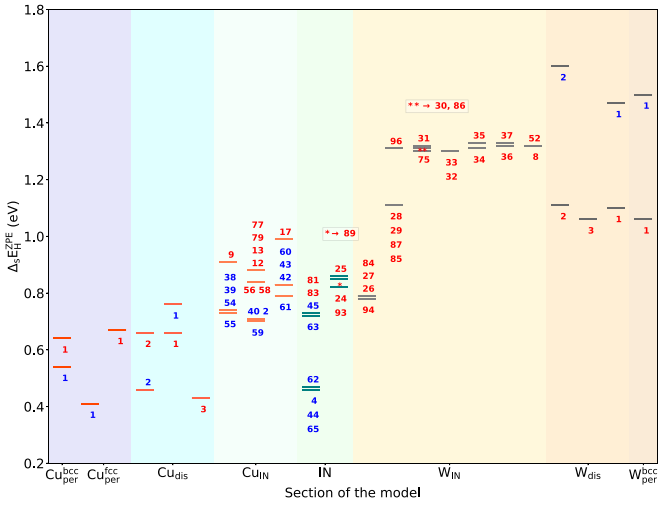

Figure 2. Solution energies $\Delta_s E_{\mathrm{H}}^{\mathrm{ZPE}}$ in the various environments here investigated for hydrogen as interstitial: $\mathrm{Cu}_{\mathrm{per}}^{\mathrm{bcc}}$, $\mathrm{Cu}_{\mathrm{per}}^{\mathrm{fcc}}$, $\mathrm{Cu}_{\mathrm{dis}}$, $\mathrm{W}_{\mathrm{per}}^{\mathrm{bcc}}$ and $\mathrm{W}_{\mathrm{dis}}$. In the $\mathrm{Cu}_{\mathrm{IN}}$, IN and W_{IN} regions are plotted $\Delta_s E_{\mathrm{H}}^{\mathrm{ZPE}}$ for the 53 final stable interstitial sites found at the $\mathrm{W}^{\mathrm{bcc}}(001)/\mathrm{Cu}^{\mathrm{hcp}}(11\bar{2}0)$ super-cell after geometry relaxation. Blue and red numbers correspond to the Oh and Td positions, respectively, which are represented in table 1 and figure 1(b).

pressure that might exceed the GPa. For this reason, we plotted in figure 4(b) the solubility of hydrogen in all regions under a hydrogen pressure of $P = 1\,\mathrm{GPa}$. This results in a difference in solubility between the real and ideal gas-phase models that reaches one order of magnitude at low temperatures. However, this does not affect the affinity of hydrogen for perfect copper, closely followed by that in the plane of the interface, while it is still the lowest in tungsten.

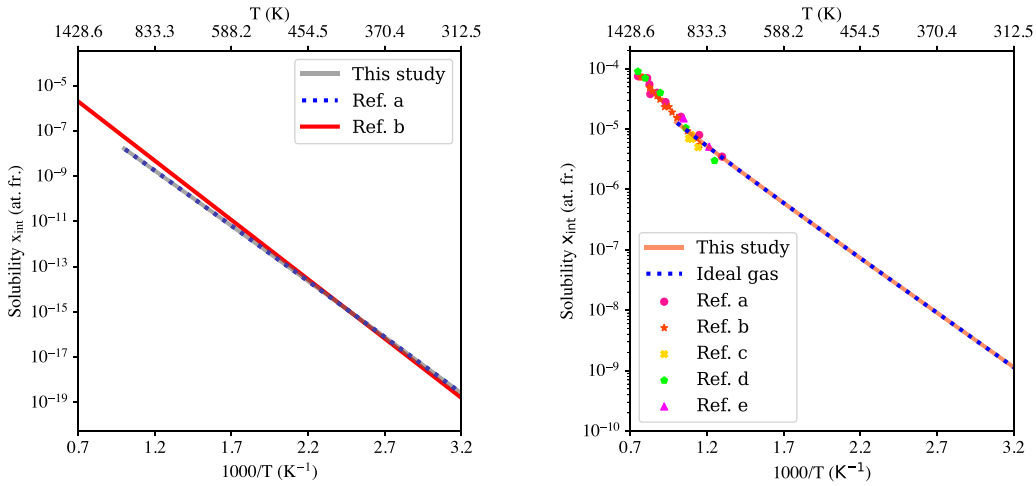

Figure 3. Solubility of H in W^{bcc}_{per} and Cu^{fcc}_{per} bulks. In (a) comparison between a previous model of H in W from us Hodille *et al* [49] (reference (a)) and experimental from Frauenfelder [46] extrapolated at low temperature.(reference (b)). In (b) this model of hydrogen in copper in equilibrium with an ideal and a real gas phase of H_2 compared to experimental data from by Thomas [13] (reference (a)), McLellan [14] (reference (b)), Lieser and Witte [15] (reference (c)), Röntgen and Möller [16] (reference (d)), and Eichenauer and Pebler [47] (reference (e)).

Table 3. Comparison of solution energies of H in Cu and W perfect bulks in Oh and Td interstitial sites. The values are displayed in eV.

System	Site	$\Delta_s E_H$ (eV)	References
Cu^{bcc}_{per}	**Oh**	0.54	This study[a]
	Td	0.64	This study[a]
Cu^{fcc}_{per}	**Oh**	0.41	This study[a]
		0.41	Zhou *et al* [52]
		0.39	Eichenauer *et al* [53]
		0.44	Wenzl [54]
	Td	0.67	This study[a]
		0.64	Zhou *et al* [52]
W^{bcc}_{per}	**Oh**	1.50	This study[a]
		1.32	Ma *et al* [33]
		1.41	Louie *et al* [44]
	Td	1.06	This study[a]
		1.05	Ma *et al* [33]
		1.08	Louie *et al* [44]
		1.04	Frauenfelder [46]
		0.89	Zhou *et al* [55]

[a] Values considering the ZPE correction.

4. Discussion

Table 3 presents a summarized comparison of the solution energies for W and Cu bulks, alongside values from other studies.

First, we analyze the impact of the distortion in the Cu network on the hydrogen solution energy. Indeed the solution energy of H in copper depends on its crystallographic structure Cu^{bcc}_{per} or Cu^{fcc}_{per}. This can be understood through an analysis of H's nearest neighbors: in an Oh site of Cu^{fcc}_{per}, H has six nearest neighbors at a distance of 1.810 Å, whereas in Cu^{bcc}_{per} it has four a distance of 1.015 Å. Cu^{fcc}_{per} offers more space for accommodating H, and as a consequence, the solution energy is lower. Similarly and considering H in a Td site of Cu^{fcc}_{per}, it has four nearest neighbors at a distance of 1.567 Å, whereas in Cu^{bcc}_{per} it has four at a distance of 1.605 Å. In Cu^{bcc}_{per}, the closer proximity among nearest neighbors results in less space for accommodating H and in a higher solution energy.

The distortion of the copper structure as it occurs in the vicinity of the interface also impacts the solution energy of H. It has the effect of lifting the degeneracy of the Td and Oh sites concerning the solution energy. In particular, the Td-3

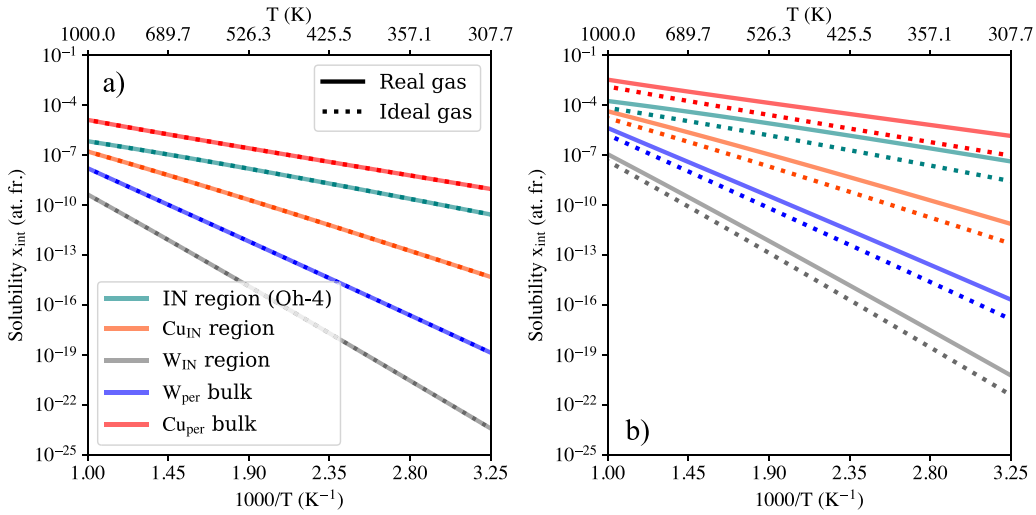

Figure 4. Comparison of the solubility of H at the interface $W^{bcc}(001)/Cu^{hcp}(11\bar{2}0)$ super-cell with those in the W and Cu bulks for (a) $P = 10^5$ Pa and (b) $P = 1$ GPa. With dotted and continuous lines, we plotted the result of the model assuming the H_2 reservoir as ideal and real gas respectively. The orange and red lines represent the solubility in the Cu_{IN} and Cu^{fcc}_{per} sections, respectively, where the number of interstitial sites per atom is $\gamma = 1$ for both. The gray and blue lines correspond to the solubility in the W_{IN} and W^{bcc}_{per} regions, respectively, where $\gamma = 6$. The teal line represents the solubility in the IN section where $\gamma = 1/2$.

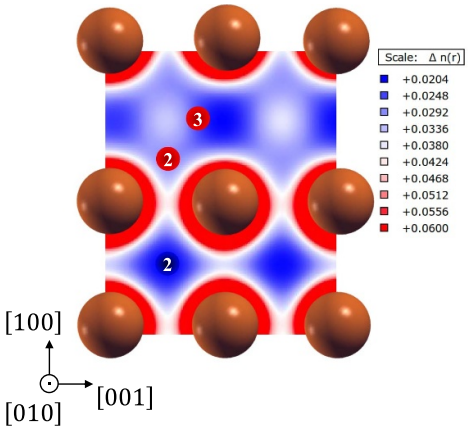

Figure 5. Charge density in the (020) plane of the Cu_{dis} bulk.

and Oh-2 sites as named in table 1 exhibit a very low solubility in Cu_{dis}. This can be understood in terms of charge density. The optimal electronic density to embed H is known by Pulska *et al* and is $n_0 = 0.0026$ a.u. ≈ 0.018 eÅ^{-3} [56]. In copper as in tungsten, the electronic density is still higher, and H finds the lowest embedding energy where the electron density is the lowest [57]. The Td-3 and Oh-2 sites belong to the (020) crystallographic plane of Cu_{dis}. In figure 5 the charge density is plotted in the (020) plane of the Cu_{dis}. Td-3 and Oh-2 lie in a region where the charge density is similar and low as compared to that of Td-2, which explains this difference in solution energy.

Regarding the full energy of hydrogen across the interface, the global picture is that the solution energy of H is comparable in Cu^{fcc}_{per} and Cu_{dis} while it is higher in the close vicinity of the interface. In tungsten, it follows the same trend and is lower in W^{bcc}_{per} than in the vicinity of the interface. In the plane of the interface, it has a similar value as in Cu^{fcc}_{per} at any P and T here considered. This region of high solubility for H is surrounded by regions of low solubility, making the full energies quite complex. However, from these results, it might be expected that the interface behaves like a sink for hydrogen, but an in-depth analysis to determine the kinetics of hydrogen across the W/Cu interface remains to be done. It will enable us to determine in which condition of pressure, temperature, flux, concentration and kinetic regime (steady-state, transient) hydrogen might segregate.

In figure 4(a), no difference between the solubility in ideal and real gas at $P = 10^5$ Pa is observed. This is expected because, at low pressures, real gases behave like ideal ones. At low pressures, the mean distance between molecules in the gas phase is much greater than the size of the individual molecules, allowing us to consider the molecules as point particles, essentially as an ideal gas. However, when pressure reaches values of GPa, as shown in figure 4(b), a clear difference is observed between the two. Figure 6 illustrates how the solubility at the plane of the W/Cu interface (IN section) changes as a function of temperature for different pressures: 10^5 Pa to 1 GPa. When examining regimes where pressure can exceed 100 MPa, the H_2 reservoir must be treated as a real gas because the ideal gas model does not accurately describe the reservoir's properties.

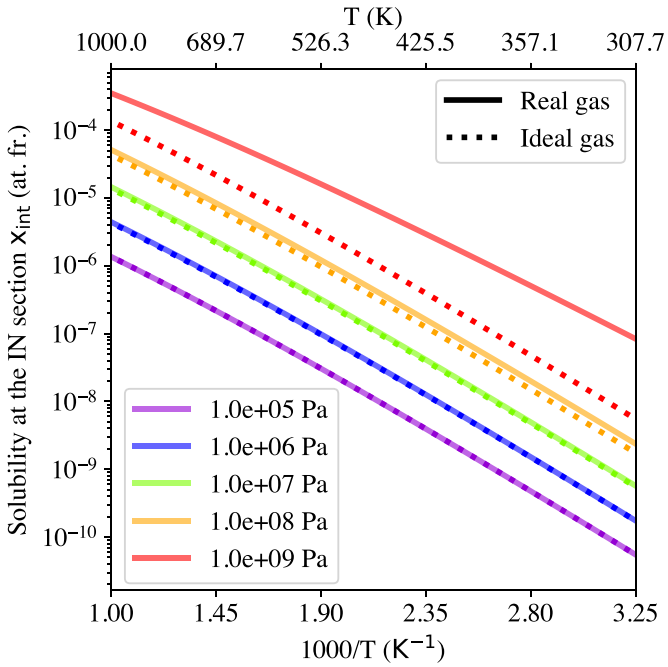

Figure 6. Solubility of H in the $W^{bcc}(001)/Cu^{hcp}(11\bar{2}0)$ at the IN section. With dotted and continuous lines, we plotted the result of the thermodynamic model assuming the H_2 as ideal and real gas respectively.

5. Conclusions

In this paper, we studied the solution and solubility of H at the $W^{bcc}(001)/Cu^{hcp}(11\bar{2}0)$ interface by using DFT and a thermodynamic model here defined. We determined the solution energy of H in two different interstitial sites: octahedral and tetrahedral; at different working cells: Cu^{bcc}_{per}, Cu^{fcc}_{per}, Cu_{dis}, $W^{bcc}(001)/Cu^{hcp}(11\bar{2}0)$, W_{dis}, and W^{bcc}_{per}. Phonon frequencies were computed to correct those values of energy considering the ZPE. It was found that in Cu^{bcc}_{per}, Cu^{fcc}_{per} bulks the most favorable interstitial sitesfor H atoms were the Oh positions, whereas in the W^{bcc}_{per} the Td sites were the most stable ones. In the case of the Cu_{dis} network was found that Oh-2 and Td-3 were the most stable ones, whereas in W_{dis} the Td sites keep being the most stable. To better analyze the behavior of the solution energy at the $W^{bcc}(001)/Cu^{hcp}(11\bar{2}0)$ super-cell, we split it into three sections: Cu_{IN}, IN, and W_{IN}. In the Cu_{IN} and IN sections we found that the Oh sites had a lower value of $\Delta_s E^{ZPE}_H$ on the contrary that in the W_{IN} section, where the Td sites were the most stable positions. The $\Delta_s E^{ZPE}_H$ and the phonon frequencies were used to build a thermodynamic model where the solubility of H was determined as a function of gas temperature. The thermodynamic model was validated against experimental results and it evidences an increment of the solubility of H at the IN section of the $W^{bcc}(001)/Cu^{hcp}(11\bar{2}0)$ super-cell. We conclude that the $W^{bcc}(001)/Cu^{hcp}(11\bar{2}0)$ could behave like a sink for H atoms, which remains to be further investigated based on kinetic modelings.

Data availability statement

All data that support the findings of this study are included within the article (and any supplementary files).

Acknowledgments

This work is supported by Région PACA. It has been carried out within the framework of the EUROfusion Consortium, funded by the European Union via the Euratom Research and Training Programme (Grant Agreement No 101052200 - EUROfusion). Views and opinions expressed are however those of the author(s) only and do not necessarily reflect those of the European Union or the European Commission. Neither the European Union nor the European Commission can be held responsible for them. The authors were granted access to the high-performance computing resources of IDRIS under Allocation No. A0120806612 made by Grand Equipement National de Calcul Intensif and to the Marconi Supercomputer at CINECA Super Computing Application and Innovation Department, Bologna, Italy.

Appendix A. Interstitial sites in Cu and W bulks

We represent the positions in which we determined $\Delta_s E_H$, ΔZPE, and $\Delta_s E^{ZPE}_H$ in every Cu and W working cell. In the supplementary information, we provided more details regarding these structures. In table A1 we show the Oh and Td sites in Cu bulks. The orange balls correspond with Cu atoms, and the blue and red points represent the Oh and Td sites, respectively. In table A2 we show the chosen Oh and Td sites in the case of W bulks.

Table A1. Positions in which $\Delta_s E_{\mathrm{H}}$, ΔZPE and $\Delta_s E_{\mathrm{H}}^{\mathrm{ZPE}}$ was determined in Cu bulks. Blue and red points correspond with Oh and Td positions respectively and the orange balls represent the Cu atoms. The images were made by the authors.

Cu_{per}^{bcc}	Cu_{per}^{fcc}	Cu_{dis}
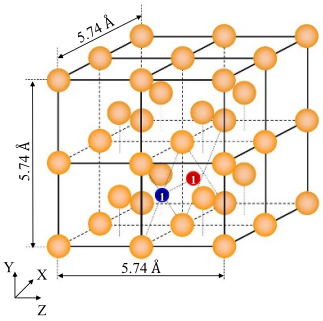	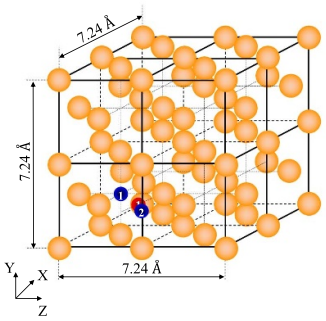	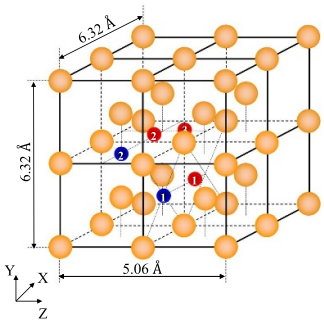
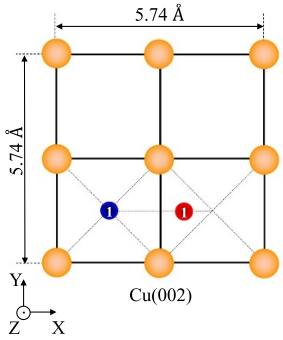	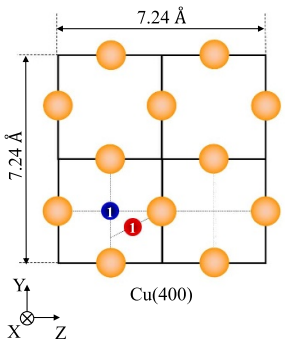	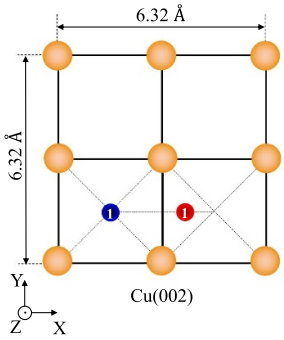
		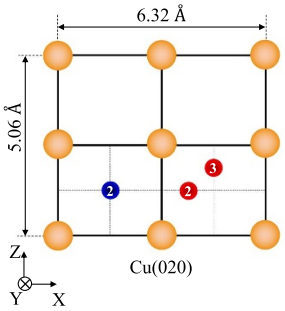

Table A2. Positions in which $\Delta_s E_{\mathrm{H}}$ was determined in Cu bulks. Blue and red points correspond with Oh and Td positions respectively and the orange balls represent the W atoms. The images were made by the authors.

$W_{\mathrm{per}}^{\mathrm{bcc}}$	W_{dis}
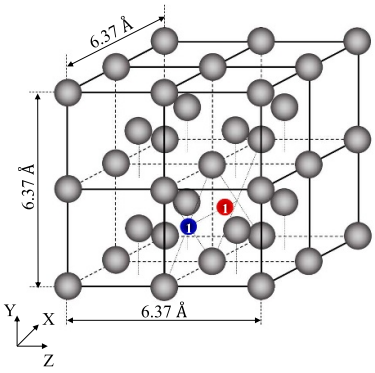	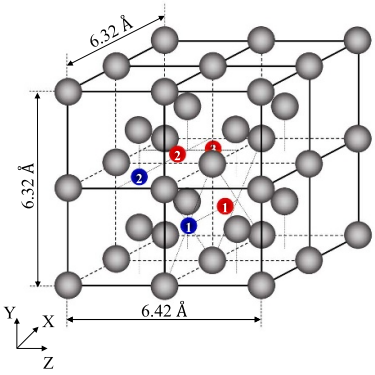
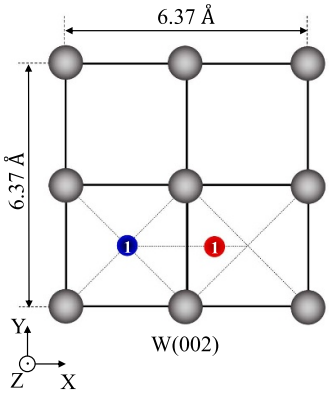	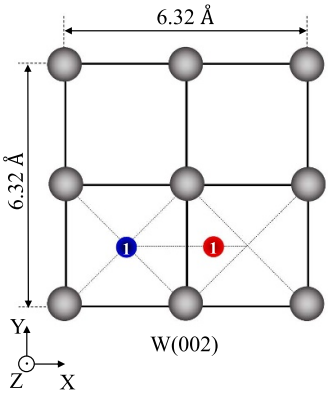
	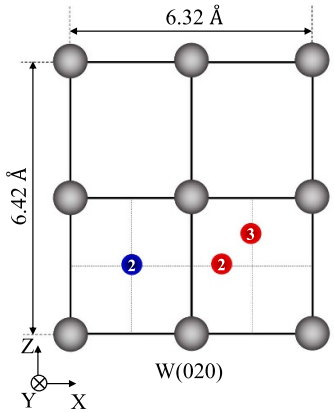

Appendix B. Vibrational frequencies of H at the $W^{bcc}(001)/Cu^{hcp}(11\bar{2}0)$ interface

We present the vibrational frequencies of H at the $W^{bcc}(001)/Cu^{hcp}(11\bar{2}0)$ super-cell. In table B1 we displayed the nine positions where the phonon calculations were computed. The phonon calculations were computed only at the Γ point. These points were chosen as samples because they represent the furthest and the closest Oh and TH, in the Cu_{IN} and W_{IN} regions, to the plane of the interface. And we chose three of the points with the lowest $\Delta_s E_H^{ZPE}$ value at the IN region. This allows us to determine if the variations of the vibrational frequencies have a significant repercussion in the Helmholtz free energy ($f_{vib} = e_{vib} - Ts_{vib}$). We determine the Helmholtz energy at the positions of the sample for a temperature of $T = 1000$ K, which delimits the validity range of our thermodynamical model.

As it is appreciable in table B1 the Helmholtz free energy values per section are very close to each other. In the case of the Oh positions in the Cu_{IN}, the difference between the values is 0.32% approximately, whereas between the Td points is 0.25% approximately. At the IN region all the Helmholtz free energies are the same and in the W_{IN} region the difference between the values is 1.01%. This evidence that the differences between the vibrational frequencies are negligible due to the variations that they represent in the vibrational energy are lower than 1.01%. Thus, it was not necessary to compute all the frequencies for the 29 final positions where the H atoms are placed at the $W^{bcc}(001)/Cu^{hcp}(11\bar{2}0)$. On the contrary, we will use the mean values of the frequencies displayed at the end of table B1.

Table B1. Vibrational frequencies at the $W^{bcc}(001)/Cu^{hcp}(11\bar{2}0)$ super-cell, the values are in THz units. Helmholtz free energy in eV units.

	Cu_{IN}				IN			W_{IN}	
	Oh-38	**Oh-42**	**Td-9**	**Td-17**	**Oh-4**	**Oh-44**	**Oh-45**	**Td-8**	**Td-27**
ν_1	68.227	67.799	68.018	68.680	64.139	64.187	64.801	58.051	58.367
ν_2	69.523	70.791	68.479	69.755	76.495	76.464	69.642	58.092	71.542
ν_3	119.402	90.936	115.962	92.263	94.942	94.943	96.948	103.316	182.061
f_{vib}	**−6.787**	**−6.809**	**−6.791**	**−6.808**	**−6.804**	**−6.804**	**−6.804**	**−6.829**	**−6.761**

Mean values of vibrational frequencies in THz

	OH	**TH**	**OH**	**TH**
ν_1	68.013	68.349	64.376	58.209
ν_2	70.157	69.117	74.200	64.817
ν_3	105.169	104.113	96.611	142.688

Appendix C. Solution energy of H at the $W^{bcc}(001)/Cu^{hcp}(11\bar{2}0)$ interface

Table C1. Values of the $\Delta_s E_H$, ΔZPE and $\Delta_s E_H^{ZPE}$ determined in the Td and Oh interstitial positions in the $W^{bcc}(001)/Cu^{hcp}(11\bar{2}0)$ super-cell. The initial and final columns represent the initial positions where the H atoms were placed and the final positions where they end after the geometry relaxation respectively (see figures 1(a) and (b)). The $\Delta_s E_H$ and $\Delta_s E_H^{ZPE}$ in bold represent the 53 final most stable positions. In orange, dark gray and teal colors, we highlighted all the positions that correspond to the Cu_{IN}, W_{IN} and IN groups, respectively. The non-highlighted values correspond to repeated positions.

Initial	Final	$\Delta_s E_H$	ΔZPE	$\Delta_s E_H^{ZPE}$	Initial	Final	$\Delta_s E_H$	ΔZPE	$\Delta_s E_H^{ZPE}$
Td-9	**Td-9**	**0.54**	0.365	**0.91**	**Oh-1**	**Td-9**	0.54	0.365	0.91
Td-10	**Oh-40**	0.34	0.369	0.71	**Oh-2**	**Oh-2**	**0.34**	0.369	**0.71**
Td-11	**Oh-2**	0.34	0.369	0.71	**Oh-3**	**Td-17**	1.12	0.365	1.49
Td-12	**Td-12**	**0.51**	0.365	**0.88**	**Oh-4**	**Oh-4**	**0.11**	0.350	**0.46**
Td-13	**Td-13**	**0.51**	0.365	**0.88**	**Oh-5**	**Td-25**	0.51	0.415	0.93
Td-14	**Oh-40**	0.34	0.369	0.71	**Oh-6**	**Td-27**	0.37	0.415	0.79
Td-15	**Oh-2**	0.34	0.369	0.71	**Oh-7**	**Td-33**	0.88	0.415	1.30
Td-16	**Oh-44**	0.11	0.350	0.46	**Oh-8**	**Td-8**	**0.90**	0.415	**1.32**
Td-17	**Td-17**	**0.62**	0.365	**0.99**	**Oh-38**	**Oh-38**	**0.37**	0.369	**0.74**
Td-18	**Oh-44**	0.11	0.350	0.46	**Oh-39**	**Oh-39**	**0.37**	0.369	**0.74**
Td-19	**Oh-4**	0.11	0.350	0.46	**Oh-40**	**Oh-40**	**0.34**	0.369	**0.71**
Td-20	**Oh-44**	0.11	0.350	0.46	**Oh-41**	**Td-13**	0.50	0.365	0.87
Td-21	**Oh-4**	0.11	0.350	0.46	**Oh-42**	**Oh-42**	**0.46**	0.369	**0.83**
Td-22	**Oh-44**	0.11	0.350	0.46	**Oh-43**	**Oh-43**	**0.46**	0.369	**0.83**
Td-23	**Oh-4**	0.11	0.350	0.46	**Oh-44**	**Oh-44**	**0.11**	0.350	**0.46**
Td-24	**Td-24**	**0.47**	0.350	**0.82**	**Oh-45**	**Oh-45**	**0.38**	0.350	**0.73**
Td-25	**Td-25**	**0.51**	0.350	**0.86**	**Oh-46**	**Td-26**	0.37	0.415	0.79
Td-26	**Td-26**	**0.37**	0.415	**0.79**	**Oh-47**	**Td-27**	0.37	0.415	0.79
Td-27	**Td-27**	**0.37**	0.415	**0.79**	**Oh-48**	**Td-26**	0.37	0.415	0.79
Td-28	**Td-28**	**0.69**	0.415	**1.11**	**Oh-49**	**Td-29**	0.69	0.415	1.11
Td-29	**Td-29**	**0.69**	0.415	**1.11**	**Oh-50**	**Td-30**	0.89	0.415	1.31
Td-30	**Td-30**	**0.89**	0.415	**1.31**	**Oh-51**	**Td-31**	0.90	0.415	1.32
Td-31	**Td-31**	**0.90**	0.415	**1.32**	**Oh-52**	**Td-52**	**0.90**	0.415	**1.32**
Td-32	**Td-32**	**0.88**	0.415	**1.30**	**Oh-53**	**Td-37**	0.90	0.415	1.32
Td-33	**Td-33**	**0.88**	0.415	**1.30**	**Oh-54**	**Oh-54**	**0.37**	0.369	**0.74**
Td-34	**Td-34**	**0.89**	0.415	**1.31**	**Oh-55**	**Oh-55**	**0.36**	0.369	**0.73**
Td-35	**Td-35**	**0.91**	0.415	**1.33**	**Oh-56**	**Td-56**	**0.47**	0.365	**0.84**
Td-36	**Td-36**	**0.90**	0.415	**1.32**	**Oh-57**	**Oh-54**	0.37	0.369	0.74
Td-37	**Td-37**	**0.91**	0.415	**1.33**	**Oh-58**	**Td-58**	**0.47**	0.365	**0.84**
Td-76	**Oh-54**	0.37	0.369	0.74	**Oh-59**	**Oh-59**	**0.33**	0.369	**0.70**
Td-77	**Td-77**	**0.51**	0.365	**0.88**	**Oh-60**	**Oh-60**	**0.46**	0.369	**0.83**
Td-78	**Oh-60**	0.46	0.369	0.83	**Oh-61**	**Oh-61**	**0.42**	0.369	**0.79**
Td-79	**Td-79**	**0.51**	0.365	**0.88**	**Oh-62**	**Oh-62**	**0.12**	0.350	**0.47**
Td-80	**Oh-60**	0.46	0.369	0.83	**Oh-63**	**Oh-63**	**0.37**	0.350	**0.72**
Td-81	**Td-81**	**0.38**	0.350	**0.73**	**Oh-64**	**Oh-62**	0.12	0.350	0.47
Td-82	**Oh-63**	0.37	0.350	0.72	**Oh-65**	**Oh-65**	**0.11**	0.350	**0.46**
Td-83	**Td-83**	**0.38**	0.350	**0.73**	**Oh-66**	**Oh-4**	0.11	0.350	0.46
Td-84	**Td-84**	**0.37**	0.415	**0.79**	**Oh-67**	**Td-84**	0.37	0.415	0.79
Td-85	**Td-85**	**0.69**	0.415	**1.11**	**Oh-68**	**Td-94**	0.36	0.415	0.78
Td-86	**Td-86**	**0.89**	0.415	**1.31**	**Oh-69**	**Td-87**	0.69	0.415	1.11
Td-87	**Td-87**	**0.69**	0.415	**1.11**	**Oh-70**	**Td-84**	0.37	0.415	0.79
Td-88	**Oh-60**	0.46	0.369	0.83	**Oh-71**	**Td-85**	0.69	0.415	1.11
Td-89	**Td-89**	**0.50**	0.350	**0.85**	**Oh-72**	**Td-94**	0.36	0.415	0.78
Td-90	**Oh-61**	0.42	0.369	0.79	**Oh-73**	**Td-73**	**0.69**	0.415	**1.11**
Td-91	**Oh-65**	0.11	0.350	0.46	**Oh-74**	**Td-86**	0.88	0.415	1.30
Td-92	**Oh-65**	0.11	0.350	0.46	**Oh-75**	**Td-75**	**0.88**	0.415	**1.30**
Td-93	**Td-93**	**0.47**	0.350	**0.82**					
Td-94	**Td-94**	**0.36**	0.415	**0.78**					
Td-95	**Oh-4**	0.12	0.350	0.47					
Td-96	**Td-96**	**0.89**	0.415	**1.31**					

ORCID iDs

Y Silva-Solís https://orcid.org/0000-0002-1047-4627
J Denis https://orcid.org/0000-0002-1478-0269
E A Hodille https://orcid.org/0000-0002-0859-390X
Y Ferro https://orcid.org/0000-0002-3178-937X

References

[1] Wen S P, Zong R L, Zeng F, Gao Y and Pan F 2007 Evaluating modulus and hardness enhancement in evaporated Cu/W multilayers *Acta Mater.* **55** 345–51
[2] Monclús M, Karlik M, Callisti M, Frutos E, LLorca J, Polcar T and Molina-Aldareguía J M 2014 Microstructure and mechanical properties of physical vapor deposited Cu/W nanoscale multilayers: influence of layer thickness and temperature *Thin Solid Films* **571** 275–82
[3] Hirai T *et al* 2016 Use of tungsten material for the ITER divertor *Nucl. Mater. Energy* **9** 612–22
[4] Richou M *et al* 2016 The WEST project: validation program for WEST tungsten coated plasma facing components *Phys. Scr.* **2016** 014029
[5] Wesson J, Campbell D J, Connor J W, Gill R D, Hugill J and Lashmore-Davies C N 2011 *Tokamaks* 4th edn (Oxford University Press)
[6] Perrault D 2016 Safety issues to be taken into account in designing future nuclear fusion facilities *Fusion Eng. Des.* **109** 1733–8
[7] Hodille E A, Bernard E, Markelj S, Mougenot J, Becquart C S, Bisson R and Grisolia C 2017 Estimation of the tritium retention in ITER tungsten divertor target using macroscopic rate equations simulations *Phys. Scr.* **170** 14033–40
[8] Hodille E A *et al* 2021 Modelling of hydrogen isotopes trapping, diffusion and permeation in divertor monoblocks under ITER-like conditions *Nucl. Fusion* **61** 126003–17
[9] Zibrov M and Schmid K 2022 Reaction–diffusion simulations of hydrogen isotope trapping and release from cavities in tungsten, I: single cavity *Nucl. Fusion* **30** 101121–32
[10] Piazza Z A, Kolasinski R D, Ajmalghan M, Hodille E A and Ferro Y 2021 Predictive atomistic model for hydrogen adsorption on metal surfaces: comparison with low-energy ion beam analysis on tungsten *J. Phys. Chem.* C **125** 16086–96
[11] Holzner G, Schwarz-Selinger T, Dürbeck T and von Toussaint U 2020 Solute diffusion of hydrogen isotopes in tungsten—a gas loading experiment *Phys. Scr.* **2020** 014034–43
[12] Magnusson H and Frisk K 2017 Diffusion, permeation and solubility of hydrogen in copper *J. Phase Equilib. Diffus.* **38** 65–69
[13] Thomas C L 1967 Solubility of hydrogen in solid copper silver and gold obtained by a rapid quench and extraction technique *Trans. Metall. Soc. AIME* **239** 485
[14] McLellan R B 1973 Solid solutions of hydrogen in gold, silver and copper *J. Phys. Chem. Solids* **34** 1137–41
[15] Lieser K H and Witte H 1954 Solubility of hydrogen in alloys i, measuring method and examination of systems mgcu2-mgzn2 and mgni2-mgzn2 *Z. Phys. Chem.(Leipzig)* **202** 321
[16] Röntgen P and Möller F 1934 The solubility of gases in copper and aluminum *Metallwirtschaft* **13** 81–83
[17] Delaporte-Mathurin R, Hodille E A, Mougenot J, Charles Y and De Temmerman G 2021 Leblond F and Grisolia C Influence of interface conditions on hydrogen transport studies *Nucl. Fusion* **61** 036038
[18] Delaporte-Mathurin R, Hodille E, Mougenot J, De Temmerman G, Charles Y and Grisolia C 2020 Parametric study of hydrogenic inventory in the ITER divertor based on machine learning *Sci. Rep.* **10** 17798
[19] Bauer E, Poppa H, Todd G and Bonczek F 2003 Adsorption and condensation of Cu on W single crystal surfaces *J. Appl. Phys.* **45** 5164–75
[20] Cetronio A, Jones J P and Roberts E W 1975 A study of copper adsorption on (100) tungsten by high field microscopy *Surf. Sci.* **52** 473–88
[21] Melmed A J 1965 Adsorption and surface diffusion of copper on tungsten *J. Chem. Phys.* **43** 3057–62
[22] Taylor N J 1966 A leed study of the epitaxial growth of copper on the (110) surface of tungsten *Surf. Sci.* **4** 161–94
[23] Moss A R L and Blott B H 1969 The epitaxial growth of copper on the (110) surface of a tungsten single crystal studied by leed, auger electron and work function techniques *Surf. Sci.* **17** 240–61
[24] Luo E Z, Cai Q, Chung W F, Orr B G and Altman M S 1996 Competing desorption pathways during epitaxial growth: leem investigation of Cu/W (110) heteroepitaxy *Phys. Rev.* B **54** 14673
[25] Wormeester H, Hüger E and Bauer E 1996 hcp and bcc cu and Pd films *Phys. Rev. Lett.* **77** 1540
[26] Wormeester H, Kiene M E, Hüger E and Bauer E 1997 Growth of hcp Cu on W (100) *Surf. Sci.* **377** 988–91
[27] Reshöft K, Jensen C and Köhler U 1999 Atomistics of the epitaxial growth of Cu on W (110) *Surf. Sci.* **421** 320–36
[28] Girault B, Villain P, Le Bourhis E, Goudeau P and Renault P O 2006 X-ray diffraction analysis of the structure and residual stresses of W/Cu multilayers *Surf. Coat. Technol.* **201** 4372–6
[29] Girault B, Eyidi D, Chauveau T, Babonneau D, Renault P O, Le Bourhis E and Goudeau P 2011 Copper coverage effect on tungsten crystallites texture development in W/Cu nanocomposite thin films *J. Appl. Phys.* **109** 014305
[30] Bollmann T R J, van Gastel R, Wormeester H, Zandvliet H J W and Poelsema B 2012 Growth and decay of hcp-like cu hut-shaped structures on w(100) *Phys. Rev.* B **85** 125417
[31] Hohenberg P and Kohn W 1964 Inhomogeneous electron gas *Phys. Rev.* **136** B864–71
[32] Liang C P, Fan J L, Gong H R, Liao X, Zhu X and Peng S 2013 Interface structure and work function of W-Cu interfaces *Appl. Phys. Lett.* **103** 211604
[33] Ma G C, Fan J L and Gong H R 2017 Fundamental effects of hydrogen on cohesion properties of Cu/W interfaces *Solid State Commun.* **250** 79–83
[34] Wang J W, Fan J L and Gong H R 2016 Effects of Zr alloying on cohesion properties of Cu/W interfaces *J. Alloys Compd.* **661** 553–6
[35] Bodlos R, Fotopoulos V, Spitaler J, Shluger A L and Romaner L 2022 Energies and structures of cu/nb and Cu/W interfaces from density functional theory and semi-empirical calculations *Materialia* **21** 101362
[36] Yang Q, Lu C, Han Y, Chen X, Yang J, Huang J, Chen S and Ye Z 2022 Influence of Cu/W interfacial structure on the resistance against harmful helium atoms: a mechanism analysis *J. Alloy Compd.* **903** 163817
[37] Silva-Solís Y, Denis J, Hodille E A and Ferro Y 2023 A model of the W/Cu interface in the ITER cooling monoblocks from density functional theory *Nucl. Mater. Energy* **37** 101516
[38] Giannozzi P *et al* 2017 Advanced capabilities for materials modelling with quantum espresso *J. Phys.: Condens. Matter* **29** 465901
[39] Born M and Von Karman T 1912 Über schwingungen in raumgittern *Phys.* Z **13** 297–309
[40] Vanderbilt D 1990 Soft self-consistent pseudopotentials in a generalized eigenvalue formalism *Phys. Rev.* B **41** 7892

[41] Louie S G, Froyen S and Cohen M L 1982 Nonlinear ionic pseudopotentials in spin-density-functional calculations *Phys. Rev.* B **26** 1738–42
[42] Perdew J P, Burke K and Ernzerhof M 1996 Generalized gradient approximation made simple *Phys. Rev. Lett.* **77** 3865–8
[43] Marzari N, Vanderbilt D, Vita A D and Payne M C 1999 Thermal contraction and disordering of the Al(110) surface *Phys. Rev. Lett.* **82** 3296–9
[44] Fernandez N, Ferro Y and Kato D 2015 Hydrogen diffusion and vacancies formation in tungsten: density functional theory calculations and statistical models *Acta Mater.* **94** 307–18
[45] Tkacz M and Litwiniuk A 2002 Useful equations of state of hydrogen and deuterium *J. Alloys Compd.* **330** 89–92
[46] Frauenfelder R 1969 Solution and diffusion of hydrogen in tungsten *J. Vac. Sci. Technol.* **6** 388–97
[47] Eichenauer W and Pebler A 1957 Messung des diffusionskoeffizienten und der löslichkeit von wasserstoff in aluminium und kupfer *Int. J. Mater. Res.* **48** 373–8
[48] Glensk A, Grabowski B, Hickel T and Neugebauer J 2014 Breakdown of the arrhenius law in describing vacancy formation energies: the importance of local anharmonicity revealed by ab initio thermodynamics *Phys. Rev.* X **4** 011018
[49] Hodille E A, Fernandez N, Piazza Z A, Ajmalghan M and Ferro Y 2018 Hydrogen supersaturated layers in H/D plasma-loaded tungsten: a global model based on thermodynamics, kinetics and density functional theory data *Phys. Rev. Mater.* **2** 093802
[50] Huber K P 2013 *Molecular Spectra and Molecular Structure: IV. Constants of Diatomic Molecules* (Springer)
[51] Heinola K and Ahlgren T 2010 Diffusion of hydrogen in BCC tungsten studied with first principle calculations *J. Appl. Phys.* **107** 113531
[52] Zhou H B, Zhang Y and Ou X 2013 Dissolution and diffusion behaviors of hydrogen in copper: a first-principles investigation *Comput. Mater. Sci.* **79** 923–8
[53] Eichenauer W, Löser W and Witte H 1965 Löslichkeit und diffusionsgeschwindigkeit von wasserstoff und deuterium in einkristallen aus nickel und kupfer *Int. J. Mater. Res.* **56** 287–93
[54] Wenzl H 1982 Properties and applications of metal hydrides in energy conversion systems *Int. Met. Rev.* **27** 140–68
[55] Zhou H B, Liu Y L, Jin S, Zhang Y, Luo G N and Lu G H 2010 Investigating behaviours of hydrogen in a tungsten grain boundary by first principles: from dissolution and diffusion to a trapping mechanism *Nucl. Fusion* **50** 025016
[56] Puska M J, Nieminen R M and Manninen M 1981 Atoms embedded in an electron gas: immersion energies *Phys. Rev.* B **24** 3037
[57] Liu Y L, Zhang Y, Zhou H B, Lu G H, Liu F and Luo G N 2009 Vacancy trapping mechanism for hydrogen bubble formation in metal *Phys. Rev.* B **79** 172103

Chapter 5

Diffusion of H at the W/Cu interface

In the preceding chapter, we identified the most stable interstitial sites for H atoms at the W/Cu interface. These findings were used to investigate the diffusion of H, which constitutes the primary goal of this chapter. The diffusion of H at the W/Cu interface is examined through two different methods. Along the plane of the interface, diffusivity is evaluated using the well-established Fick's law, whereas perpendicular to the interface, diffusion is characterized using a kinetic model based on the Macroscopic Rate Equation (MRE) theory. Similar to the prior chapter, diffusion in perfect W and Cu bulks were determined as reference values. The first section presents the two methodologies employed to study H diffusion at the W/Cu interface. The chapter concludes with the corresponding paper for this section submitted to *Nuclear Fusion*.

5.1 Presentation of the study

Several atomic mechanisms contribute to the diffusion of atoms within a lattice. The primary mechanisms are the *vacancy mechanism* and the *direct interstitial mechanism*. In addition to these, there are less common but significant mechanisms, particularly observed in semiconductors, such as the *indirect interstitial mechanism* for self-interstitial atoms, *kick-out mechanism* for impurity atoms, and the *Frank-Turnbull* also known as *dissociative mechanism* [144]. In this chapter, our focus is on studying the direct interstitial mechanism, where H atoms serve as the interstitial species diffusing within a perfect lattice, including the W/Cu interface as well as the W and Cu bulks, devoid of vacancies. In the subsequent sections, we will outline the models developed to characterize the diffusion of H at the W/Cu interface.

Numerous investigations have delved into the diffusion of HIs in W and Cu bulks independently [73, 115, 116, 145–152]. In 1968, R. Frauenfelder [145] conducted degassing experiments to investigate the solution and diffusion of H in W. Employing mass spectroscopic and ultrahigh vacuum techniques, the experiments spanned a pressure range of 600 to 10^{-8} Torr and temperatures from 1100 to 2400 K. The resulting diffusion coefficient was expressed as $D(T) = 4.1 \times 10^{-7} \exp\left(-\frac{0.39 \text{ eV}}{k_B T}\right)$ [m^2/s]. Subsequently, Zakharov et al. [146] reported a diffusion coefficient of $D(T) = (6 \pm 2) \times 10^{-4} \exp\left(-\frac{1.07 \pm 0.09 \text{ eV}}{k_B T}\right)$ [m^2/s] at lower temperatures ($400 - 1200$°C) and pressures

$(1 - 200$ torr). The discrepancy between these measurements is attributed to increased defect interaction within the tungsten bulk at temperatures below 1500 K [147, 153]. Benamati et al. [147] employed the time-dependent permeation method and obtained diffusion coefficients similar to those of Zakharov et al. [146], with experiments conducted in the temperature range $673 - 873$ K and pressure range $10 - 100$ kPa. In a more recent study in 2020, Holzner et al. [148] reported a diffusion coefficient of $D(T) = 1.60 \times 10^{-7} \exp\left(-\frac{0.28 \pm 0.06 \text{ eV}}{k_B T}\right)$ [m^2/s] using gas loading experiments performed in both polycrystalline and single-crystalline tungsten, at a pressure of 500 mbar and temperatures ranging from $1600 - 2600$ K.

Theoretical investigations conducted on perfect W bulk have supported the diffusion values obtained by Frauenfelder at high temperatures [145] and Holzner et al. [148]. Heinola and Ahlgren [115], employing DFT calculations in conjunction with the harmonic Transition State Theory (hTST) [154], determined the diffusion coefficient of H atoms in perfect W bulk, yielding a value of $D(T) = 0.52 \times 10^{-7} \exp\left(-\frac{0.21 \text{ eV}}{k_B T}\right)$ [m^2/s]. These values of activation energy and pre-exponential factor were consistent with the numerical fit applied to Frauenfelder's data [145] at temperatures above 1500 K [115]. Similarly, Fernandez et al. [116] obtained similar values using a model combining DFT with statistical methods employing hTST and thermodynamics. They obtained a diffusion constant of $D(T) = 1.93 \times 10^{-7} \exp\left(-\frac{0.20 \text{ eV}}{k_B T}\right)$ [m^2/s], which also correlated with the high-temperature fit to Frauenfelder's data [145].

Experimental investigations conducted in Cu exhibit a higher level of agreement compared to those carried out in W. In 1965, Eichenauer et al. [149] examined the solubility and diffusion of H and D in nickel (Ni) and Cu single crystals, evaluating the rate of sample degassing at thermal equilibrium. This study, conducted at elevated temperatures, yielded a diffusion constant of $D(T) = 11.5 \times 10^{-7} \exp\left(-\frac{0.42 \text{ eV}}{k_B T}\right)$ [m^2/s]. Similarly, Katz et al. [150] obtained comparable results six years later using the same methodology as Eichenauer et al. [149], determining the diffusion constant of HIs, including T, in Ni and Cu crystals. Their measurements in Cu, conducted in a temperature range of $450 - 925$°C, yielded a diffusion rate of $D(T) = 11.3 \times 10^{-7} \exp\left(-\frac{0.41 \text{ eV}}{k_B T}\right)$ [m^2/s]. Low-temperature experiments in Cu were conducted by Sakamoto and Takao [151] in 1982, followed by Ishikawa and McLellan [152] in 1985. Sakamoto and Takao [151] assessed H solubility and diffusion in annealed and cold-rolled Cu at room temperature using the electrochemical permeation method with galvanostatic charging of Cu. They reported an H diffusivity in Cu of $D(T) = (3.69 \pm 0.64) \times 10^{-7} \exp\left(-\frac{0.38 \pm 0.01 \text{ eV}}{k_B T}\right)$ [m^2/s]. The diffusivity of cold-rolled Cu was lower and with slightly higher activation energy barriers than annealed Cu. Ishikawa and McLellan [152] employed an electrochemical technique called the "pulse method", introducing a "peak" of H concentration into the sample with a cathodic current pulse to observe diffusion of H through the bulk sample. They used both coated (with a thin layer of palladium) and uncoated Cu films to address surface corrosion effects caused by the current pulse. They reported a fit for their diffusivity data of $D(T) = 21.1 \times 10^{-7} \exp\left(-\frac{0.46 \text{ eV}}{k_B T}\right)$ [m^2/s].

Zhou et al. [73] investigated the dissolution and diffusion of H atoms in a perfect Cu^{fcc} bulk using DFT. They calculated the activation barrier for H diffusion on the $(\bar{1}10)$ plane between two octahedral sites, considering two different paths. The first path involved passing through a tetrahedral site (Td), while the second path went directly between two octahedral sites (Oh). The activation barriers they found were 0.23 eV and 0.58 eV for the Oh-Td-Oh and Oh-Oh paths, respectively. These results enabled them to determine

a diffusion coefficient of $D(T) = 1.74 \times 10^{-7} \exp\left(-\frac{0.23}{k_B T}\right)$ [m^2/s].

Despite the considerable research conducted on W and Cu, further investigation is essential to gain a comprehensive understanding of the mechanisms occurring at the interface between these two materials. This objective constitutes the central focus of our current study. We applied the Wert and Zener theory [154] to ascertain the diffusion coefficient of H atoms parallel to the plane of the W/Cu interface. Concurrently, we developed a 0-dimensional kinetic model to explore diffusion perpendicular to this plane. Given the limited availability of information on H diffusion at the W/Cu interface in existing literature, we juxtapose our findings with other experimental and theoretical studies conducted on W and Cu bulks.

5.1.1 Diffusion parallel to the plane of the interface

All of the above mentioned diffusion mechanisms are thermally driven process and their respective diffusion constants can be obtained from the Arrhenius equation [155]:

$$D = D_0 \exp\left(-\frac{E_a}{k_B T}\right), \tag{5.1}$$

where D_0 is the pre-exponential factor, which is a temperature independent term and E_a is the activation energy for the atomic jump mechanism. This term is commonly employed by both theorists and experimentalists to describe diffusion mechanisms in materials. Experimentalists measure D at various temperatures and then use expression (5.1) to fit their results, optimizing the parameters D_0 and E_a. In contrast, theorists determine D_0 and E_a, allowing them to ascertain how D changes with temperature T.

In this study, the E_a were determined using the well-known Nudged Elastic Band (NEB) method [156, 157] implemented in the open-source code Quantum Espresso [137], while D_0 was estimated using the Wert and Zener theory [154]. The numerical parameters used for the NEB calculations can be found in the Methodology part of the paper in the next section. Subsequently, we will delve into a discussion of the Wert and Zener theory and explain how the diffusion coefficient was determined parallel to the plane of the W/Cu interface.

Wert and Zener [154] based on the absolute rate theory [158] proposed an expression to determine the pre-exponential factor of the Arrhenius law for the diffusion of interstitial solute atoms in metals as follows:

$$D_0 = n\alpha a^2 \nu_0. \tag{5.2}$$

Where n is the number of nearest neighbor interstitial positions in the bulk, i.e. the number of paths by which the interstitial atom can move, α is a numerical parameter that depends upon the location of the interstitial position within the bulk, a is the lattice constant, and ν_0 is the vibrational frequency of the solute atom in an interstitial position. Wert and Zener [154] introduced an expression for ν_0 under the assumption that the solute atom transitions between interstitial sites within a potential surface characterized by a

sinusoidal variation in potential energy given by the following expression:

$$V(x) = \frac{1}{2}E_a\left(1 - \cos\frac{2\pi x}{\lambda}\right). \tag{5.3}$$

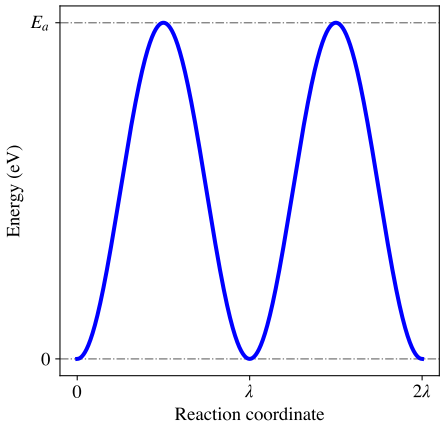

FIGURE 5.1. Potential energy along the diffusion path between two interstitial sites assumed by Wert and Zener [154].

From such a potential expression, which is represented in Figure 5.1, the following expression is obtained for the vibration frequency:

$$\nu_0 = \sqrt{\frac{E_a}{2m\lambda^2}}. \tag{5.4}$$

The values of the parameter α for a fcc and bcc lattices are reported in reference [154], while Hodille et al. [159] determined it for a wurtzite lattice. For the diffusion of H atoms in perfect W and Cu bulks, we used the respective α parameters reported in reference [154]. However, considering the particular diffusion of H atoms in the plane of the W/Cu interface, we determined the α parameter, which is presented in the following.

Based on the results of the previous chapter, the diffusion of H atoms at the plane of the W/Cu interface can be assumed jumping from Oh-4 to Oh-62 and their equivalents since they have the lowest value of solution energy [160]. Both of them have a value of 0.46 eV and 0.47 eV, thus we can consider them to be energetically equivalents. Consequently, planar diffusion of H will occur through these sites. Such a plane is represented in Figure 5.2, where the green squares denote the (2×2) unit cell surface of the W/Cu interface, and the grey lines denote the images of this unit cell under periodic boundary conditions. The blue and red points represent the Oh and Td positions that lie on this plane, and the orange balls are the Cu atoms in the unit cell, whereas the light-orange ones correspond to their respective images.

Let us call the concentration of the diffusing species at position (i, j), $\mathrm{C}_{i,j}$. Since there are 4 nearest neighbors (see Figure 5.2), there are $\frac{1}{4}$ chance to increase the concentration $\mathrm{C}_{i,j}$ from the particles in a neighboring site of (i, j). Thus the growth rate of $\mathrm{C}_{i,j}$ is:

$$\frac{\mathrm{dC}_{i,j}}{\mathrm{dt}} = \left[\begin{array}{l}\left(\frac{1}{4}\mathrm{C}_{i-1,j} - \frac{2}{4}\mathrm{C}_{i,j} + \frac{1}{4}\mathrm{C}_{i+1,j}\right) + \\ \left(\frac{1}{4}\mathrm{C}_{i,j-1} - \frac{2}{4}\mathrm{C}_{i,j} + \frac{1}{4}\mathrm{C}_{i,j+1}\right)\end{array}\right] p_0\nu_0 \exp\left(-\frac{E_a}{k_BT}\right), \tag{5.5}$$

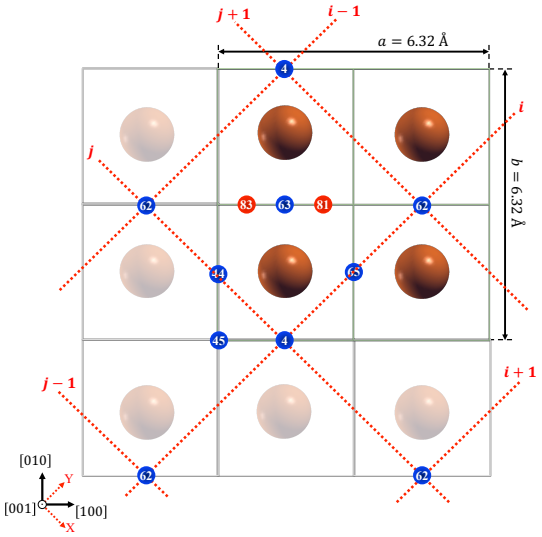

FIGURE 5.2. Nearest interstitial sites at the plane of the W/Cu interface.

where $p_0 = 4$ is the probability factor (or the number of equivalent paths to reach another interstitial site), ν_0 is the vibrational frequency which is determined using equation (5.4), E_a, k_B and T were already presented in the above expressions. The term between the brackets can be understood as the discretization of the second derivative along the X and Y directions in Cartesian coordinates:

$$\left.\frac{\partial^2 \mathrm{C}}{\partial x^2}\right|_{i,j} = \frac{\mathrm{C}_{i-1,j} - 2\mathrm{C}_{i,j} + \mathrm{C}_{i+1,j}}{\Delta x^2}, \tag{5.6a}$$

$$\left.\frac{\partial^2 \mathrm{C}}{\partial y^2}\right|_{i,j} = \frac{\mathrm{C}_{i,j-1} - 2\mathrm{C}_{i,j} + \mathrm{C}_{i,j+1}}{\Delta y^2}. \tag{5.6b}$$

Thus, expression (5.5) reduces to:

$$\frac{\mathrm{dC}_{i,j}}{\mathrm{dt}} = \left[\frac{1}{4}\left.\frac{\partial^2 \mathrm{C}}{\partial x^2}\right|_{i,j} \Delta x^2 + \frac{1}{4}\left.\frac{\partial^2 \mathrm{C}}{\partial y^2}\right|_{i,j} \Delta y^2\right] p_0 \nu_0 \exp\left(-\frac{E_a}{k_B T}\right). \tag{5.7}$$

As $\Delta x = \Delta y = \lambda$, being λ the distance between two interstitial sites, we obtain that:

$$\frac{\mathrm{dC}_{i,j}}{\mathrm{dt}} = \frac{p_0 \nu_0 \lambda^2}{4} \exp\left(-\frac{E_a}{k_B T}\right)\left[\left.\frac{\partial^2 \mathrm{C}}{\partial x^2}\right|_{i,j} + \left.\frac{\partial^2 \mathrm{C}}{\partial y^2}\right|_{i,j}\right], \tag{5.8}$$

which considering Fick's law leads to the following expression for the diffusion coefficient:

$$D = \frac{p_0 \nu_0 \lambda^2}{4} \exp\left(-\frac{E_a}{k_B T}\right). \tag{5.9}$$

Which, considering the Arrhenius law results in the following pre-exponential factor:

$$D_0 = \frac{p_0 \nu_0 \lambda^2}{4} = \nu_0 \lambda^2. \tag{5.10}$$

As D_0 can be related to the dimensionality of the diffusion process by [144]:

$$D_0 = \frac{n}{2d} \nu_0 \lambda^2, \tag{5.11}$$

it can be confirmed that, in this case, the number of nearest neighbors is $n = 4$ and the dimensionality of the motion is $d = 2$. Considering that in this case $\lambda = a/\sqrt{2}$ and $n = 4$, expression (5.2) can be transform in (5.10) only if $\alpha = 1/8$.

5.1.2 Diffusion perpendicular to the interface

To study the diffusion of H atoms through the W/Cu interface, we developed a kinetic model based on MRE theory. Such a model constitutes an extension of the framework established by Hodille et al. [20] and in Appendix A of reference [44]. Within the Methodology section of the paper in the following section, we provide comprehensive details regarding the factors considered in our model, along with the equation governing flux balance. In summary, the MRE model comprises N trapping/detrapping equations governing the evolution of H concentration at position i, being N the number of interstitial sites considered along the path.

As will be discussed later in the paper, three diffusion paths were examined, each identified by distinct colors: green, pink, and blue (see Figure 1 of the paper). Since H atoms are expected to migrate from the W network to the Cu network, our model considers diffusion in this direction. Consequently, the green path traverses the following interstitial sites: Td-8 → Td-37 → Td-35 → Td-33 → Td-31 → Td-29 → Td-27 → Td-25 → Oh-4 → Oh-43 → Oh-2 → Oh-39, primarily situated in the (001) plane. The pink path predominantly lies in the (002) crystallographic plane and includes the sites Td-86 → Td-87 → Td-84 → Td-89 → Oh-63 → Oh-60 → Td-79 → Oh-54. Meanwhile, the blue path serves as a connection between the green and pink paths, comprising the sites Td-25, Td-24, and Td-89.

Initially, we constructed the kinetic model solely for the green and pink paths, excluding the blue path. Equations (5.12) and (5.13) denote the flux balance for the green and pink paths, respectively. In the green path, we omitted the positions Td-8, Td-37, Td-35, and Td-33 due to their similar activation barriers, as they reside deep within the W_{IN} region. This omission was made to streamline the equation-solving process by reducing the number of equations involved.

$$
\begin{cases}
\dfrac{dC_{29}}{dt} = \nu_{27\to29}C_{27}(1-\theta_{29}) - \nu_{29\to27}C_{29}(1-\theta_{27}) + \nu_{31\to29}C_{31}(1-\theta_{29})\lambda_{31} - \nu_{29\to31}C_{29} \\
\dfrac{dC_{27}}{dt} = \nu_{25\to27}C_{25}(1-\theta_{27}) - \nu_{27\to25}C_{27}(1-\theta_{25}) + \nu_{29\to27}C_{29}(1-\theta_{27}) - \nu_{27\to29}C_{27}(1-\theta_{29}) \\
\dfrac{dC_{25}}{dt} = \nu_{4\to25}C_{4}(1-\theta_{25}) - \nu_{25\to4}C_{25}(1-\theta_{4}) + \nu_{27\to25}C_{27}(1-\theta_{25}) - \nu_{25\to27}C_{25}(1-\theta_{27}) \\
\dfrac{dC_{4}}{dt} = \nu_{43\to4}C_{43}(1-\theta_{4}) - \nu_{4\to43}C_{4}(1-\theta_{43}) + \nu_{25\to4}C_{25}(1-\theta_{4}) - \nu_{4\to25}C_{4}(1-\theta_{25}) \\
\dfrac{dC_{43}}{dt} = \nu_{2\to43}C_{2}(1-\theta_{43})\lambda_{2} - \nu_{43\to2}C_{43} + \nu_{4\to43}C_{4}(1-\theta_{43}) - \nu_{43\to4}C_{43}(1-\theta_{4}) \\
\lambda_2\left(\dfrac{dC_{2}}{dt}\right) = \nu_{43\to2}C_{43} - \nu_{2\to43}C_{2}(1-\theta_{43})\lambda_{2}
\end{cases}
\tag{5.12}
$$

$$
\begin{cases}
\frac{\mathrm{dC_{87}}}{\mathrm{dt}} = \nu_{84\to87}\mathrm{C_{84}}(1-\theta_{87}) - \nu_{87\to84}\mathrm{C_{87}}(1-\theta_{84}) + \nu_{86\to87}\mathrm{C_{86}}(1-\theta_{87})\lambda_{86} - \nu_{87\to86}\mathrm{C_{87}} \\
\frac{\mathrm{dC_{84}}}{\mathrm{dt}} = \nu_{89\to84}\mathrm{C_{89}}(1-\theta_{84}) - \nu_{84\to89}\mathrm{C_{84}}(1-\theta_{89}) + \nu_{87\to84}\mathrm{C_{87}}(1-\theta_{84}) - \nu_{84\to87}\mathrm{C_{84}}(1-\theta_{87}) \\
\frac{\mathrm{dC_{89}}}{\mathrm{dt}} = \nu_{63\to89}\mathrm{C_{63}}(1-\theta_{89}) - \nu_{89\to63}\mathrm{C_{89}}(1-\theta_{63}) + \nu_{84\to89}\mathrm{C_{84}}(1-\theta_{89}) - \nu_{89\to84}\mathrm{C_{89}}(1-\theta_{84}) \\
\frac{\mathrm{dC_{63}}}{\mathrm{dt}} = \nu_{60\to63}\mathrm{C_{60}}(1-\theta_{63}) - \nu_{63\to60}\mathrm{C_{63}}(1-\theta_{60}) + \nu_{89\to63}\mathrm{C_{89}}(1-\theta_{63}) - \nu_{63\to89}\mathrm{C_{63}}(1-\theta_{89}) \\
\frac{\mathrm{dC_{60}}}{\mathrm{dt}} = \nu_{79\to60}\mathrm{C_{79}}(1-\theta_{60}) - \nu_{60\to79}\mathrm{C_{60}}(1-\theta_{79}) + \nu_{63\to60}\mathrm{C_{63}}(1-\theta_{60}) - \nu_{60\to63}\mathrm{C_{60}}(1-\theta_{63}) \\
\frac{\mathrm{dC_{79}}}{\mathrm{dt}} = \nu_{54\to79}\mathrm{C_{54}}(1-\theta_{79})\lambda_{54} - \nu_{79\to54}\mathrm{C_{79}} + \nu_{60\to79}\mathrm{C_{60}}(1-\theta_{79}) - \nu_{79\to60}\mathrm{C_{79}}(1-\theta_{60}) \\
\lambda_{54}\left(\frac{\mathrm{dC_{54}}}{\mathrm{dt}}\right) = \nu_{79\to54}\mathrm{C_{79}} - \nu_{54\to79}\mathrm{C_{54}}(1-\theta_{79})\lambda_{54}
\end{cases}
\tag{5.13}
$$

In equations (5.12) and (5.13), $\frac{\mathrm{dC}_i}{\mathrm{dt}}$ represents the change in concentration C_i at the i-th site over time. $\nu_{i\to j}$ denotes the jumping frequency of H atoms transitioning from the i-th site to the j-th site. Additionally, θ_i defines the coverage of the i-th position as the ratio of the amount of occupied sites C_i to the total number n_i: $\theta_i = \frac{\mathrm{C}_i}{n_i}$. To solve those system of differential equations the concentration of H atoms in the $\mathrm{W_{IN}}$ region was fixed to the same value obtained from the thermodynamic model developed in the prior chapter. This is, the concentration at Td-31 for the green path and Td-86 for the pink one. The transition rates $\nu_{i\to j}$ were determined using the Arrhenius equation:

$$
\nu_{i\to j} = \nu_0^{i\to j} \exp\left(-\frac{E_a^{i\to j}}{k_B T} \right). \tag{5.14}
$$

Where the values of $\nu_0^{i\to j}$ were initially estimated using the Wert and Zener expression (5.4). As previously discussed, this expression for ν_0 was derived for a periodic potential resembling Figure 5.1, which does not precisely match the potential shape in any of our considered diffusion paths (see Figure 3 in the paper). Nevertheless, these frequency values served as initial estimates. Subsequently, we compared the concentrations in the IN and $\mathrm{Cu_{IN}}$ regions at steady-state conditions with those predicted by the thermodynamic model. Such a comparison enabled us to correct the values of $\nu_0^{i\to j}$ in order to attain equivalent concentrations at steady-state, thereby ensuring consistency between the models.

The correction of the $\nu_0^{i\to j}$ was done considering the analytical solution of the system of equations (5.12) and (5.13) at steady-state conditions. During this regime, the concentration in all the interstitial sites remains constant over time, thus the terms $\frac{\mathrm{dC}_i}{\mathrm{dt}}$ are zero. Given that the number of H atoms occupying interstitial positions is typically orders of magnitude lower than the available interstitial sites within the bulk material, we can approximate the coverage term θ_i in the flux balance equation to be nearly zero. Consequently, we derive the following expressions as analytical solutions:

$$
\mathrm{C}_i[\mathrm{m}^{-2}] = \prod_{j=1}^{i} \frac{\nu_{j-1\to j}}{\nu_{j\to j-1}} \lambda_0 \mathrm{C}_0, \tag{5.15a}
$$

$$\mathrm{C}_k[\mathrm{m}^{-3}] = \prod_{j=1}^{k} \frac{\nu_{j-1\to j}}{\nu_{j\to j-1}} \frac{\lambda_0}{\lambda_k} \mathrm{C}_0. \tag{5.15b}$$

C_i and C_k represent the solutions for the points in the middle and the ending points, respectively. $\nu_{j-1\to j}$ and $\nu_{j\to j-1}$ denote the forward and backward jumping frequencies, respectively. The forward frequencies account for all jumps from the $\mathrm{W_{IN}}$ to the $\mathrm{Cu_{IN}}$ region (from right to left), while the backward frequencies encompass the reverse direction (from left to right). More details are done in the paper in the following section.

Once the frequencies were corrected to achieve consistency at steady-state between our models we proceeded to consider the blue path as connector. The system of differential equations to solve once the blue path is considered is the following:

$$\begin{cases}
\frac{\mathrm{dC}_{29}}{\mathrm{dt}} = \nu_{27\to29}\mathrm{C}_{27}(1-\theta_{29}) - \nu_{29\to27}\mathrm{C}_{29}(1-\theta_{27}) + \nu_{31\to29}\mathrm{C}_{31}(1-\theta_{29})\lambda_{31} - \nu_{29\to31}\mathrm{C}_{29} \\
\frac{\mathrm{dC}_{27}}{\mathrm{dt}} = \nu_{25\to27}\mathrm{C}_{25}(1-\theta_{27}) - \nu_{27\to25}\mathrm{C}_{27}(1-\theta_{25}) + \nu_{29\to27}\mathrm{C}_{29}(1-\theta_{27}) - \nu_{27\to29}\mathrm{C}_{27}(1-\theta_{29}) \\
\frac{\mathrm{dC}_{25}}{\mathrm{dt}} = \nu_{4\to25}\mathrm{C}_{4}(1-\theta_{25}) - \nu_{25\to4}\mathrm{C}_{25}(1-\theta_{4}) + \nu_{27\to25}\mathrm{C}_{27}(1-\theta_{25}) - \nu_{25\to27}\mathrm{C}_{25}(1-\theta_{27}) \\
\qquad +\nu_{24\to25}\mathrm{C}_{24}(1-\theta_{25}) - \nu_{25\to24}\mathrm{C}_{25}(1-\theta_{24}) \\
\frac{\mathrm{dC}_{4}}{\mathrm{dt}} = \nu_{43\to4}\mathrm{C}_{43}(1-\theta_{4}) - \nu_{4\to43}\mathrm{C}_{4}(1-\theta_{43}) + \nu_{25\to4}\mathrm{C}_{25}(1-\theta_{4}) - \nu_{4\to25}\mathrm{C}_{4}(1-\theta_{25}) \\
\frac{\mathrm{dC}_{43}}{\mathrm{dt}} = \nu_{2\to43}\mathrm{C}_{2}(1-\theta_{43})\lambda_2 - \nu_{43\to2}\mathrm{C}_{43} + \nu_{4\to43}\mathrm{C}_{4}(1-\theta_{43}) - \nu_{43\to4}\mathrm{C}_{43}(1-\theta_{4}) \\
\lambda_2\left(\frac{\mathrm{dC}_{2}}{\mathrm{dt}}\right) = \nu_{43\to2}\mathrm{C}_{43} - \nu_{2\to43}\mathrm{C}_{2}(1-\theta_{43})\lambda_2 \\
\frac{\mathrm{dC}_{24}}{\mathrm{dt}} = \nu_{25\to24}\mathrm{C}_{25}(1-\theta_{24}) - \nu_{24\to25}\mathrm{C}_{24}(1-\theta_{25}) + \nu_{89\to24}\mathrm{C}_{89}(1-\theta_{24}) - \nu_{24\to89}\mathrm{C}_{24}(1-\theta_{89}) \\
\frac{\mathrm{dC}_{87}}{\mathrm{dt}} = \nu_{84\to87}\mathrm{C}_{84}(1-\theta_{87}) - \nu_{87\to84}\mathrm{C}_{87}(1-\theta_{84}) + \nu_{86\to87}\mathrm{C}_{86}(1-\theta_{87})\lambda_{86} - \nu_{87\to86}\mathrm{C}_{87} \\
\frac{\mathrm{dC}_{84}}{\mathrm{dt}} = \nu_{89\to84}\mathrm{C}_{89}(1-\theta_{84}) - \nu_{84\to89}\mathrm{C}_{84}(1-\theta_{89}) + \nu_{87\to84}\mathrm{C}_{87}(1-\theta_{84}) - \nu_{84\to87}\mathrm{C}_{84}(1-\theta_{87}) \\
\frac{\mathrm{dC}_{89}}{\mathrm{dt}} = \nu_{63\to89}\mathrm{C}_{63}(1-\theta_{89}) - \nu_{89\to63}\mathrm{C}_{89}(1-\theta_{63}) + \nu_{84\to89}\mathrm{C}_{89}(1-\theta_{89}) - \nu_{89\to84}\mathrm{C}_{89}(1-\theta_{84}) \\
\qquad +\nu_{24\to89}\mathrm{C}_{24}(1-\theta_{89}) - \nu_{89\to24}\mathrm{C}_{89}(1-\theta_{24}) \\
\frac{\mathrm{dC}_{63}}{\mathrm{dt}} = \nu_{60\to63}\mathrm{C}_{60}(1-\theta_{63}) - \nu_{63\to60}\mathrm{C}_{63}(1-\theta_{60}) + \nu_{89\to63}\mathrm{C}_{89}(1-\theta_{63}) - \nu_{63\to89}\mathrm{C}_{63}(1-\theta_{89}) \\
\frac{\mathrm{dC}_{60}}{\mathrm{dt}} = \nu_{79\to60}\mathrm{C}_{79}(1-\theta_{60}) - \nu_{60\to79}\mathrm{C}_{60}(1-\theta_{79}) + \nu_{63\to60}\mathrm{C}_{63}(1-\theta_{60}) - \nu_{60\to63}\mathrm{C}_{60}(1-\theta_{63}) \\
\frac{\mathrm{dC}_{79}}{\mathrm{dt}} = \nu_{54\to79}\mathrm{C}_{54}(1-\theta_{79})\lambda_{54} - \nu_{79\to54}\mathrm{C}_{79} + \nu_{60\to79}\mathrm{C}_{60}(1-\theta_{79}) - \nu_{79\to60}\mathrm{C}_{79}(1-\theta_{60}) \\
\lambda_{54}\left(\frac{\mathrm{dC}_{54}}{\mathrm{dt}}\right) = \nu_{79\to54}\mathrm{C}_{79} - \nu_{54\to79}\mathrm{C}_{54}(1-\theta_{79})\lambda_{54}
\end{cases} \tag{5.16}$$

The system of differential equations represented in (5.16) was the one that defined our kinetic model. These fourteen equations allow us to determine how the concentration of

H atoms change over time across the W/Cu interface.

By the end of the paper, we propose a simplification of this kinetic model based on the time required to achieve steady-state, denoted as τ_s. The kinetic model was executed over a temperature range of $300 - 1000$ K. This enabled us to discern the trend of the inverse of τ_s, referred to as the characteristic frequency ν_s, as a function of temperature T. We employed the Arrhenius equation for this fit, with the parameters to be optimized being E_a and ν_0. Consequently, the W/Cu interface could be replaced by a fictitious system whose activation energy and vibrational frequency of H atoms are optimized as E_a and ν_0, respectively.

5.2 Publication

Diffusion properties of H atoms at the W/Cu interface.

Y. Silva-Solís, J. Denis, E.A. Hodille and Y. Ferro.

Submitted to Nuclear Fusion on July 8th, 2024.

Diffusion properties of H atoms at the W/Cu interface.

Y. Silva-Solís[a], J. Denis[a], E. A. Hodille[b] and Y. Ferro[a,*].

[a]Aix-Marseille University, CNRS, PIIM, F-13013 Marseille, France.

[b]CEA, IRFM, F-13108 Saint-Paul-lez-Durance, France.

*Corresponding author: yves.ferro@univ-amu.fr

Abstract

The study explored hydrogen (H) atom diffusion at the W/Cu interface through a combination of the Arrhenius law and Macroscopic Rate Equation (MRE) modeling. This investigation considered two diffusion paths crossing the interface, along with a third path within the W/Cu interface plane. The activation barriers within the Cu network displayed significant variations among these paths due to the reconstruction of the Cu bulk. Additionally, diffusion characteristics in perfect W and Cu bulks were established as reference values using the Arrhenius law to calculate diffusivity within the bulks and parallel to the W/Cu interface plane. Notably, diffusion parallel to the interface was observed to be lower than that within the W and Cu bulks across the temperature range from 260 K to 1000 K. In the subsequent part of the study, the diffusion of H perpendicular to the interface plane was analyzed using a 0-dimensional kinetic model based on MRE. This analysis unveiled an inhomogeneous H concentration at the W/Cu interface under steady-state conditions, with H atoms diffusing from the pink path to the green path facilitated by the blue path as a connector. Lastly, a reduced model of the W/Cu interface was proposed based on the correlation between the time required to achieve steady-state and the system's temperature.

Keywords: interface, diffusion, activation energy, steady-state.

1 Introduction

Understanding the retention and diffusion of Hydrogen isotopes (HIs) in the plasma-facing components (PFCs) of fusion devices is crucial due to its potential implications for system contamination and fuel losses [1]. In diverted configurations of tokamaks, the most intense plasma-wall interaction occurs at the divertor [2]. The ITER-like divertor is constructed using tungsten (W) monoblocks with copper-chromium-zirconium (CuCrZr) pipes passing through them. To mitigate mechanical stress between these materials, a 1 mm interlayer of pure copper (Cu) is strategically placed between the W and CuCrZr surfaces [3, 4]. While the machine is in operation, HIs originating from the plasma can diffuse through the W bulks, ultimately reaching the W/Cu interface [5–7]. Our previous work [8] demonstrated that HIs can accumulate and stabilize at this interface, potentially leading to defect formations. They may also diffuse through the W/Cu interface, reaching the Cu layer and continuing their diffusion up to the coolant, ultimately allowing them to escape into the environment.

Numerous investigations have explored the diffusion of HIs in W and Cu bulks independently [9–19]. In 1968, R. Frauenfelder [9] conducted degassing experiments to study the solution and diffusion of H in W, employing mass spectrometry and ultrahigh vacuum techniques across a pressure range of 600 to 10^{-8} Torr and temperatures spanning 1100 to 2400 K. The resulting diffusion coefficient was expressed as $D(T) = 4.1 \times 10^{-7} \exp\left(-\frac{0.39 \text{ eV}}{k_B T}\right)$ [m^2/s]. Subsequently, Zakharov et al. [12] reported a diffusion coefficient of $D(T) = (6 \pm 2) \times 10^{-4} \exp\left(-\frac{1.07 \pm 0.09 \text{ eV}}{k_B T}\right)$ [m^2/s] at lower temperatures ($400 - 1200$°C) and pressures ($1 - 200$ torr). The discrepancy between these measurements is attributed to increased defect interaction within the W bulk at temperatures below 1500 K [13, 20]. Benamati et al. [13]

utilized the time-dependent permeation method and obtained diffusion coefficients similar to those of Zakharov et al. [12], with experiments conducted in the temperature range $673 - 873$ K and pressure range $10 - 100$ kPa. In a more recent study in 2020, Holzner et al. [14] reported a diffusion coefficient of $D(T) = 1.60 \times 10^{-7} \exp\left(-\frac{0.28 \pm 0.06 \text{ eV}}{k_B T}\right)$ [m^2/s] using gas loading experiments performed in both polycrystalline and single-crystalline W, at a pressure of 500 mbar and temperatures ranging from $1600 - 2600$ K.

Theoretical studies conducted on perfect W bulk have corroborated the diffusion values obtained by Frauenfelder [9] and Holzner et al. [14]. Heinola and Ahlgren [15], employing DFT calculations in conjunction with the harmonic Transition State Theory (hTST) [21], determined the diffusion coefficient of H atoms in perfect W bulk, yielding a value of $D(T) = 0.52 \times 10^{-7} \exp\left(-\frac{0.21 \text{ eV}}{k_B T}\right)$ [m^2/s]. These values of activation energy and pre-exponential factor were in good agreement with the numerical fit applied to Frauenfelder's data [9] at temperatures above 1500 K [15]. Similarly, Fernandez et al. [16] reported comparable values while studying the interaction of H with W through DFT and statistical methods based on transition-state theory (TST) and thermodynamics. They obtained a diffusion constant of $D(T) = 1.93 \times 10^{-7} \exp\left(-\frac{0.20 \text{ eV}}{k_B T}\right)$ [m^2/s], which also aligned with the high-temperature fit to Frauenfelder's data [9].

Experimental studies conducted in Cu exhibit a higher level of agreement compared to those carried out in W. In 1965, Eichenauer et al. [17] investigated the solubility and diffusion of H and deuterium (D) in nickel (Ni) and Cu single crystals, evaluating the rate degassing of samples at thermal equilibrium. This study, conducted at high temperatures, yielded a diffusion constant of $D(T) = 11.5 \times 10^{-7} \exp\left(-\frac{0.42 \text{ eV}}{k_B T}\right)$ [m^2/s]. Similarly, Katz et al. [18] obtained comparable results six years later using the same method as Eichenauer et al. [17], determining the diffusion constant of HIs, including tritium (T), in Ni and Cu crystals. Their measurements in Cu, conducted in a temperature range of $450 - 925$°C, yielded a diffusion rate of $D(T) = 11.3 \times 10^{-7} \exp\left(-\frac{0.41 \text{ eV}}{k_B T}\right)$ [m^2/s]. Low-temperature experiments were conducted by Sakamoto and Takao [19] in 1982, followed by Ishikawa and McLellan [10] in 1985. Sakamoto and Takao [19] evaluated H solubility and diffusion in annealed and cold-rolled Cu at room temperature using the electrochemical permeation method with galvanostatic charging of Cu. They reported a H diffusivity in Cu of $D(T) = (3.69 \pm 0.64) \times 10^{-7} \exp\left(-\frac{0.38 \pm 0.01 \text{ eV}}{k_B T}\right)$ [m^2/s]. The diffusivity of cold-rolled Cu was lower and with slightly higher activation energy barriers than those previously reported at thigh temperatures [17, 18]. Ishikawa and McLellan [10] employed an electrochemical technique called "pulse method", introducing a "peak" of H concentration into the sample with a cathodic current pulse to observe diffusion. They used coated (with a thin layer of palladium) and uncoated Cu films to address surface corrosion effects caused by the current pulse. They reported a fit for their diffusivity data of $D(T) = 21.1 \times 10^{-7} \exp\left(-\frac{0.46 \text{ eV}}{k_B T}\right)$ [m^2/s].

Zhou et al. [11] investigated the dissolution and diffusion of H atoms in a perfect Cu_{fcc} bulk using DFT data. They calculated the activation barrier for H diffusion on the $(\bar{1}10)$ plane between two octahedral sites, considering two different paths. The first path involved passing through a tetrahedral site (Td), while the second path went directly between two octahedral sites (Oh). The activation barriers they found were 0.23 eV and 0.58 eV for the Oh-Td-Oh and Oh-Oh paths, respectively. These results enabled them to determine a diffusion coefficient of $D(T) = 1.74 \times 10^{-7} \exp\left(-\frac{0.23}{k_B T}\right)$ [m^2/s].

Despite the extensive research conducted on W and Cu, further investigation is necessary to fully comprehend the mechanisms occurring at the interface between these two materials. This objective forms the primary focus of the current study. We utilized the Wert and Zener theory [21] to determine the diffusion coefficient of H atoms parallel to the plane of the W/Cu interface. Simultaneously, a 0-dimensional kinetic model was developed to investigate diffusion perpendicular to this plane. Due to the limited availability of information on H diffusion at the W/Cu interface in the literature, we compare our findings with other experimental and theoretical studies conducted on W and Cu bulks. The paper is structured as follows: Section 2 details the methodology and numerical parameters employed in this work. Section 3 presents the activation barriers observed at the W/Cu interface,

which were used to determine the diffusion coefficient and develop the 0-dimensional kinetic model. In Section 4, we compare the diffusion coefficients in W and Cu bulks against experimental and theoretical studies, and compare the results from our kinetic model with the thermodynamic model developed in our previous study [8]. Finally, we present the conclusions, acknowledgments, bibliography and appendices.

2 Methodology

2.1 Nudge Elastic Band calculations

The activation energy barriers of H atoms were determined through the Nudged Elastic Band (NEB) method [22, 23] and density functional theory (DFT) in the open code Quantum Espresso [24]. For the NEB calculations we employed three images as intermediate states between the initial and final positions, the quasi-Newton Broyden's method [25] was used as a scheme of optimization, whereas the convergence was guaranteed once the norm of the forces orthogonal to the path was less than 0.01 eV/Å. We employed the same $W^{bcc}(001)/Cu^{hcp}(11\bar{2}0)$ supercell obtained in our previous work [26] with the following cell parameters: $a = b = 6.32$ Å and $c = 22.84$ Å. The ultrasoft pseudopotentials (USPP) were generated using as exchange-correlation functional the PBE-GGA [27] with 14 valance and semi-core electrons for W atoms ($5s^2 5p^6 5d^4 6s^2$), 11 valance electrons for Cu ($4s^2 3d^9$) and 1 for H ($1s^1$). In all our simulations, a $10 \times 10 \times 1$ k-points mesh was used to sample the Brillouin zone of the W/Cu supercell.

2.2 Diffusion paths along W/Cu

Our choice of diffusion paths was influenced by the findings reported in our previous work [8]. The green path primarily traverses the crystallographic plane (010), while the pink path predominantly follows the plane (020). Additionally, we considered the blue path, which serves as a link between the green and pink paths. In Figure 1, we show these diffusion paths, with the represented interstitial positions corresponding to the 52 final stable sites for H at the interface, as determined in [8]. The red and blue points represent the tetrahedral (Td) and octahedral (Oh) sites, respectively. Both the green and pink paths were intentionally selected to explore pathways with differing values of H solution energies, while the blue path facilitates the exchange of H atoms between these pathways. In Figure 2, we illustrate the values of solution energies, considering the Zero Point Energy (ZPE) correction, along these chosen paths. The red and blue numbers in Figure 2 correspond to the Td and Oh positions depicted in Figure 1. On the X-axis of Figure 2, the different sections of the interface are defined as per [8]: Cu_{IN} and W_{IN} represent regions where each Oh or Td position is constructed using only Cu or W atoms, respectively, while IN denotes regions where the Oh or Td sites are composed of both types of atoms simultaneously. These energy values were extracted from reference [8].

The diffusion coefficients $D(T)$ ($m^2 s^{-1}$) of H were determined using the Arrhenius law:

$$D(T) = D_0 \exp\left(-\frac{E_a}{k_B T}\right), \tag{1}$$

where D_0 ($m^2 s^{-1}$) is the pre-exponential factor, E_a (eV) is the activation energy, k_B (eV/K) is the Boltzmann constant and T (K) is the substrate's temperature. The pre-exponential factor was estimated using the same methodology as Wert and Zener in reference [21]:

$$D_0 = n\alpha a^2 \nu_0, \tag{2}$$

where n represents the number of nearest neighbor interstitial positions, α is a numerical parameter that depends upon the location of the interstitial positions, a (m) is the lattice constant and ν_0 (s^{-1})

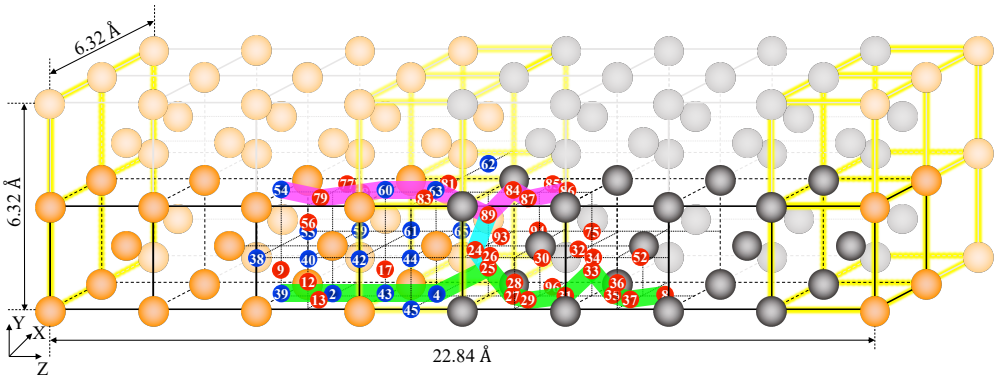

Figure 1: Diffusion paths considered in this work. The red and blue points represent the stable tetrahedral and octahedral sites at the $W^{bcc}(001)/Cu^{hcp}(11\bar{2}0)$ supercell. These interstitial sites had been taken from reference [8].

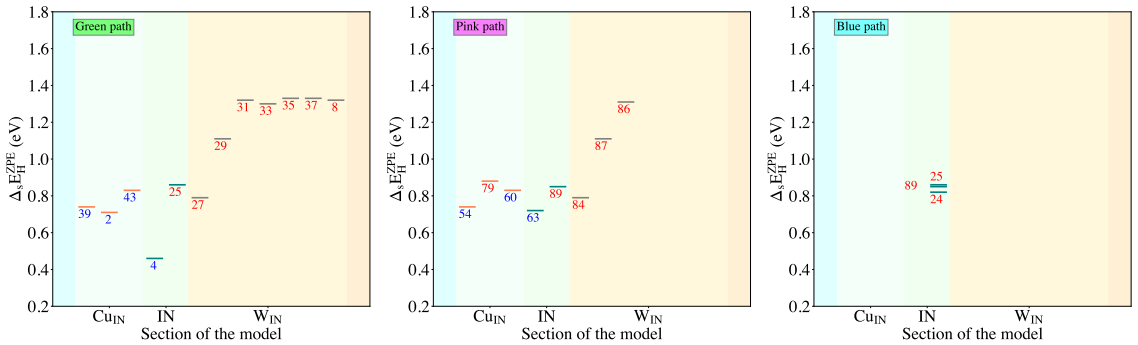

Figure 2: Solution energy of H atoms considering the ZPE correction along the chosen paths. Red and blue numbers correspond with the Td and Oh positions shown in Figure 1. The X-axis represents the region of the interface considered. The data was extracted from reference [8].

is the vibrational frequency of H atom in an interstitial position. In the Wert and Zener theory the value of ν_0 is determined by:

$$\nu_0 = \sqrt{\frac{E_a}{2m\lambda^2}}, \tag{3}$$

where m (kg) is the mass of one H atom and λ (m) is the distance between two interstitial sites, which were determined by making use of the software XCrySDen [28].

2.3 Defining the 0-dimensional kinetic model

We developed a 0-dimensional kinetic model based on the energy diagram extracted from the diffusion paths. This model extends the framework established by Hodille et al. [29] for the Be/BeO interface and in Appendix A of reference [6]. Their model encompassed only three sites: one on the Be side, one on the BeO side, and one at the interface. In contrast, ours considers more than three points to assess the impact of these intermediate positions between the endpoints and the interface.

Since the activation barriers at positions Td-8, Td-37, Td-35, Td-33, and Td-31 have similar values (with a variance $\sigma^2 = 1.2 \times 10^{-4}$ eV^2), we will choose as the initial position of H in the W$_{IN}$, the Td-31 site for the green path and the Td-86 for the pink one. In the Cu$_{IN}$ region, the selected endpoints are

Oh-2 and Oh-54 for the green and pink paths, respectively. Therefore, the green path goes from Td-31 to Oh-2, encompassing 7 interstitial sites along the W/Cu interface. Similarly, the pink path extends from Td-86 to Oh-54, covering 8 interstitial sites along the interface. Thus, these types of traps are considered:

1. H atoms at the interstitial sites Td-31 (green path) and Td-86 (pink path) in the W_{IN} region, whose concentration are C_{31} and C_{86} respectively, both expressed in (m^{-3}).
2. H atoms trapped at the interstitial sites Oh-2 (green path) and Oh-54 (pink path) in the Cu_{IN} region, whose concentration are C_2 and C_{54} respectively, both expressed in (m^{-3}).
3. H atoms trapped at the i-th positions in between, with a concentration C_i expressed in (m^{-2}), and a maximum number of traps (number of interstitial sites) denoted as n_i (m^{-2}).

We define the coverage of the intermediate positions as the amount of site occupied: $\theta_i = \frac{C_i}{n_i}$. We consider that the concentrations at the extreme sites: C_{31}, C_2, C_{86} and C_{54}, are lower than the concentration of traps at those positions, this way there will be always free interstitial sites to detrap from the positions next to them. Similarly to reference [29] the interface is considered as a 2D defect (like a surface), hence their concentrations are expressed in m^{-2}. Thus, two types of reactions are considered: the trapping from j-th to i-th ($j \to i$) and the detrapping from i-th to j-th ($i \to j$). The rate (s^{-1}) of each reaction is expressed by Arrhenius law as:

$$\nu_{i\to j} = \nu_0^{i\to j} \exp\left(- \frac{E_a^{i\to j}}{k_B T} \right), \tag{4}$$

where $\nu_0^{i\to j}$ (s^{-1}) is the pre-exponential factor which is determined using the expression (3), $E_a^{i\to j}$ (eV) is the energy barrier of H atoms for jumping from the i-th interstitial site to j-th, k_B (eV/K) is the Boltzmann constant and T (K) is the temperature of the reservoir.

The rate equation model that results from this system can be expressed as follows:

$$\lambda_i \left(\frac{dC_i}{dt} \right) = \sum_j \nu_{j\to i} C_j - \nu_{i\to j} C_i (1-\theta_j)\lambda_i, \tag{5a}$$

$$\frac{dC_i}{dt} = \sum_j \nu_{j\to i} C_j (1-\theta_i) - \nu_{i\to j} C_i (1-\theta_j) + \sum_k \nu_{k\to i} C_k (1-\theta_i)\lambda_k - \nu_{i\to k} C_i, \tag{5b}$$

$$\frac{dC_i}{dt} = \sum_j \nu_{j\to i} C_j (1-\theta_i) - \nu_{i\to j} C_i (1-\theta_j). \tag{5c}$$

Expression (5a) is used to determine the concentration at the extreme points, specifically for the Td-31, Td-2, Td-86, and Td-54 sites, where the concentration is expressed in m^{-3}. Equation (5b) describes the concentration at points adjacent to the extreme points. Equation (5c) calculates the concentration of the interstitial sites between the extreme points, with concentrations also expressed in m^{-3}.

In expressions (5a) and (5c), the sums in both expressions run over all the j-th interstitial positions next to the i-th site. Thus, the first term in both expressions represents the trapping from the site j-th to i-th (it is a positive term because this reaction increases the value of C_i) and the second term is the detrapping from i-th to j-th (it is a negative term due to this reaction decrease the value of C_i). In the case of (5b), there are two distinct summations: one across every j-th non-extreme point and another across every k-th extreme point connected to the i-th site. Similar to equations (5a) and (5c), negative terms represent detrapping reactions from the i-th site to the j-th or k-th sites, while positive terms denote trapping reactions from the j-th or k-th sites to the i-th site. In Appendix B we show the system of differential equations resulting of considering the expressions (5). The system of

differential equations is solved using SciPy package [30] in Python. To enhance clarity in interpreting the results, we initially analyzed the green and pink paths separately. Subsequently, we integrated them by examining the blue path.

We considered that the system reaches the steady-state conditions once the following condition is satisfied:

$$\delta \mathrm{C}_i(t_k) = \frac{\Big(\mathrm{C}_i(t_M) - \mathrm{C}_i(t_k)\Big)}{\mathrm{C}_i(t_M)} \times 100\% \leq \varepsilon. \tag{6}$$

M defines the total number of intervals in which the time is divided, the sub-index $k = 1, 2, ..., M$ is an integer that denotes the intervals of time, $\mathrm{C}_i(t_k)$ is the concentration of the interstitial site i-th at time t_k, and ε is the convergence threshold. When the condition (6) is satisfied for all the i-th interstitial sites considered in the system of differential equations, we said that the system has reached steady-state at iteration k at time τ_s. We chose a threshold of $\varepsilon = 1\%$, which means that the difference between all the values of $\mathrm{C}_i(t_k)$ and their respective final values $\mathrm{C}_i(t_M)$ represents less than 1% of $\mathrm{C}_i(t_M)$.

Three different temperatures were considered for our simulations: 340 K, 430 K and 550 K. Such values of temperature are the temperature at the rear of the W armor (real position of the W/Cu interface at the W monoblocks in the ITER-like divertor) in the exposure conditions for the three different scenarios considered during the steady-state plasma in reference [7].

3 Results

3.1 Activation energy barriers

The activation barriers for H atoms were determined in W and Cu bulks. Those values were used as a reference to appreciate the effect of the W/Cu interface in the diffusion of H atoms. It is well-known that H atoms diffuse in W bulks jumping using tetrahedral sites only [9, 15, 16]. In contrast, in Cu bulks, H atoms can use tetrahedral sites to displace between two octahedral sites [11], similar behavior was found in other fcc structures as iron [31]. That is why we consider only one path in the W bulk: Td-Td, and two in the Cu bulk: Oh-Oh and Oh-Td-Oh. We obtained a value of 0.23 eV for the activation energy in W, which is in agreement with the values reported by other studies [9, 15, 16]. For the Oh-Oh path in Cu, the activation barrier was 0.63 eV, whereas 0.34 eV and 0.15 eV were the obtained values for the Oh-Td and Td-Oh transitions in the Oh-Td-Oh path respectively. More details about these calculations appear in the Appendix A.

After obtaining the reference activation barriers within the W and Cu bulks, we extended this analysis to the W/Cu interface. The corresponding values along three selected paths are visualized in Figure 3. Along the green path, the highest diffusion barriers were observed within the $\mathrm{Cu_{IN}}$ region, specifically at the transitions from Td-27 to Td-25 sites. Conversely, in the $\mathrm{W_{IN}}$ region, further from the interface plane (Td-8 to Td-33), activation barrier energies fluctuated around 0.23 eV and 0.22 eV, contrasting sharply with the $\mathrm{Cu_{IN}}$ region, where values ranged between 0.93 eV and 0.81 eV. Notably, the most substantial barriers for H diffusion occurred between Td-27 to Td-25 and Oh-2 to Oh-43, with respective values of 0.85 eV and 0.93 eV. In contrast, the transitions from Td-25 to Td-4 and from Td-29 to Td-27 exhibited the lowest activation barriers, both at 0.07 eV.

In contrast to the green path, along the pink path, the activation barriers within the $\mathrm{Cu_{IN}}$ region are lower compared to those in the $\mathrm{W_{IN}}$ region, with values ranging between 0.11 eV and 0.25 eV. Additionally, it is notable that the activation barriers for transitions from the $\mathrm{W_{IN}}$ and $\mathrm{Cu_{IN}}$ regions to the interface are much lower than those observed along the green path. The highest barriers for H atoms occur during the transitions from Td-87 to Td-86 and from Td-84 to Td-87, with values of

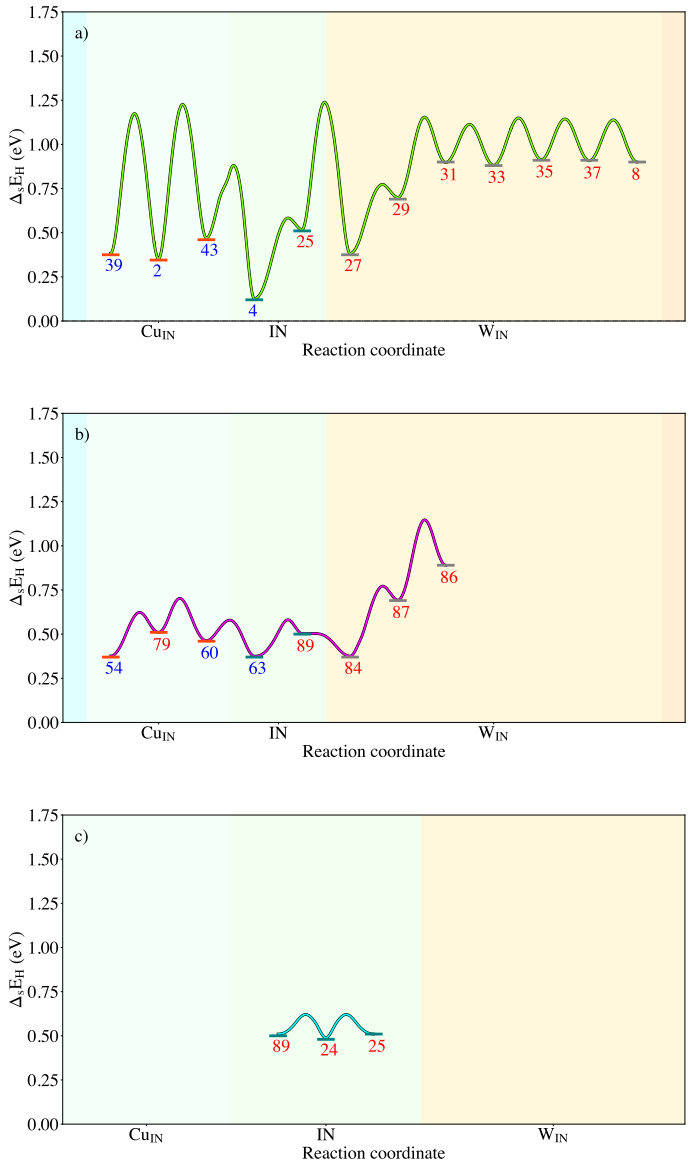

Figure 3: Activation energies along the (a) green, (b) pink, and (c) blue diffusion paths at the W/Cu interface. The solution energy values for the interstitial sites do not consider the ZPE and were extracted from reference [8].

0.46 eV and 0.40 eV, respectively. Conversely, the transition from Td-89 to Td-84 exhibits the lowest activation energy value at 0.08 eV.

In the blue path, both activation barriers were of 0.11 eV to trap H in the Td-24 site and 0.13 eV to detrap from Td-24 to Td-25 and Td-89. Those values were lower than those in the W_{IN} region, further from the interface plane (Td-8 to Td-33). Such decrement can be explained by considering the reconstruction of the W atoms at this layer, which leads to a lower charge density than those at the W_{IN}. All the values of activation energies for the three paths are summarized in Table 1:

Table 1: Values of the λ and activation energies at the W/Cu interface along the diffusion paths.

Path	Transition ($i \leftrightarrow j$)	λ (Å)	$E_a^{i\to j}$ (eV)	$E_a^{i\leftarrow j}$ (eV)
Green	$31 \leftrightarrow 29$	1.286	0.257	0.455
	$29 \leftrightarrow 27$	1.260	0.073	0.390
	$27 \leftrightarrow 25$	1.038	0.856	0.721
	$25 \leftrightarrow 4$	1.389	0.065	0.456
	$4 \leftrightarrow 43$	1.401	0.754	0.410
	$43 \leftrightarrow 2$	1.319	0.756	0.873
Pink	$86 \leftrightarrow 87$	1.305	0.257	0.455
	$87 \leftrightarrow 84$	1.272	0.080	0.396
	$84 \leftrightarrow 89$	0.803	0.128	0.001
	$89 \leftrightarrow 63$	1.241	0.078	0.206
	$63 \leftrightarrow 60$	1.562	0.204	0.117
	$60 \leftrightarrow 79$	1.593	0.240	0.192
	$79 \leftrightarrow 54$	1.468	0.113	0.247
Blue	$25 \leftrightarrow 24$	1.260	0.111	0.132
	$24 \leftrightarrow 89$	1.260	0.110	0.130

3.2 Diffusion coefficients

Knowing the activation energies in W and Cu bulks, we determined the diffusion coefficient, whose variation with temperature is represented in Figure 4. Those values were considered as a reference to appreciate the effect of the W/Cu interface in the diffusion of H atoms. The numerical parameters used in equation (2) for W bulk were: $\alpha = 1/24$, $n = 4$ and $\lambda = a/\sqrt{8}$, resulting in a pre-exponential factor of $D_0 = 4.99 \times 10^{-7}$ m^2/s. For the Cu bulk, we employed: $\alpha = 1/12$, $n = 12$ and $\lambda = a/\sqrt{2}$, resulting in a value of $D_0 = 2.07 \times 10^{-6}$ m^2/s. For the case of the Cu bulk, we considered an activation barrier of $E_a = 0.34$ eV, which is the maximum value of activation energy in the Oh-Td-Oh path, this choice is justified in reference [31], where the diffusion of H in Fe bulks is studied. Thus, the following expressions are derived for the diffusion coefficient in W and Cu bulks: $D(T) = 4.99 \times 10^{-7} \exp\left(-\frac{0.23 \text{ eV}}{k_b T}\right)$ [m^2/s] and $D(T) = 2.07 \times 10^{-6} \exp\left(-\frac{0.34 \text{ eV}}{k_b T}\right)$ [m^2/s], respectively.

The diffusion at the W/Cu interface was determined in a plane parallel to the plane of the interface. For the planar diffusion of H atoms, we employed the following numerical parameters: $\alpha = 1/8$, $n = 4$ and $\lambda = a/\sqrt{2}$. In appendix C we explained in detail how to determine such values. We obtained a value of $D_0 = 2.09 \times 10^{-6}$, resulting in the following expression for the planar diffusion at the W/Cu interface: $D(T) = 2.09 \times 10^{-6} \exp\left(-\frac{0.46 \text{ eV}}{k_b T}\right)$ [m^2/s].

3.3 Kinetic model

Extended model

As previously mentioned in Section 2.3, our initial approach involves analyzing the variation in the concentration of H along the green and pink paths separately, without considering the blue path. This

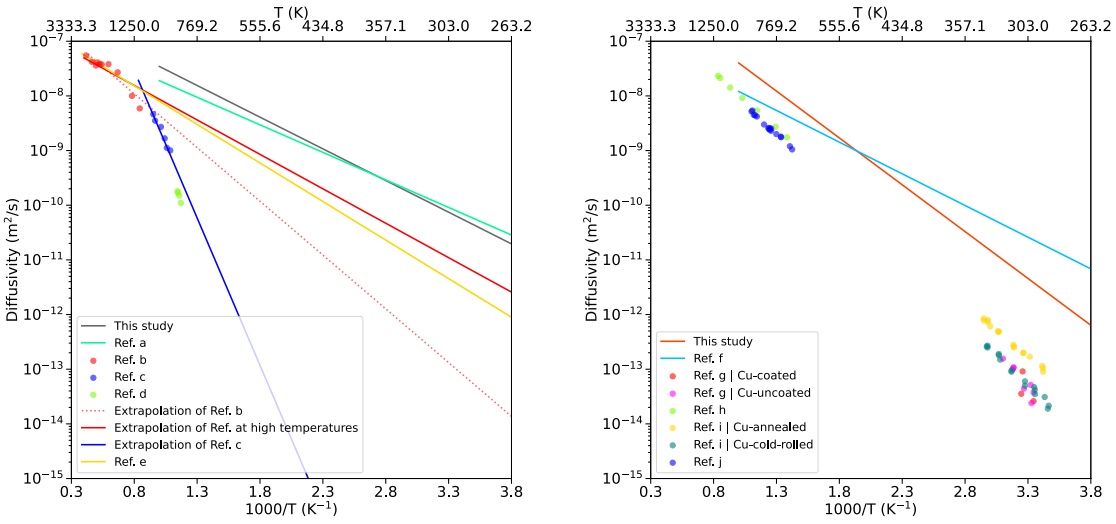

(a) W (b) Cu

Figure 4: Comparison of the calculated diffusion coefficient of H in a) W and b) Cu bulks using Wert and Zener theory [21] against different theoretical and experimental results. Ref. a [16], Ref. b [9], Ref. c [12], Ref. d [13], Ref. e [14], Ref. f [11], Ref. g [10], Ref. h [18], Ref. i [19] and Ref. j [17].

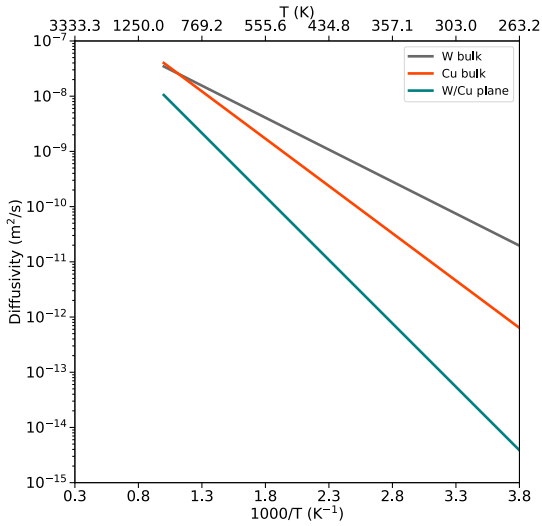

Figure 5: Comparison of the calculated diffusion coefficients of H atoms in W and Cu bulks and at the plane of the W/Cu interface.

way we can identify the most prominent traps in both paths. Then, considering the blue path we established the connection between both paths allowing H atoms to exchange from one to the other. In the extended model, the green path encompasses all interstitial sites between Td-31 and Oh-2, while the pink path includes those between Td-86 and Oh-54. The systems of differential equations arising from the flux balance for this extended model can be found in Appendix B.1.

The concentration at steady-state from the kinetic model was compared with those obtained from our previously established thermodynamic model [8]. To ensure consistency among the results, we

determined the solubility x_{int} at steady-state in the W_{IN} region at temperature T using the thermodynamic model [8]. This solubility was assumed to represent the concentration in the Td-31 and Td-86 sites. Subsequently, the kinetic model was executed at the same temperature T, providing as output the concentration over time for all the interstitial sites in the considered path. Once the system reached steady-state, determined by the expression (6), we exported the concentrations in the IN and Cu_{IN} regions to compare them against the values obtained from the thermodynamic model. Such comparison is shown in Table 2. It is important to highlight that the values of x_{int} were multiplied by the volumetric or surface density of interstitial sites per unit cell to convert it from at.fr. to m^{-3} or m^{-2} respectively.

Table 2: Comparison of x_{int} in the thermodynamic model against the concentration at the steady-state obtained from the kinetic model.

			Thermodynamic model		Kinetic model	
T (K)	Region	Site	x_{int} (at.fr.)	x_{int} (m^{-2} | m^{-3})	Green path	Pink path
340	W_{IN}	Td-31 | Td-86	3.75×10^{-22}	2.30×10^{7}		
	IN	Oh-4	1.21×10^{-10}	1.75×10^{9}	9.09×10^{7}	
	IN	Oh-63	3.83×10^{-14}	5.55×10^{5}		2.56×10^{5}
	Cu_{IN}	Oh-2	5.86×10^{-14}	1.73×10^{15}	3.87×10^{14}	
	Cu_{IN}	Oh-54	1.09×10^{-13}	3.22×10^{15}		1.93×10^{15}
430	W_{IN}	Td-31 | Td-86	2.94×10^{-18}	1.81×10^{11}		
	IN	Oh-4	2.20×10^{-9}	3.19×10^{10}	2.90×10^{9}	
	IN	Oh-63	4.35×10^{-12}	6.30×10^{7}		5.09×10^{7}
	Cu_{IN}	Oh-2	7.66×10^{-12}	2.26×10^{17}	6.24×10^{16}	
	Cu_{IN}	Oh-54	1.25×10^{-11}	3.70×10^{17}		3.87×10^{17}
550	W_{IN}	Td-31 | Td-86	4.38×10^{-15}	2.69×10^{14}		
	IN	Oh-4	2.20×10^{-8}	3.19×10^{11}	4.60×10^{10}	
	IN	Oh-63	1.97×10^{-10}	2.86×10^{9}		3.65×10^{9}
	Cu_{IN}	Oh-2	3.89×10^{-10}	1.15×10^{19}	3.77×10^{18}	
	Cu_{IN}	Oh-54	5.71×10^{-10}	1.69×10^{19}		2.79×10^{19}

Concentration values in m^{-2} and m^{-3} units for the IN and Cu_{IN} regions respectively.

The discrepancy between the kinetic model stems from our approach to determining jumping frequencies using the Wert and Zener theory [21]. This theory, originally intended for calculating jumping frequencies in ideal bulk materials with periodic energy barriers, which is not the case of the interfaces between materials. Nevertheless, the Wert and Zener theory serves as an initial estimation, after which the kinetic model can be optimized to achieve the same steady-state conditions as the thermodynamic model. To optimize the frequencies across all positions outlined in Table 2, we will leverage the exact analytical solution of the steady-state for a simplified pathway. This optimization process will allow us to align the kinetic model more closely with the thermodynamic one.

The analytical solution for the concentration at steady-state conditions can be recursively derived from the flux balance equations represented in Appendix B. For a single path (either the green or the pink), the concentrations at steady-state can be generalized as follows:

$$C_i[m^{-2}] = \frac{n_i \prod_{j=1}^{i} \nu_{j-1\to j}}{n_i \prod_{j=1}^{i} \nu_{j\to j-1} + \prod_{j=1}^{i} \nu_{j-1\to j}} \lambda_0 C_0, \tag{7a}$$

$$C_k[m^{-3}] = \prod_{j=1}^{k} \frac{\nu_{j-1\to j}}{\nu_{j\to j-1}} \frac{\lambda_0}{\lambda_k} C_0. \tag{7b}$$

C_i and C_k represent concentrations at the middle and extreme sites, expressed in units of m^{-2} and m^{-3}, respectively. The terms $\nu_{j-1\to j}$ and $\nu_{j\to j-1}$ refer to the forward and backward jumping frequencies relative to the initial position. The forward frequencies originate from the initial site of the path (always located in the W_{IN} region) and extend to the final site (located in the Cu_{IN} region), while the backward frequencies operate in the opposite direction. j represents the names of the sites along the considered pathway. For instance, in the green path, whose initial site is Td-31 and the final one is Oh-2, j takes values such as 31, 29, 27, 25, 4, 43, and 2. Therefore, for this case, the forward frequencies are denoted as $\nu_{31\to29}, \nu_{29\to27}, \ldots, \nu_{43\to2}$, and the backward frequencies are $\nu_{2\to43}, \nu_{43\to4}, \ldots, \nu_{29\to31}$. Furthermore, λ_0 and C_0 denote the distance between interstitial sites and the concentration at the starting point, which varies depending on the pathway. For the green one, this corresponds to Td-31, and for the pink one, it corresponds to Td-86.

The thermodynamic model described in reference [8] confirmed that under steady-state conditions, the number of H atoms occupying interstitial positions is typically several orders of magnitude lower than the number of available interstitial sites within the bulk material. This allows us to assume that the coverage term θ_i in the flux balance equation is approximately zero, simplifying the expressions (7) to:

$$C_i[m^{-2}] = \prod_{j=1}^{i} \frac{\nu_{j-1\to j}}{\nu_{j\to j-1}} \lambda_0 C_0, \tag{8a}$$

$$C_k[m^{-3}] = \prod_{j=1}^{k} \frac{\nu_{j-1\to j}}{\nu_{j\to j-1}} \frac{\lambda_0}{\lambda_k} C_0. \tag{8b}$$

These equations were used to optimize the frequencies at Oh-4 and Oh-63 (via (8a)), and Oh-2 and Oh-54 (via (8b)). We adjusted the forward frequencies for jumping to the j-th site: $\nu_{25\to4}$, $\nu_{43\to2}$, $\nu_{89\to63}$, and $\nu_{79\to54}$, corresponding to the Oh-4, Oh-2, Oh-63, and Oh-54 sites, respectively. The values of C_i and C_k were set to those obtained from the thermodynamic model while C_0 was set to the values of concentration in the Td-31 and Td-86 depending on the considered path.

For a single pathway, the total number of jumping frequencies is $(2N-2)$, and the number of analytical solutions is $(N-1)$, where N represents the total number of considered sites along the pathway. From the thermodynamic model only two concentrations are known for each path (specifically, Oh-4, Oh-2, Oh-63, and Oh-54 sites). As a result, only 2 analytical solutions out of the $(N-1)$ available can be directly compared against the thermodynamic model. This limitation restricts the number of jumping frequencies that can be corrected from $(N-1)$ down to 2 for each pathway, ensuring the system of equations remains solvable. The remaining $2N$ frequencies were treated as parameters, and their values were determined using equation (4). Table 3 presents a comparison between the frequencies calculated using equation (4) and the corrected values obtained from expressions (8). Additionally, it displays the steady-state concentrations predicted by both the kinetic model and the thermodynamic model to demonstrate that both models achieve the same steady-state once the frequencies are corrected.

In general, the correction of the frequencies involved increasing their values in the W_{IN} region and decreasing their values in the Cu_{IN} region. The only exception to this trend was observed with the frequency at Oh-63 at 550 K, which will be explained in detail in the Discussion section. Looking at Table 3, it is also evident that the rate of trapping H at the W/Cu interface is much higher when the interstitial atoms diffuse through the green path compared to the pink path. This result is implicitly linked to the lower solution energy at the W_{IN} region along the green path compared to the pink path. The increase in trapping frequency corroborates the observation that the Oh-4 site and its equivalents act as a sink at the plane of the W/Cu interface [8].

Table 3: Correction of the jumping frequencies in the kinetic model. $\nu_{j-1\to j}$ represents the frequency by the Wert and Zener theory, while $\nu^*_{j-1\to j}$ stands for the corrected values. The columns kinetic model and thermo model represent the values of concentrations of H at the position j-th.

				Kinetic model		Thermo model
T (K)	j-th site	$\nu_{j-1\to j}$ (Hz)	$\nu^*_{j-1\to j}$ (Hz)	Green path	Pink path	x_{int} (m^{-2} | m^{-3})
340	Oh-4	1.38×10^{12}	2.66×10^{13}	1.75×10^{9}		1.75×10^{9}
	Oh-63	1.09×10^{12}	2.36×10^{12}		5.55×10^{5}	5.55×10^{5}
	Oh-2	2.84×10^{2}	6.59×10^{1}	1.73×10^{15}		1.73×10^{15}
	Oh-54	3.35×10^{11}	2.56×10^{11}		3.22×10^{15}	3.22×10^{15}
430	Oh-4	2.20×10^{12}	2.42×10^{13}	3.19×10^{10}		3.19×10^{10}
	Oh-63	1.90×10^{12}	2.35×10^{12}		6.30×10^{7}	6.30×10^{7}
	Oh-2	6.28×10^{4}	2.07×10^{4}	2.26×10^{17}		2.26×10^{17}
	Oh-54	7.51×10^{11}	5.81×10^{11}		3.70×10^{17}	3.70×10^{17}
550	Oh-4	3.22×10^{12}	2.24×10^{13}	3.19×10^{11}		3.19×10^{11}
	Oh-63	3.01×10^{12}	2.36×10^{12}		2.86×10^{9}	2.86×10^{9}
	Oh-2	5.39×10^{6}	2.37×10^{6}	1.15×10^{19}		1.15×10^{19}
	Oh-54	1.46×10^{12}	1.13×10^{12}		1.69×10^{19}	1.69×10^{19}

After ensuring consistency at steady-state between the two models, the updated frequency values were used to establish connections between the two paths through the blue one. To assess the impact of temperature on the system's kinetics, we fixed the concentration in the W_{IN} region at both sites, Td-31 and Td-86, to 2.30×10^{7} m^{-3} (a value used in the previous simulations for $T = 340$ K, see Table 3) and computed the evolution of the H concentrations at 340 K, 430 K, and 550 K. The results are displayed in Figure 6.

The black vertical dotted line indicates the time τ_s at which the system reaches steady-state, as determined by expression (6). The horizontal black line represents the initial concentration in the W_{IN} region, which was adjusted by multiplying it with their respective values of λ to convert it into units of m^{-2} (see Table 1). The steady-state was reached in 2.63×10^{3} s, 1.06 s and 1.55×10^{-3} s for T = 340 K, T = 430 K and T = 550 K, respectively. It is evident that the higher the temperature the faster the system reaches the steady-state. This is due to the increment of the mobility of H atoms which is expressed by the increment of the jumping frequencies. Another important observation to highlight is the decrease in the concentration at steady-state as the temperature increases. This decrease occurs because the fixed concentration in the W_{IN} region was set to 2.30×10^{7} m^{-3}, which no longer represents the actual value of H concentration in the W_{IN} region when the temperature rises to 550 K.

Once the two paths are linked, the dynamics of H trapping at the W/Cu interface are marked by a progressive rise in the concentration of interstitial sites along both the pink and blue pathways. The pink and blue paths reach a "transient" steady-state due to their lower activation barriers, which allow H atoms to diffuse more easily and stabilize the concentrations at their respective sites. During this regime, H atoms start to migrate from the pink and blue paths to the sites of the green path, resulting in a continuous increase in concentration along the green path since the beginning of the simulations. After some time, this transient steady-state ends, and both paths begin to increase their concentrations at a rate similar to that of the green path. This increase continues until the entire system reaches steady-state conditions at τ_s. As the temperature increases, the duration of the transient steady-state for the pink and blue paths decreases. This is attributed to the higher kinetic energy of H atoms at

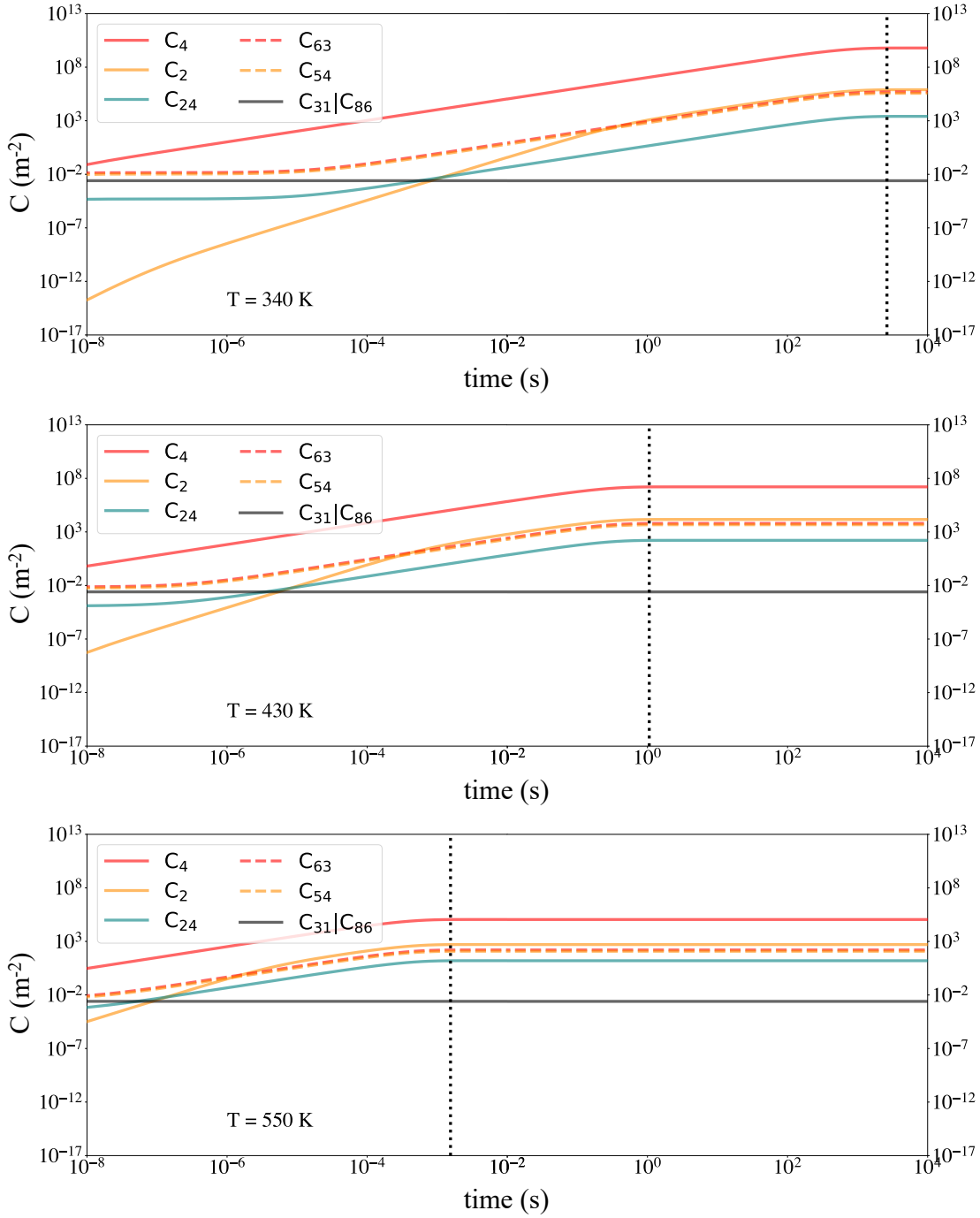

Figure 6: Temporal evolution of H concentration considering the three diffusion paths. The H concentration in the W_{IN} region (Td-31 and Td-86 sites) was fixed at 2.30×10^{7} m^{-3} for all temperatures. Concentration values are displayed for the IN and Cu_{IN} regions of the three paths, with the remaining sites shown in Appendix B.1. The black vertical dotted line indicates the τ_s when the steady-state starts.

higher temperatures, leading to faster diffusion from the pink and blue paths to the green path and thereby reducing the duration of this transitional regime. Throughout all temperatures considered, the site Oh-4 consistently remained the largest trap for H atoms, even outside of the steady-state conditions

of the system. This observation highlights that Oh-4 and its equivalents are not only crucial traps for retaining H under equilibrium conditions but also remain significant traps even under non-equilibrium conditions.

The relationship between τ_s and temperature T can be used to develop a simplified model of the W/Cu interface suitable for implementation in codes like MHIMS [32] and FESTIM [33]. To achieve such a reduction of the W/Cu interface system, our model was executed for a temperature range of $340 - 1000$ K to determine the values of τ_s for each T. For all the temperatures the values of $\nu_{25\to4}$, $\nu_{43\to2}$, $\nu_{89\to63}$, and $\nu_{79\to54}$ were corrected as previously presented. In Figure 7, we plot the inverse of τ_s plotted against T. This term can be interpreted as a characteristic frequency of the system, which the Arrhenius law models its variation with temperature.

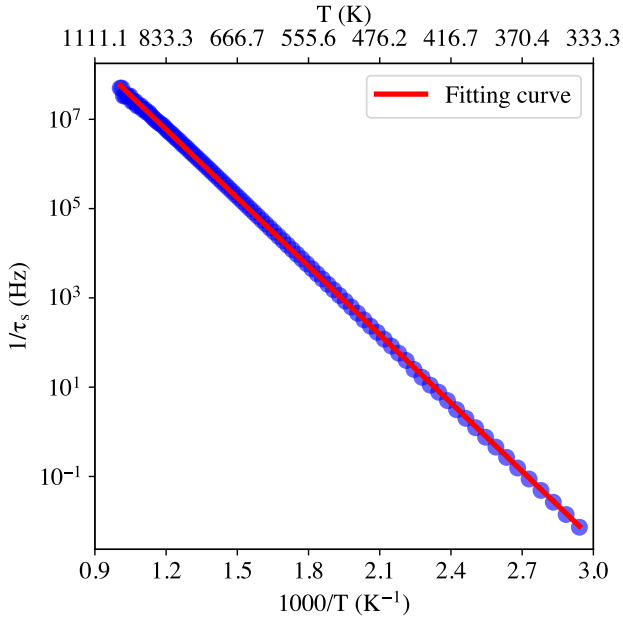

Figure 7: Variation of the characteristic frequency of the W/Cu interface as a function of the temperature.

The characteristic frequency was fitted to an exponential function given by the expression: $A_0 \exp\left(-\frac{A_1}{k_B T}\right)$, resulting in the following pair of parameters: $A_0 = 7.84 \times 10^{12}$ Hz and $A_1 = 1.01$ eV. Thus, a fictitious system with the dynamic variables $\nu_0 = 7.84 \times 10^{12}$ Hz and $E_a = 1.01$ eV could replace the W/Cu interface.

4 Discussion

4.1 Activation energy barriers

The activation barriers obtained from our DFT calculations for W and Cu were found to be consistent with experimental data and other theoretical studies. Table 4 summarizes our results compared to those reported in the literature. Specifically, our calculated activation energy (E_a) of 0.23 eV for perfect W bulk was higher than values reported in prior theoretical works [15, 16]. The discrepancies among these studies can be attributed to differences in numerical parameters for the NEB calculations done by DFT.

Heinola and Ahlgren [15] used a PAW pseudopotential with the PBE exchange-correlation functional, considering 6 valence electrons ($5d^46s^2$) for W bulk. Middleburgh et al. [34] demonstrated that changing to a pseudopotential with 12 valence electrons rather than 6 can significantly affect the system's ground state. Based on this, we chose to include semi-core electrons, for a total of 14 electrons ($5s^25p^65d^46s^2$), using the USPP pseudopotential and the same PBE functional. This change may explain why our calculated E_a differs from that reported in [15]. On the other hand, Fernandez et al. [16] employed the same pseudopotential, exchange-correlation functional, and number of electrons as used in our work. However, the difference in our results can be attributed to the chosen cutoff energies. Specifically, we employed cutoff energies of 50 Ry (680 eV) for the wave-function and 400 Ry (5442 eV) for the electronic density, whereas Fernandez et al. [16] used 40 Ry (544 eV) and 320 Ry (4352 eV) for these parameters. The higher energy thresholds in our calculations reflect our aim for better accuracy, although at the cost of requiring more computational resources.

Against the experimental values exists a bigger discrepancy regarding the values of E_a in W bulks. This difference lies in the fact that our E_a is determined in a perfect monocrystal W bulk without any defect, which is not the case for the samples used in the experiments. To achieve diffusion of H atoms from Td-Td sites in a W sample, it is crucial to minimize the presence of point defects (ideally all of them) to avoid H interacting with them. At high temperatures (approximately above 1500 K) traps in W will not retain H atoms and their diffusion is done from Td-Td sites like in a perfect bulk [13, 15, 16, 20]. That's why to have a fair comparison Heinola and Ahlgren [15] proposed to interpolate the Frauenfelder's data [9] only considering those measurements above 1500 K. This consideration decreased the E_a from 0.39 EV originally obtained from Frauenfelder [9] to 0.25 eV [15], which is in agreement with our determined value (see Table 4). In a more recent study, Holzner et al. [14] performed TDS measurements in a W sample heated in a range of $1600\ \mathrm{K} - 2200\ \mathrm{K}$ in the presence of H and D atmospheres at 500 mbar of pressure. They reported an activation energy (E_a) of 0.28 eV, which is consistent with our obtained results.

Regarding the values in the Cu^{fcc} bulk, the discrepancy between our results and the theoretical work of Zhou et al. [11] mainly lies in the activation energies for the Oh-Td-Oh path. Their E_a barrier for the Oh-Oh path was 0.58 eV, which is close to our reported value of 0.63 eV. This difference can be attributed to the numerical parameters and methods used in the simulations. Zhou et al. determined their activation barriers using the drag method [35] and performed their DFT calculations with the PAW method, using a cutoff energy for the wave-function of 400 eV (approximately 30 Ry). In contrast, we used the NEB method for determining the activation energy barriers and the USPP method with a wave function cutoff energy of 50 Ry (approximately 680 eV). The highest discrepancy between our results was found in the shape of the potential energy through the Oh-Td-Oh path. In fcc materials like Cu, H can diffuse from Oh sites by using metastable sites such as Td positions to facilitate its diffusion. This phenomenon is energetically favorable and has been observed in other materials like Fe [31, 36]. Given that Td sites are metastable, the energy profile along the Oh-Td-Oh path should exhibit a local minimum at the Td site, which Zhou et al. [11] did not observe in their study. Moreover, if we sum up the activation energy of 0.23 eV reported by Zhou et al. [11] for this Oh-Td-Oh path, to the solution energy of H in the Oh site 0.40 eV we obtain 0.63 eV which is 0.08 eV higher than the value reported in the Table 1 of their article. As the solution energy values were consistent with those from our previous work [8], we conclude that the discrepancy originates from the drag method calculations for two reasons. First, the expected profile from fcc materials along the diffusion path was not observed. Second, the solution energy for the Td site was contradictory. It seems that the drag method does not identify the minimum energy path. Instead, H found an alternative path where the metastable site is not a Td position, which explains the presence of a maximum energy value rather than the expected local minimum.

Our E_a compared against the experimental data presented a lower value [10, 19]. This result was kind of expected because as in the W case, our model is a perfect monocrystal Cu bulk. We already discussed that in real samples there is a concentration of defects that can trap the H and increase the

E_a. Experiments carried out at high temperatures [17, 18] exhibited the best agreements.

When examining the W/Cu interface, we observed that the activation barriers in the Cu_{IN} region along the green path were significantly higher compared to those along the pink path. To understand this behavior, we will rely on the values of the electronic charge density. The electronic charge density is commonly used in the literature to identify interstitial sites where H atoms can stabilize [26, 37–41]. If the electronic charge density exceeds a threshold of $n_0 = 0.0026$ a.u. (approximately 0.018 e/Å^3), H atoms are expected to stabilize in regions where the electronic density is lower. Consequently, the solution energy of H increases with increasing electronic charge density. Given that the minimum electronic charge density at the W/Cu interface was 0.0204 a.u., which surpasses n_0, we can employ the electronic charge density to identify zones with higher solution energy for H.

In Figure 8, we represent the electronic charge density along the crystallographic plane (010) of the W/Cu interface, where most interstitial sites are located for both the green and pink paths. Due to the reconstruction of the Cu network at the W/Cu interface [26], the pink path has become wider than the green path. This reconstruction causes transitions along the pink path to occur in regions with a significantly lower gradient of electronic charge density compared to the green path, resulting in much lower activation barriers. This explains why the activation barriers in the Cu_{IN} region for the green path were oscillating around 0.73 eV, while those for the pink path were approximately 0.24 eV.

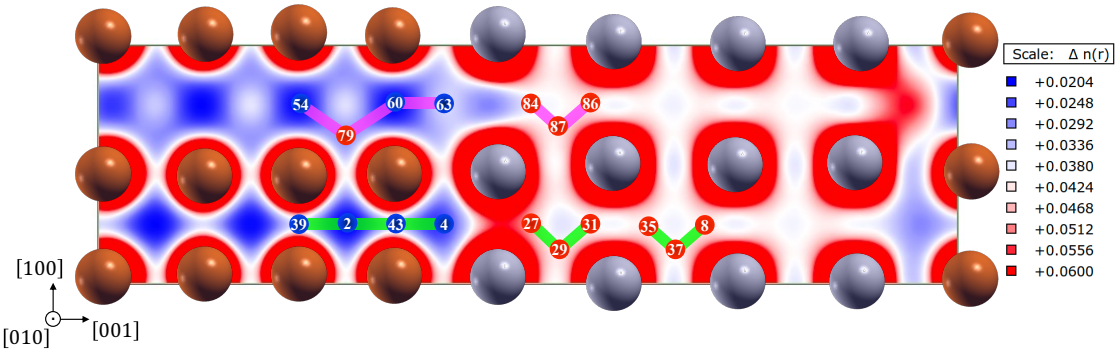

Figure 8: Electronic charge density along the (010) crystallographic plane of the W/Cu interface. Considering the symmetry of the distortion of the supercell discussed in [26], we place the positions of the pink path in their equivalent sites in this crystallographic plane.

4.2 Diffusion coefficients

The variation in diffusion coefficients originates from the discrepancies in the E_a values discussed above. However, different methods are employed in theoretical studies to determine the pre-exponential factor D_0 and the jump rate. Heinola and Ahlgren [15] and Fernandez et al. [16] used the well-known hTST incorporating the concept of the activated complex [42]. In contrast, in our study and in reference [11], the Wert and Zener method was employed [21]. The hTST approach requires knowledge of the vibrational frequencies at the saddle point in addition to the frequencies at the interstitial sites. Wert and Zener developed their method precisely to determine the jump rate without requiring knowledge of the frequencies at the saddle points. Since in our case we only knew the vibrational frequencies at the interstitial sites [8] and not at the saddle points, we opted to use the Wert and Zener method for determining the jump rate. In Table 4 we summarize the comparison of the diffusion constants determined in this study by using Wert and Zener theory [21] against different experimental and theoretical studies.

Table 4: Comparison of diffusion constants in W and Cu bulks.

Element	D_0 (m^2/s)	E_a (eV)	ν_0 (THz)	Comments
W	4.99×10^{-7}	0.23	29.5	DFT in this study
	0.52×10^{-7}	0.21	26	DFT in [15]
	1.93×10^{-7}	0.20	-	DFT in [16]
	4.10×10^{-7}	0.39	200	Experiments [9]
	2.06×10^{-7}	0.28	-	Experiments [14]
	1.58×10^{-7}	0.25	30	Experiments [15]*
Cu	2.07×10^{-6}	0.34	15.8	DFT in this study
	1.74×10^{-7}	0.23	42.4	DFT in [11]
	11.50×10^{-7}	0.42	17.5	Experiments [17]
	11.30×10^{-7}	0.41	17.3	Experiments [18]
	3.69×10^{-7}	0.38	16.7	Experiments [19]
	21.10×10^{-7}	0.46	18.3	Experiments [10]

* Fitting proposed by [15] only considering the experimental data at high temperature of [9].

4.3 Inhomogeneous H diffusion through the W/Cu interface

The concentrations at steady-state conditions varied between the green and pink paths when considered independently, compared to when the blue path was included. In Table 5, we compared these values at $T = 340$ K as an example.

Table 5: Comparison among the kinetic models depending on the considered path. The values of concentration were obtained considering the corrected jumping frequencies. The system of differential equations for each of the systems appears in Appendix B.1.

		Concentration in the considered paths ($m^{-2}|m^{-3}$)		
T (K)	Region	Green	Pink	Green + blue + pink
340	IN (Oh-4)	1.75×10^{9}		6.28×10^{9}
	IN (Oh-63)		5.55×10^{5}	4.97×10^{5}
	Cu_{IN} (Oh-2)	1.73×10^{15}		6.20×10^{15}
	Cu_{IN} (Oh-54)		3.22×10^{15}	2.88×10^{15}

The inclusion of the blue path alters the steady-state of the system, leading to a phenomenon where H atoms diffuse from the pink path to the green one through the blue path during a transient phase. This results in increased concentrations of H in certain sites, creating an uneven distribution of H atoms at the interface and in the Cu_{IN} region. A similar effect was observed at the Be/BeO interface [29], where H tends to be trapped in expanded regions of the material and avoids compressed areas. As the temperature increases, this phenomenon becomes more pronounced. Specifically, the H concentration decreases significantly along the pink path while increasing more substantially along the green one. This behavior is expected because at higher temperatures, H atoms possess greater kinetic energy, leading to an increase in the rate of atom jumping and diffusion.

5 Conclusions

In this work, the diffusion of H atoms in the W/Cu interface was studied. The Arrhenius law was used to determine the diffusivity parallel to the plane of the interface, obtaining the following expression: $D(T) = 2.09 \times 10^{-6} \exp\left(-\frac{0.46 \text{ eV}}{k_b T}\right)$ [m^2/s]. The diffusion across the W/Cu interface was carried out using a 0-dimensional kinetic model based on RE modeling. The jumping frequencies used in such model were initially estimated by the Wert and Zener theory and then corrected to achieve the same steady-state as the thermodynamic model reported in reference [8]. The kinetic model showed an inhomogeneous H concentration along the W/Cu interface, an effect that increases with temperature. A reduced model of the kinetic through the interface was proposed, where the parameters for such an equivalent system were: $\nu_0^{eq} = 7.84 \times 10^{12}$ Hz and $E_a^{eq} = 1.01$ eV. Thus the W/Cu interface could be replaced by a fictitious system with such dynamic parameters.

6 Acknowledgments

This work is supported by Région PACA. It has been carried out within the framework of the EUROfusion Consortium, funded by the European Union via the Euratom Research and Training Programme (Grant Agreement No 101052200 — EUROfusion). Views and opinions expressed are however those of the author(s) only and do not necessarily reflect those of the European Union or the European Commission. Neither the European Union nor the European Commission can be held responsible for them. The authors were granted access to the high-performance computing resources of IDRIS under Allocation No. A0120806612 made by Grand Equipement National de Calcul Intensif and to the Marconi Supercomputer at CINECA Super Computing Application and Innovation Department, Bologna, Italy.

References

[1] D. Perrault. “Safety issues to be taken into account in designing future nuclear fusion facilities”. *Fusion Engineering and Design* 109.111 (2016), pp. 1733–1738.

[2] J. Wesson et al. *Tokamaks*. Fourth Edition. Oxford University Press, 2011, pp. 1–812.

[3] T. Hirai et al. “Use of tungsten material for the ITER divertor”. *Nuclear Materials and Energy* 9 (2016), pp. 612–622.

[4] M. Richou et al. “The WEST project: validation program for WEST tungsten coated plasma facing components”. *Physica Scripta* 2016.T167 (2016), p. 014029.

[5] E. A. Hodille et al. “Estimation of the tritium retention in ITER tungsten divertor target using macroscopic rate equations simulations”. *Physica Scripta* 170 (2017), pp. 14033–14040. DOI: 10.1088/1402-4896/aa8787.

[6] R. Delaporte-Mathurin et al. “Influence of interface conditions on hydrogen transport studies”. *Nuclear Fusion* 61.3 (2021), p. 036038.

[7] E. A. Hodille et al. “Modelling of hydrogen isotopes trapping, diffusion and permeation in divertor monoblocks under ITER-like conditions”. *Nuclear Fusion* 61.12 (2021), p. 126003.

[8] Y. Silva-Solís et al. “Solution and solubility of H atoms at the W/Cu interface” (2024). Submitted to J. Phys.: Condens. Matter, under revision.

[9] R. Frauenfelder. “Solution and Diffusion of Hydrogen in Tungsten”. *Journal of Vacuum Science and Technology* 6.3 (May 1969), pp. 388–397. DOI: 10.1116/1.1492699. URL: https://doi.org/10.1116/1.1492699.

[10] T. Ishikawa and R. B. McLellan. "The diffusivity of hydrogen in copper at low temperatures". *Journal of Physics and Chemistry of Solids* 46.4 (1985), pp. 445–447.

[11] H. B. Zhou, Y. Zhang, and X. Ou. "Dissolution and diffusion behaviors of hydrogen in copper: A first-principles investigation". *Comp. Mater. Sci.* 79 (2013), pp. 923–928. URL: https://doi.org/10.1016/j.commatsci.2013.08.002.

[12] A. P. Zakharov, V. M. Sharapov, and E. I. Evko. "Hydrogen permeability of polycrystalline and monocrystalline molybdenum and tungsten". *Soviet materials science: a transl. of Fiziko-khimicheskaya mekhanika materialov/Academy of Sciences of the Ukrainian SSR* 9 (1975), pp. 149–153.

[13] G. Benamati, E. Serra, and C. H. Wu. "Hydrogen and deuterium transport and inventory parameters through W and W-alloys for fusion reactor applications". *Journal of nuclear materials* 283 (2000), pp. 1033–1037.

[14] G. Holzner et al. "Solute diffusion of hydrogen isotopes in tungsten—a gas loading experiment". *Physica Scripta* 2020.T171 (2020), p. 014034. DOI: 10.1088/1402-4896/ab4b42. URL: https://dx.doi.org/10.1088/1402-4896/ab4b42.

[15] K. Heinola and T. Ahlgren. "Diffusion of hydrogen in bcc tungsten studied with first principle calculations". *Journal of Applied Physics* 107.11 (June 2010), p. 113531. DOI: 10.1063/1.3386515. URL: https://doi.org/10.1063/1.3386515.

[16] N. Fernandez, Y. Ferro, and D. Kato. "Hydrogen diffusion and vacancies formation in tungsten: density functional theory calculations and statistical models". *Acta Materialia* 94 (2015), pp. 307–318.

[17] W. Eichenauer, W. Löser, and H. Witte. "Löslichkeit und diffusionsgeschwindigkeit von wasserstoff und deuterium in einkristallen aus nickel und kupfer". *International Journal of Materials Research* 56.5 (1965), pp. 287–293.

[18] L. Katz, M. Guinan, and R. J. Borg. "Diffusion of H2, D2, and T2 in single-crystal Ni and Cu". *Physical Review B* 4.2 (1971), p. 330.

[19] Y. Sakamoto and K. Takao. "The electrochemical determination of diffusivity and solubility of hydrogen in copper". *J. Japan Inst. Metals* 46.3 (1982), pp. 285–290.

[20] E. Serra, G. Benamati, and O. V. Ogorodnikova. "Hydrogen isotopes transport parameters in fusion reactor materials". *Journal of nuclear materials* 255.2-3 (1998), pp. 105–115.

[21] C. Wert and C. Zener. "Interstitial Atomic Diffusion Coefficients". *Phys. Rev.* 76 (8 1949), pp. 1169–1175. DOI: 10.1103/PhysRev.76.1169. URL: https://link.aps.org/doi/10.1103/PhysRev.76.1169.

[22] Weinan E, Weiqing Ren, and Eric Vanden-Eijnden. "String method for the study of rare events". *Phys. Rev. B* 66 (5 2002), p. 052301. DOI: 10.1103/PhysRevB.66.052301. URL: https://link.aps.org/doi/10.1103/PhysRevB.66.052301.

[23] Y. Kanai et al. "First-principles string molecular dynamics: An efficient approach for finding chemical reaction pathways". *The Journal of Chemical Physics* 121.8 (Aug. 2004), pp. 3359–3367. DOI: 10.1063/1.1773159. URL: https://doi.org/10.1063/1.1773159.

[24] P. Giannozzi et al. "Advanced capabilities for materials modelling with Quantum ESPRESSO". *J.Phys.: Condens. Matter* 29.46 (2017), p. 465901. DOI: 10.1088/1361-648X/aa8f79.

[25] Charles G Broyden. "A class of methods for solving nonlinear simultaneous equations". *Mathematics of computation* 19.92 (1965), pp. 577–593.

[26] Y. Silva-Solís et al. "A model of the W/Cu interface in the ITER cooling monoblocks from density functional theory". *Nuclear Materials and Energy* 37 (2023), p. 101516. DOI: https://doi.org/10.1016/j.nme.2023.101516.

[27] J. P. Perdew, K. Burke, and M. Ernzerhof. "Generalized Gradient Approximation made simple". *Phys. Rev. Lett.* 77.18 (1996), pp. 3865–3868. DOI: https://doi.org/10.1103/PhysRevLett.77.3865.

[28] Anton K. "XCrySDen—a new program for displaying crystalline structures and electron densities". *Journal of Molecular Graphics and Modelling* 17.3 (1999), pp. 176–179. DOI: https://doi.org/10.1016/S1093-3263(99)00028-5.

[29] E. A. Hodille et al. "Molecular dynamics study of hydrogen isotopes at the Be/BeO interface". *Journal of Physics: Condensed Matter* 34.40 (2022), p. 405001.

[30] P. Virtanen et al. "SciPy 1.0: Fundamental Algorithms for Scientific Computing in Python". *Nature Methods* 17 (2020), pp. 261–272. DOI: 10.1038/s41592-019-0686-2.

[31] K. Hirata et al. "First-principles study on hydrogen diffusivity in BCC, FCC, and HCP iron". *Metallurgical and materials transactions A* 49 (2018), pp. 5015–5022.

[32] E. A. Hodille et al. "Estimation of the tritium retention in ITER tungsten divertor target using macroscopic rate equations simulations". *Physica Scripta* 2017.T170 (2017), p. 014033.

[33] R. Delaporte-Mathurin et al. "FESTIM: An open-source code for hydrogen transport simulations". *International Journal of Hydrogen Energy* 63 (2024), pp. 786–802.

[34] S. C. Middleburgh et al. "Hydrogen induced vacancy formation in tungsten". *Journal of nuclear materials* 448.1-3 (2014), pp. 270–275.

[35] G. Henkelman, G. Jóhannesson, and H. Jónsson. "Methods for finding saddle points and minimum energy paths". *Theoretical methods in condensed phase chemistry* (2002), pp. 269–302.

[36] C. Fu, F. Willaime, and P. Ordejón. "Stability and mobility of mono-and di-interstitials in α-Fe". *Physical review letters* 92.17 (2004), p. 175503.

[37] M. J. Puska, R. M. Nieminen, and M. Manninen. "Atoms embedded in an electron gas: Immersion energies". *Physical Review B* 24.6 (1981), p. 3037. URL: https://doi.org/10.1103/PhysRevB.24.3037.

[38] Y. L. Liu et al. "Vacancy trapping mechanism for hydrogen bubble formation in metal". *Phys. Rev. B* 79.17 (2009), p. 172103.

[39] L. Yang and B. D. Wirth. "Surface stability and H adsorption and diffusion near surfaces of W borides: a first-principles study". *Nuclear Fusion* 63.6 (2023), p. 066002. DOI: 10.1088/1741-4326/acc6de.

[40] L. Yang and B. D. Wirth. "First-principles study of hydrogen behavior near W/WC interfaces". *Journal of Applied Physics* 127.11 (2020), p. 115107. URL: https://doi.org/10.1063/1.5141761.

[41] L. Yang and B. D. Wirth. "First-principles study of hydrogen diffusion and self-clustering below tungsten surfaces". *Journal of Applied Physics* 125.16 (2019), p. 165105. URL: https://doi.org/10.1063/1.5092595.

[42] Stephen Elliott. *The physics and chemistry of solids*. John Wiley & Sons, 1998.

A Diffusion in W and Cu bulks

The activation barriers for H atoms were determined in W and Cu bulks as reference values. H atoms diffuse in W bulks jumping only using tetrahedral sites [9, 15, 16], whereas in Cu bulks, H atoms can use tetrahedral sites to displace between two octahedral sites [11]. That is why we consider only one path in the W bulk: Td-Td, and two in the Cu bulk: Oh-Oh and Oh-Td-Oh. In Figure 9, we represent the diffusion paths considered to determine the activation barrier energies in both bulks.

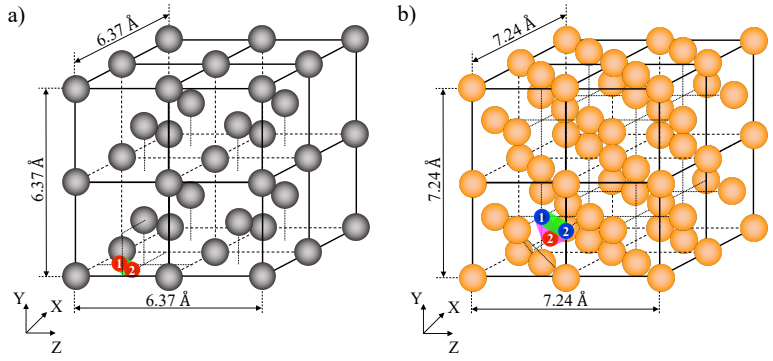

Figure 9: Diffusion paths in a) W and b) Cu bulks. Red and blue points represent the Td and Oh sites respectively. The green line in a) corresponds to the Td-Td path, whereas in b) it represents the Oh-Oh path, and the pink one, the Oh-Td-Oh.

In Figure 10 we represented the activation barriers in the respective paths in W and Cu bulks. It is appreciable that in the case of Cu bulks the diffusion of H atoms is done using the Oh-Td-Oh path because it is less energy demanding. Thus the energy necessary for an H atom to jump from Oh-Oh site in Cu is 0.46 eV approximately and it is done using a Th position and intermediate position, which is in agreement with experimental results [10, 17–19].

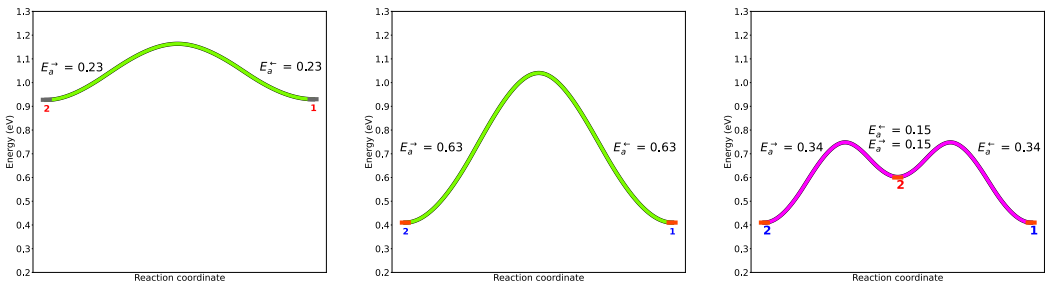

(a) Td-Td path in W bulk. (b) Oh-Oh path in Cu bulk. (c) Oh-Td-Oh path in Cu bulk.

Figure 10: Activation barriers in W and Cu bulks through the paths represented in Figure 9.

B System of differential equations for the kinetic model

B.1 Extended model

The extended kinetic model was constructed considering all the activation barriers in the green and pink path from Td-31 to Td-2 and from Td-86 to Oh-54 respectively. Figure 11 is the sketch of such paths.

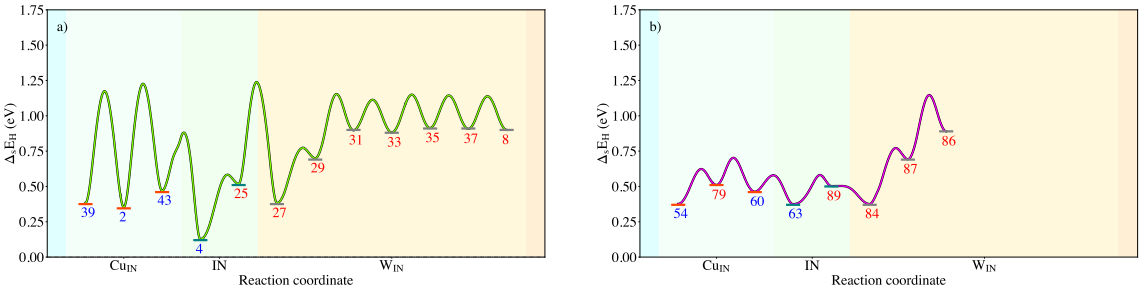

Figure 11: Activation energies in the (a) green and (b) pink diffusion paths.

The flux balance for the kinetic model in the green path when it is analyzed independently from the pink one is given by:

$$\begin{cases} \frac{dC_{29}}{dt} = \nu_{27\to29}C_{27}(1-\theta_{29}) - \nu_{29\to27}C_{29}(1-\theta_{27}) + \nu_{31\to29}C_{31}(1-\theta_{29})\lambda_{31} - \nu_{29\to31}C_{29} \\ \frac{dC_{27}}{dt} = \nu_{25\to27}C_{25}(1-\theta_{27}) - \nu_{27\to25}C_{27}(1-\theta_{25}) + \nu_{29\to27}C_{29}(1-\theta_{27}) - \nu_{27\to29}C_{27}(1-\theta_{29}) \\ \frac{dC_{25}}{dt} = \nu_{4\to25}C_{4}(1-\theta_{25}) - \nu_{25\to4}C_{25}(1-\theta_{4}) + \nu_{27\to25}C_{27}(1-\theta_{25}) - \nu_{25\to27}C_{25}(1-\theta_{27}) \\ \frac{dC_{4}}{dt} = \nu_{43\to4}C_{43}(1-\theta_{4}) - \nu_{4\to43}C_{4}(1-\theta_{43}) + \nu_{25\to4}C_{25}(1-\theta_{4}) - \nu_{4\to25}C_{4}(1-\theta_{25}) \\ \frac{dC_{43}}{dt} = \nu_{2\to43}C_{2}(1-\theta_{43})\lambda_{2} - \nu_{43\to2}C_{43} + \nu_{4\to43}C_{4}(1-\theta_{43}) - \nu_{43\to4}C_{43}(1-\theta_{4}) \\ \lambda_2\left(\frac{dC_2}{dt}\right) = \nu_{43\to2}C_{43} - \nu_{2\to43}C_{2}(1-\theta_{43})\lambda_{2} \end{cases} \tag{9}$$

Where λ_{31} (m) and λ_2 (m) represent the distance between two interstitial sites in the W_{IN} and Cu_{IN} sections, respectively. In the case of the pink path we obtained the following flux balance:

$$\begin{cases} \frac{dC_{87}}{dt} = \nu_{84\to87}C_{84}(1-\theta_{87}) - \nu_{87\to84}C_{87}(1-\theta_{84}) + \nu_{86\to87}C_{86}(1-\theta_{87})\lambda_{86} - \nu_{87\to86}C_{87} \\ \frac{dC_{84}}{dt} = \nu_{89\to84}C_{89}(1-\theta_{84}) - \nu_{84\to89}C_{84}(1-\theta_{89}) + \nu_{87\to84}C_{87}(1-\theta_{84}) - \nu_{84\to87}C_{84}(1-\theta_{87}) \\ \frac{dC_{89}}{dt} = \nu_{63\to89}C_{63}(1-\theta_{89}) - \nu_{89\to63}C_{89}(1-\theta_{63}) + \nu_{84\to89}C_{84}(1-\theta_{89}) - \nu_{89\to84}C_{89}(1-\theta_{84}) \\ \frac{dC_{63}}{dt} = \nu_{60\to63}C_{60}(1-\theta_{63}) - \nu_{63\to60}C_{63}(1-\theta_{60}) + \nu_{89\to63}C_{89}(1-\theta_{63}) - \nu_{63\to89}C_{63}(1-\theta_{89}) \\ \frac{dC_{60}}{dt} = \nu_{79\to60}C_{79}(1-\theta_{60}) - \nu_{60\to79}C_{60}(1-\theta_{79}) + \nu_{63\to60}C_{63}(1-\theta_{60}) - \nu_{60\to63}C_{60}(1-\theta_{63}) \\ \frac{dC_{79}}{dt} = \nu_{54\to79}C_{54}(1-\theta_{79})\lambda_{54} - \nu_{79\to54}C_{79} + \nu_{60\to79}C_{60}(1-\theta_{79}) - \nu_{79\to60}C_{79}(1-\theta_{60}) \\ \lambda_{54}\left(\frac{dC_{54}}{dt}\right) = \nu_{79\to54}C_{79} - \nu_{54\to79}C_{54}(1-\theta_{79})\lambda_{54} \end{cases} \tag{10}$$

Whereas in the previous case λ_{86} (m) and λ_{54} (m) represent the distance between two interstitial sites in the W_{IN} and Cu_{IN} sections, respectively. Considering the transition between the green and pink paths through the blue one we obtained the following flux balance:

$$
\begin{cases}
\frac{dC_{29}}{dt} = \nu_{27\to29}C_{27}(1-\theta_{29}) - \nu_{29\to27}C_{29}(1-\theta_{27}) + \nu_{31\to29}C_{31}(1-\theta_{29})\lambda_{31} - \nu_{29\to31}C_{29} \\
\frac{dC_{27}}{dt} = \nu_{25\to27}C_{25}(1-\theta_{27}) - \nu_{27\to25}C_{27}(1-\theta_{25}) + \nu_{29\to27}C_{29}(1-\theta_{27}) - \nu_{27\to29}C_{27}(1-\theta_{29}) \\
\frac{dC_{25}}{dt} = \nu_{4\to25}C_{4}(1-\theta_{25}) - \nu_{25\to4}C_{25}(1-\theta_{4}) + \nu_{27\to25}C_{27}(1-\theta_{25}) - \nu_{25\to27}C_{25}(1-\theta_{27}) \\
\qquad\qquad +\nu_{24\to25}C_{24}(1-\theta_{25}) - \nu_{25\to24}C_{25}(1-\theta_{24}) \\
\frac{dC_{4}}{dt} = \nu_{43\to4}C_{43}(1-\theta_{4}) - \nu_{4\to43}C_{4}(1-\theta_{43}) + \nu_{25\to4}C_{25}(1-\theta_{4}) - \nu_{4\to25}C_{4}(1-\theta_{25}) \\
\frac{dC_{43}}{dt} = \nu_{2\to43}C_{2}(1-\theta_{43})\lambda_{2} - \nu_{43\to2}C_{43} + \nu_{4\to43}C_{4}(1-\theta_{43}) - \nu_{43\to4}C_{43}(1-\theta_{4}) \\
\lambda_{2}\left(\frac{dC_{2}}{dt}\right) = \nu_{43\to2}C_{43} - \nu_{2\to43}C_{2}(1-\theta_{43})\lambda_{2} \\
\frac{dC_{24}}{dt} = \nu_{25\to24}C_{25}(1-\theta_{24}) - \nu_{24\to25}C_{24}(1-\theta_{25}) + \nu_{89\to24}C_{89}(1-\theta_{24}) - \nu_{24\to89}C_{24}(1-\theta_{89}) \\
\frac{dC_{87}}{dt} = \nu_{84\to87}C_{84}(1-\theta_{87}) - \nu_{87\to84}C_{87}(1-\theta_{84}) + \nu_{86\to87}C_{86}(1-\theta_{87})\lambda_{86} - \nu_{87\to86}C_{87} \\
\frac{dC_{84}}{dt} = \nu_{89\to84}C_{89}(1-\theta_{84}) - \nu_{84\to89}C_{84}(1-\theta_{89}) + \nu_{87\to84}C_{87}(1-\theta_{84}) - \nu_{84\to87}C_{84}(1-\theta_{87}) \\
\frac{dC_{89}}{dt} = \nu_{63\to89}C_{63}(1-\theta_{89}) - \nu_{89\to63}C_{89}(1-\theta_{63}) + \nu_{84\to89}C_{89}(1-\theta_{89}) - \nu_{89\to84}C_{89}(1-\theta_{84}) \\
\qquad\qquad +\nu_{24\to89}C_{24}(1-\theta_{89}) - \nu_{89\to24}C_{89}(1-\theta_{24}) \\
\frac{dC_{63}}{dt} = \nu_{60\to63}C_{60}(1-\theta_{63}) - \nu_{63\to60}C_{63}(1-\theta_{60}) + \nu_{89\to63}C_{89}(1-\theta_{63}) - \nu_{63\to89}C_{63}(1-\theta_{89}) \\
\frac{dC_{60}}{dt} = \nu_{79\to60}C_{79}(1-\theta_{60}) - \nu_{60\to79}C_{60}(1-\theta_{79}) + \nu_{63\to60}C_{63}(1-\theta_{60}) - \nu_{60\to63}C_{60}(1-\theta_{63}) \\
\frac{dC_{79}}{dt} = \nu_{54\to79}C_{54}(1-\theta_{79})\lambda_{54} - \nu_{79\to54}C_{79} + \nu_{60\to79}C_{60}(1-\theta_{79}) - \nu_{79\to60}C_{79}(1-\theta_{60}) \\
\lambda_{54}\left(\frac{dC_{54}}{dt}\right) = \nu_{79\to54}C_{79} - \nu_{54\to79}C_{54}(1-\theta_{79})\lambda_{54}
\end{cases}
\tag{11}
$$

The obtained values for the transition from Td-81 to Oh-65 in the blue paths were used to describe the transition Td-81 to Oh-4 due to the sites Oh-65 and Oh-4 are equivalent energetically speaking [8].

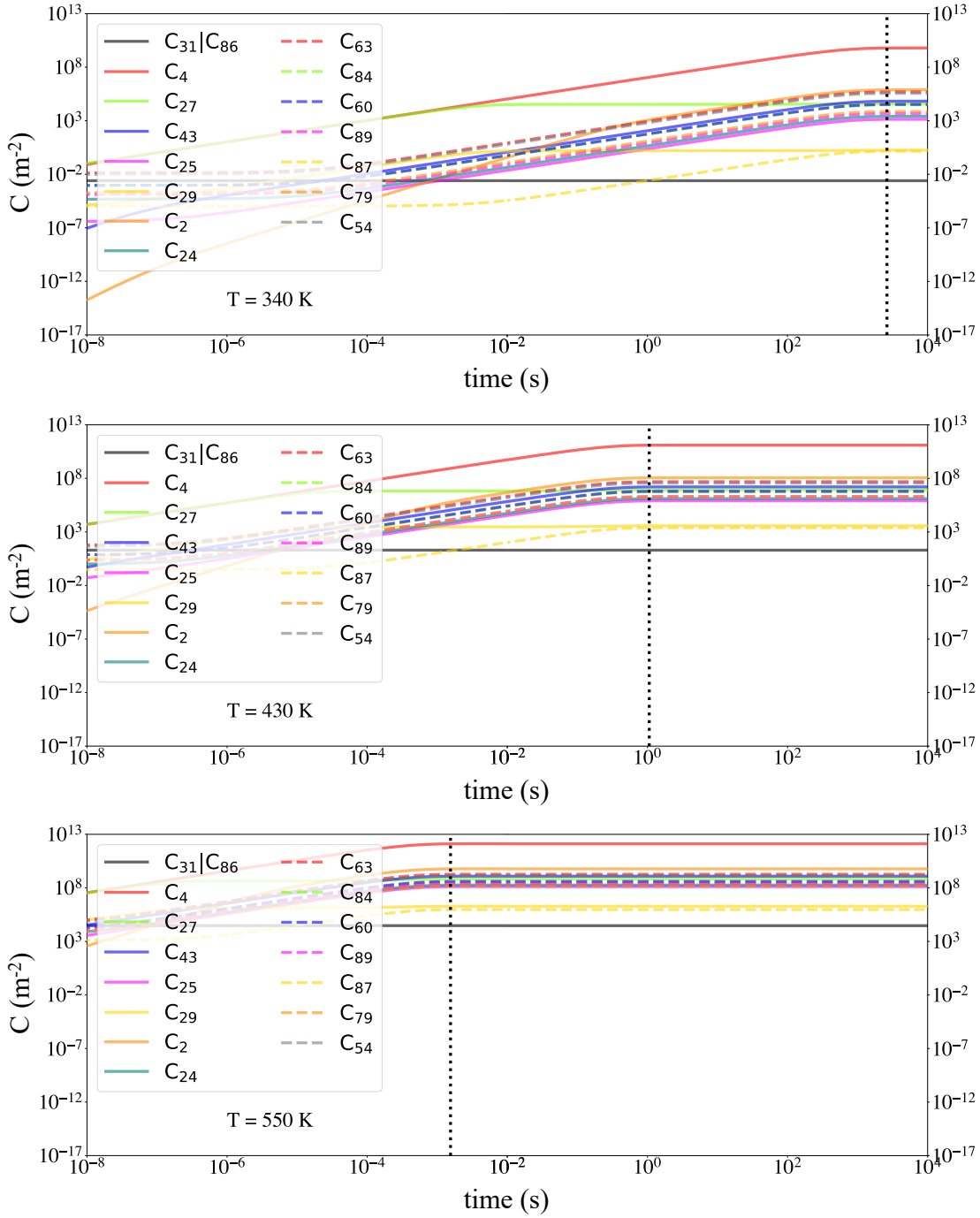

Figure 12: Temporal evolution of H concentration considering the three diffusion paths. The H concentration in the W_{IN} region (Td-31 and Td-86 sites) was fixed to 2.30×10^{7} m^{-3}, 1.81×10^{11} m^{-3} and 2.69×10^{14} m^{-3}, for 340 K, 430 K and 550 K, respectively. The black vertical dotted line indicates the τ_s when the steady-state starts.

C Diffusion of H at the plane of the W/Cu interface

To study the diffusion at the plane of the W/Cu, we consider Oh-4 and Oh-62 as the interstitial sites where H atoms will be placed because they have the lowest value of solution energy [8]. Both of them

have a value of 0.46 eV and 0.47 eV, thus we can consider them to be energetically equivalents. Thus, the planar diffusion of H will be through those sites. Such a plane is represented in Figure 13, the green squares represent the $(2 \times 2 \times 8)$ unit cell of the W/Cu interface, and the grey lines represent the images of such unit cell applying periodic boundary conditions. The blue and red points represent the Oh and Td positions that lie on this plane, and the orange balls are the Cu atoms in the unit cell, whereas the light-orange ones correspond to their respective images.

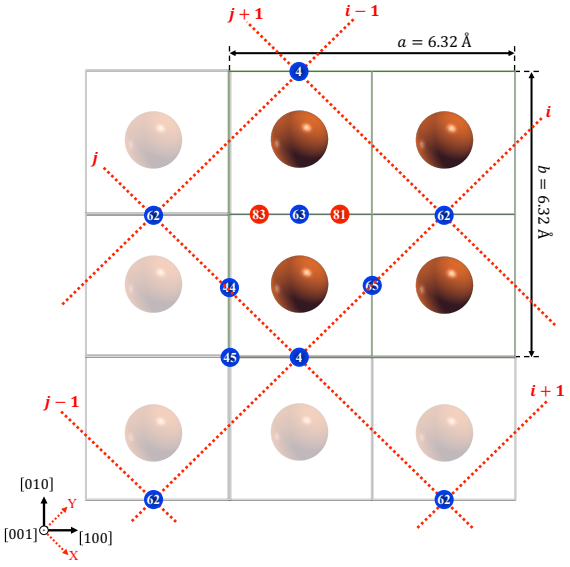

Figure 13: Nearest interstitial sites at the plane of the W/Cu interface.

Let us call the concentration of the diffusing species at position (i, j), $\mathrm{C}_{i,j}$. Since there are 4 nearest neighbors (see Figure 13), there are $\frac{1}{4}$ chance to increase the concentration $\mathrm{C}_{i,j}$ from the particles in a neighboring site of (i, j). Thus the growth rate of $\mathrm{C}_{i,j}$ is:

$$\frac{\mathrm{dC}_{i,j}}{\mathrm{dt}} = \left[\begin{array}{l}\left(\frac{1}{4}\mathrm{C}_{i-1,j} - \frac{2}{4}\mathrm{C}_{i,j} + \frac{1}{4}\mathrm{C}_{i+1,j}\right) + \\ \left(\frac{1}{4}\mathrm{C}_{i,j-1} - \frac{2}{4}\mathrm{C}_{i,j} + \frac{1}{4}\mathrm{C}_{i,j+1}\right)\end{array}\right] p_0 \nu_0 \exp\left(-\frac{E_a}{k_B T}\right), \tag{12}$$

where $p_0 = 4$ is the probability factor (or the number of equivalent paths to reach another interstitial site), ν_0 is the vibrational frequency which is determined using equation (3), E_a is the activation energy, k_B Boltzmann's constant and T the temperature of the reservoir. The term between the brackets can be understood as the discretization of the second derivative along the X and Y directions in Cartesian coordinates: $\frac{\partial^2 \mathrm{C}}{\partial x^2}_{i,j} = \frac{\mathrm{C}_{i-1,j} - 2\mathrm{C}_{i,j} + \mathrm{C}_{i+1,j}}{\Delta x^2}$, $\frac{\partial^2 \mathrm{C}}{\partial y^2}_{i,j} = \frac{\mathrm{C}_{i,j-1} - 2\mathrm{C}_{i,j} + \mathrm{C}_{i,j+1}}{\Delta y^2}$, thus:

$$\frac{\mathrm{dC}_{i,j}}{\mathrm{dt}} = \left[\frac{1}{4}\frac{\partial^2 \mathrm{C}}{\partial x^2}_{i,j}\Delta x^2 + \frac{1}{4}\frac{\partial^2 \mathrm{C}}{\partial y^2}_{i,j}\Delta y^2\right] p_0 \nu_0 \exp\left(-\frac{E_a}{k_B T}\right). \tag{13}$$

As $\Delta x = \Delta y = \lambda$, where λ is the distance between two interstitial sites, we obtain that:

$$\frac{\mathrm{dC}_{i,j}}{\mathrm{dt}} = \frac{p_0 \nu_0 \lambda^2}{4} \exp\left(-\frac{E_a}{k_B T}\right)\left[\frac{\partial^2 \mathrm{C}}{\partial x^2}_{i,j} + \frac{\partial^2 \mathrm{C}}{\partial y^2}_{i,j}\right], \tag{14}$$

which considering Fick's law leads to the following expression for the diffusion coefficient:

$$D_{\mathrm{H}} = \frac{p_0 \nu_0 \lambda^2}{4} \exp\left(-\frac{E_a}{k_B T}\right). \tag{15}$$

Resulting in the following pre-exponential factor:

$$D_0 = \frac{p_0 \nu_0 \lambda^2}{4} = \nu_0 \lambda^2. \tag{16}$$

As $D_0 = \frac{n}{2d}\nu_0\lambda^2$, it can be confirmed that, in this case, the number of nearest neighbors is $n = 4$ and the dimensionality of the motion is $d = 2$. Considering that in this case $\lambda = a/\sqrt{2}$ and $n = 4$, the expression (1) can be transform in (16) only if $\alpha = 1/8$.

Chapter 6

Propagation of the reconstruction in the Cu network

In chapter 3 it was observed a reconstruction of the Cu network at the interface, changing from Cu^{fcc}_{per} and Cu^{bcc}_{per} to Cu^{hcp}. Additionally, in Chapter 4, the inquiry arose regarding whether there would be segregation of H at the interface or within the Cu part, particularly where the thermodynamic model indicated a higher solubility of H. To address both inquiries, we modeled and characterized the boundary between Cu^{fcc}_{per} and Cu^{hcp} structures, which constitutes the main goal of this chapter. To thoroughly characterize such boundary, it is essential to incorporate a significantly larger number of atoms than those used in the DFT models. Consequently, this demands scaling up and implementing Classical Molecular Dynamics, which allows for the modeling of hundreds of thousands of atoms.

6.1 Misfit parameter

As previously discussed in Section 3.1.1, Bramfitt's lattice mismatch theory [126] can be applied to assess the impact of disregistry between two phases on the interfacial free energy. This approach was also employed in this chapter to ascertain the optimal match between the Cu^{fcc}_{per} and Cu^{hcp} structures. However, as these models lie in a larger scale we also study the effect of rotating one structure with respect to the other along the Z axis, an aspect that was not considered in the DFT model of the W/Cu interface, due to its size constraints.

When establishing an interface between two phases, and without assuming atomic forces acting between the two faces, the two superimposed crystals create what is known as a Moiré pattern at the interface [161, 162]. In zones where the crystals fit perfectly, empty areas are observed, while areas with misfit appear as occupied ones; this phenomenon is termed "geometrical fit". If atomic forces act between the two crystals, the empty zones of perfect fit will expand, and the occupied bands corresponding to misfit will contract into dislocation lines, thereby forming a dislocation network at the interface. This is referred in the bibliography as "physical fit" [161].

The Bramfitt's mismatch parameter was determined for different boundaries and various orientation angles to ascertain the optimal geometrical fit between the Cu^{fcc}_{per} and Cu^{hcp} structures. The $Cu^{hcp}(11\bar{2}0)$ plane served as the substrate, with three adsorbates: $Cu^{fcc}_{per}(001)$, $Cu^{fcc}_{per}(001)R45°$, and $Cu^{fcc}_{per}(111)$. All adsorbates corresponded to the bulk Cu^{fcc}_{per} structure, which is expected to be present far from the interface due to its stability under low pressures [163, 164]. Figure 6.1 illustrates the $[uvw]^i_s$ and $[uvw]^i_n$ vectors considered in expression (3.2) to determine their respective $\delta^{(hkl)_s}_{(hkl)_n}$.

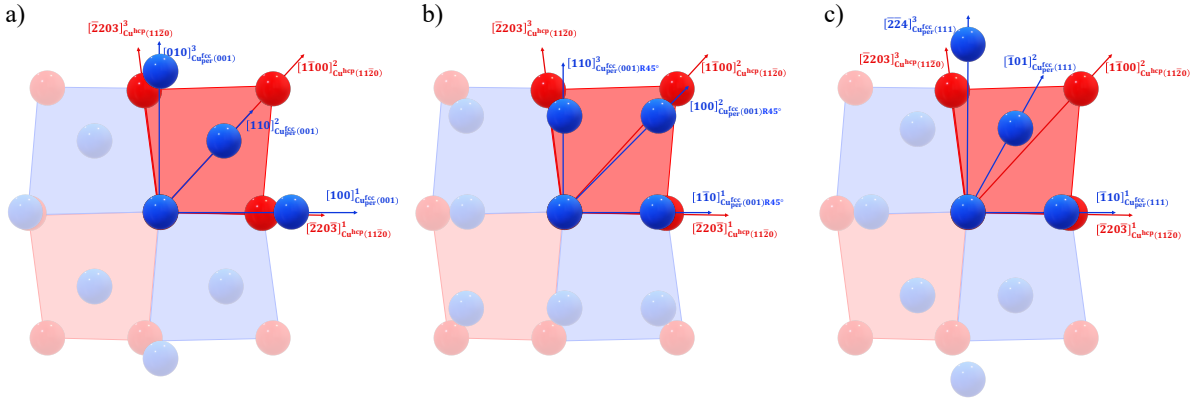

FIGURE 6.1. Crystallographic relationship for Cu^{hcp} (substrate) and Cu^{fcc}_{per} (adsorbate) structures: a) $Cu^{fcc}_{per}(001)$, b) $Cu^{fcc}_{per}(001)R45°$ and c) $Cu^{fcc}_{per}(111)$. The red and blue spheres represent the Cu^{hcp} and Cu^{fcc}_{per} atoms, respectively. Similarly, in red and blue are represented their corresponding $[uvw]^i$ vectors. In the sketch is represented the regions with similar deformations in the Cu^{hcp} network as was previously reported in Section 3.2.

The mismatch parameters for these initial configurations were: 37.54%, 16.94% and 34.36% for $Cu^{fcc}_{per}(001)$, $Cu^{fcc}_{per}(001)R45°$ and $Cu^{fcc}_{per}(111)$ adsorbates, respectively. These results evidence that the most stable and with the highest likelihood of formation among them is the $Cu^{hcp}(11\bar{2}0)/Cu^{fcc}_{per}(001)R45°$ boundary. As previously mentioned, the effect of rotate one structure respect the other was considered, in this case we rotate the adsorbate in the XY plane while keeping fixed the substrate. The Bramfitt's mismatch parameter was determined for each angle of rotation θ formed by the $[1\bar{1}0]$ lattice vector of the adsorbate (see Figure 6.1-b) and the X-axis. The results are shown in Figure 6.2. It is also represented the variation in δ_1, δ_2 and δ_3 which are the terms of the generalized form of the Bramfitt's expression (3.1).

For all the different values of θ, lowest mismatch is observed with $Cu^{fcc}_{per}(001)R45°$ as the adsorbate. This was an expected result, given that the $Cu^{hcp}(11\bar{2}0)$ structure formed at the W/Cu interface, prior to full relaxation, was $Cu^{fcc}_{per}(001)R45°$, as discussed in Chapter 3. Based on this result, the $Cu^{fcc}_{per}(001)R45°$ structure was chosen as the adsorbate, aligning with Bramfitt's statement [126] that a lower misfit ensures greater stability of the interface and a higher likelihood of formation. Subsequently, two of its orientations were considered to construct the $Cu^{hcp}(11\bar{2}0)/Cu^{fcc}_{per}(001)R45°$ boundary. The first orientation was set to $\theta = 0°$, with a mismatch of $\delta^{(hkl)_s}_{(hkl)_n} = 16.94\%$, as mentioned previously, while the second one corresponded to $\theta = 28.2°$, which yielded the lowest mismatch of $\delta^{(hkl)_s}_{(hkl)_n} = 5.27\%$. Henceforth, we will refer to both boundaries as $Cu^{hcp}/Cu^{fcc}_{per}(\theta = 0°)$ and $Cu^{hcp}/Cu^{fcc}_{per}(\theta =$

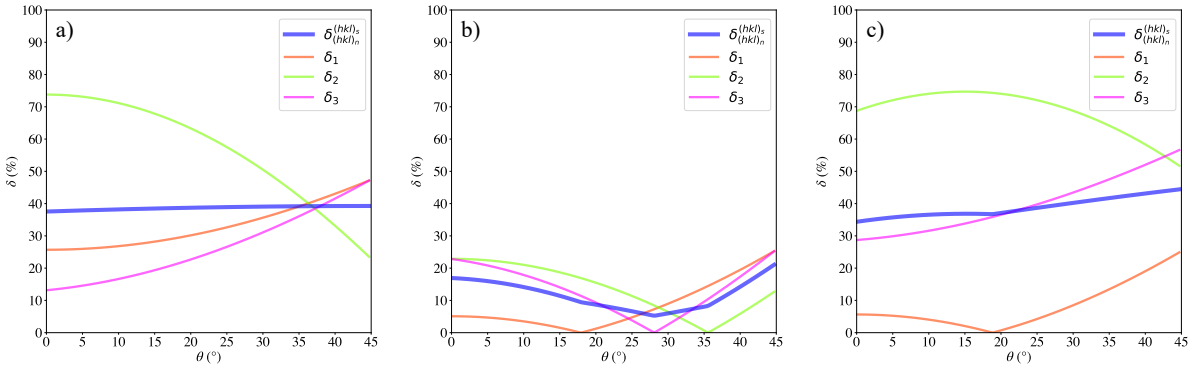

FIGURE 6.2. Variation of the Bramfitt's mismatch parameter as function of the rotation angle θ of the Cu^{fcc}_{per} adsorbate: a) $Cu^{fcc}_{per}(001)$, b) $Cu^{fcc}_{per}(001)R45°$ and c) $Cu^{fcc}_{per}(111)$.

28°) for clarity.

6.1.1 Supercell of the boundaries

At this point, we find a similar challenge to that discussed in Chapter 3 in building the W/Cu interface: how to create the unit cells of the $Cu^{hcp}/Cu^{fcc}_{per}(\theta = 0°)$ and $Cu^{hcp}/Cu^{fcc}_{per}(\theta = 28°)$ boundaries? In Chapter 3, we opted to employ the mean values of the W and Cu lattice parameters in the X and Y directions to construct the unit cell of the interface. This decision was driven by the limitations imposed by the size of the model, which was dictated by the computational resources required for DFT calculations. However, in this case, as we intend to conduct MD simulations, the size of the unit cells is no longer a limiting factor. Consequently, to ensure symmetry in both lattices, we constructed a sufficiently large supercell that minimizes the linear disregistry in the X and Y directions.

When the lattices that are coupled at the boundary are similar to each other, the size of the supercell can be graphically determined through the respective Moiré pattern of the boundary, as demonstrated in reference [20]. However, the several transformations are done in one of the lattice, the Moiré pattern is not enough to find a symmetric cell and it is necessary to used a mathematical method [71]. In Figure 6.3 is represented the Moiré pattern of the $Cu^{hcp}/Cu^{fcc}_{per}(\theta = 0°)$ and $Cu^{hcp}/Cu^{fcc}_{per}(\theta = 28°)$ boundaries. The $Cu^{hcp}/Cu^{fcc}_{per}(\theta = 0°)$ (Figure 6.3-a) is one of those cases where the sizes of the supercell can be identified graphically analysing its Moiré pattern, where the empty areas are the regions where a perfect geometrical fit is found between substrate and adsorbate. However, the $Cu^{hcp}/Cu^{fcc}_{per}(\theta = 28°)$ has a Moiré pattern more complex, as it is appreciable in Figure 6.3-b, therefore this graphical way cannot be used, but a mathematical one.

Let's consider two orthorhombic lattices with parameters $2a_1$, $2b_1$ and $2c_1$, and $2a_2$, $2b_2$ and $2c_2$, respectively. The size of both structures in the XY plane are $(2n_{1_x}a_1 \times 2n_{1_y}b_1)$ for lattice 1 and $(2n_{2_x}a_2 \times 2n_{2_y}b_2)$ for the lattice 2, being n_{i_x} and n_{i_y} the number of primitive cells for the i-th lattice in the X and Y directions respectively. First, let's consider that both lattices are perfectly aligned as shown in Figure 6.4-a, which will be the equivalent of the $Cu^{hcp}/Cu^{fcc}_{per}(\theta = 0°)$ boundary in Figure 6.3-a.

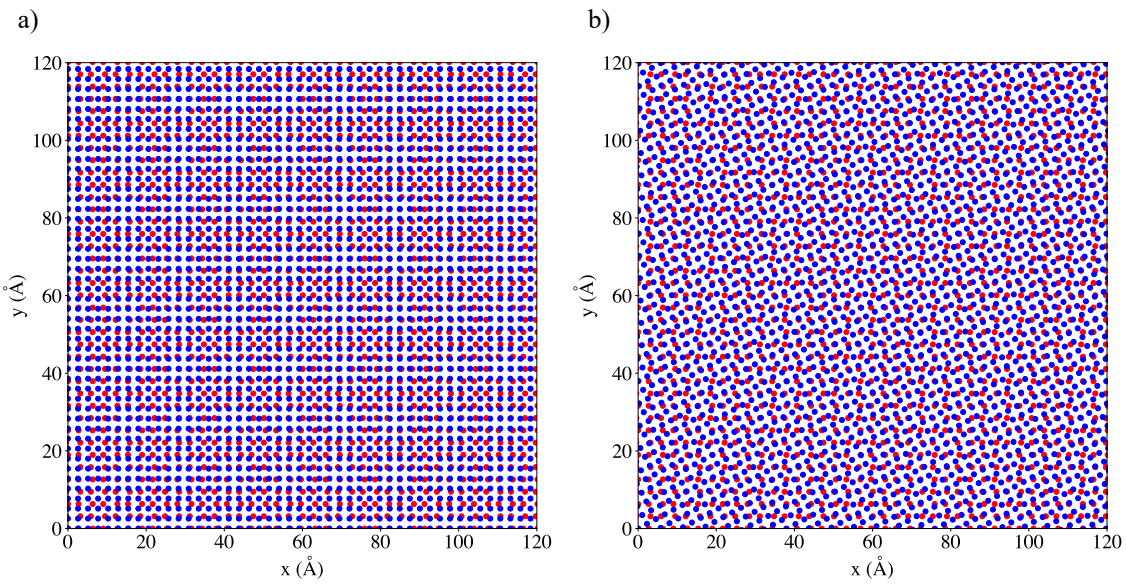

Figure 6.3. Moiré pattern of a) $Cu^{hcp}/Cu^{fcc}_{per}(\theta = 0°)$ and b) $Cu^{hcp}/Cu^{fcc}_{per}(\theta = 28°)$ boundaries. Red and blue balls stand for the substrate Cu^{hcp} and the adsorbate $Cu^{fcc}_{per}(001)R45°$, respectively. The adsorbate rotation for b) was performed along the axis perpendicular to the XY plane, passing through the origin (0,0).

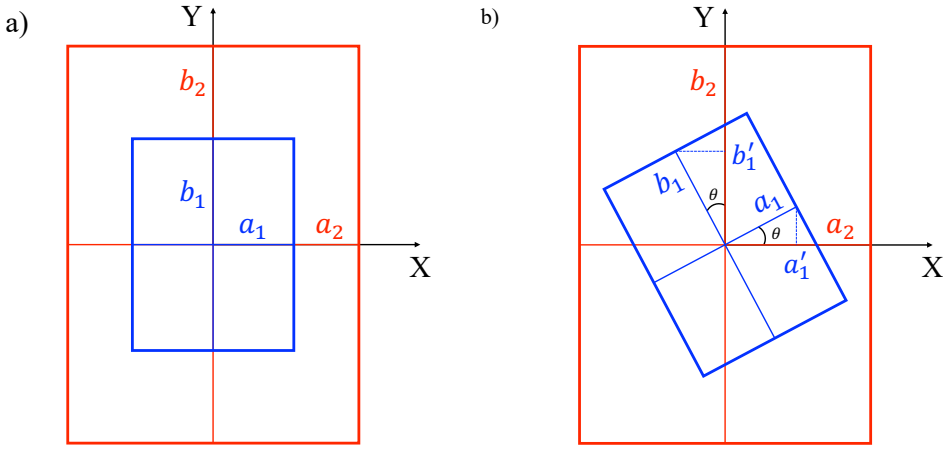

Figure 6.4. Schematic representations in the XY plane of two orthorhombic lattices. a) both lattices are aligned and b) lattice 1 is rotated θ degrees respect to lattice 2.

The residual differences in the X and Y directions between both lattices, when they are coupled in their middle point (see Figure 6.4), are defined as:

$$\Delta_x = |n_{1_x} a_1 - n_{2_x} a_2|, \tag{6.1a}$$

$$\Delta_y = |n_{1_y} b_1 - n_{2_y} b_2|. \tag{6.1b}$$

To achieve a symmetric supercell in the XY plane, the values of Δ_x and Δ_y need to be minimized with respect to n_{i_x} and n_{i_y}, respectively. Since expressions (6.1) represent non-negative values, their minimum values are zero. This implies that the following equalities hold:

$$n_{1_x} a_1 = n_{2_x} a_2, \tag{6.2a}$$

$$n_{1_y} b_1 = n_{2_y} b_2. \tag{6.2b}$$

Where the following ratios are obtained:

$$\frac{n_{1_x}}{n_{2_x}} = \frac{a_2}{a_1}, \tag{6.3a}$$

$$\frac{n_{1_y}}{n_{2_y}} = \frac{b_2}{b_1}. \tag{6.3b}$$

Thus, an expression to determine the number of primitive cells in the X and Y directions that only depends of the cells parameters is obtained. If one of the lattices is rotated by an angle θ relative to the other, as shown in Figure 6.4-b, the values of a_1 and b_1 are substituted in expressions (6.3) with their respective projections onto the X and Y axes, denoted as $a_1' = a_1 \cos\theta$ and $b_1' = b_1 \cos\theta$. This scenario corresponds to the $\mathrm{Cu^{hcp}/Cu^{fcc}_{per}}(\theta = 28°)$ boundary case:

$$\frac{n_{1_x}}{n_{2_x}} = \frac{a_2}{a_1'} = \frac{a_2}{a_1 \cos\theta}, \tag{6.4a}$$

$$\frac{n_{1_y}}{n_{2_y}} = \frac{b_2}{b_1'} = \frac{a_2}{b_1 \cos\theta}. \tag{6.4b}$$

It is appreciable that when $\theta = 0°$, expressions (6.4) become in (6.3). For our boundaries, both lattice 1 and 2 are squares in the XY plane, hence $\Delta_x = \Delta_y$, indicating that an equal number of primitive cells must be considered in both directions. Consequently, we will exclusively focus on the ratio in the X direction. Considering the $\mathrm{Cu^{hcp}}(11\bar{2}0)$ and $\mathrm{Cu^{fcc}_{per}}(001)\mathrm{R}45°$ structures as lattice 2 and 1, respectively, with cell parameters $a_2 = 6.32$ Å and $a_1 = 2.57$ Å[1], we can determine their ratios for both the $\mathrm{Cu^{hcp}/Cu^{fcc}_{per}}(\theta = 0°)$ and $\mathrm{Cu^{hcp}/Cu^{fcc}_{per}}(\theta = 28°)$ boundaries, through expressions (6.3a) and (6.4a), respectively:

$$\frac{n_{1_x}}{n_{2_x}} = \frac{6.3242}{2.5732} = 2.4577, \tag{6.5a}$$

$$\frac{n_{1_x}}{n_{2_x}} = \frac{a_2}{a_1 \cos\theta} = \frac{6.3242}{2.5732 \cos(28.2°)} = 2.7835. \tag{6.5b}$$

In these expressions, more decimal digits were considered for the values of a_1 and a_2, due to it is necessary to have a very precise ratios due to they directly affect n_{1_x} and n_{2_x}. The next step is to find a pair of values n_{1_x} and n_{2_x} that satisfy the expressions 6.5a and 6.5b, which is summarized in Table 6.1.

Table 6.1. Ratios for the $\mathrm{Cu^{hcp}/Cu^{fcc}_{per}}(\theta = 0°)$ and $\mathrm{Cu^{hcp}/Cu^{fcc}_{per}}(\theta = 28°)$ supercells.

Boundary	n_{1_x}	n_{2_x}	$\frac{n_{1_x}}{n_{2_x}}$	$\frac{a_2}{a_1 \cos\theta}$	Relative error (%)
$\mathrm{Cu^{hcp}/Cu^{fcc}_{per}}(\theta = 0°)$	86	35	2.4571	2.4577	0.02
$\mathrm{Cu^{hcp}/Cu^{fcc}_{per}}(\theta = 28°)$	103	37	2.7838	2.7835	0.01

The values reported for n_{1_x} and n_{2_x} for both boundaries exhibit a ratio that deviates from the $\frac{a_2}{a_1 \cos\theta}$ term lower than 0.02%. Consequently, these specific values were selected to construct the respective supercells. In the following section is explained how their supercells were built as well as the simulation setup.

[1]The values of cell parameters in the $\mathrm{Cu^{fcc}_{per}}$ bulk employed in the MD simulation were different from those used in DFT. For MD we used the value to which the $\mathrm{Cu^{fcc}_{per}}$ bulk converge using embedded-atom method (EAM) potential for Cu reported in reference [165]. See section 6.2.

6.2 Molecular Dynamics simulation setup

The MD simulations were carried out in the LAMMPS code [166], whereas the free version of OVITO software [167] was used for the visualization of the atoms and their positions. The simulation cells contain only Cu species whose interactions were described by the EAM potential [168, 169] developed by Mendelev and King [165]. Such a potential was developed to study point and extended defects in fcc materials, and it constitutes an improvement of the previous version [170] to better describe the energy of stacking fault.

6.2.1 Interatomic potential

The origins of the EAM potentials stem from the corollary established by Stott and Zaremba [171], which asserts that the energy of an impurity in a host (or embedding energy) is a functional of the electron density of the unperturbed (i.e., without impurity) host. This is,

$$E = \mathcal{F}_{Z,R}[\rho_h(r)], \tag{6.6}$$

where $\rho_h(r)$ is the unperturbed host electron density, and Z and R are the type and position of the impurity, respectively. In practical application, this statement is used by considering each atom within a system as an impurity embedded within a host comprising all the other atoms. The functional $\mathcal{F}$ is universal and independent of the considered host and its form is unknown. A straightforward approximation involves assuming that the embedding energy solely relies on the immediate surroundings of the impurity [172], or alternatively, that the impurity encounters a locally uniform electron density [171]. This is considered a local approximation or the lowest-order term involving successive gradients of the density:

$$E_{tot} = \sum_i F_i(\rho_{h,i}), \tag{6.7}$$

being F_i the embedding energy, which is a function of $\rho_{h,i}$, the electronic density of the host at the position R_i but without the atom i-th. In this case each atom is assumed to experience a locally uniform electron gas, and the embedding energy is defined to be the energy of that atom in a uniform electron gas relative to the atom separated from the electron gas. The final expression for the total energy of EAM potential includes a short-range pairwise repulsion between the cores to take into account the core-core repulsion, originally neglected from expression (6.7):

$$E_{tot} = \sum_i F_i(\rho_{h,i}) + \frac{1}{2}\sum_i \sum_{j\neq i} \phi_{ij}(r_{ij}). \tag{6.8}$$

Where ϕ_{ij} is the short-range pair potential and r_{ij} is the distance between atoms the i-th and j-th. Assuming that the host density is closely approximated by a sum of the atomic densities (ρ_j^a), we end up with the expression of the total energy of the EAM potential:

$$E_{tot} = \sum_i F_i\Big(\sum_{j\neq i} \rho_j^a(r_{ij})\Big) + \frac{1}{2}\sum_i \sum_{j\neq i} \phi_{ij}(r_{ij}). \tag{6.9}$$

Both summations in the formula are over all neighbors j-th of atom i-th within the cutoff distance. The ground-state properties of the system can be calculated from

expression (6.9), which is precisely what LAMMPS does. Details regarding the way of proceeding with the calculations of the solid properties can be found in reference [169].

6.2.2 Geometry of the boundaries

Currently, we have established the interatomic potential to characterize the Cu-Cu interactions, a crucial step preceding MD simulations. Consequently, the next phase involves defining the working cells to be modeled, which is treated here. In the preceding section, the number of primitive cells was determined to ensure a nearly symmetric supercell for both boundaries in the XY plane (see Table 6.1). Therefore, only remains to establish the dimensions in the Z direction.

In this direction, the substrate and adsorbate sub-supercells were created with a thickness of $z_{subs} = 41.36$ Å and $z_{ads} = 58.22$ Å, respectively. The boundary supercells were then assembled using two substrate sub-supercells separated by an adsorbate sub-supercell in the Z direction, without any gap or vacuum layers. This configuration allows for the application of periodic boundary conditions in the Z direction. As a result, the boundary supercells were composed by two substrate-adsorbate interfaces and no surfaces. The description of these working cells is summarized in Table 6.2.

Table 6.2. Details of the boundary supercell geometries. The substrate layers (Cu^{hcp}) are shown by the red and yellow-green sub-supercells, while the adsorbate sub-supercell (Cu^{fcc}_{per}) is represented in blue.

Boundary supercells	$Cu^{hcp}/Cu^{fcc}_{per}(\theta = 0°)/Cu^{hcp}$	$Cu^{hcp}/Cu^{fcc}_{per}(\theta = 28°)/Cu^{hcp}$
Number of atoms	550272	615104
Gap layer	0 Å	0 Å
Vacuum layer	0 Å	0 Å
Cross section (XY plane)	(221.3×221.3) Å^2	(234.0×234.0) Å^2
$(n_{2_x} \times n_{2_y} \times n_{2_z})$	$(35 \times 35 \times 4)$	$(37 \times 37 \times 4)$
$(n_{1_x} \times n_{1_y} \times n_{1_z})$	$(86 \times 86 \times 16)$	$(103 \times 103 \times 16)$
$(n_{3_x} \times n_{3_y} \times n_{3_z})$	$(35 \times 35 \times 4)$	$(37 \times 37 \times 4)$
	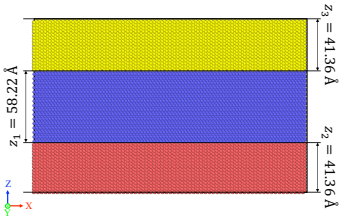	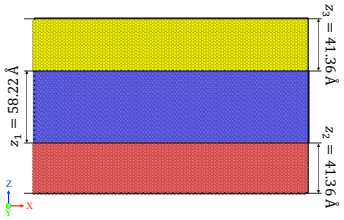

The primitive cell for the Cu^{hcp} structure was adopted from the model of the W/Cu interface developed in Chapter 5.1. As a result, this primitive cell has dimensions of $(2 \times 2 \times 4)$. Additionally, to construct the Cu^{fcc}_{per} bulk, a lattice parameter of 3.639 Å

was employed, which is 0.019 Å greater than the value used in the DFT calculations. This parameter was determined through volume relaxation of a small Cu_{per}^{fcc} cell using the interatomic potential developed by Mendelev and King [165].

6.2.3 Sequence of calculations

Once the supercells of the boundaries were correctly defined we proceed to run the MD simulations. To remove any stress created by the coupling procedure, the system was initially fully relaxed at 0 K temperature. The system's volume and atomic positions were allowed to change while an external pressure of 0 Pa was applied to the supercell. The energy minimization was performed with stopping tolerance values of 10^{-25} for the energy and 10^{-25} eV/Å for the forces.

After the volume relaxation, both simulation cells were subjected to an NPT ensemble during 100 ps with a time step of 5 fs. The calculations were performed at four distinct temperatures: 300 K, 430 K, 550 K, and 700 K. The 300 K temperature was selected for analyzing behavior at room temperature. The 430 K and 550 K temperatures correspond to the two highest temperatures at the rear of the W armor (the actual position of the W/Cu interface at the W monoblocks in the ITER-like divertor) under the exposure conditions for the three different scenarios considered during the steady-state plasma in reference [173]. Meanwhile, the 700 K temperature was considered an extreme condition. The external pressure was fixed to 0 Pa at the beginning and the end of the simulations. The Nosé-Hoover barostat and thermostat [174, 175] were employed to equilibrate the system to the target external pressure of $P = 0$ Pa and the temperatures of $T = 300$ K, 430 K, 550 K, and 700 K.

After the 100 ps of the NPT simulations, the simulation cells were subjected to a micro-canonical (NVE) environment. The atomic positions in a slab of 10 Å in the Cu^{hcp} structure were fixed to simulate the reconstruction of the Cu network induced by the W/Cu interface. The NVE ensemble was simulated during 100 ns with the same time step as the NPT, 5 fs.

6.2.4 Physical quantities

To assess the characterization of the supercells, certain quantities were analyzed both temporally and spatially. Temporal analysis helped ascertain the convergence conditions of the simulations, while spatial analysis contributed in identifying the propagation of the reconstruction within the Cu network. The quantities observed temporally included: temperature (T), pressure (P), the size of the supercell in the X, Y, and Z directions (l_x, l_y, and l_z), volume of the supercell, mean potential energy per atom ($\overline{U}$), mean kinetic energy per atom ($\overline{K}$), and mean total energy per atom ($\overline{E}_{tot}$).

For the spatial analysis the supercells were divided in slices of thickness Δz along the Z direction. In such slices, it was determined the mean potential energy per atom and the mean concentration of structure types. The mean potential energy per atom was

determined as following:

$$\overline{U} = \frac{\sum_i U_i}{N}, \tag{6.10}$$

where U_i is the potential energy of the atom i-th within the slice, and N is the total number of atoms in the slice. The mean concentration of structure types were identified by using the modifier Common Neighbor Analysis (CNA) [176] in OVITO [167]:

$$\overline{c_x} = \frac{N_x}{N}, \tag{6.11}$$

where x defines the structure types: fcc, bcc, hcp, icosahedral (ico) and other, N_x is the number of atoms in the slice with the structure x, and N is the total number of atoms in the slice.

The CNA method serves as a filtering technique for categorizing atoms within crystalline systems [177]. Its primary aim is to achieve a detailed comprehension of the association of atoms with specific phases and the identification of those associated with defects. In OVITO, this method can be implemented through four distinct modes: conventional, adaptive, interval, and bond-based. These modes vary in their criteria for selecting the threshold distance used to ascertain whether a pair of atoms is bonded or not. In our case we employed the adaptive CNA [178], which determines the optimal cutoff radius automatically for each individual particle.

During the characterization of the boundaries we also study the formation of point and extended defects. The point defects, or 0-dimensionl defects, such as vacancies and self-interstitial atoms were identified through the Wigner-Seitz defect analysis modifier of OVITO. This method compares the atomic positions of two configurations: the *reference* and the *displaced* [179]. To use the same formulation than OVITO, we will refer to the atoms of the reference and displaced systems as *sites* and *atoms*, respectively. The method creates the Wigner-Seitz cells for the sites of the reference system and count how many atoms from the displaced system occupy the cells. If an atom resides on or in the vicinity to a site, we say that the site has been occupied by the atom, while if the site remains unoccupied by any atom, is termed as *vacancy sites*. Alternatively, some sites may accommodate more than one atom, denoted as *interstitial sites*, with the atoms occupying them referred to as interstitial atoms. An illustrative representation how the method works is done in reference [179].

1-dimensional defects such as dislocations lines were identified in both supercells at the end of the NVE simulations. This was done implementing the so-called Dislocation Extraction Algorithm (DXA) [180, 181]. This approach converts the initial atomistic depiction of a dislocated crystal into a line-oriented representation of the dislocation network. It also establishes the Burgers vector for each dislocation and discerns dislocation junctions. A deeper explanation of how this modifier works can be found in reference [179]. Readers interested in a more detailed explanation about dislocation lines can find it in reference [182].

Grain boundaries, as example of 2-dimensional defects, were identified by a combination of the modifiers Polyhedral Template Matching (PTM) [183] followed by the Grain segmentation in OVITO. PTM has the same goal as CNA, however, it classifies other structures that are treated as other in CNA such as, simple cubic, cubic diamond, hexagonal diamond and graphene. The local structural environment and orientation of

each atom determined by PTM are used to create a graph representation of the system. In such representation each atom is a graph node and each neighbor bond is considered a graph edge. The different grains are formed by hierarchical clustering of the graph, which is done by the Grain segmentation modifier [179].

6.3 Volume relaxation simulations

6.3.1 $Cu^{hcp}/Cu^{fcc}_{per}(\theta = 0°)/Cu^{hcp}$ supercell

The $Cu^{hcp}/Cu^{fcc}_{per}(\theta = 0°)/Cu^{hcp}$ boundary took 5.39 ps approximately to converge to its final structure during the volume relaxation. During this relaxation process, the working supercell underwent compression in the X and Y directions, decreasing from 221.3 Å to 215.3 Å, while in the Z direction, the supercell expanded from 140.9 Å to 143.5 Å. Such modifications lead to a decrement of the volume from 6.91×10^6 Å^3 to 6.65×10^6 Å^3. The mean potential energy per atom converged to −3.40 eV, and since these calculations were conducted at 0 K, the mean kinetic energy per atom was zero. Consequently, the mean total energy per atom was −3.40 eV. In Figure 6.5, it is possible to appreciate the evolution of such variable over time. The lavender region delimits the zone where the dispersion is less than 0.05% of the converged value for each variable.

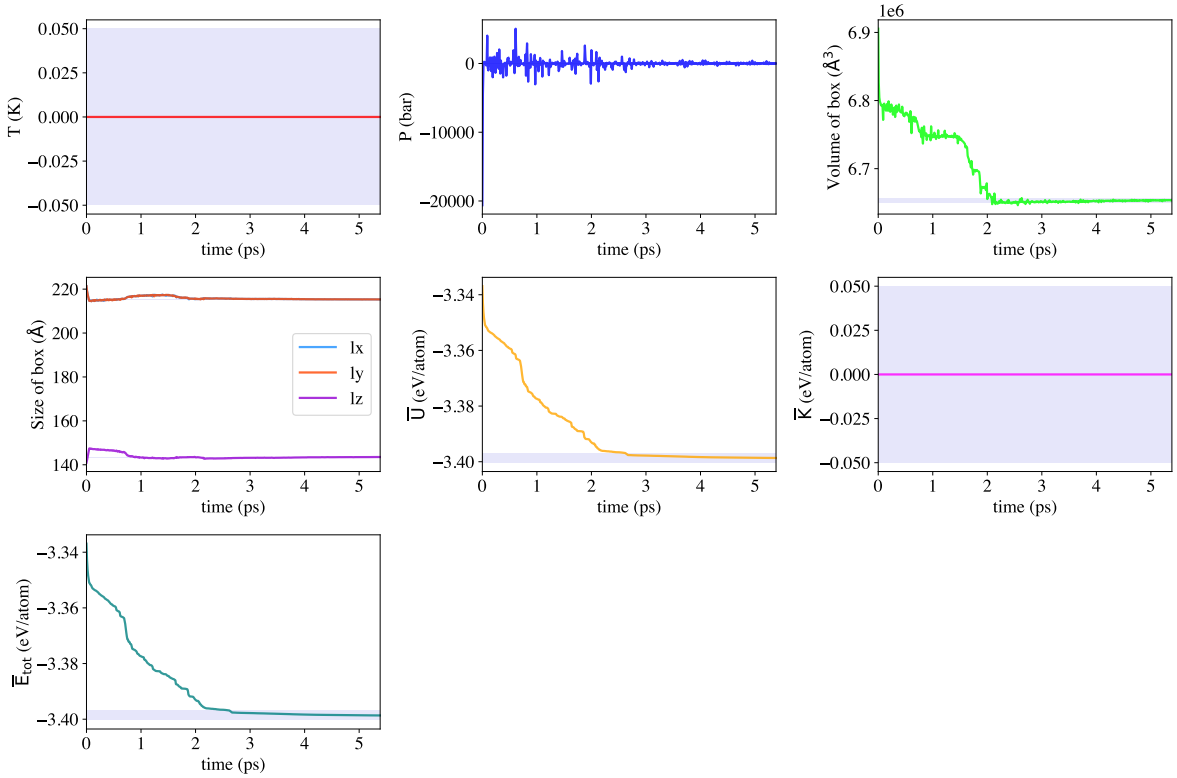

Figure 6.5. Temporal analysis of the physical quantities during the volume relaxation of the $Cu^{hcp}/Cu^{fcc}_{per}(\theta = 0°)/Cu^{hcp}$ structure. The convergence zone, marked by the lavender region, was determined based on a dispersion of 0.05% of the value of each quantity at time 5.39 ps. A video of this relaxation process is available in reference [21].

Once the $Cu^{hcp}/Cu^{fcc}_{per}(\theta = 0°)/Cu^{hcp}$ converged to its final structure we proceed to spatially analyze its configuration. A slice thickness of $\Delta z = 2.5$ Å was utilized to section the supercell along the Z direction. The CNA modifier identified the structure types within the supercell, revealing that at the interface between the $Cu^{hcp}/Cu^{fcc}_{per}(\theta = 0°)$ structures, there is an amorphous layer of 8 Å approximately. The formation of this amorphous layer is associated to the matching process between the two grains, which is accompanied by a rise in the potential energy per atom to -3.27 eV. In Figure 6.6 is represented the mean potential energy per atom and the structure type concentrations along the Z direction of the supercell. The vertical lavender regions mark the area where initially the interface between the grains was placed within the supercell. In Figure 6.6-a is appreciable the increment of the potential energy per atom at the amorphous layer, which is majorly represented by atoms whose structure is classified as "Other" by the CNA modifier (see Figure 6.6-b). The final state of the types of structures can be appreciated in Appendix C.1 and the evolution of the system's relaxation in reference [21].

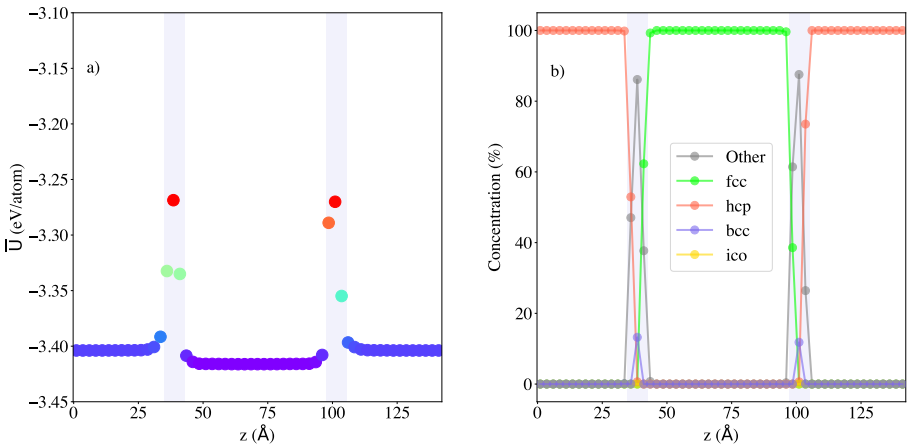

Figure 6.6. Spatial analysis of the $Cu^{hcp}/Cu^{fcc}_{per}(\theta = 0°)/Cu^{hcp}$ boundary. The initial position of the interfaces between the $Cu^{hcp}/Cu^{fcc}_{per}(\theta = 0°)$ structures are represented by the lavender region.

6.3.2 $Cu^{hcp}/Cu^{fcc}_{per}(\theta = 28°)/Cu^{hcp}$ supercell

The $Cu^{hcp}/Cu^{fcc}_{per}(\theta = 28°)/Cu^{hcp}$ cell needed more time to reach the ground-state, in this case was necessary 6.07 ps as shown in Figure 6.7. The relaxed supercell experienced approximately the same compression in the X and Y directions and expansion along the Z axis as observed in the $Cu^{hcp}/Cu^{fcc}_{per}(\theta = 0°)/Cu^{hcp}$ boundary. The structure changed its cell parameter in the X and Y directions from 234.0 Å to 228.1 Å, while in the Z direction, it changed from 140.9 Å to 143.1 Å. These modifications approximately lead to the same decrement in the volume than in the above supercell, which changed from 7.72×10^6 Å^3 to 7.44×10^6 Å^3. The mean potential energy per atom converged to a value of -3.80 eV. It is crucial to note that while the mean potential energy per atom did converge to a lower value than in the $Cu^{hcp}/Cu^{fcc}_{per}(\theta = 0°)/Cu^{hcp}$ boundary, this does not necessarily imply that the $Cu^{hcp}/Cu^{fcc}_{per}(\theta = 28°)/Cu^{hcp}$ structure is more stable than the $Cu^{hcp}/Cu^{fcc}_{per}(\theta = 0°)/Cu^{hcp}$

one. The mean potential energy variable averages individual values of U with respect to the number of atoms in the system. Since the $Cu^{hcp}/Cu^{fcc}_{per}(\theta = 28°)/Cu^{hcp}$ supercell has 64832 more atoms than the $Cu^{hcp}/Cu^{fcc}_{per}(\theta = 0°)/Cu^{hcp}$, the mean potential energy in the $Cu^{hcp}/Cu^{fcc}_{per}(\theta = 28°)/Cu^{hcp}$ structure is approximately 1.12 times larger. Similarly to the previous case, the mean total energy per atom was equal to the mean potential energy due to the null value of the mean kinetic energy per atom. In Figure 6.8, it is possible to appreciate the spatial evolution of those variables in the $Cu^{hcp}/Cu^{fcc}_{per}(\theta = 28°)/Cu^{hcp}$ supercell and the structure type. As in the above figure the horizontal lavender region delimits the zone where the dispersion is less than 0.05% of the converged value for each variable.

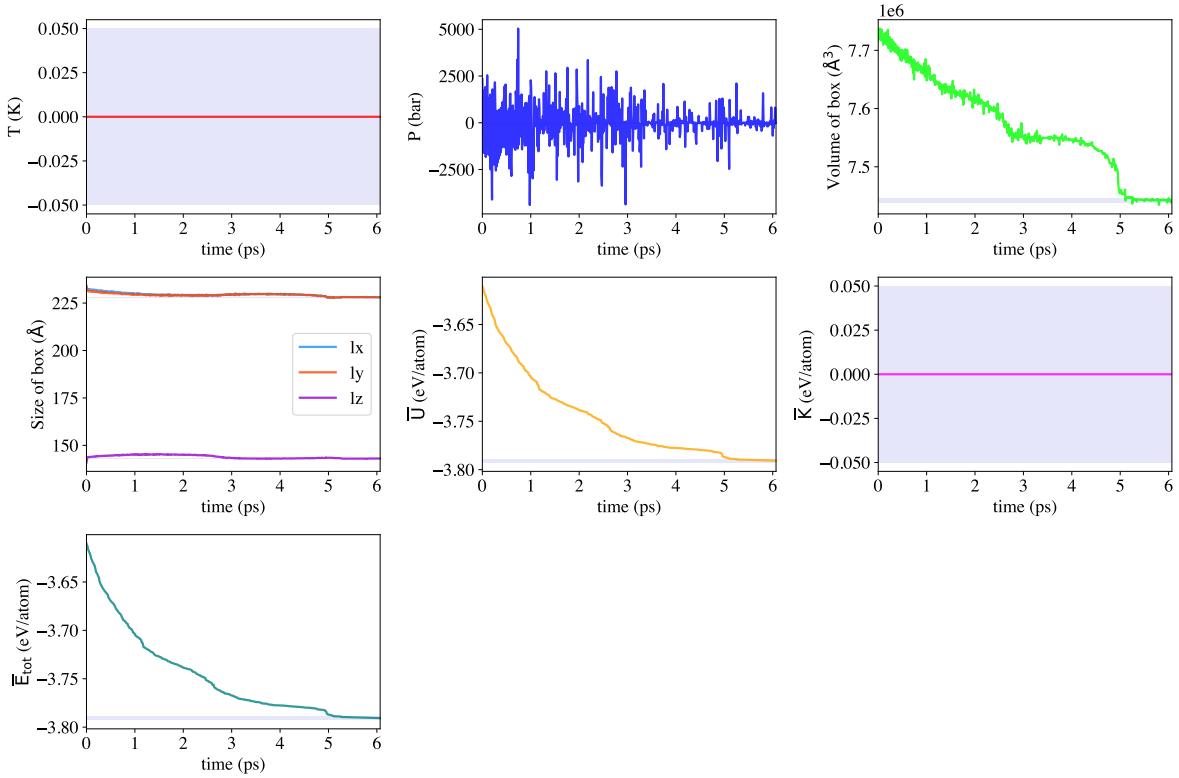

Figure 6.7. Temporal analysis of the physical quantities during the volume relaxation of the $Cu^{hcp}/Cu^{fcc}_{per}(\theta = 28°)/Cu^{hcp}$ structure. The convergence zone, marked by the lavender region, was determined based on a dispersion of 0.05% of the value of each quantity at time 6.07 ps. A video of this relaxation process is available in reference [21].

The spatial analysis was conducted using the same slice thickness of $\Delta z = 2.5$ Å to divide the supercell along the Z direction. In Appendix C.1 is represented the final structure of the supercell after the volume relaxation. This structure differs from the one obtained for the $Cu^{hcp}/Cu^{fcc}_{per}(\theta = 0°)/Cu^{hcp}$ boundary. On one side, the atoms on the edges of the Cu^{fcc}_{per} sub-supercell underwent a reconstruction, resulting in them being arranged in bands resembling an interference pattern, with one band corresponding to fcc type, the next to "Other", and so forth in succession. On the other side the two $Cu^{hcp}/Cu^{fcc}_{per}(\theta = 28°)$ interfaces along the Z direction evolved differently during the relaxation. The interface located at 38.8 Å presented the same amorphous layer of 8 Å thickness as in the $Cu^{hcp}/Cu^{fcc}_{per}(\theta = 0°)/Cu^{hcp}$ structure, while the interface located at 101.4 Å increased its amorphous layer up to 12 Å approximately. In this second interface, there are some loops of atoms that the CNA modifier recognizes as "Other" structure,

which start and end in the amorphous layer while propagating into the Cu^{hcp} bulk.

The interference pattern in the edges of the Cu^{fcc}_{per} sub-supercell is an artifact resulting from the periodic boundary conditions in the XY plane. As the Cu^{fcc}_{per} sub-supercell was rotated $\theta = 28.2°$ this leads to cluster of atoms uniformly spread along the surface when the supercell was created by cutting along the X and Y directions. The disparate behavior of the two interfaces can be attributed to their inherent differences. The stacking of the Cu^{hcp} and Cu^{fcc}_{per} structures along the [100] direction follows an ABABA pattern. Specifically, the interface at 38.8 Å was formed by aligning the B layer of the Cu^{hcp} structure with the A layer of the Cu^{fcc}_{per} structure, whereas the interface at 101.4 Å was formed with the opposite arrangement. The interface located at 38.8 Å exhibits a Bramfitt's misfit of 5.27% (as detailed in Section 6.1). However, the misfit at the interface positioned at 101.4 Å is approximately 22.9%. The higher misfit observed at the second interface directly implies a lower stability and match between the grains, consequently resulting in the formation of defects such as dislocations. This issue could potentially be addressed by introducing an additional layer in the Cu^{fcc}_{per} sub-supercell to achieve uniform stacking in both interfaces. However, our decision to maintain the structure as it is stemmed from our interest in exploring the impact of different grain stackings in the propagation of the Cu^{hcp} at different temperatures.

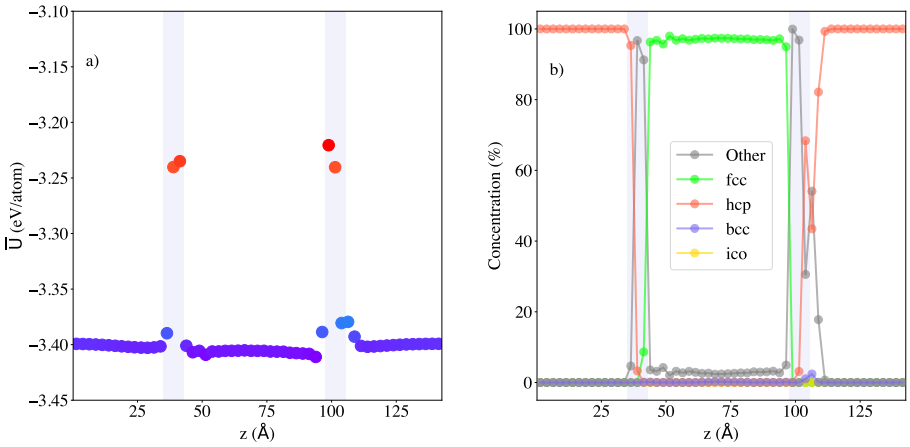

Figure 6.8. Spatial analysis of the $Cu^{hcp}/Cu^{fcc}_{per}(\theta = 28°)/Cu^{hcp}$ boundary. The initial position of the interfaces between the $Cu^{hcp}/Cu^{fcc}_{per}(\theta = 28°)$ structures are represented by the lavender region.

In Figure 6.8 are plotted the spatial variation of the mean potential energy per atom and the concentration of structure types along the Z direction. As in the previous case, it is appreciable the increment of the mean potential energy per atom at the interfaces between the grains. Those values were higher than at the interfaces in the $Cu^{hcp}/Cu^{fcc}_{per}(\theta = 0°)/Cu^{hcp}$ indicating a higher strain at the amorphous layers. It is important to highlight that these results do not contradict the predictions done using the Bramfitt's misfit parameter. Such a parameter was an initial guess of the geometrical misfit between two surfaces placed one on top of the other. After volume relaxation is completed, the structure of the matching layers is defined by the actual physical fit rather than the initial geometrical fit estimated by the Bramfitt's misfit parameter. In Figure 6.8-b, the decrease in the fcc concentration at the interface located at 101.4 Å is noticeable, indicating an increase in the thickness of the amorphous layer.

6.4 NPT ensemble

Once the volume relaxation converged to the defined thresholds, both boundaries were subjected to a NPT simulation as described in Section 6.2.3. In this section, we will focus in the influence of the temperature in the morphology of both structures. The full results of the spatial analysis can be found in Appendix C.2.

6.4.1 $Cu^{hcp}/Cu^{fcc}_{per}(\theta = 0°)/Cu^{hcp}$ supercell

The discrepancy between the $Cu^{hcp}/Cu^{fcc}_{per}(\theta = 0°)/Cu^{hcp}$ boundary at the end of the NPT simulation and the reference structure (the one at the end of the volume relaxation) rose with increasing temperature. This progression is illustrated in Figure C.5 of Appendix C.2, showing the fluctuations in mean potential energy and structure type concentration across all temperatures.

The CNA modifier revealed that the amorphous layer at the interfaces between the grains, initially measuring 8 Å in thickness, expanded to approximately 10 Å at $T = 300$ K and 13 Å at $T = 700$ K. As the temperature increased, there was a decline in the concentration of fcc and hcp structures, coupled with a rise in the proportion of "Other" types. This phenomenon is attributed to the formation of defects (see Section 6.4.3) as well as the increase in the kinetic energy of atoms with rising temperature, leading to stronger interactions among them. Atoms with elevated kinetic energy are capable of altering their distance from neighboring atoms, leading to lattice distortions and categorization as "Other" types. This phenomenon also directly impacts the mean potential energy per atom, increasing its value, as these atoms are no longer in their equilibrium positions. The variation of the concentration of structure types as a function of the temperature after the NPT simulation is plotted in Figure 6.9. The horizontal lines represent their values at the end of the volume relaxation, which were the initial values for the NPT simulations.

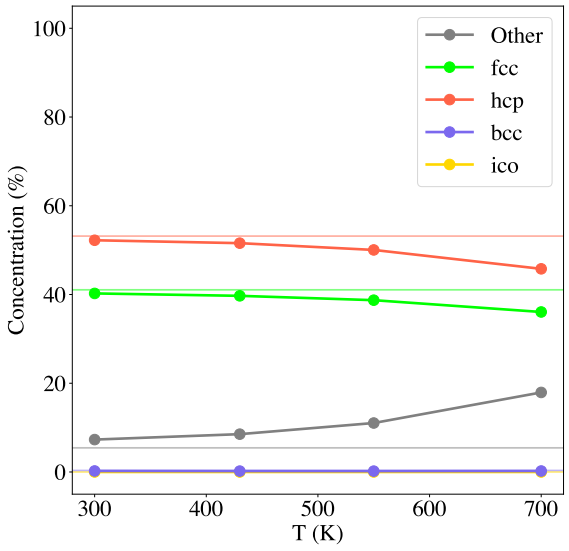

Figure 6.9. Concentrations of the structure types as a function of the temperature in the $Cu^{hcp}/Cu^{fcc}_{per}(\theta = 0°)/Cu^{hcp}$ boundary.

6.4.2 $Cu^{hcp}/Cu^{fcc}_{per}(\theta = 28°)/Cu^{hcp}$ supercell

The $Cu^{hcp}/Cu^{fcc}_{per}(\theta = 28°)/Cu^{hcp}$ exhibited much greater variations compared to the $Cu^{hcp}/Cu^{fcc}_{per}(\theta = 0°)/Cu^{hcp}$ during the NPT simulation at high temperatures. At 300 K, no variations were observed at the amorphous layers of the interfaces between the grains. However, as the temperature increased, the thickness of the amorphous layers at both interfaces increased up to 15 Å. Such results can be appreciated in Figure C.6 of Appendix C.2, where the spatial evolution of the mean potential energy per atom and the concentration of structure types is illustrated. An increment of the "Other" structure types was also observed in this structure. The particularity of the NPT simulation of this boundary is the considerable rising of dislocations in the Cu^{hcp} grains, but this will be discussed in the following section.

As in the above case, in Figure 6.10 we plotted the variation of the total concentration of structure types as a function of the temperature. A common trend as in the $Cu^{hcp}/Cu^{fcc}_{per}(\theta = 0°)/Cu^{hcp}$ is observed in the shape of the concentration of "Other" type. However, the fcc and hcp concentrations experimented a different behavior in this case. At 430 K and 550 K the concentration of fcc types incremented due to the propagation of dislocation lines originated at the amorphous layers that diffuses into the Cu^{hcp} sub-grain changing atoms in the Cu^{hcp} to fcc types. Such transformation of hcp into fcc precisely justifies the increment of the fcc concentration at those temperatures. In the case of 700 K, no diffusion of the dislocations lines from the amorphous layer into the Cu^{hcp} sub-grain was appreciated. This made that the concentration of fcc decreases respect to the cases of 430 K and 550 K. However, some dislocations are created at the Cu^{hcp} sub-grain which transform the atoms from hcp to "Other", this is the main reason why the concentration of hcp remains almost equal to the case of 550 K. In the following section we will go more in details in the analyzis of the point and extended defects in the supercells through the Wigner-Seitz defect analysis and DXA modifiers [180, 181].

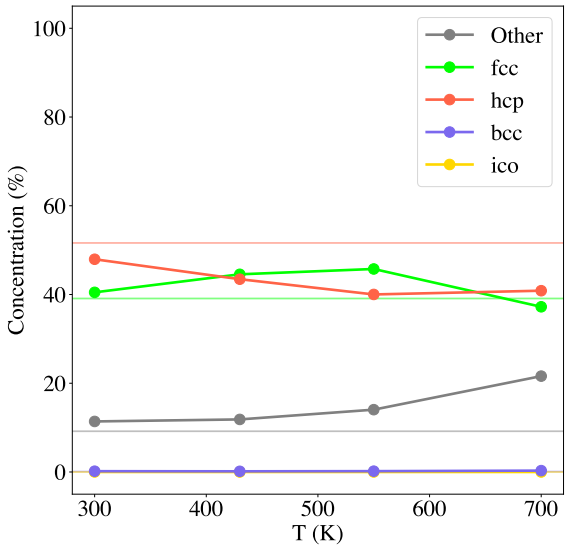

Figure 6.10. Concentrations of the structure types as a function of the temperature in the $Cu^{hcp}/Cu^{fcc}_{per}(\theta = 28°)/Cu^{hcp}$ boundary.

6.4.3 Point and extended defects

After completing the NPT simulations, we proceeded to analyze both point and extended defects present at the boundaries. Our analysis was conducted using the supercells obtained after the volume relaxation as reference. We employed the Wigner-Seitz defect analysis modifier to determine the number of vacancies and interstitial sites within both boundaries. Applying the same spatial analysis method described earlier, we delved deeper into examining the number of point defects along the Z direction. Additionally, we utilized the DXA modifier to identify various types of dislocation lines and the effect of the temperature in their lengths.

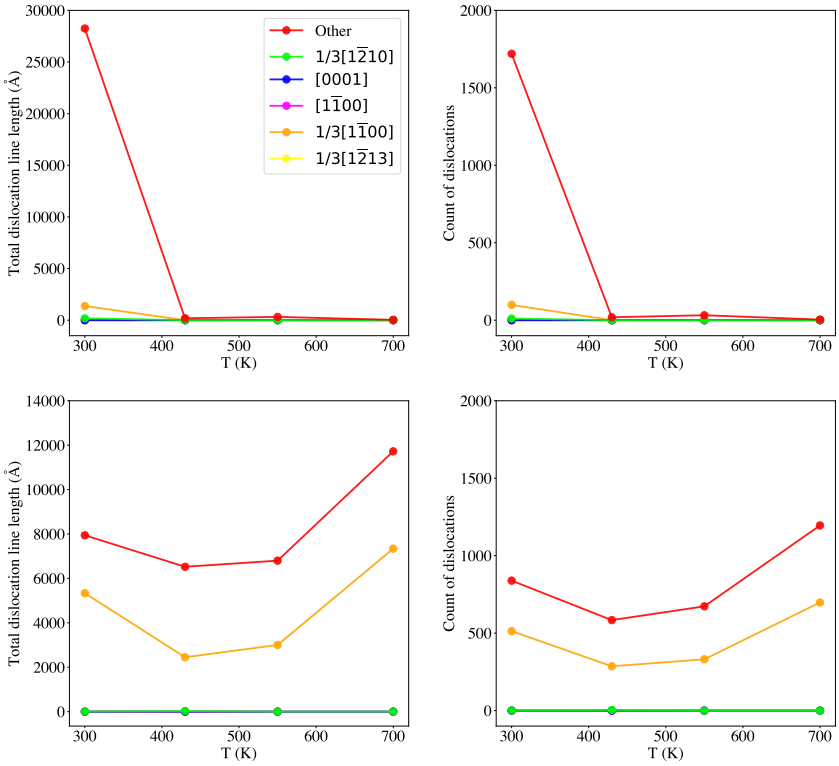

Figure 6.11. Dislocation lines as a function of temperature. Top and bottom panels represent the results for $Cu^{hcp}/Cu^{fcc}_{per}(\theta = 0°)/Cu^{hcp}$ and $Cu^{hcp}/Cu^{fcc}_{per}(\theta = 28°)/Cu^{hcp}$ boundaries, respectively. In the left and right panels the total dislocation length and the number of dislocation segments, respectively.

In Figure C.7 of Appendix C.2, we illustrate the spatial distribution of point defects for both boundaries, while in Figure 6.11 are displayed the variation of the dislocations with temperature. In the $Cu^{hcp}/Cu^{fcc}_{per}(\theta = 0°)/Cu^{hcp}$ supercell, all vacancies and interstitial sites were located within the amorphous layer at the interfaces between the grains. As the temperature increased, the number of point defects within these amorphous layers also increased. Consequently, the concentration of "Other" structure types increased, leading to an expansion of the amorphous layers, as observed previously. The dislocation lines were located within the amorphous layers. As the temperature rose, the density of dislocations decreased, resulting in an increment of the number of point defects within these layers.

The spatial distribution of the point defects in the $Cu^{hcp}/Cu^{fcc}_{per}(\theta = 28°)/Cu^{hcp}$ is considerably different than in the $Cu^{hcp}/Cu^{fcc}_{per}(\theta = 0°)/Cu^{hcp}$ supercell. The point defects were not only located at the interfaces between the grains, but within the Cu^{hcp} and Cu^{fcc}_{per} sub-supercells. At all temperatures considered, the concentration of point defects was higher in the Cu^{hcp} sub-grains compared to the Cu^{fcc}_{per} ones. Specifically, the number of point defects in the Cu^{fcc}_{per} sub-grains at 300 K and 700 K was higher than at 430 K and 550 K. This behavior is linked to the considerably higher number of dislocations at 300 K and 700 K compared to 430 K and 550 K, as Figure 6.11 reveals. The dislocation lines for all temperatures originated at the amorphous layer in the interface between the grains and propagated into the Cu^{hcp} sub-supercell, where they eventually stabilized. This effect can be observed for 550 K in reference [21].

6.5 NVE ensemble

As previously described, the NVE simulation involved fixing a 10 Å layer within one of the Cu^{hcp} sub-grains. This action aimed to maintain the hcp structure within the supercell, simulating the influence of the W/Cu interface. As the temperature rose, both $Cu^{hcp}/Cu^{fcc}_{per}(\theta = 0°)/Cu^{hcp}$ and $Cu^{hcp}/Cu^{fcc}_{per}(\theta = 28°)/Cu^{hcp}$ supercells underwent a recrystallization process characterized by an expansion of the fcc structure. This expansion entailed shifting the interfaces between the grains until they reached the boundaries of the fixed atoms zone. In Figures C.8 and C.9 we plot the spatial analysis of the mean potential energy and the concentration of structure types after the NVE simulation. The $Cu^{hcp}/Cu^{fcc}_{per}(\theta = 0°)/Cu^{hcp}$ begins to recrystallize at 550 K, whereas the $Cu^{hcp}/Cu^{fcc}_{per}(\theta = 0°)/Cu^{hcp}$ starts the process at 430 K.

In Figures C.8 and C.9 is evident the translation experimented by the interfaces between the cells. The position of these interfaces aligns with the location of the maximum of the "Other" structure type, which, as previously described, also corresponds to the peaks of the mean potential energy values. Additionally, an increase in the mean potential energy per atom was observed in the new fcc sub-grain formed in the center of the supercells. This was attributed to a higher concentration of "Other" atom types within this structure. Since these atoms have higher potential energy values than those classified as fcc, the mean potential energy per atom experienced an overall increment.

Table 6.3. Grain characterization resulting from the NVE simulation of both supercells. The grain sizes are indicated by the number of aggregated atoms, in parentheses is the percentage relative to the total number of atoms in the supercell.

		$Cu^{hcp}/Cu^{fcc}_{per}(\theta = 0°)/Cu^{hcp}$		$Cu^{hcp}/Cu^{fcc}_{per}(\theta = 28°)/Cu^{hcp}$	
T(K)	No. of grains	Grain size	Structure	Grain size	Structure
300	1	305988 (55.6%)	hcp	310276 (56.4%)	fcc
	2	244284 (44.4%)	fcc	179184 (32.6%)	hcp
	3			59346 (10.8%)	hcp
	4			46223 (8.4%)	hcp
	5			9530 (1.7%)	hcp
	6			10545 (1.9%)	fcc
430	1	292839 (53.2%)	hcp	489486 (89.0%)	fcc

	2	152520 (27.7%)	fcc	60768 (11.0%)	hcp
	3	69001 (12.5%)	fcc	40817 (7.4%)	hcp
	4	35912 (6.5%)	hcp	14291 (2.6%)	hcp
	5			9742 (1.8%)	hcp
550	1	381473 (69.3%)	fcc	535579 (97.3%)	fcc
	2	168799 (30.7%)	hcp	41883 (7.6%)	hcp
	3			21747 (4.0%)	hcp
	4			15895 (2.9%)	hcp
700	1	481871 (87.6%)	fcc	544191 (98.9%)	fcc
	2	68401 (12.4%)	hcp	51374 (9.3%)	hcp
	3			19539 (3.6%)	hcp

By combining the PTM method [183] with the Grain segmentation modifier in OVITO, we identified the grains within both supercells. Table 6.3 displays the total number of grains, along with their sizes and corresponding structure types. Only grains with sizes exceeding 5503 and 6151 atoms were treated as individual grains for the $Cu^{hcp}/Cu^{fcc}_{per}(\theta = 0°)/Cu^{hcp}$ and $Cu^{hcp}/Cu^{fcc}_{per}(\theta = 28°)/Cu^{hcp}$ respectively. This criterion ensures the identification of grains comprising more than 1% of the total number of atoms in their respective supercells. Table 6.3 illustrates a trend where higher temperatures correspond to fewer grains, which means higher recrystallization. This table also highlights the expansion of the fcc structure as the temperature rises, evident in the increased size of grains exhibiting the such structure type.

In summary, these MD simulations enabled us to determine whether the propagation of the Cu^{hcp} structure into a Cu supercell occurs. Our volume relaxations at 0 K revealed the presence of an amorphous layer extending up to 12 Å. During the coupling process between the boundaries, dislocation lines formed in these amorphous layers to release the system's ground state. NPT simulation considered the thermostat's effect on the boundary configuration. Simulations in this ensemble demonstrated the creation of point and extended defects, such as vacancies and self-interstitials and their diffusion from the amorphous layers to the Cu^{hcp} sub-grain. Finally, NVE simulations revealed a complete propagation of the Cu^{fcc}_{per} structure into the Cu^{hcp} as the temperature increased. This propagation occurred via a recrystallization process, where grains with an fcc structure grew, altering the orientation of the surrounding ones. Consequently, the amorphous layers shifted until they were positioned at the boundaries of the fixed atoms zone. This indicates that solely considering Cu-Cu interactions cannot replicate the effect of the W/Cu interface by fixing the Cu^{hcp}. Instead, modeling the full W/Cu interface necessitates considering W-Cu, W-W, and Cu-Cu interactions. Therefore, employing a W-Cu interatomic potential, as discussed in Section 3.1.1, is one of our future perspectives.

General conclusions

This work aimed to enhance our understanding of retention and diffusion of H atoms at the W/Cu interface, a system of interest for the PFU of the ITER-like divertor. While this study is likely just a small addition to a vast amount of research, we believe it sheds light on another important aspect of H retention within the PFCs, which is crucial for the safe operation of fusion machines like ITER. We hope we have captured the reader's attention and successfully demonstrated that the W/Cu interface acts as a sink for H atoms, leading to their segregation and promoting defect formation, a phenomenon with significant implications for the lifetime of PFCs and the technological and economic feasibility of future fusion power plants.

We presented a multiscale approach that relies on electronic structure calculations based on Density Functional Theory, Classical Molecular Dynamics, and kinetic and thermodynamic theories. DFT provides an accurate description of the material's structure based on its electronic properties; but, due to its precision, it is limited to systems with only a few hundred atoms. In contrast, Classical Molecular Dynamics allows us to simulate, with lower precision than DFT, larger systems of hundreds of thousands of atoms. This allows for the study of defects and phenomena that are beyond the scope of DFT alone. Finally, kinetic and thermodynamic theories receive as input the atomic data reported by DFT and CMD and deliver macro-scale physical quantities as output. Such a multiscale approach provides a comprehensive understanding of H interaction with the W/Cu interface.

Two models of the W/Cu interface were constructed for DFT calculations: $W(001)/Cu^{bcc}(001)$ and $W(001)/Cu^{fcc}(001)R45°$. Each model comprises a $2 \times 2 \times 8$ supercell (consisting of 4 cells of W and Cu in the Z direction) without any vacuum layer, resulting in the working cells being separated from their replicated images by another W/Cu interface. After a full relaxation of the models, both converged to the same $W^{bcc}(001)/Cu^{hcp}(11\bar{2}0)$ structure, where the Cu network transitioned from its initial structures Cu^{bcc} and Cu^{fcc} to Cu^{hcp}. This reconstruction of the Cu network was induced to match the reconstruction of the $W^{bcc}(001)$ surface and was consistent with previous experimental findings [17, 18]. Such reconstruction stabilized the interface reducing the mismatch between the $Cu^{hcp}(11\bar{2}0)$ and $W^{bcc}(001)$ surfaces to 2.28%. This model of the interface was then used to incorporate H into it and determine its retention and diffusion properties.

Ninety-six different $W^{bcc}(001)/Cu^{hcp}(11\bar{2}0)$ structures were created with various interstitial positions for the H atom in the vicinity of the interface. Following relaxation of the W/Cu+H system, only fifty-three positions retained stability, while the H atoms in the remaining forty-three sites migrated to these stable sites. The solution energy and

vibrational properties of H were then evaluated in each of these stable sites, as well as in the W and Cu bulks, for comparison. The solution energy at the plane of the W/Cu interface was the lowest among the surrounding sites, with a value of 0.46 eV. However, this value is comparable to those obtained in Cu^{fcc}_{per} and Cu^{fcc}_{dis} bulks, where certain sites yielded values of 0.41 eV and 0.43 eV, respectively. From these findings, we cannot conclude that there is segregation of H at the W/Cu interface, as lower values of solution energy were found further away from the interface, where Cu is expected to have its most stable Cu^{fcc}_{per} structure. Therefore, the question of whether the H atoms will segregate at the W/Cu interface remained unanswered at this stage of the research work.

To address this open question, a thermodynamic model was developed using the earlier DFT data to ascertain the solubility of H as a function of gas temperature and chemical potential. We assumed that the W/Cu interface was in equilibrium with a H_2 reservoir in a grand-canonical ensemble. As previously done, the same model was applied to Cu and W structures for comparison. The H_2 reservoir was treated as both an ideal and a real gas, using the parametrization from reference [19]. This approach showed that the solubility of H at the W/Cu interface plane was higher than in the W and Cu networks within the W/Cu supercell. This was due to the lowest solution energy at the interface plane compared to other sites within the $W^{bcc}(001)/Cu^{hcp}(11\bar{2}0)$ supercell. However, the solubility of H in the Cu^{fcc}_{per} bulk was higher than at the interface plane, suggesting that H atoms will not segregate at the interface but will instead segregate into the Cu interlayer within the PFUs. Nevertheless, this result belongs to the system at equilibrium conditions. What about the evolution of H atoms before equilibrium is reached? In other words, how do H atoms behave dynamically under non-equilibrium conditions? This brought us to the kinetic theory, where we could understand the variation of H concentration, and consequently its solubility, as a function of time under non equilibrium conditions.

To study the diffusion of H atoms, determining the activation energy barriers is essential. Therefore, we went back to our DFT model where by using the Nudged-Elastic Band method such activation barriers were determined along three different diffusion paths. From the NEB calculations, we uncovered that the (001) and (002) planes of the W/Cu interface possess distinct diffusion properties due to their differing activation barriers within the Cu network. While no variations were observed in the W network due to the reconstruction of the $W^{bcc}(001)$, which does not extend into the bulk, the reconstruction in the Cu network resulted in an arrangement of narrow and wide channels along the Y direction. The sites considered in the (001) plane were situated in a narrow channel, whereas those in the (002) plane were in a wider path. Consequently, the activation energies in the (001) plane were higher than those in the (002) plane, directly influencing the diffusion of H across the W/Cu interface.

Once all the activation barriers were determined, our first step was to calculate the diffusion coefficient of H atoms parallel to the plane of the W/Cu interface using the Arrhenius equation. We observed lower diffusivity at this plane compared to the pristine W and Cu bulks. By focusing on the W/Cu supercell and integrating the findings from the thermodynamic model with those from the Arrhenius equation, it becomes evident that H atoms will accumulate at the interface plane. This conclusion may initially appear to contradict our thermodynamic model, but it does not. The thermodynamic model indicates that both the plane of the W/Cu interface and the Cu^{fcc}_{per} bulk exhibit high H solubility **at equilibrium**. However, these regions are separated by the Cu^{hcp} reconstructed region, which has much lower H solubility. H atoms coming from the W

side will first reach the W/Cu interface, where they will encounter lower diffusivity and higher solubility, leading to their initial accumulation there. As time progresses, H atoms will begin to diffuse through the Cu^{hcp} reconstructed region and eventually reach the Cu^{fcc}_{per} bulk, where they find more stable sites. Therefore, when equilibrium is reached, the solubility in the Cu^{fcc}_{per} bulk will be higher than at the plane of the W/Cu interface.

After characterizing the diffusion parallel to the plane of the interface, we proceeded to study the diffusion of H atoms across the W/Cu interface, perpendicular to the plane, using Rate Equation Theory. We constructed a 0-dimensional kinetic model that considers the trapping/detrapping reactions of interstitial H atoms within the W/Cu interface. This model aimed to determine how the concentration of H changes over time, fixing the concentration of H in the W network at the interface. The results showed that the sites corresponding to the pink path, which primarily lay in the (002) plane, reached a transient stabilization at the beginning of the diffusion process. During this period, H atoms began to diffuse from the pink path to the green one, which mainly lay in the (001) plane, leading to an inhomogeneous concentration of H at the W/Cu interface. This phenomenon has also been observed in the Be/BeO interface [20]. The characteristic frequency of the system, defined as the inverse of the time to reach a steady state, was determined. This allowed us to model the dynamics of H atoms across the W/Cu interface using a simplified system with a single activation barrier of 1.01 eV and a vibration frequency of 7.84×10^{12} Hz.

As mentioned previously, the regions with higher solubility for H atoms - the plane of the W/Cu interface and the Cu^{fcc}_{per} bulk - are separated by the Cu^{hcp} reconstructed structure. Thus, the following question arises: what is the thickness of these reconstructed Cu layers? In other words, how deep does the reconstruction induced by the W/Cu interface propagate into the Cu bulk? To address this question, Classical Molecular Dynamics simulations were conducted on the $Cu^{hcp}/Cu^{fcc}_{per}(\theta = 0°)/Cu^{hcp}$ and $Cu^{hcp}/Cu^{fcc}_{per}(\theta = 28°)/Cu^{hcp}$ boundaries. Our focus was solely on characterizing both boundaries by examining the creation of punctual and extended defects. It was obtained that the Cu^{hcp} does not propagates into the Cu^{fcc}_{per} bulk, but the opposite. The propagation of the grain boundary between the Cu^{hcp} and Cu^{fcc}_{per} was accompanied with an increment of point defects such as, vacancies and self-interstitial Cu atoms, and 1-D defects such as, dislocation lines. As the temperature rises the propagation of such defects were more prominent to the Cu^{hcp}, which means that an increment of defects will occur in the vicinity of the W/Cu interface due to the recrystallization of Cu.

Naturally, such defects will significantly impact the solubility and diffusion of H atoms within and across the interface, aspects not considered in this study. Addressing these complexities will require more sophisticated models that account for defects, which will be the focus of future stages of this project. Developing an interatomic W-Cu and W-Cu-H potential will enable us to fully model the W/Cu interface using Classical Molecular Dynamics, allowing for the consideration of defects. While this research began with idealized systems to provide an initial perspective, we recognize that it is only the beginning, and there is much more to explore and understand.

Appendix A

Quantum states and Dirac notation

This appendix offers a succinct summary of key principles in quantum mechanics, with a focus on aiding readers. We explore significant attributes of Dirac notation [75], while more comprehensive explanations and demonstrations are available in references such as [76, 98, 184, 185].

For an arbitrary bra $\langle\Phi|$ and ket $|\Psi\rangle$, the *inner product* $\langle\Phi|\Psi\rangle$ is defined by:

$$\langle\Phi|\Psi\rangle = \sum_i \Phi_i^*(\vec{r})\Psi_i(\vec{r}). \tag{A.1}$$

This is for the case that both $\langle\Phi|$ and $|\Psi\rangle$ are represented in a discrete basis with components Φ_i^* and Ψ_i. Is both are represented in a continuous basis set, the sum is replaced by an integral:

$$\langle\Phi|\Psi\rangle = \int \Phi_i^*(\vec{r})\Psi_i(\vec{r})\, d\vec{r}. \tag{A.2}$$

The inner product of a ket and a bra is a complex number and satisfies:

$$\langle\Phi|\Psi\rangle = \langle\Psi|\Phi\rangle^*. \tag{A.3}$$

If

$$\langle\Psi|\Psi\rangle = 1, \tag{A.4}$$

we say that $|\Psi\rangle$ and $\langle\Psi|$ are normailized. The bra $\langle\Psi|$ is said to be the *conjugate* of the ket $|\Psi\rangle$.

Considering a complete discrete basis set $\{|f_i\rangle\}$ that satisfy the orthonormality conditions:

$$\langle f_i|f_i\rangle = \delta_{ij}, \tag{A.5}$$

any ket $|\Psi\rangle$ can be expressed as a linear combination of the ket basis set $|f_i\rangle$ by:

$$|\Psi\rangle = \sum_i \Psi_i|f_i\rangle. \tag{A.6}$$

Taking the inner product of $|\Psi\rangle$ with a bra $\langle f_j|$, it is possible to find the j-th component of $|\Psi\rangle$ in the representation of the $|f_i\rangle$,

$$\Psi_j = \langle f_j|\Psi\rangle. \tag{A.7}$$

If the basis set is continuous, the condition of orthonormality is expressed as:

$$\langle \vec{r} | \vec{r}' \rangle = \delta(\vec{r} - \vec{r}'), \tag{A.8}$$

where $\delta(\vec{r} - \vec{r}')$ represents the Dirac delta function. Thus, an arbitrary ket $|\Psi\rangle$ can be expressed as:

$$|\Psi\rangle = \int \Psi(\vec{r}) | \vec{r} \rangle d\vec{r}, \tag{A.9}$$

and

$$\Psi(\vec{r}) = \langle r | \Psi \rangle, \tag{A.10}$$

where $\Psi(\vec{r})$ precisely represents the conventional wave function in coordinate space.

An *operator* $\widehat{\mathrm{A}}$ transforms a ket into another ket within the Hilbert space:

$$\widehat{\mathrm{A}} | \Psi \rangle = | \widehat{\mathrm{A}} \Psi \rangle = | \Psi' \rangle. \tag{A.11}$$

The *adjoint* of $\widehat{\mathrm{A}}$, denoted by $\widehat{\mathrm{A}}^\dagger$, transforms the corresponding bra:

$$\langle \Psi | \widehat{\mathrm{A}}^\dagger = \langle \widehat{\mathrm{A}} \Psi | = \langle \Psi' |. \tag{A.12}$$

When a bra $\langle |$ and a ket $| \rangle$ are juxtaposed, we obtain the inner product if $\langle |$ is positioned before $| \rangle$: $\langle | | \rangle = \langle | \rangle$, and an operator if $| \rangle$ precedes $\langle |$. An important operator in quantum mechanics is the *projection operator* onto a normalized ket $|X\rangle$:

$$\widehat{\mathrm{P}}_x = | X \rangle \langle X |. \tag{A.13}$$

The projection property manifests when the operator $\widehat{\mathrm{P}}_i$ acts on the ket $|\Psi\rangle$:

$$\widehat{\mathrm{P}}_i | \Psi \rangle = | f_i \rangle \langle f_i | | \Psi \rangle = | f_i \rangle \langle f_i | \Psi \rangle, \tag{A.14}$$

and considering (A.7):

$$\widehat{\mathrm{P}}_i | \Psi \rangle = \Psi_i | f_i \rangle, \tag{A.15}$$

where only the part of $|\Psi\rangle$ associated with $|f_i\rangle$ is left. The identity operator $\widehat{\mathrm{I}}$ is defined as:

$$\widehat{\mathrm{I}} \doteq \sum_i | f_i \rangle \langle f_i | = \sum_i \widehat{\mathrm{P}}_i. \tag{A.16}$$

For a continuous basis set we get:

$$\widehat{\mathrm{I}} \doteq \int d\vec{r} | \vec{r} \rangle \langle \vec{r} | = \int d\vec{r} \widehat{\mathrm{P}}_{\vec{r}}. \tag{A.17}$$

This a the *closure relation*, which facilitates transformation between different representations, making the Dirac notation so useful. For instance, we can compute the inner product:

$$\langle \Phi | \Psi \rangle = \langle \Phi | \widehat{\mathrm{I}} | \Psi \rangle, \tag{A.18a}$$

$$= \sum_i \langle \Phi | f_i \rangle \langle f_i | \Psi \rangle, \tag{A.18b}$$

$$= \sum_i \Phi_i^* \Psi_i, \tag{A.18c}$$

which is exactly the same expression than (A.1), or the effect of the operator $\widehat{\mathrm{A}}$ in (A.11):

$$\langle f_i|\widehat{\mathrm{A}}|\Psi\rangle = \sum_j \langle f_i|\widehat{\mathrm{A}}|f_i\rangle\langle f_i|\Psi\rangle = \langle f_i|\Psi'\rangle, \tag{A.19}$$

where the complex numbers $\langle f_i|\widehat{\mathrm{A}}|f_i\rangle$ constitute the matrix representation of $\widehat{\mathrm{A}}$ in the basis set $|f_i\rangle$. This matrix fully define the operator. if we consider a continuous basis set, (A.19) becomes:

$$\langle \vec{r}\,'|\widehat{\mathrm{A}}|\Psi\rangle = \int d\vec{r}\; A(\vec{r}\,', \vec{r})\, \Psi(\vec{r}) = \Psi'(\vec{r}\,'). \tag{A.20}$$

Being $A(\vec{r}\,', \vec{r}) = \langle \vec{r}\,'|\widehat{\mathrm{A}}|\vec{r}\rangle$. This expression indicates that an operator could be *non-local*. An operator $\widehat{\mathrm{A}}$ is *local* if:

$$A(\vec{r}\,', \vec{r}) = A(\vec{r})\delta(\vec{r} - \vec{r}). \tag{A.21}$$

One example of local and non-local operators are the Coulomb (2.29) and the exchange (2.30) operators defined in the Hartree-Fock theory, respectively.

Appendix B

Mismatch representations

In Table 3.1, we calculated Bramfitt's mismatch parameter for 12 distinct W/Cu interfaces. To provide clarity regarding the selected vectors in the corresponding crystallographic planes, we illustrate these planes and the $[uvw]^i$ vectors in Table B.1. For better visualization, the atoms used in determining the misfit parameter were highlighted, while the remaining atoms were rendered transparent.

Table B.1. Sketch of the 12 structures for which the Bramfitt's mismatch parameter was determined in Table 3.1. The brown and grey spheres represent the Cu and W atoms respectively. Similarly, in brown and gray are represented their corresponding $[uvw]^i$ vectors. The atoms selected for determining the mismatch were highlighted, while the rest were rendered transparent to enhance visualization.

No. 1 $(100)_W/(100)_{Cu}$	No. 2 $(110)_W/(100)_{Cu}$	No. 3 $(111)_W/(100)_{Cu}$
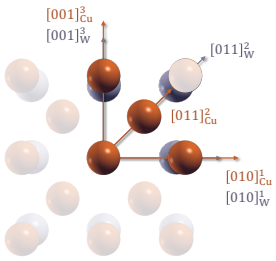	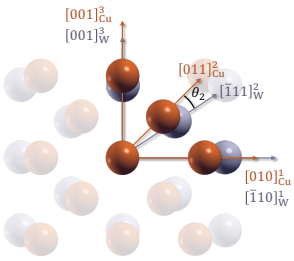	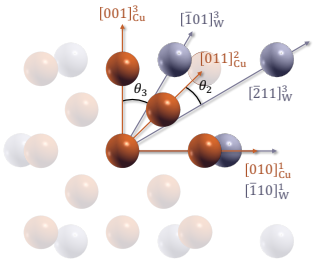
No. 4 $(100)_W/(110)_{Cu}$	No. 5 $(110)_W/(110)_{Cu}$	No. 6 $(111)_W/(110)_{Cu}$
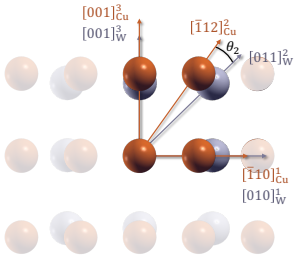	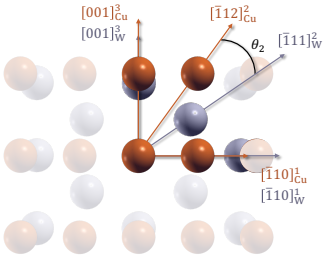	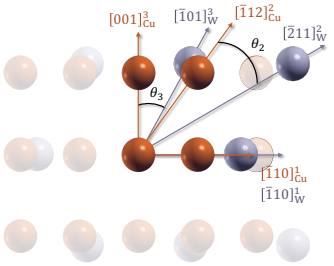
No. 7 $(100)_W/(111)_{Cu}$	No. 8 $(110)_W/(111)_{Cu}$	No. 9 $(111)_W/(111)_{Cu}$

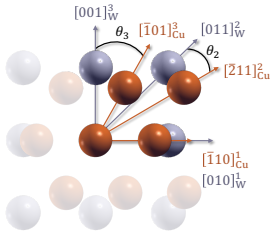

No. 10 $(100)_W/(100)_{Cu}$

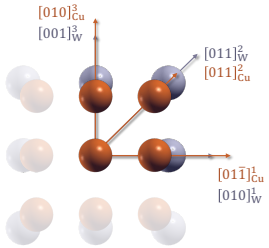

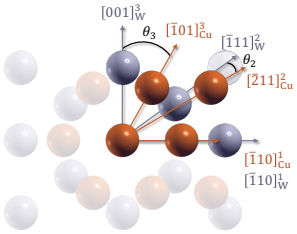

No. 11 $(110)_W/(111)_{Cu}$

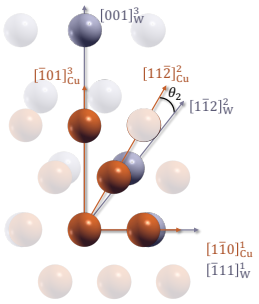

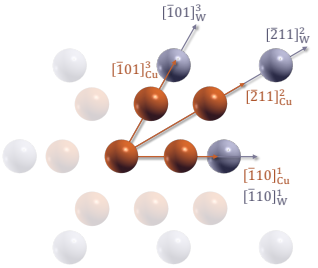

No. 12 $(110)_W/(111)_{Cu}$

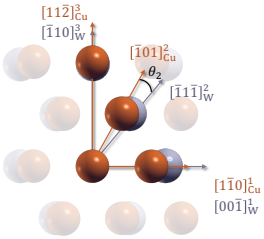

Appendix C

Molecular dynamics simulations

C.1 Volume relaxation of the boundaries

In Figure C.1 and C.2, we present the final structure of the $Cu^{hcp}/Cu^{fcc}_{per}(\theta = 0°)/Cu^{hcp}$ and $Cu^{hcp}/Cu^{fcc}_{per}(\theta = 28°)/Cu^{hcp}$ boundaries after the volume relaxation, respectively. The identification of structure types was performed using the CNA modifier [176] in OVITO [167]. The evolution from the initial structure to the final one can be accessed at reference [21].

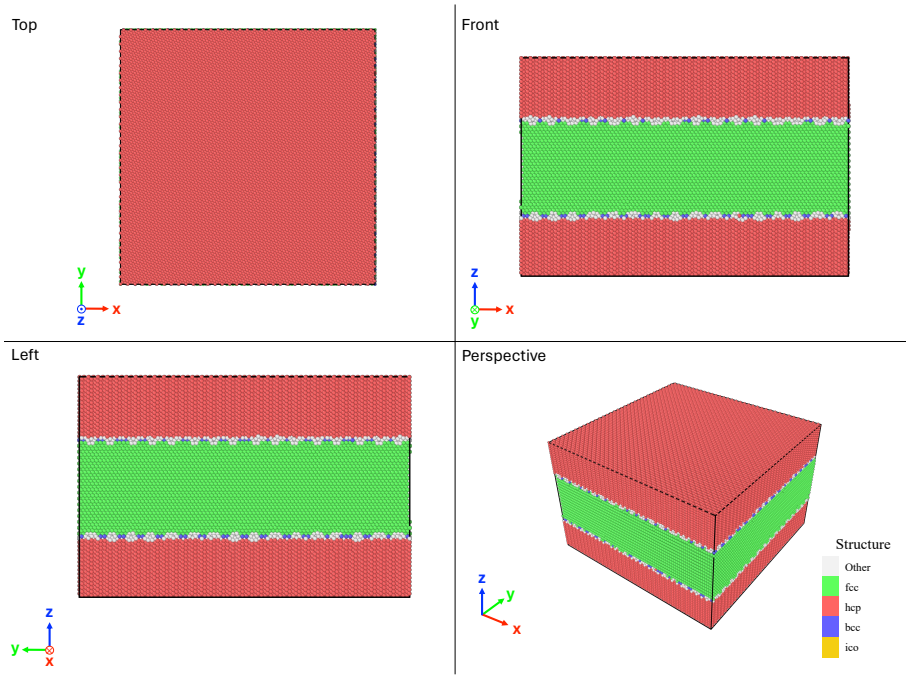

Figure C.1. $Cu^{hcp}/Cu^{fcc}_{per}(\theta = 0°)/Cu^{hcp}$ after the volume relaxation.

In Figure C.2, the reconstruction of the atoms in the Cu^{fcc}_{per} sub-supercell, resulting in the interference pattern described in Section 6.3.2, is evident. In Figure C.3, a cut was made in the XY plane at $z = 60$ Å to demonstrate that this pattern is solely present at the surface, resulting from the arrangement of atoms due to the periodic boundary conditions.

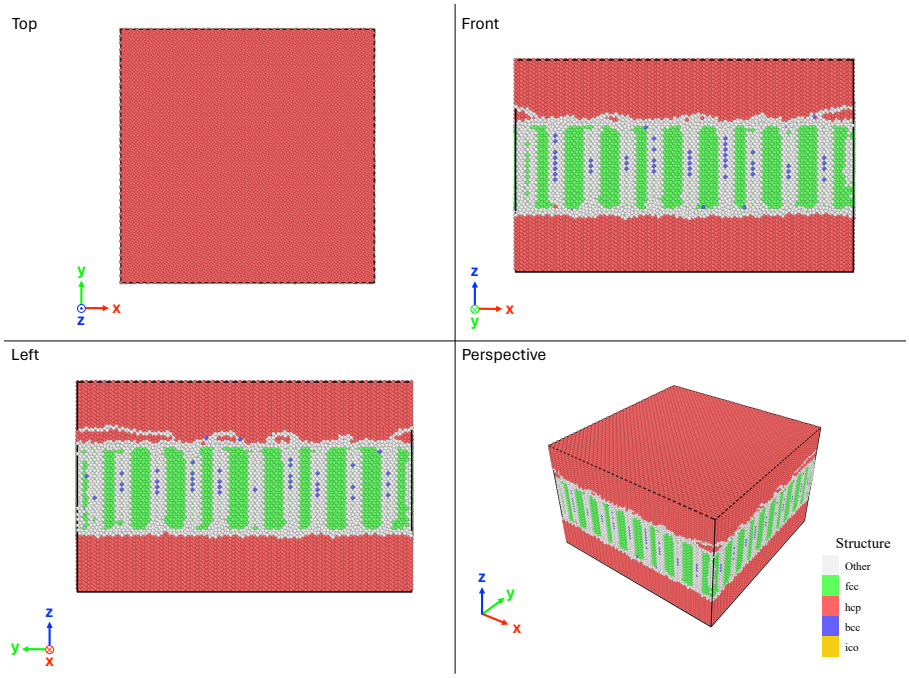

Figure C.2. $Cu^{hcp}/Cu^{fcc}_{per}(\theta = 28°)/Cu^{hcp}$ after the volume relaxation.

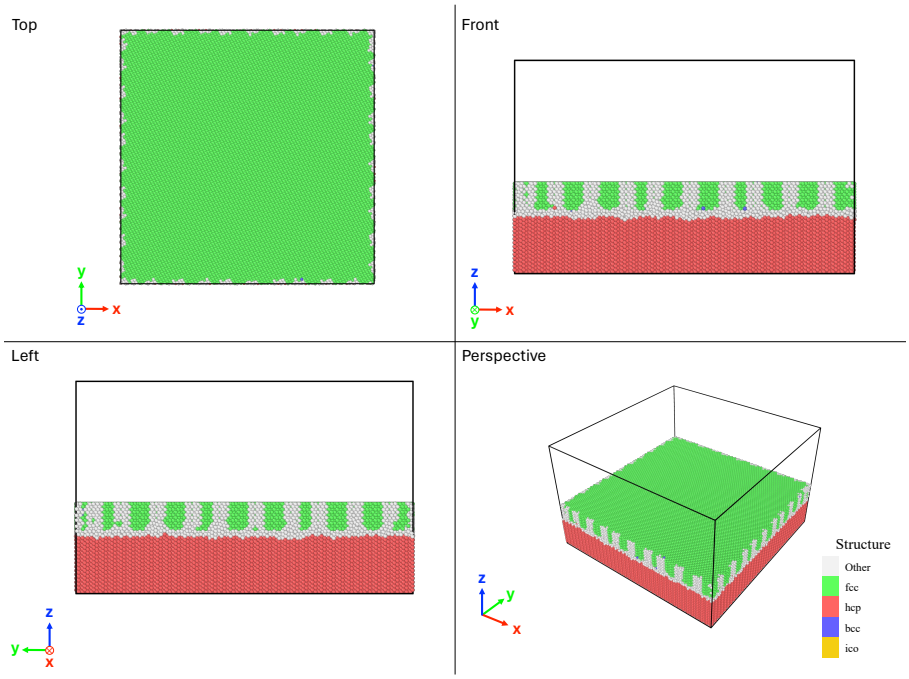

Figure C.3. Cut along the XY plane at $z = 60$ Å in the $Cu^{hcp}/Cu^{fcc}_{per}(\theta = 28°)/Cu^{hcp}$ after the volume relaxation.

In Section 6.3.2, we discussed the matching of the interface located at 101.4 Å in the $Cu^{hcp}/Cu^{fcc}_{per}(\theta = 28°)/Cu^{hcp}$ supercell. We mentioned that the loops of "Other" structure, which initiate and terminate within the amorphous layer while extending into the Cu^{hcp} bulk, are associated with the manner in which the bulk releases strain at the interface, leading to the creation of defects. Using the DXA modifier [180, 181] in OVITO [167],

we identified the type of dislocations present in this interface. Figure C.4 illustrates that these dislocation lines only appear at the interface located at 101.4 Å. To identify such dislocations we used the hcp structure as input crystal, which instructs to the software how to determine the Burgers vectors and how to compute the local crystal orientation [179]. In the classification of dislocation types, the "Other" category is designated for dislocations whose Burgers vector does not belong to any of the predefined families.

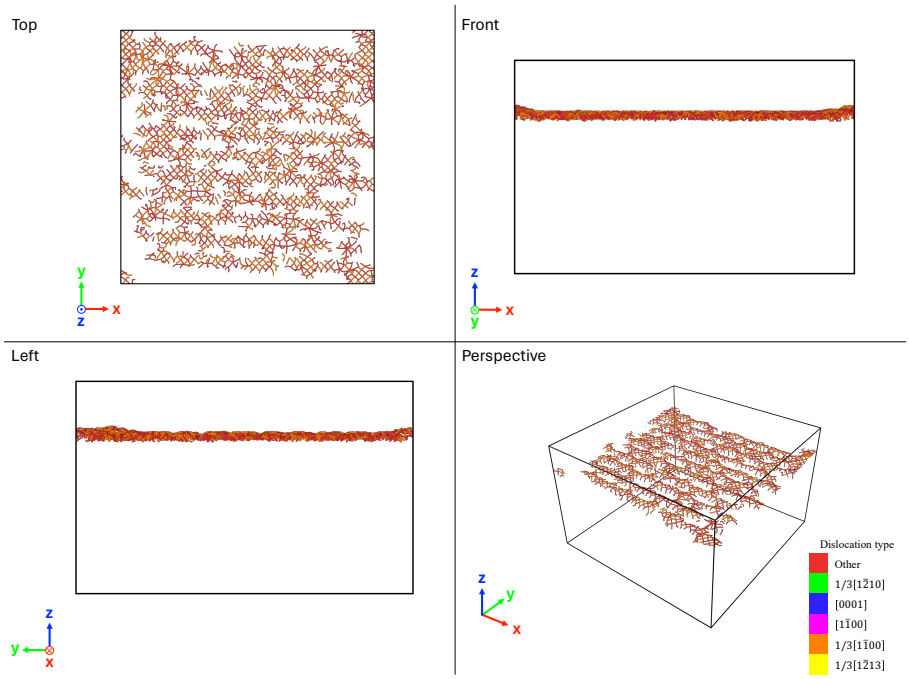

Figure C.4. Dislocation analysis using the DXA modifier in the $Cu^{hcp}/Cu^{fcc}_{per}(\theta = 28°)/Cu^{hcp}$ after the volume relaxation.

C.2 NPT ensembles

Summary of the NPT relaxation in the $Cu^{hcp}/Cu^{fcc}_{per}(\theta = 0°)/Cu^{hcp}$ and $Cu^{hcp}/Cu^{fcc}_{per}(\theta = 28°)/Cu^{hcp}$ boundaries. The structure types were identified using the CNA modifier [176] in OVITO [167]. The point and extended defects were identified using the Wigner-Seitz defect analysis and the DXA [180, 181] modifiers in OVITO, respectively. For identifying the point defects, we used the structures after the volume relaxation as references, whereas for the detection of the dislocation types we considered the hcp structure as reference.

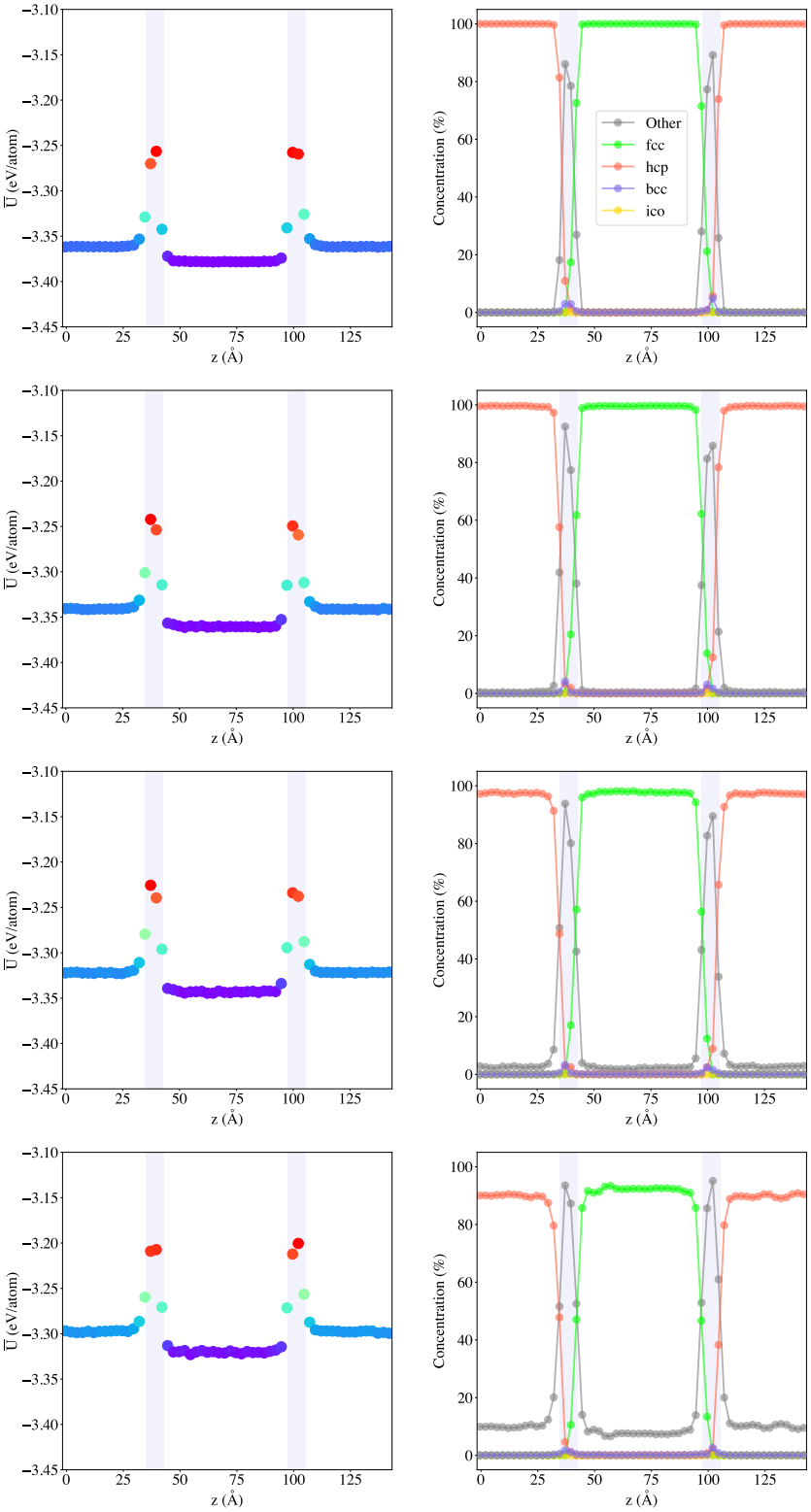

Figure C.5. Spatial analysis of the $Cu^{hcp}/Cu^{fcc}_{per}(\theta = 0°)/Cu^{hcp}$ boundary after the NPT relaxation. From top to bottom are shown the results for temperatures 300 K, 430 K, 500 K, and 700 K, respectively. The left panels represent the mean potential energy per atom, while the right panels display the concentration of structure types. The initial position of the interfaces between the $Cu^{hcp}/Cu^{fcc}_{per}(\theta = 0°)$ structures is highlighted by the lavender region.

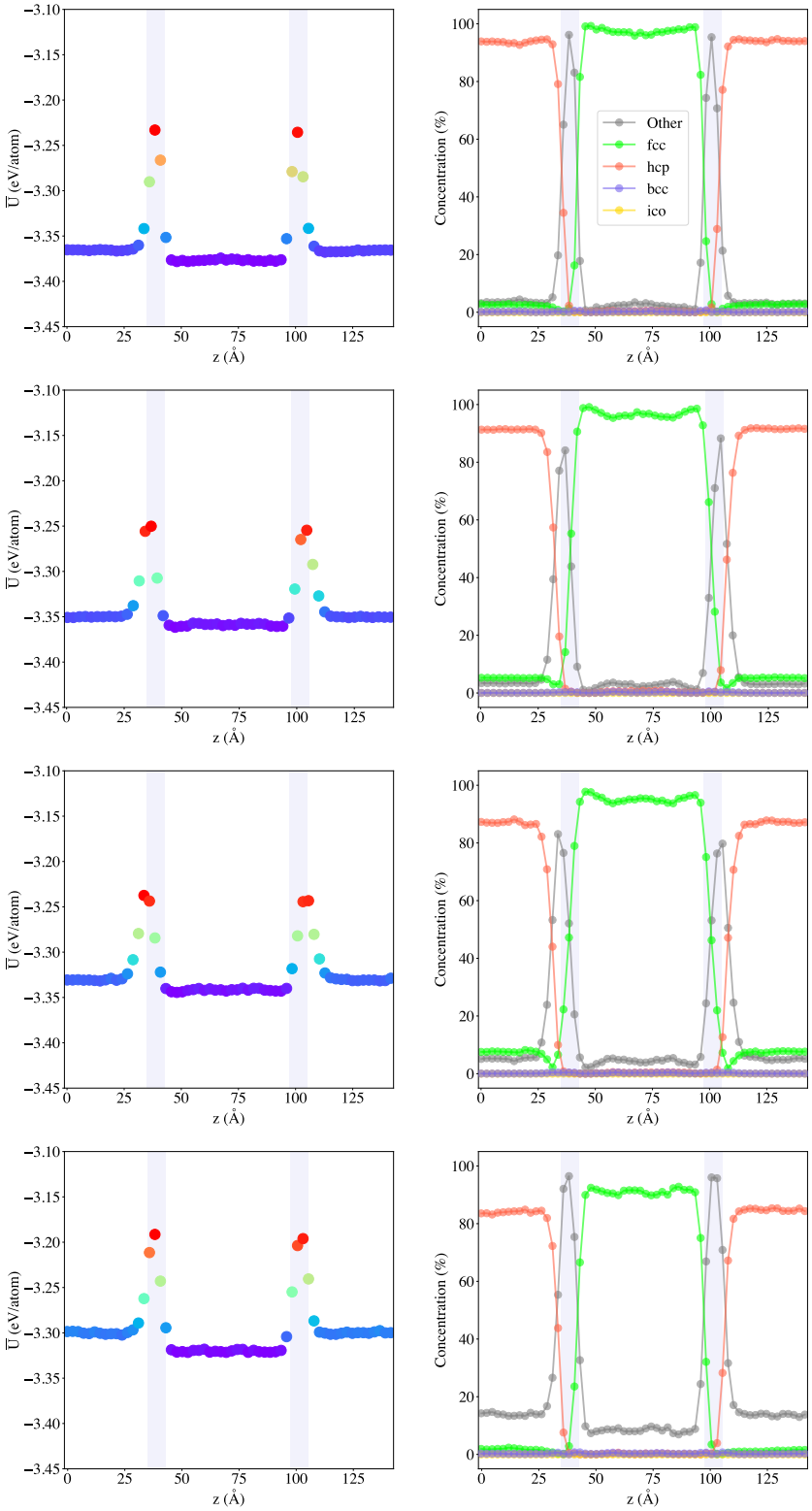

Figure C.6. Spatial analysis of the $Cu^{hcp}/Cu^{fcc}_{per}(\theta = 28°)/Cu^{hcp}$ boundary after the NPT relaxation. From top to bottom are shown the results for temperatures 300 K, 430 K, 500 K, and 700 K, respectively. The left panels represent the mean potential energy per atom, while the right panels display the concentration of structure types. The initial position of the interfaces between the $Cu^{hcp}/Cu^{fcc}_{per}(\theta = 28°)$ structures is highlighted by the lavender region.

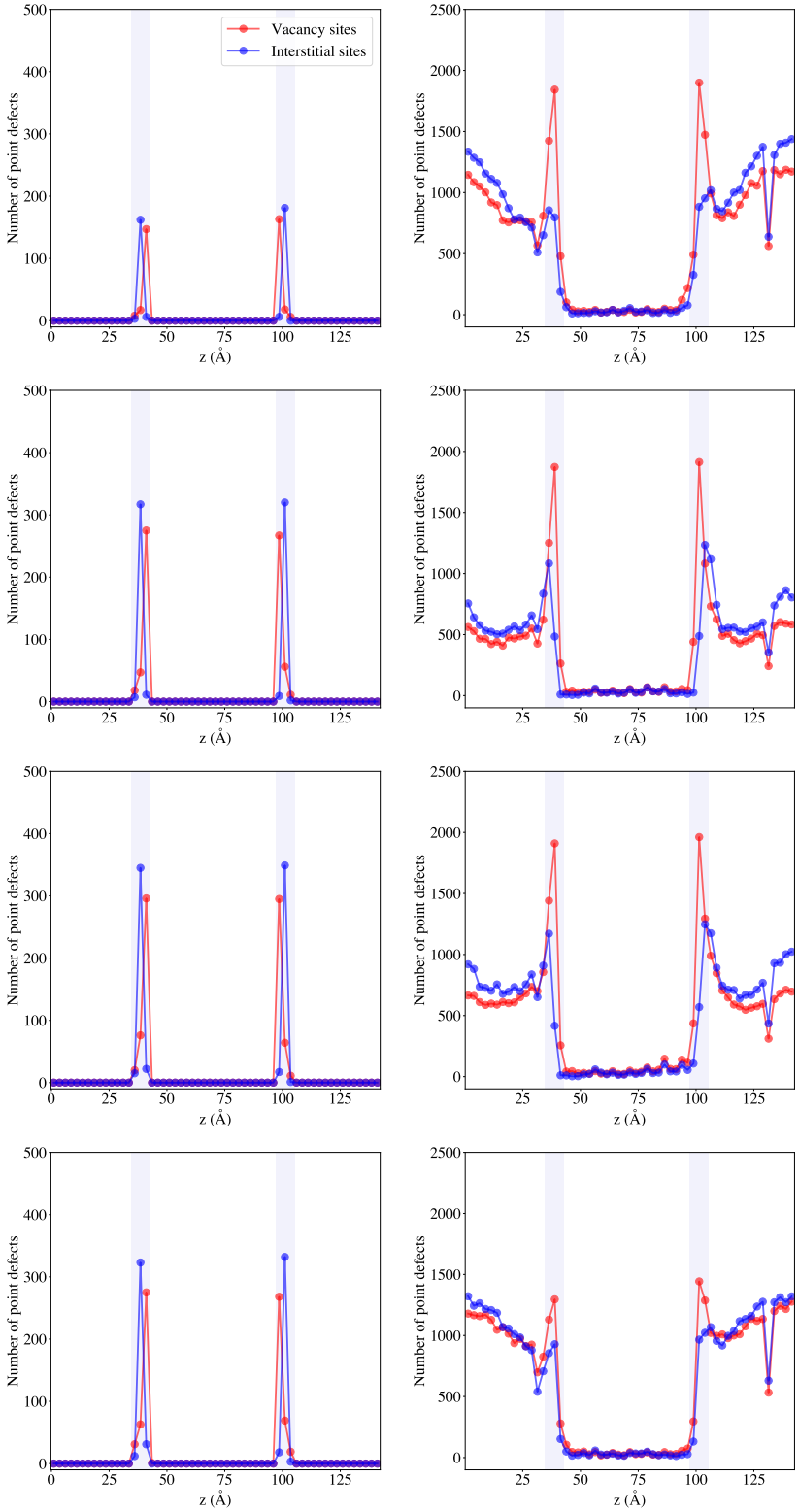

Figure C.7. Point defects (vacancy sites and interstitial sites) along the Z direction after the NPT relaxation. From top to bottom are displayed the results for 300 K, 430 K, 500 K and 700 K, respectively. The left and right panels correspond to $Cu^{hcp}/Cu^{fcc}_{per}(\theta = 0°)/Cu^{hcp}$ and $Cu^{hcp}/Cu^{fcc}_{per}(\theta = 28°)/Cu^{hcp}$ boundaries, respectively. The initial position of the interfaces between the grains are represented by the lavender region.

C.3 NVE ensembles

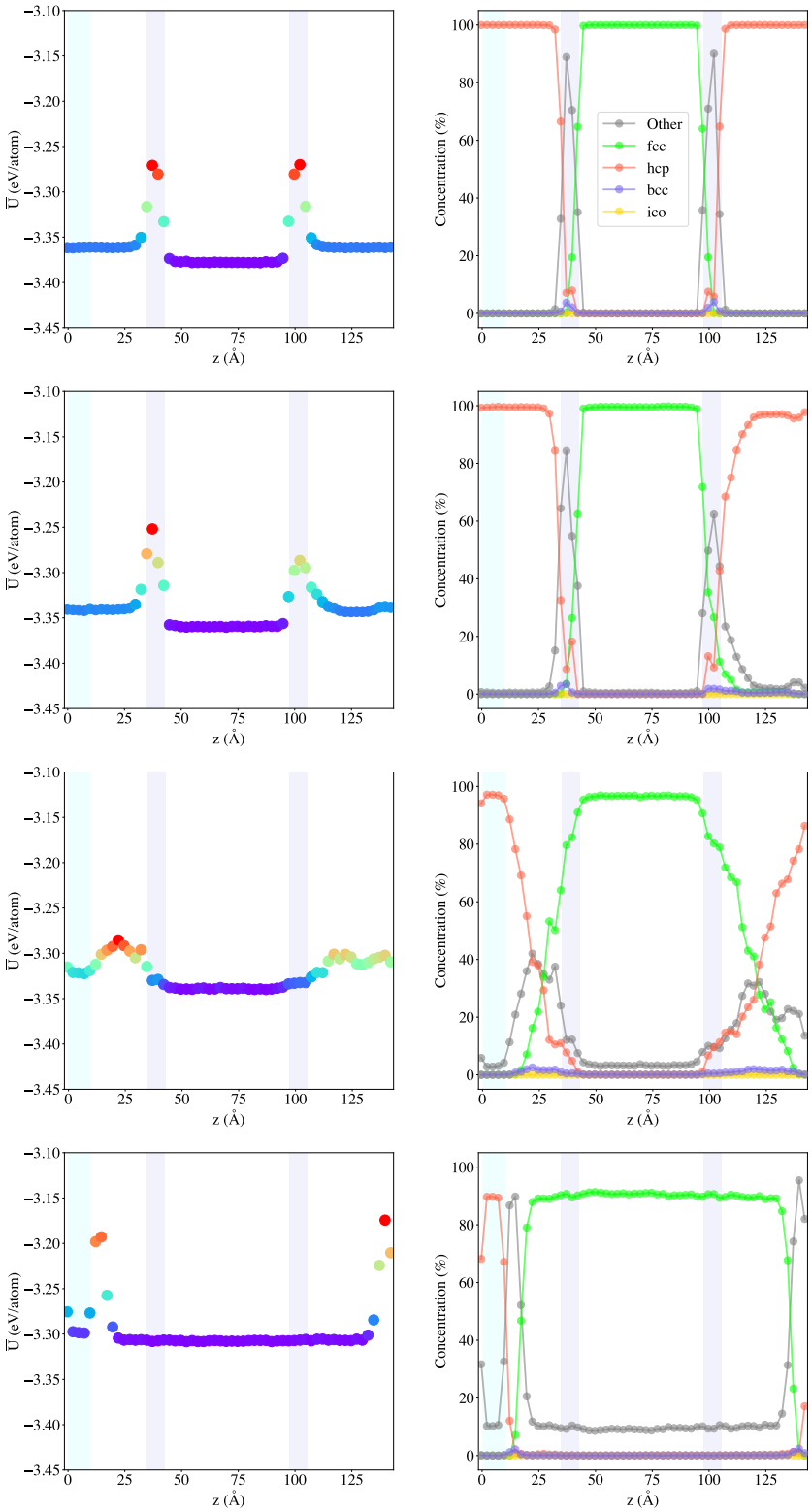

Figure C.8. Spatial analysis of the $Cu^{hcp}/Cu^{fcc}_{per}(\theta = 0°)/Cu^{hcp}$ boundary after NVE relaxation. Results for temperatures 300 K, 430 K, 500 K, and 700 K are shown from top to bottom. Left panels display mean potential energy per atom, while right panels show structure type concentration. Lightcyan and lavender regions indicate fixed atoms within the Cu^{hcp} grain and initial interfaces of $Cu^{hcp}/Cu^{fcc}_{per}(\theta = 0°)$ structures.

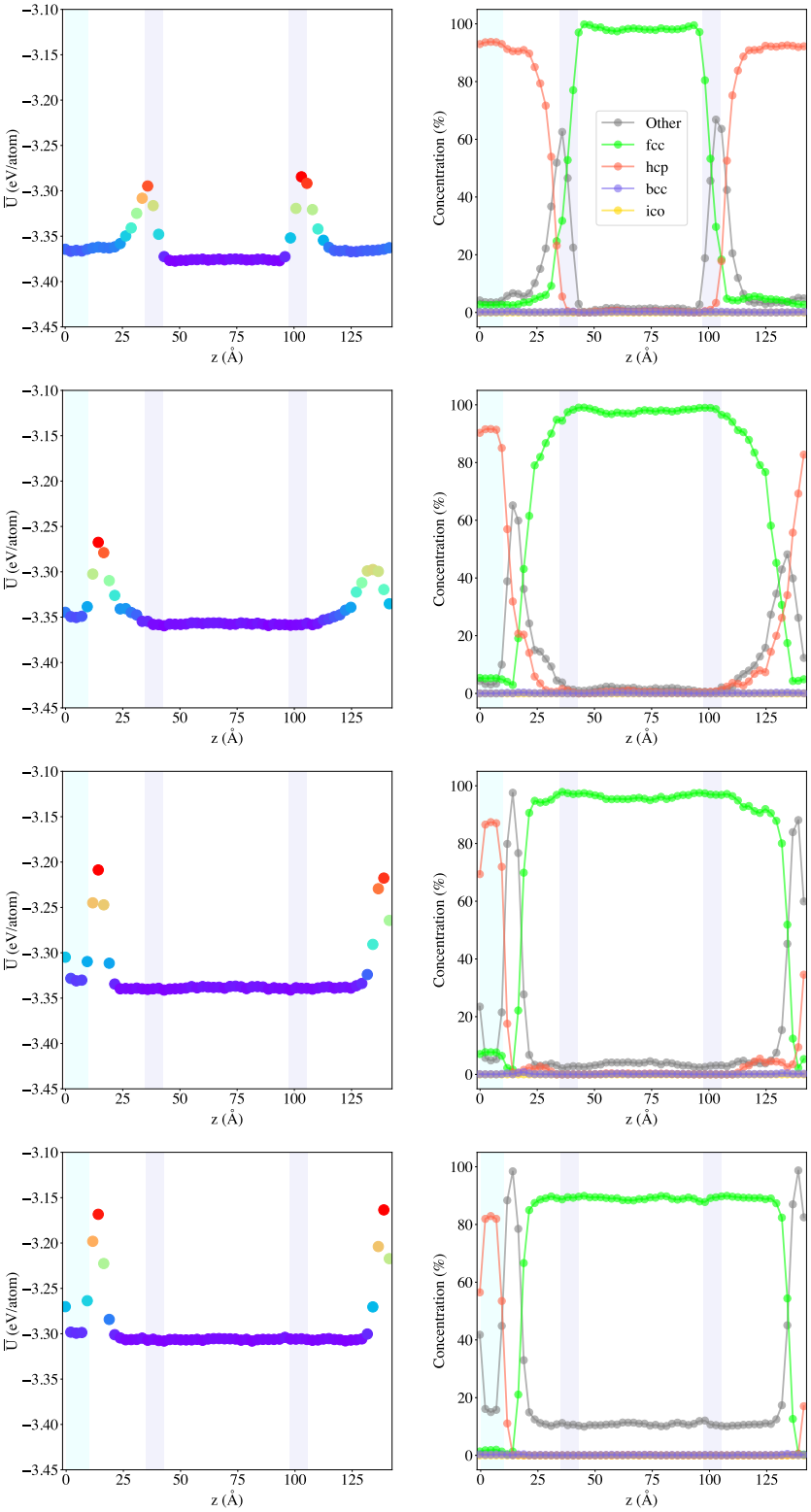

Figure C.9. Spatial analysis of the $Cu^{hcp}/Cu^{fcc}_{per}(\theta = 28°)/Cu^{hcp}$ boundary after NVE relaxation. Results for temperatures 300 K, 430 K, 500 K, and 700 K are shown from top to bottom. Left panels display mean potential energy per atom, while right panels show structure type concentration. Lightcyan and lavender regions indicate fixed atoms within the Cu^{hcp} grain and initial interfaces of $Cu^{hcp}/Cu^{fcc}_{per}(\theta = 28°)$ structures.

Bibliography

[1] Population Division United Nations - Department of Economic and Social Affairs. *World Urbanization Prospects: The 2014 Revision, (ST/ESA/SER.A/366)*. Department of Economic and Social Affairs, Population Division, 2015, pp. 1–517.

[2] *IEA website*. URL: `https://www.iea.org/` (visited on 2023).

[3] International Energy Agency. *World Energy Outlook 2022*. 2022, pp. 1–524.

[4] D. M. Duffy. "Fusion power: A challenge for materials science". *Philosophical Transactions of the Royal Society A* 368 (1923 2010), pp. 3315–3328.

[5] N. Taylor, D. Baker, V. Barabash, et al. "Preliminary safety analysis of ITER". *Fusion Science and Technology* 56 (2 2017), pp. 573–580.

[6] *ITER Organization website*. URL: `https://www.iter.org/` (visited on 2023).

[7] D. Perrault. "Safety issues to be taken into account in designing future nuclear fusion facilities". *Fusion Engineering and Des.* 109.111 (2016), pp. 1733–1738. URL: `https://doi.org/10.1016/j.fusengdes.2015.10.012`.

[8] G. M. Wright, A. W. Kleyn, E. Alves, et al. "Hydrogenic retention in tungsten exposed to ITER divertor relevant plasma flux densities". *Journal of nuclear materials* 390 (2009), pp. 610–613.

[9] D. Kato, H. Iwakiri, Y. Watanabe, et al. "Super-saturated hydrogen effects on radiation damages in tungsten under the high-flux divertor plasma irradiation". *Nuclear Fusion* 55.8 (2015), p. 083019.

[10] R. Delaporte-Mathurin, E. A. Hodille, J. Mougenot, et al. "Finite element analysis of hydrogen retention in ITER plasma facing components using FESTIM". *Nuclear Materials and Energy* 21 (2019), p. 100709.

[11] A. Yoshikawa, Y. Hirohata, Y. Oya, et al. "Hydrogen retention and depth profile in divertor tiles of Jt-60 exposed to hydrogen discharges". *Fusion engineering and design* 81.1-7 (2006), pp. 289–294.

[12] J. Likonen, K. Heinola, A. De Backer, et al. "Investigation of deuterium trapping and release in the JET ITER-like wall divertor using TDS and TMAP". *Nuclear Materials and Energy* 19 (2019), pp. 166–178.

[13] K. Ohya and Y. Soneda. "Simulation of deuterium retention in tungsten exposed to divertor plasmas". *Plasma and Fusion Research* 7 (2013), pp. 2403083–2403083.

[14] P. C. Stangeby and J. D. Elder. "Impurity retention by divertors. I. One dimensional models". *Nuclear fusion* 35.11 (1995), p. 1391.

[15] C. H. Skinner, A. A. Haasz, V. Kh. Alimov, et al. "Recent advances on hydrogen retention in ITER's plasma-facing materials: Beryllium, carbon, and tungsten". *Fusion Science and Technology* 54.4 (2008), pp. 891–945.

[16] E. A. Hodille, E. Bernard, S. Markelj, et al. "Estimation of the tritium retention in ITER tungsten divertor target using macroscopic rate equations simulations". *Phys. Scr.* 170 (2017), pp. 14033–14040.

[17] H. Wormeester, M. E. Kiene, E. Hüger, et al. "Growth of hcp Cu on W (100)". *Surf. Sci.* 377 (1997), pp. 988–991.

[18] T. R. J. Bollmann, R. van Gastel, H. Wormeester, et al. "Growth and decay of hcp-like Cu hut-shaped structures on W(100)". *Phys. Rev. B* 85 (12 Mar. 2012), p. 125417.

[19] M. Tkacz and A. Litwiniuk. "Useful equations of state of hydrogen and deuterium". *Journal of alloys and compounds* 330 (2002), pp. 89–92.

[20] E. A. Hodille, J. Byggmästar, Y. Ferro, et al. "Molecular dynamics study of hydrogen isotopes at the Be/BeO interface". *Journal of Physics: Condensed Matter* 34.40 (2022), p. 405001.

[21] Y. Silva-Solís. *3D objects and animations of my thesis results*. URL: `https://yosvanyss.github.io/phd_thesis/`.

[22] F. F. Chen. *An Indispensable Truth*. Springer New York, 2011, pp. 1–433.

[23] A. S. Eddington. *The Internal Constitution of the Stars*. Jan. 1988. URL: `https://doi.org/10.1126/science.52.1341.233`.

[24] R. E. Atkinson and F. G. Houtermans. "Zur Frage der Aufbaumöglichkeit der Elemente in Sternen". *Zeitschrift für Physik* 54.9 (1929), p. 656. URL: `https://doi.org/10.1007/BF01341595`.

[25] M. L. E. Oliphant, B. B. Kinsey, and E. Rutherford. "The transmutation of lithium by protons and by ions of the heavy isotope of hydrogen". *Proceedings of the Royal Society of London. Series A, Containing Papers of a Mathematical and Physical Character* 141.845 (1933), pp. 722–733.

[26] M. L. E. Oliphant and E. Rutherford. "Experiments on the transmutation of elements by protons". *Proceedings of the Royal Society of London. Series A, Containing Papers of a Mathematical and Physical Character* 141.843 (1933), pp. 259–281.

[27] M. L. E. Oliphant, P. Harteck, and E. Rutherford. "Transmutation effects observed with heavy hydrogen". *Proceedings of the Royal Society of London. Series A, Containing Papers of a Mathematical and Physical Character* 144.853 (1934), pp. 692–703.

[28] M. L. E. Oliphant, P. Harteck, and E. Rutherford. "100 kilovolt discharges in deuterium plasmas". *Proc. Roy. Soc. London A* 144 (1934), pp. 692–714.

[29] M. Wang, W. J. Huang, F. G. Kondev, et al. "The AME 2020 atomic mass evaluation (II). Tables, graphs and references". *Chinese Physics C* 45.3 (2021), p. 030003.

[30] J. Wesson, D. J. Campbell, W. Connor J, et al. *Tokamaks*. Fourth Edition. Oxford University Press, 2011, pp. 1–812.

[31] R. Dautray. *La fusion thermonucléaire contrôlée par confinement magnétique. Collection du Commissariat à l'Energie Atomique*. Masson, 1987.

[32] L. Spitzer. "The stellarator concept". *The Physics of Fluids* 1.4 (1958), pp. 253–264.

[33] *Max Planck Institute website*. URL: `https://www.ipp.mpg.de/en` (visited on 2023).

[34] W. Picot. "Magnetic fusion confinement with tokamaks and stellarators". *IAEA bulletin* (May 2021), pp. 6–7. URL: `www.iaea.org/bulletin`.

[35] I. E. Tamm and A. D. Sakharov. *Reports on magnetic thermonuclear reactors*. Physica Institute of the Academy of Sciences of U.S.S.R. OTCHETY.(Russian title:Otchety o magnitnom termoyadernykh reaktorakh). Dec. 1951.

[36] G. G. Dolgov-Saveliev, D. P. Ivanov, V. S. Mukhovatov, et al. "Investigations of the stability and heating of plasmas in toroidal chambers". *Proceedings of the 2nd Geneva Conference on the Peaceful Uses of Atomic Energy, P/2527* (1958), pp. 82–91.

[37] *European Fusion Development Agreement, "Limiters and divertors"*. (Visited on 2023).

[38] M. Shimada, D. J. Campbell, V. Mukhovatov, et al. "Overview and summary". *Nuclear Fusion* 47.6 (2007), S1.

[39] A. Loarte, B. Lipschultz, A. S. Kukushkin, et al. "Power and particle control". *Nuclear Fusion* 47.6 (2007), S203.

[40] R. A. Pitts, A. Kukushkin, A. Loarte, et al. "Status and physics basis of the ITER divertor". *Physica Scripta* 2009.T138 (2009), p. 014001.

[41] R. A. Pitts, S. Bardin, B. Bazylev, et al. "Physics conclusions in support of ITER W divertor monoblock shaping". *Nuclear Materials and Energy* 12 (2017), pp. 60–74.

[42] J. P. Gunn, S. Carpentier-Chouchana, F. Escourbiac, et al. "Surface heat loads on the ITER divertor vertical targets". *Nuclear Fusion* 57.4 (2017), p. 046025.

[43] J. P. Gunn, S. Carpentier-Chouchana, R. Dejarnac, et al. "Ion orbit modelling of ELM heat loads on ITER divertor vertical targets". *Nuclear Materials and Energy* 12 (2017), pp. 75–83.

[44] R. Delaporte-Mathurin, E. A. Hodille, J. Mougenot, et al. "Influence of interface conditions on hydrogen transport studies". *Nuclear Fusion* 61.3 (2021), p. 036038.

[45] J. Huang, G. M. Fadel, V. Y. Blouin, et al. "Bi-objective optimization design of functionally gradient materials". *Materials & Design* 23.7 (2002), pp. 657–666.

[46] K. Liu, P. Chen, C. Ran, et al. "Investigation on the interfacial microstructure and mechanical properties of the W-Cu joints fabricated by hot explosive welding". *Journal of Materials Processing Technology* 300 (2022), p. 117400.

[47] K. Liu, P. Chen, Q. Zhou, et al. "Interfacial evolution mechanism of W/Cu explosive welding interface affected by preheating". *International Journal of Refractory Metals and Hard Materials* 116 (2023), p. 106351.

[48] J. Zhang, Y. Huang, Y. Liu, et al. "Direct diffusion bonding of immiscible tungsten and copper at temperature close to Copper's melting point". *Materials & Design* 137 (2018), pp. 473–480.

[49] H. Yan, J. Fan, Y. Han, et al. "Vacuum diffusion bonding W to W-Cu composite: interfacial microstructure and mechanical properties". *Vacuum* 165 (2019), pp. 19–25.

[50] K. P. Singh, S. S. Khirwadkar, K. Bhope, et al. "Feasibility study on joining of multi-layered W/Cu-CuCrZr-SS316L-SS316L materials using vacuum brazing". *Fusion Engineering and Design* 127 (2018), pp. 73–82.

[51] Y. Ahuja, R. Ibrahim, A. Paradowska, et al. "Friction stir forming to fabricate copper–tungsten composite". *Journal of materials processing technology* 217 (2015), pp. 222–231.

[52] J. Boscary, S. Suzuki, K. Nakamura, et al. "Thermal fatigue tests on CVD-W/Cu divertor mock-ups". *Fusion engineering and design* 39 (1998), pp. 537–542.

[53] G. Pintsuk, I. Smid, J.-E. Döring, et al. "Fabrication and characterization of vacuum plasma sprayed W/Cu-composites for extreme thermal conditions". *Journal of materials science* 42 (2007), pp. 30–39.

[54] V. Barabash, M. Akiba, A. Cardella, et al. "Armor and heat sink materials joining technologies development for ITER plasma facing components". *Journal of Nuclear Materials* 283 (2000), pp. 1248–1252.

[55] J. Wang, J. Huang, H. Sun, et al. "Effect of composite interlayer on bonding quality of W and steel HIP joint". *Fusion Engineering and Design* 149 (2019), p. 111337.

[56] E. Sal, J. de Prado, M. Sánchez, et al. "Joining of self-passivating W-Cr-Y alloy to ferritic-martensitic steel by hot isostatic pressing". *Fusion Engineering and Design* 170 (2021), p. 112499.

[57] D. Liu, H. Ma, C. Ruan, et al. "Interface diffusion and mechanical properties of ODS-W/Cu prepared by spark plasma sintering". *Vacuum* 190 (2021), p. 110278.

[58] E. Bauer, H. Poppa, G. Todd, et al. "Adsorption and condensation of Cu on W single-crystal surfaces". *Journal of Applied Physics* 45.12 (Oct. 2003), pp. 5164–5175. URL: https://doi.org/10.1063/1.1663211.

[59] A. Cetronio, J. P. Jones, and E. W. Roberts. "A study of copper adsorption on (100) tungsten by high field microscopy". *Surface Science* 52.3 (1975), pp. 473–488.

[60] B. Girault, P. Villain, E. Le Bourhis, et al. "X-ray diffraction analysis of the structure and residual stresses of W/Cu multilayers". *Surface and Coatings Technology* 201.7 (2006). Proceedings of the 33rd International Conference on Metallurgical Coatings and Thin Films, pp. 4372–4376. URL: https://www.sciencedirect.com/science/article/pii/S0257897206008541.

[61] B. Girault, D. Eyidi, T. Chauveau, et al. "Copper coverage effect on tungsten crystallites texture development in W/Cu nanocomposite thin films". *Journal of Applied Physics* 109.1 (2011).

[62] E. Z. Luo, Q. Cai, W. F. Chung, et al. "Competing desorption pathways during epitaxial growth: LEEM investigation of Cu/W (110) heteroepitaxy". *Physical Review B* 54.20 (1996), p. 14673.

[63] A. J. Melmed. "Adsorption and surface diffusion of copper on tungsten". *The Journal of Chemical Physics* 43.9 (1965), pp. 3057–3062.

[64] A. R. L. Moss and B. H. Blott. "The epitaxial growth of copper on the (110) surface of a tungsten single crystal studied by LEED, Auger electron, and work function techniques". *Surface Science* 17.1 (1969), pp. 240–261.

[65] K. Reshöft, C. Jensen, and U. Köhler. "Atomistics of the epitaxial growth of Cu on W (110)". *Surface science* 421.3 (1999), pp. 320–336.

[66] N. J. Taylor. "A LEED Study of the Epitaxial Growth of Copper on the (110) Surface of Tungsten". *Surface Science* 4.2 (1966), pp. 161–194.

[67] S. P. Wen, R. L. Zong, F. Zeng, et al. "Evaluating modulus and hardness enhancement in evaporated Cu/W multilayers". *Acta Materialia* 55.1 (2007), pp. 345–351.

[68] H. Wormeester, E. Hüger, and E. Bauer. "hcp and bcc Cu and Pd films". *Phys. Rev. Lett.* 77.8 (1996), p. 1540.

[69] C. P. Liang, J. L. Fan, H. R. Gong, et al. "Interface structure and work function of W-Cu interfaces". *Appl. Phys. Lett.* 103.21 (2013), p. 211604. URL: https://doi.org/10.1063/1.4833249.

[70] G. C. Ma, J. L. Fan, and H. R. Gong. "Fundamental effects of hydrogen on cohesion properties of Cu/W interfaces". *Solid State Communications* 250 (2017), pp. 79–83. URL: https://doi.org/10.1016/j.ssc.2016.11.018.

[71] R. Bodlos, V. Fotopoulos, J. Spitaler, et al. "Energies and structures of Cu/Nb and Cu/W interfaces from density functional theory and semi-empirical calculations". *Materialia* 21 (2022), p. 101362.

[72] Q. Yang, Ch. Lu, Y. Han, et al. "Influence of Cu/W interfacial structure on the resistance against harmful helium atoms: A mechanism analysis". *J. Alloy. and Compd.* 903 (2022), p. 163817. URL: https://doi.org/10.1016/j.jallcom.2022.163817.

[73] H. B. Zhou, Y. Zhang, and X. Ou. "Dissolution and diffusion behaviors of hydrogen in copper: A first-principles investigation". *Comp. Mater. Sci.* 79 (2013), pp. 923–928. URL: https://doi.org/10.1016/j.commatsci.2013.08.002.

[74] J. W. Wang, J. L. Fan, and H. R. Gong. "Effects of Zr alloying on cohesion properties of Cu/W interfaces". *Journal of Alloys and Compounds* 661 (2016), pp. 553–556.

[75] P. A. M. Dirac. *The principles of Quantum Mechanics*. Fourth Edition. Oxford University Press, 1958, pp. 1–323.

[76] I. N. Levine. *Quantum Chemistry*. Seventh Edition. Pearson, 2013.

[77] M. Planck. "Zur theorie des gesetzes der energieverteilung im normalspektrum". *Berlin* (1900), pp. 237–245.

[78] A. Einstein. "The photoelectric effect". *Annal der Physik* 17.132 (1905), p. 4.

[79] W. Heisenberg. "Über den anschaulichen Inhalt der quantentheoretischen Kinematik und Mechanik". *Zeitschrift für Physik* 43 (1927), pp. 172–198.

[80] E. Schrödinger. "An undulatory theory of the mechanics of atoms and molecules". *Physical review* 28.6 (1926), p. 1049.

[81] W. Koch and M. C. Holthausen. *A chemist's guide to density functional theory*. John Wiley & Sons, 2015.

[82] M. Born and J. R. Oppenheimer. "Zur Quantentheorie der Molekeln". *Annalen der Physik* 389.20 (1927), pp. 457–484.

[83] V. Volterra. *Theory of functionals*. New York: Dover, 1959.

[84] C. C. J. Roothaan. "New developments in molecular orbital theory". *Reviews of modern physics* 23.2 (1951), p. 69.

[85] D. P. Bertsekas. *Constrained optimization and Lagrange multiplier methods*. Academic press, 2014.

[86] R. F. W. Bader. *An introduction to the electronic structure of atoms and molecules*. Clarke, Irwin, 1970.

[87] E. Davidson. *Reduced density matrices in quantum chemistry*. Vol. 6. Elsevier, 2012.

[88] R. McWeeny. "Some recent advances in density matrix theory". *Reviews of Modern Physics* 32.2 (1960), p. 335.

[89] E. J. Baerends and O. V. Gritsenko. "A quantum chemical view of density functional theory". *The Journal of Physical Chemistry A* 101.30 (1997), pp. 5383–5403.

[90] L. H. Thomas. "The calculation of atomic fields". *Mathematical proceedings of the Cambridge philosophical society*. Vol. 23. 5. Cambridge University Press. 1927, pp. 542–548.

[91] E. Fermi. "Un Metodo Statistico per la Determinazione di alcune Prioprieta dell'Atomo". *Rend. Accad. Naz. Lincei* 6 (1927), pp. 602–607.

[92] E. Fermi. "Sulla deduzione statistica di alcune proprietá dell'atomo. Applicazione alla teoria del sistema periodico degli elementi". *Rend. Lincei* 7 (1928), p. 342.

[93] P. A. M. Dirac. "Note on exchange phenomena in the Thomas atom". *Mathematical proceedings of the Cambridge philosophical society*. Vol. 26. 3. Cambridge University Press. 1930, pp. 376–385.

[94] J. C. Slater. "A simplification of the Hartree-Fock method". *Physical review* 81.3 (1951), p. 385.

[95] P. Hohenberg and W. Kohn. "Inhomogeneous electron gas". *Physical review* 136.3B (1964), B864.

[96] M. Levy. "Universal variational functionals of electron densities, first-order density matrices, and natural spin-orbitals and solution of the v-representability problem". *Proceedings of the National Academy of Sciences* 76.12 (1979), pp. 6062–6065.

[97] M. Levy. "Electron densities in search of Hamiltonians". *Physical Review A* 26.3 (1982), p. 1200.

[98] R. G. Parr and Y. Weitao. *Density-Functional Theory of Atoms and Molecules*. Oxford University Press, 1989.

[99] P. Hohenberg and W. Kohn. "Inhomogeneous Electron Gas". *Physical Review* 136.3B (1964), B864–B871.

[100] D. M. Ceperley and B. J. Alder. "Ground state of the electron gas by a stochastic method". *Physical review letters* 45.7 (1980), p. 566.

[101] J. P. Perdew. "Accurate density functional for the energy: Real-space cutoff of the gradient expansion for the exchange hole". *Physical Review Letters* 55.16 (1985), p. 1665.

[102] J. P. Perdew and W. Yue. "Accurate and simple density functional for the electronic exchange energy: Generalized gradient approximation". *Physical review B* 33.12 (1986), p. 8800.

[103] A. D. Becke. "Density-functional exchange-energy approximation with correct asymptotic behavior". *Physical review A* 38.6 (1988), p. 3098.

[104] M. Filatov and W. Thiel. "A new gradient-corrected exchange-correlation density functional". *Molecular Physics* 91.5 (1997), pp. 847–860.

[105] J. P. Perdew. "Unified theory of exchange and correlation beyond the local density approximation". *Electronic structure of solids' 91* 11 (1991).

[106] K. Burke, J. P. Perdew, and Y. Wang. "Derivation of a generalized gradient approximation: The PW91 density functional". *Electronic Density Functional Theory: recent progress and new directions*. Springer, 1998, pp. 81–111.

[107] G. J. Laming, V. Termath, and N. C. Handy. "A general purpose exchange-correlation energy functional". *The Journal of chemical physics* 99.11 (1993), pp. 8765–8773.

[108] A. D. Becke. "Density functional calculations of molecular bond energies". *The Journal of Chemical Physics* 84.8 (1986), pp. 4524–4529.

[109] J. P. Perdew. "Density-functional approximation for the correlation energy of the inhomogeneous electron gas". *Physical review B* 33.12 (1986), p. 8822.

[110] D. J. Lacks and R. G. Gordon. "Pair interactions of rare-gas atoms as a test of exchange-energy-density functionals in regions of large density gradients". *Physical Review A* 47.6 (1993), p. 4681.

[111] J. P. Perdew, K. Burke, and M. Ernzerhof. "Generalized gradient approximation made simple". *Physical review letters* 77.18 (1996), p. 3865.

[112] J. P Perdew and Y. Wang. "Accurate and simple analytic representation of the electron-gas correlation energy". *Physical review B* 45.23 (1992), p. 13244.

[113] Ch. Lee, W. Yang, and R. G. Parr. "Development of the Colle-Salvetti correlation-energy formula into a functional of the electron density". *Physical review B* 37.2 (1988), p. 785.

[114] Z. A. Piazza, R. D. Kolasinski, M. Ajmalghan, et al. "Predictive Atomistic Model for Hydrogen Adsorption on Metal Surfaces: Comparison with Low-Energy Ion Beam Analysis on Tungsten". *J. Phys. Chem. C* 125 (2021), pp. 16086–16096.

[115] K. Heinola and T. Ahlgren. "Diffusion of hydrogen in bcc tungsten studied with first principle calculations". *Journal of Applied Physics* 107.11 (June 2010), p. 113531. URL: https://doi.org/10.1063/1.3386515.

[116] N. Fernandez, Y. Ferro, and D. Kato. "Hydrogen diffusion and vacancies formation in tungsten: density functional theory calculations and statistical models". *Acta Materialia* 94 (2015), pp. 307–318.

[117] J. P. Perdew, M. Ernzerhof, and K. Burke. "Rationale for mixing exact exchange with density functional approximations". *The Journal of chemical physics* 105.22 (1996), pp. 9982–9985.

[118] J. P. Perdew, M. Ernzerhof, K. Burke, et al. "On-top pair-density interpretation of spin density functional theory, with applications to magnetism". *International journal of quantum chemistry* 61.2 (1997), pp. 197–205.

[119] C. Adamo and V. Barone. "Toward reliable density functional methods without adjustable parameters: The PBE0 model". *The Journal of chemical physics* 110.13 (1999), pp. 6158–6170.

[120] J. P. Perdew, S. Kurth, A. Zupan, et al. "Accurate density functional with correct formal properties: A step beyond the generalized gradient approximation". *Physical review letters* 82.12 (1999), p. 2544.

[121] E. I. Proynov, A. Vela, and D. R. Salahub. "Nonlocal correlation functional involving the Laplacian of the density". *Chemical physics letters* 230.4-5 (1994), pp. 419–428.

[122] R. M. Martin. *Electronic structure: basic theory and practical methods*. Cambridge university press, 2020.

[123] Neil W Ashcroft and N David Mermin. *Solid state physics*. Cengage Learning, 2022.

[124] L. Kantorovich. *Quantum theory of the solid state: an introduction*. Vol. 136. Springer Science & Business Media, 2004.

[125] S. L. Altmann. *Band theory of solids an introduction from the point of view of symmetry*. Oxford University Press, 1991.

[126] B. L. Bramfitt. "The effect of carbide and nitride additions on the heterogeneous nucleation behavior of liquid iron". *Metallurgical Transactions* 1 (1970), pp. 1987–1995. URL: https://doi.org/10.1007/BF02642799.

[127] D. Turnbull and B. Vonnegut. "Nucleation catalysis." *Industrial & Engineering Chemistry* 44.6 (1952), pp. 1292–1298.

[128] K. Momma and F. Izumi. "VESTA 3 for three-dimensional visualization of crystal, volumetric and morphology data". *Journal of applied crystallography* 44.6 (2011), pp. 1272–1276.

[129] K. Anton. "XCrySDen—a new program for displaying crystalline structures and electron densities". *Journal of Molecular Graphics and Modelling* 17.3 (1999), pp. 176–179.

[130] G. Kurdjumov and G. Sachs. "Over the mechanisms of steel hardening". *Z. Phys* 64.325-343 (1930).

[131] Z. Nishiyama. "X-ray investigation of the mechanism of the transformation from face centered cubic lattice to body centered cubic". *Sci. Rep. Tohoku Univ.* 23 (1934), p. 637.

[132] I. J. Beyerlein, N. A. Mara, J. Wang, et al. "Structure–property–functionality of bimetal interfaces". *Jom* 64 (2012), pp. 1192–1207.

[133] S. Zheng, J. S Carpenter, R. J. McCabe, et al. "Engineering interface structures and thermal stabilities via SPD processing in bulk nanostructured metals". *Scientific reports* 4.1 (2014), p. 4226.

[134] Z. A. Piazza, M. Ajmalghan, Y. Ferro, et al. "Saturation of tungsten surfaces with hydrogen: A density functional theory study complemented by low energy ion scattering and direct recoil spectroscopy data". *Acta Materialia* 145 (2018), pp. 388–398. URL: https://doi.org/10.1016/j.actamat.2017.12.029.

[135] Z. A. Piazza, R. D. Kolasinski, M. Ajmalghan, et al. "Predictive atomistic model for hydrogen adsorption on metal surfaces: Comparison with low-energy ion beam analysis on tungsten". *The Journal of Physical Chemistry C* 125.29 (2021), pp. 16086–16096. URL: https://doi.org/10.1021/acs.jpcc.1c01068.

[136] K. Heinola and T. Ahlgren. "First-principles study of H on the reconstructed W(100) surface". *Phys. Rev. B* 81 (7 Feb. 2010), p. 073409. URL: https://link.aps.org/doi/10.1103/PhysRevB.81.073409.

[137] P. Giannozzi, O. Andreussi, T. Brumme, et al. "Advanced capabilities for materials modelling with Quantum ESPRESSO". *J.Phys.: Condens. Matter* 29.46 (2017), p. 465901.

[138] D. Vanderbilt. "Soft self-consistent pseudopotentials in a generalized eigenvalue formalism". *Physical review B* 41.11 (1990), p. 7892.

[139] J. P. Perdew, K. Burke, and M. Ernzerhof. "Generalized Gradient Approximation made simple". *Phys. Rev. Lett.* 77.18 (1996), pp. 3865–3868. URL: https://doi.org/10.1103/PhysRevLett.77.3865.

[140] Y. Ferro, E. A. Hodille, J. Denis, et al. "Hydrogen and oxygen on tungsten (110) surface: adsorption, absorption and desorption investigated (vol 63, 036017, 2023)". *Nuclear fusion* 63.4 (2023).

[141] Y. Fukai. *The metal-hydrogen system: basic bulk properties*. Vol. 21. Springer Science & Business Media, 2006.

[142] H. Robbins. "A Remark on Stirling's Formula". *The American Mathematical Monthly* 62.1 (1955), pp. 26–29. URL: http://www.jstor.org/stable/2308012 (visited on 02/12/2024).

[143] A. Glensk, B. Grabowski, T. Hickel, et al. "Breakdown of the Arrhenius law in describing vacancy formation energies: The importance of local anharmonicity revealed by ab initio thermodynamics". *Physical Review X* 4.1 (2014), p. 011018.

[144] D. Shaw. *Atomic diffusion in semiconductors*. Springer Science & Business Media, 2012.

[145] R. Frauenfelder. "Solution and Diffusion of Hydrogen in Tungsten". *Journal of Vacuum Science and Technology* 6.3 (May 1969), pp. 388–397. URL: https://doi.org/10.1116/1.1492699.

[146] A. P. Zakharov, V. M. Sharapov, and E. I. Evko. "Hydrogen permeability of polycrystalline and monocrystalline molybdenum and tungsten". *Soviet materials science: a transl. of Fiziko-khimicheskaya mekhanika materialov/Academy of Sciences of the Ukrainian SSR* 9 (1975), pp. 149–153.

[147] G. Benamati, E. Serra, and C. H. Wu. "Hydrogen and deuterium transport and inventory parameters through W and W-alloys for fusion reactor applications". *Journal of nuclear materials* 283 (2000), pp. 1033–1037.

[148] G. Holzner, T. Schwarz-Selinger, T. Dürbeck, et al. "Solute diffusion of hydrogen isotopes in tungsten—a gas loading experiment". *Physica Scripta* 2020.T171 (2020), p. 014034. URL: https://dx.doi.org/10.1088/1402-4896/ab4b42.

[149] W. Eichenauer, W. Löser, and H. Witte. "Löslichkeit und diffusionsgeschwindigkeit von wasserstoff und deuterium in einkristallen aus nickel und kupfer". *International Journal of Materials Research* 56.5 (1965), pp. 287–293.

[150] L. Katz, M. Guinan, and R. J. Borg. "Diffusion of H2, D2, and T2 in single-crystal Ni and Cu". *Physical Review B* 4.2 (1971), p. 330.

[151] Y. Sakamoto and K. Takao. "The electrochemical determination of diffusivity and solubility of hydrogen in copper". *J. Japan Inst. Metals* 46.3 (1982), pp. 285–290.

[152] T. Ishikawa and R. B. McLellan. "The diffusivity of hydrogen in copper at low temperatures". *Journal of Physics and Chemistry of Solids* 46.4 (1985), pp. 445–447.

[153] E. Serra, G. Benamati, and O. V. Ogorodnikova. "Hydrogen isotopes transport parameters in fusion reactor materials". *Journal of nuclear materials* 255.2-3 (1998), pp. 105–115.

[154] C. Wert and C. Zener. "Interstitial Atomic Diffusion Coefficients". *Phys. Rev.* 76 (8 1949), pp. 1169–1175. URL: https://link.aps.org/doi/10.1103/PhysRev.76.1169.

[155] S. Arrhenius. "Über die Reaktionsgeschwindigkeit bei der Inversion von Rohrzucker durch Säuren". *Zeitschrift für physikalische Chemie* 4.1 (1889), pp. 226–248.

[156] Weinan E, Weiqing Ren, and Eric Vanden-Eijnden. "String method for the study of rare events". *Phys. Rev. B* 66 (5 2002), p. 052301. URL: https://link.aps.org/doi/10.1103/PhysRevB.66.052301.

[157] Y. Kanai, A. Tilocca, A. Selloni, et al. "First-principles string molecular dynamics: An efficient approach for finding chemical reaction pathways". *The Journal of Chemical Physics* 121.8 (Aug. 2004), pp. 3359–3367. URL: https://doi.org/10.1063/1.1773159.

[158] S. Glasstone, K. J. Laidler, and H. Eyring. *The theory of rate processes: the kinetics of chemical reactions, viscosity, diffusion and electrochemical phenomena*. New York & London, 1941.

[159] E. A. Hodille, Y. Ferro, Z. A. Piazza, et al. "Hydrogen in beryllium oxide investigated by DFT: on the relative stability of charged-state atomic versus molecular hydrogen". *Journal of Physics: Condensed Matter* 30.30 (2018), p. 305201.

[160] Y. Silva-Solís, J. Denis, E. Hodille, et al. "Solution and solubility of H atoms at the W/Cu interface". *Journal of Physics: Condensed Matter* 36.46 (2024), p. 465001.

[161] W. Bollmann. *Crystal defects and crystalline interfaces*. Springer Science & Business Media, 2012.

[162] D. A. Smith and R. C. Pond. "Bollmann's 0-Iattice theory; a geometrical approach to interface structure". *International Metals Reviews* 21.1 (1976), pp. 61–74.

[163] C. W. Greeff, J. C. Boettger, M. J. Graf, et al. "Theoretical investigation of the Cu EOS standard". *Journal of Physics and Chemistry of Solids* 67.9-10 (2006), pp. 2033–2040.

[164] J. C. Boettger. "Theoretical calculation of the zero-temperature isotherm and phase stability of silver up to 2 Gbar using the linear combinations of gaussian type orbitals method". *International Journal of Quantum Chemistry* 112.24 (2012), pp. 3822–3828.

[165] M. I. Mendelev and A. H. King. "The interactions of self-interstitials with twin boundaries". *Philosophical Magazine* 93.10-12 (2013), pp. 1268–1278.

[166] A. P. Thompson, H. M. Aktulga, R. Berger, et al. "LAMMPS - a flexible simulation tool for particle-based materials modeling at the atomic, meso, and continuum scales". *Comp. Phys. Comm.* 271 (2022), p. 108171.

[167] A. Stukowski. "Visualization and analysis of atomistic simulation data with OVITO–the Open Visualization Tool". *Modelling and simulation in materials science and engineering* 18.1 (2009), p. 015012.

[168] M. S. Daw and M. I. Baskes. "Semiempirical, quantum mechanical calculation of hydrogen embrittlement in metals". *Physical review letters* 50.17 (1983), p. 1285.

[169] M. S. Daw and M. I. Baskes. "Embedded-atom method: Derivation and application to impurities, surfaces, and other defects in metals". *Physical Review B* 29.12 (1984), p. 6443.

[170] M. I. Mendelev, M. J. Kramer, Chandler A. Becker, et al. "Analysis of semi-empirical interatomic potentials appropriate for simulation of crystalline and liquid Al and Cu". *Philosophical Magazine* 88.12 (2008), pp. 1723–1750.

[171] M. J. Stott and E. Zaremba. "Quasiatoms: An approach to atoms in nonuniform electronic systems". *Physical Review B* 22.4 (1980), p. 1564.

[172] J. K. Nørskov. "Covalent effects in the effective-medium theory of chemical binding: Hydrogen heats of solution in the 3 d metals". *Physical Review B* 26.6 (1982), p. 2875.

[173] E. A. Hodille, R. Delaporte-Mathurin, J. Denis, et al. "Modelling of hydrogen isotopes trapping, diffusion and permeation in divertor monoblocks under ITER-like conditions". *Nuclear Fusion* 61.12 (2021), p. 126003.

[174] S. Nosé. "A molecular dynamics method for simulations in the canonical ensemble". *Molecular Physics* 52.2 (1984), pp. 255–268.

[175] W. G. Hoover. "Canonical dynamics: Equilibrium phase-space distributions". *Phys. Rev. A* 31 (3 1985), pp. 1695–1697.

[176] J. D. Honeycutt and H. C. Andersen. "Molecular dynamics study of melting and freezing of small Lennard-Jones clusters". *Journal of Physical Chemistry* 91.19 (1987), pp. 4950–4963.

[177] D. Faken and H. Jónsson. "Systematic analysis of local atomic structure combined with 3D computer graphics". *Computational Materials Science* 2.2 (1994), pp. 279–286.

[178] A. Stukowski. "Structure identification methods for atomistic simulations of crystalline materials". *Modelling and Simulation in Materials Science and Engineering* 20.4 (2012), p. 045021.

[179] *OVITO - Open Visualization Tool*. URL: `https://www.ovito.org/` (visited on 2024).

[180] A. Stukowski and K. Albe. "Extracting dislocations and non-dislocation crystal defects from atomistic simulation data". *Modelling and Simulation in Materials Science and Engineering* 18.8 (2010), p. 085001.

[181] A. Stukowski, V. V. Bulatov, and A. Arsenlis. "Automated identification and indexing of dislocations in crystal interfaces". *Modelling and Simulation in Materials Science and Engineering* 20.8 (2012), p. 085007.

[182] M. L. dos Reis. "Étude de l'interaction dislocation-amas de lacunes par simulations numériques". PhD thesis. Université Paris Saclay (COmUE), 2019.

[183] P. M. Larsen, S. Schmidt, and J. Schiøtz. "Robust structural identification via polyhedral template matching". *Modelling and Simulation in Materials Science and Engineering* 24.5 (2016), p. 055007.

[184] A. Szabo and N. S. Ostlund. *Modern quantum chemistry: introduction to advanced electronic structure theory*. Courier Corporation, 2012.

[185] M. Weissbluth. *Atoms and molecules*. Elsevier, 2012.